FOSSIL ENERGY

DOE/BC/14446-10
(DE94000121)

DEVELOPMENT OF NUCLEAR MAGNETIC RESONANCE IMAGING/SPECTROSCOPY FOR IMPROVED PETROLEUM RECOVERY

Final Report

By
M.A. Barrufet
R.W. Flumerfelt
M.P. Walsh
A.T. Watson

April 1994

Performed Under Contract No. DE-FG22-89BC14446

Texas A&M University
College Station, Texas

Bartlesville Project Office
U. S. DEPARTMENT OF ENERGY
Bartlesville, Oklahoma

DOE/BC/14446-10
Distribution Category UC-122

Development of Nuclear Magnetic Resonance Imaging/Spectroscopy for Improved Petroleum Recovery

Final Report

By
M.A. Barrufet
R.W. Flumerfelt
M.P. Walsh
A.T. Watson

April 1994

Work Performed Under Contract No. DE-FG22-89BC14446

Prepared for
U.S. Department of Energy
Assistant Secretary for Fossil Energy

Chandra Nautiyal, Project Manager
Bartlesville Project Office
P.O. Box 1398
Bartlesville, OK 74005

Prepared by
Texas A&M University
College Station, TX 77843

CONTENTS

LIST OF FIGURES

Subtask 1

Subtask 2

Subtask 3

Subtask 4

LIST OF TABLES

Subtask 1

Subtask 2

Subtask 3

Subtask 4

ABSTRACT

The overall objectives of this program are to develop and apply Nuclear Magnetic Resonance Imaging (NMRI) and CT X-Ray Scanning methods for determining rock, fluid, and petrophysical properties and for fundamental studies of multiphase flow behavior in porous media. Specific objectives are divided into four subtasks:

(1) Subtask 1: The development of NMRI and CT scanning for the determination of rock-fluid and petrophysical properties

The initial stage of this research involved measurement of porosity and two-phase saturations of reservoir rocks on a global and on a local basis. From the distribution of these properties within core samples, a statistical measure of the heterogeneity of the core, called the correlation length, was developed. Secondly, we designed and built a core holder suitable for NMR experiments which can withstand pressures up to 2000 psia. Thirdly, we used NMRI and conventional techniques to evaluate the effectiveness of a biopolymer as a mobility control agent in enhanced oil recovery processes.

(2) Subtask 2: Development of NMRI and CT scanning for characterizing conventional multiphase displacement processes

Experimental methods and computational procedures were developed for acquiring and analyzing fluid phase distributions during two-phase immiscible fluid displacements in order to estimate porosity and saturation distributions with great accuracy. Other computational procedures were developed for estimating two- and three-phase relative permeability functions from displacement data that includes those measures of the saturation distribution. New approaches for characterization of fluid distributions and pore structures using NMR relaxation and restricted diffusion measurements were investigated. In particular, apparent diffusivities were introduced for characterizing pore sizes in different model porous media. Methods for analyzing diffusivity distributions, arising from diffusional processes in different compartments of fluids, were developed. In addition, saturation-dependent relaxation measurements were carried out to study fluid distributions at different saturation levels. Computational procedures for obtaining those distributions were developed.

(3) Subtask 3: Development of NMR and CT scanning for characterizing dispersed phase processes

In subtask 3, we have successfully developed the technique of using NMR relaxation methods to characterize wettability of porous media. The method has been thoroughly investigated in model porous systems with different surface wettability properties. Through these extensive and systematic studies, we have clarified some confusion on this technique caused by previous researches. We have also tested this technique on rock samples. We demonstrated that the NMR relaxation method can become a fast and convenient tool for characterizing wettability of porous media. To enhance the oil recovery in fractured, low permeability reservoirs, we studied a surfactant based imbibition/solution gas drive process. NMR imaging is a powerful tool for studying such processes. Very encouraging results were obtained which revealed the potential use of this new process for enhanced oil recovery. We also used NMR restricted diffusion and X-ray CT scanning methods to study the behavior of dispersed phases in porous

media. The data provided by these studies are of great importance in developing improved theories of dispersed phase flow in porous media.

(4) Subtask 4: Miscible displacement studies.

Miscible flooding is a form of enhanced oil recovery whereby injected solvents are miscible, or develop miscibility, with the in-place oil. Miscible flooding is complicated by the formation of viscous fingers which lower volumetric sweep efficiency and ultimately lower oil recovery. The objectives of Subtask 4 are: (1) to develop the CT scanner as a general tool to study flow in porous media, with specific interest for studying miscible displacement and (2) to demonstrate the utility of the CT apparatus by studying the mechanics of viscous fingering. We have successfully developed the CT scanner by developing viable experimental procedures and equipment. These include: (1) designing a core containment device, (2) designing a flow system, (3) developing viable CT scanner operating procedures, (4) developing data transfer procedures from the CT scanner to post-processors, and (5) developing post-processing software for image reconstruction. Our experimental methods have been tested by successfully applying the CT scanner to study viscous fingering in laboratory core samples. The utility of the CT scanner is demonstrated by showing two-dimensional cross-sectional images of viscous fingers using state-of-the-art image processing software. This work contributes to our understanding of viscous fingering and will be helpful in future studies.

The final reports for each of the subtasks are provided in this document.

EXECUTIVE SUMMARY

The first overall objective is the development of Nuclear Magnetic Resonance Imaging (NMRI) and spectroscopy methods for characterizing porous media structures, fluid distributions, and fluid-rock interactions. The second overall objective is the application of NMRI and X-ray CT scanning to fundamental studies of multiphase flow in porous media. The research was organized along four subtasks.

The work in subtask 1 was directed to the determination of porosity distributions and the study of enhanced oil recovery using a biopolymer.

In subtask 2, a number of new methods have been developed for the determination of various petrophysical properties which are important for describing multiphase flow in porous media. Specifically, the following accomplishments were achieved. (1) Experimental and analysis procedures were developed for quantitative determination of porosity and fluid saturation distributions during static and dynamic flow experiments; the methods were used to analyze a number of structurally different rock samples, (2) pulsed field gradient diffusion measurements and computational analyses were developed and applied for the characterization of pore structures in model porous media and rock samples, and (3) a new approach for investigation of multiphase fluid distributions via NMR relaxation measurements at different saturation states was developed and empirical relationships between relaxation parameter and fluid saturation were obtained.

Subtask 3 was directed to developing new techniques and oil recovery processes for the oil industry. The objective of this subtask is to obtain a detailed understanding of the behavior and mechanisms of dispersed phase systems in porous media using advanced NMR and CT imaging methods. Three different projects are designed to achieve the overall objective: 1) characterization of fractional wettability of porous media using NMR relaxation methods; 2) study of a surfactant based imbibition and solution gas drive process using NMR imaging methods; and 3) study of dispersed phase flow in porous media using CT imaging methods. As indicated by our report, the prospect for future applications of these techniques is very encouraging.

In Subtask 4, we have successfully developed experimental methods to use the CT scanner as an effective instrument to study dynamic flow tests. Our developed experimental methods include: (1) designing a core containment device, (2) designing a flow system, (3) developing viable CT scanner operating procedures, (4) developing data transfer procedures from the CT scanner to post-processors, and (5) developing post-processing software for image reconstruction. We have tested our methods by successfully applying the CT scanner to study viscous fingering in laboratory core samples. The utility of the CT scanner is demonstrated by showing two-dimensional cross-sectional images of viscous fingers using state-of-the-art image processing software. This work contributes to our understanding of viscous fingering and will be helpful in future studies.

SUBTASK 1. THE DEVELOPMENT OF NMRI AND CT SCANNING FOR THE DETERMINATION OF ROCK-FLUID AND PETROPHYSICAL PROPERTIES

Principal Investigators: James W. Jennings (9/89-9/91)
Maria A. Barrufet (9/91-12/92)

Department of Petroleum Engineering

I. Objectives

Essential to the success of any reservoir management program is detailed knowledge of rock and fluid property variations within the reservoir. Conventional reservoir characterization techniques often do not take into account such spatial variability. The nature of the spatial variability of these properties on large and small scales affects significantly displacement performance.

The overall goal of this research proposal was to develop NMR/NMRI procedures to determine porosity, fluid saturations and permeability distributions within the reservoir rock. Subordinate objectives of this research were: (1) Assemble a flow system which will permit conducting two-phase immiscible flow displacement inside the magnet. (2) Develop NMR techniques that would allow the measurement of three-dimensional porosity and fluid saturations in the core sample during displacement. (3) Investigate various methods to refine and process the three dimensional NMRI data and investigate several data analysis techniques. (4) Develop an enhanced oil recovery (EOR) process that is cost-effective and environmentally safe using a modified biopolymer, and apply NMRI and conventional techniques to evaluate the effectiveness of the developed process over conventional EOR processes, and (5) develop NMR imaging and spectroscopic techniques to measure fluid self-diffusion coefficients and estimate porous media permeabilities.

Project Conduction

This project can be divided in two parts. The first part of the project started September 1989 and lasted until September 1991. This part was conducted by Professor James W. Jennings who upon retirement left the conduction of the project to Dr. Maria A. Barrufet, who conducted the project until its termination. That was a transition and decision time with a shift, or change, in some of the methodologies to accomplish basically the same goals.

After analyzing the research capabilities the overall objectives remained similar, although some intermediate steps needed to be redefined. New people were involved, some without NMR training, and therefore the projected completion times were stretched.

Dr. Maria A. Barrufet was involved with a refinement of objective (1), and with objectives (4) and (5). The following report contains the information that Dr. Maria A. Barrufet could gather from the first part of the project. A more complete description may appear in former reports submitted by Prof. James W. Jennings. Objectives (1), (4) and (5) concerning Dr. Barrufet's management of the project are explained with more detail in the following pages.

II. Part I of Subtask 1

Development of NMRI for the Determination of Porosity and Fluid Saturation Distributions

(From 9/89 to 9/91)

Principal Investigator: James W. Jennings

Experimental Work for Porosity Distribution

The preliminary work involved gathering a suite of cores representing various porosity distributions. This suite of cores included a wide range of lithologies including sandstones, dolomites, and limestones. A glass bead pack was also constructed using 3 mm diameter beads. The glass bead pack was used as a standard to verify the experimental procedures.

The experimental work initially involved the preparation of cores for three-dimensional porosity data acquisition. This consisted of cleaning the cores by extraction with toluene. Core samples were saturated with distilled water having a 0.005 M concentration of copper sulfate. Average porosities were determined for each core by the Modified Barnes Method.

The intensity of the recorded NMR signal consists of two components. The first component is the portion of the signal generated by the sample. The second component is the portion of the signal generated by the NMRI instrument itself and it is random. One of the major problems of this work was to minimize this random noise or to improve the signal-to-noise ratio.

In an effort to solve this problem the following techniques were tried:

1) Increase the number of data acquisitions from 1 to 4. The variance was reduced by half at the expense of increasing the imaging time by four.

2) Use block averaging. The variance is reduced but the cost is a coarser resolution from 0.106 mm^3 to 1.696 mm^3.

Currently, there are available more efficient pulsing techniques and a new coil design has been bought which will maximize the signal to noise ratio.

Porosity values for each core were measured using the NMR. Sizes of the cores were 1" in diameter by 3" in length. The data sets obtained consist of three-dimensional values in a 64x64x256 array. The resolution obtained for this array was approximately the same in all directions and was approximately 0.10 mm^3. To improve the signal-to-noise ratio, the data was collected using four signal averages.

An initial study was done to determine the magnitude of signal variation due to inherent noise in the NMR. This study was conducted using a homogeneous sample consisting of a vial containing a 0.005 M copper sulfate solution. Data sets were collected using a single signal acquisition. The results showed that the coefficient of variation for a single signal acquisition was 12% . The magnitude of this variation was determined to be

unacceptable. Therefore efforts were made to improve the signal to noise ratio of the data. Various methods were tried and it was determined that taking four signal acquisitions and averaging significantly improved this ratio. The coefficient of variation was reduced to 4%. Further improvements were made by increasing the number of signal averages beyond four. Due to time constraints, however, four signal averages was determined to be the optimum. To further reduce noise in the data, a block averaging technique was examined. This technique reduces noise but also decreases resolution. The final decision was made to use four signal averages along with block averaging over sixteen voxels. The combination of these two methods reduced the coefficient of variation to 1%. The resolution resulting from this block average was decreased from approximately 0.1 mm^3 to approximately 1 mm^3.

Three-dimensional porosity data sets have been collected on several core samples. The data sets consist of 64x64x256 arrays. Signal averaging and block averaging were applied to these data sets to reduce the signal to noise ratio. The resulting data sets consist of 32x32x64 arrays.

Table 1 indicates the improvement in the standard deviation obtained of the signals using four signal averages. The drawback however, was the increase in acquisition time.

	one signal average	four signal average
average value	1.03	1.04
standard deviation	0.13	0.07
variance	0.017	0.005
coefficient of variance	12.4%	6.1%
acquisition time	1.25 hour	5.0 hour

Table 1. Comparison of one signal average and four signal average.

Figures 1 and 2 show examples of porosity profiles obtained in the x-y plane at a distance of 20 mm into the core for Austin Chalk and for German sandstone. Further details of the procedures and results of this work can be found in the thesis work by Shivers [1].

Software has been developed that utilizes the localized porosity values to obtain this parameter. The process has been checked against known cases to verify the calculation procedure. Several cores were examined using this procedure and porosity correlation lengths determined.

Spatial statistics were used to characterize the porosity distribution of core size samples. A statistical summary of these spatial relationships provided a more sound method of heterogeneity estimation [2].

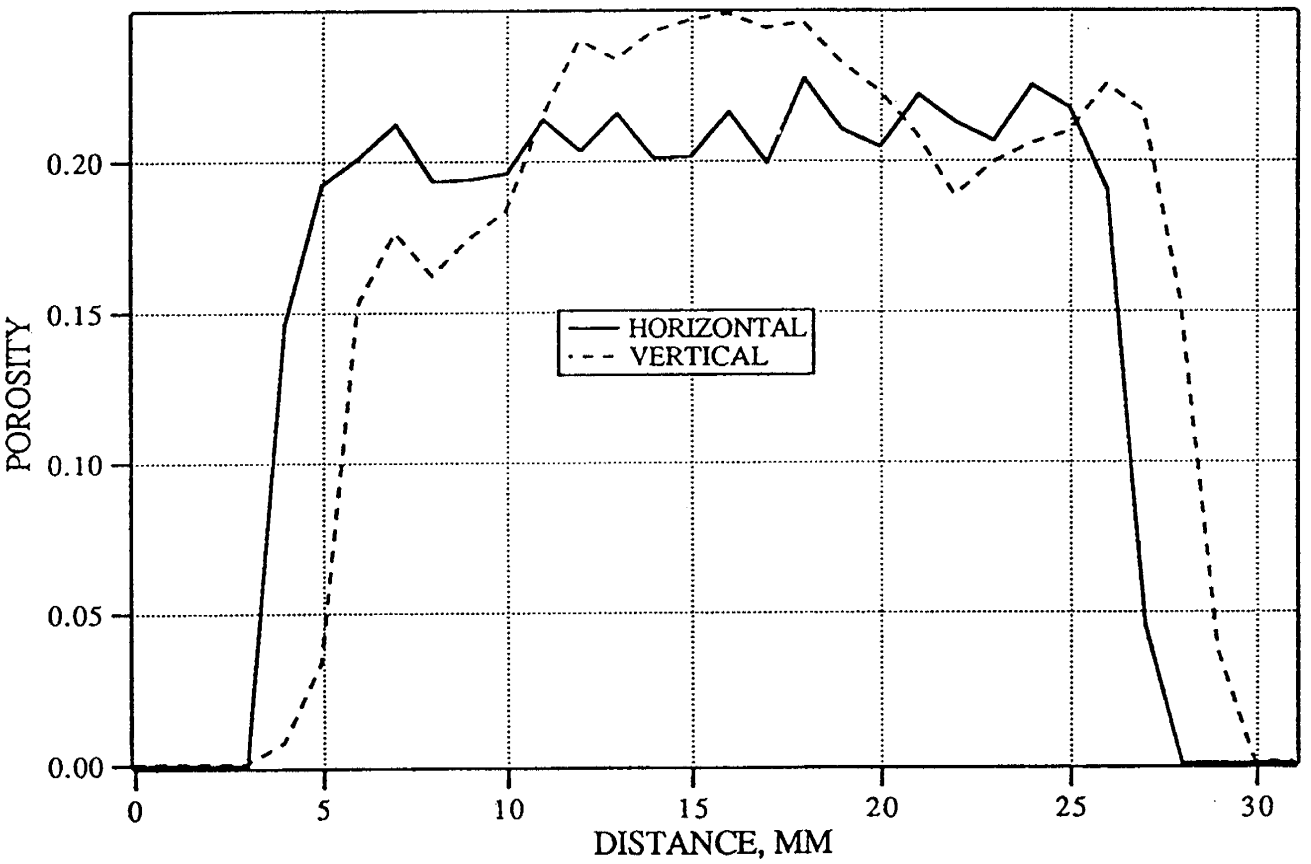

Figure 1. Austin chalk profile slice 20 mm.

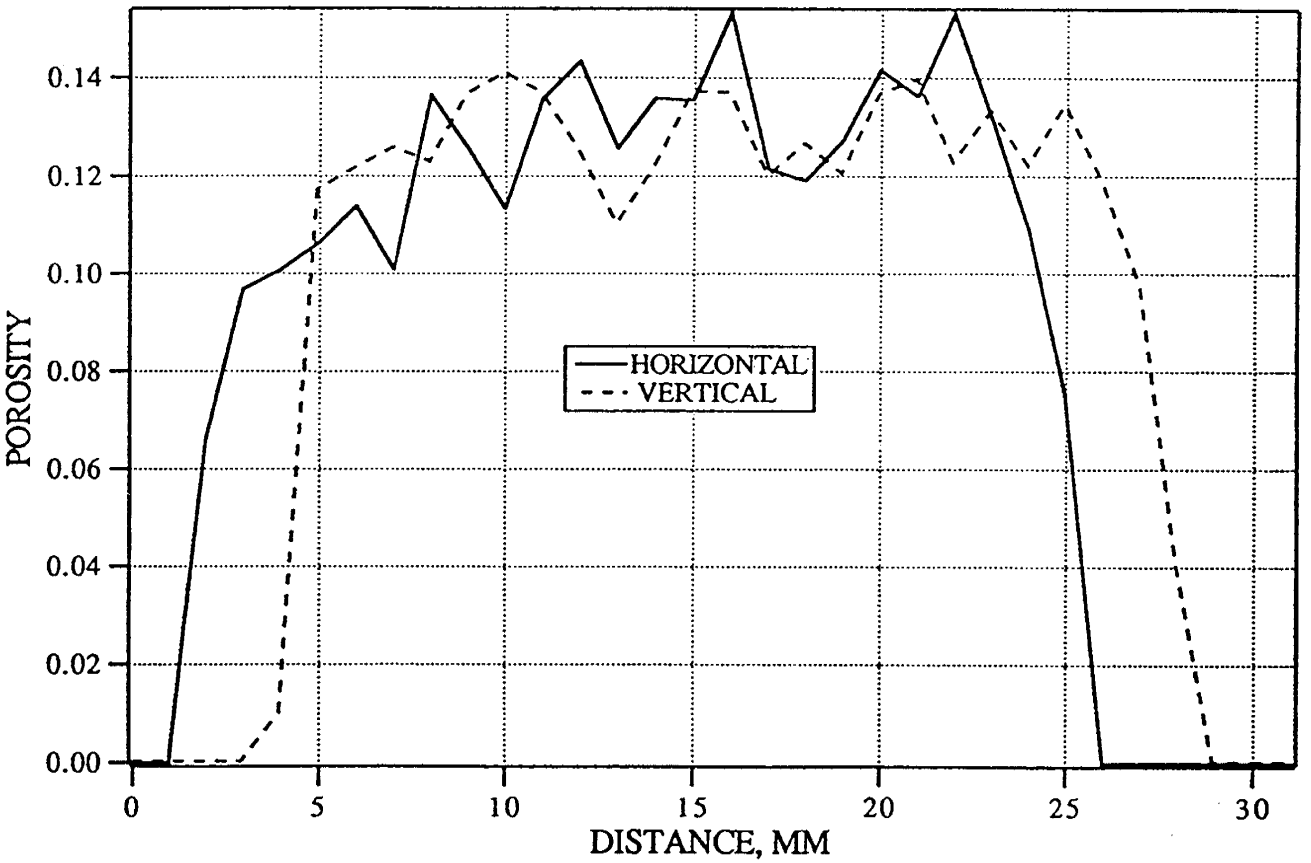

Figure 2. German sandstone profile slice 20 mm.

A method to describe heterogeneities in core samples based on the porosity distribution was developed. This method involves a graphical technique whereby the correlation of porosities at different distances can be displayed. The correlating function is given by the following:

$$2\,A(h) = (1 / N(h))\, S\, (f(r) - f(r+h))^2,$$

where N(h) is the number of samples separated by the distance h, f(r) and f(r+h) are the values of porosity measured at a distance h apart. Application of this technique provides information about the distance between the correlated and uncorrelated points. High correlation between neighboring points is expected for small values of h, while for large values of h the porosities become independent of one another and the variability reaches a maximum equal to the sample variance. The distance at which the dependence between neighboring points disappears is called the correlation length.

NMR Flow-Experiments for Saturation Distribution

Three-dimensional saturation distributions were obtained for Austin chalk cores and composite cores. The purpose of the analysis was to determine the effect of the displacement process on the saturation.

The experimental procedure allowed a determination of two-phase saturation distributions during an immiscible displacement process .

Three-dimensional saturation data sets were collected on cores with various porosity distributions as well as composite cores with two distributions. This preliminary analysis includes correlating the two-phase saturation distributions with the results from the porosity distribution experiments.

Saturation profiles for various cores were compared with porosity distributions. Saturation values are essentially uniform at breakthrough regardless of the core average porosity, suggesting that porosity does not affect the saturation distribution during the initial stages of the displacement process. Non-uniformity of water saturations at gas floodout suggest that the porosity distributions affect the saturation distribution towards the end of the displacement process. Again, additional data is required at a variety of confining pressures and displacement fluid flow rates.

This constraint pointed to the need for building an appropriate core holder for more realistic reservoir pressures. The maximum achievable pressure at that time was below 200 psia.

Saturation and porosity profiles in the directions perpendicular to flow (x and y) as well as parallel to the flow direction (z) were reported for a variety of core samples. The saturation profiles, under the process conditions used, in the x- and y- directions do not show a significant channeling or fingering. Figures 3 and 4 show examples of these distributions at breakthrough and floodout for an Austin Chalk core sample and a composite core. These figures were included in the third quarterly report. Additional details of this work can be found in the thesis work of Sherman[3] and Marek.[4]

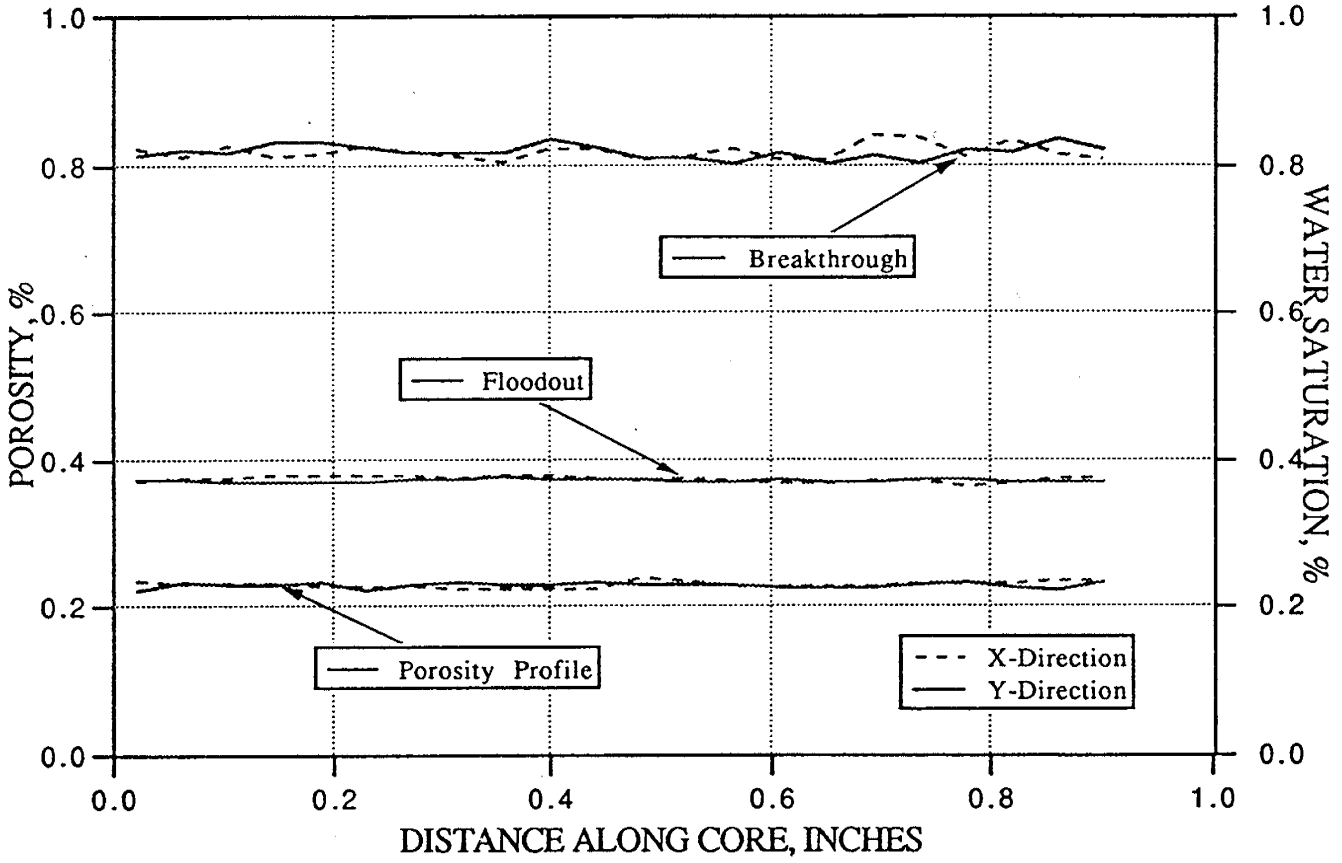

Figure 3. Austin chalk saturation profile in the X- and Y- directions.

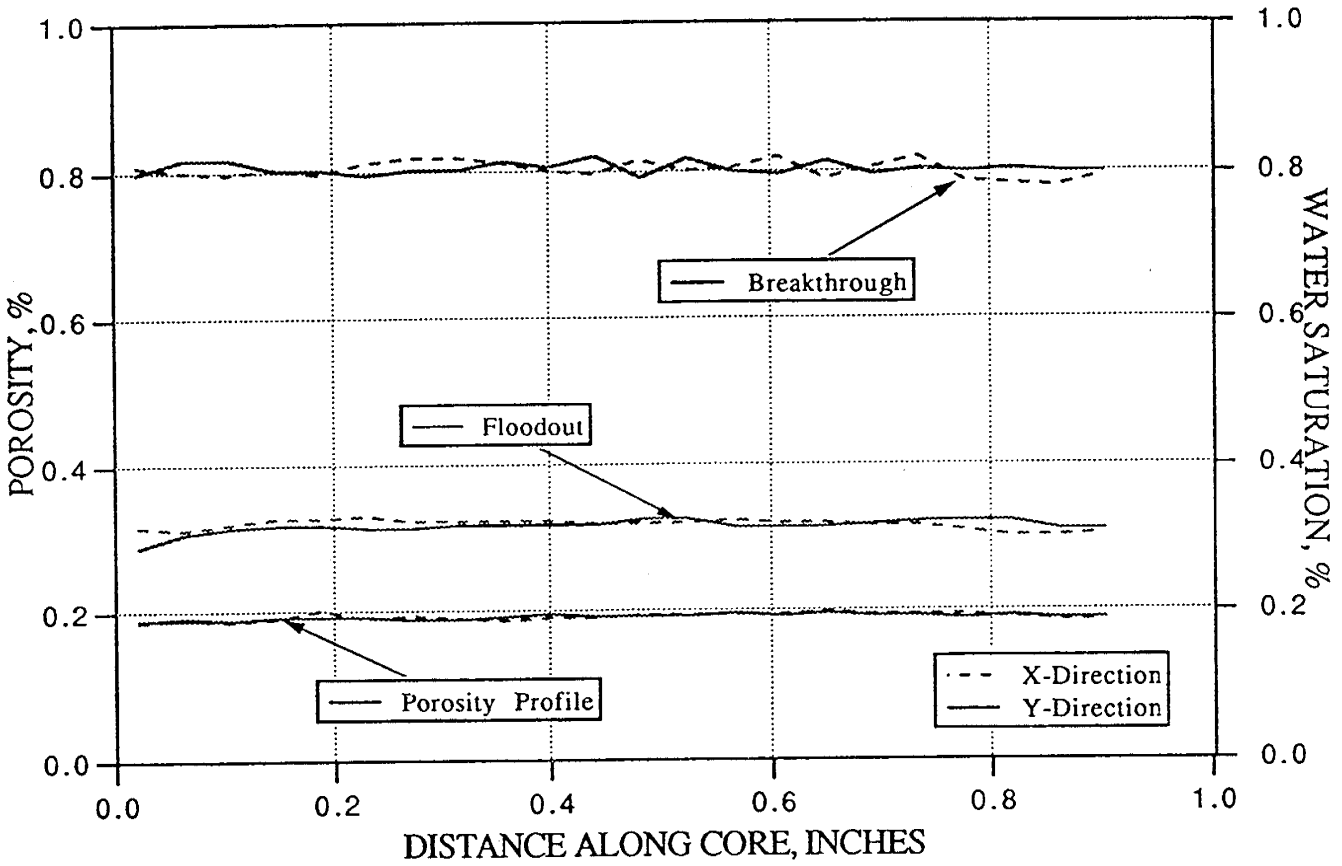

Figure 4. Composite saturation profiles in the X- and Y- directions.

Statistical Analysis and Software Development

The students Matt Marek and Blake Shivers developed algorithms for reading 3-D local porosity data and converting it to profile data to have it ready for further statistical manipulation. The transformation of the raw NMR signal to useful data appears not to be applicable to other forms of NMR sequences.

The graduate student Blake Shivers applied spatial statistics to summarize the spatial variability of porosity in reservoir rocks. These statistical indicators provide a means for quantifying the similarity between sample values as a function of the distance between their locations. The statistical indicators were: the h-scatterplot, correlation coefficient, autocorrelation, semivariance and porosity correlation length.

III. Part II of Subtask 1

NMR/NMRI Permeability Studies Using Biopolymers for Vertical Profile Modification

(From 9/91 to 12/92)

Principal Investigator: Maria A. Barrufet

Department of Petroleum Engineering

Objectives

The determination of permeabilities and permeability distributions for core samples were among the original goals of this project. To accomplish this we needed to establish and/or customize current techniques and to define some subordinate objectives.

These subordinate objectives were: 1) to develop an enhanced oil recovery (EOR) process whereby one could determine permeability and permeability changes of the original sample over a sensible range, i.e. from about 1000 millidarcies to about 10 millidarcies, 2) select some natural rocks, sandstones as well as limestones, suitable for NMRI studies. 3) apply NMRI and conventional techniques to evaluate the effectiveness of the developed process over conventional EOR processes, and 4) to develop NMR techniques to measure fluid self-diffusion coefficients. The reason behind the last objective was to correlate these to the in-situ viscosities of the displacing fluid.

Selection of EOR Process

Severe changes in rock permeability among adjacent oil bearing horizons present problems for enhanced oil recovery. Fluids used to displace indigenous oil tend to follow the high permeability avenues, bypassing large reserves of oil.

Most reservoirs are abandoned after about one-third of the Original Oil in Place (OOIP) has been recovered because of technical and/or economical constraints. Severe changes in rock permeability usually lead to inefficient oil recoveries. Conventional secondary recovery methods sweep oil from high permeability zones and bypass substantial amounts of oil trapped in the lower permeability zones. The main disadvantage of water flooding is that low water viscosity compared to that of oil allows bypassing of oil in place. This detrimental effect results in low recovery efficiencies and high water to oil production ratios. However, waterflooding costs are minimal when compared to other oil displacement processes. Therefore, its use is widespread.

Polymer flooding has been identified as an effective procedure to redistribute flow paths to lower the residual oil saturation and to improve sweep efficiencies. Polymer flooding could become the least expensive and by far the most popular of all Enhanced Oil Recovery (EOR) processes because the cost per barrel of oil recovered may be low [5] .This process could offer a significant economic potential over common waterflooding techniques because it improves the efficiency of oil recovery by two principal mechanisms: 1) decrease of the relative mobility of the displacing fluids with respect to oil, and 2) selective modification of the permeability in highly heterogeneous reservoirs.

Several commercially available polymers have been used when severe changes occur in the permeability profile. Polymers remediate this problem by obstructing the high permeability avenues where water tends to flow. High cost is often times the factor that limits their use. The expected increase in recovery must yield profit beyond a high initial investment.

NMR Compatible Biopolymer Selection

Conventional secondary recovery methods sweep oil from high permeability zones bypassing substantial amounts of oil trapped in the lower permeability zones. Effective techniques and inexpensive materials to modify the permeability scenarios are essential to improve the volumetric sweep efficiencies and lower the cost. Our primary effort was to develop a cost-effective and environmentally safe biopolymer as an enhanced recovery agent and use NMR imaging and spectroscopic techniques to study (a) the effectiveness of the polymer displacement through enhanced mobility control and permeability reduction and (b) the changes in polymer rheology due to the interaction with the porous media and (c) other effects such as viscous fingering.

The primary biopolymer investigated during this research effort was starch. Starch is a cost effective polymer that presents good characteristics as an oil recovering agent. Actual price is about 4¢/lb for feed grade starch; the manufacture of the powdered corn starch eliminates the dependency on service companies and this clearly translates to favorable economics. Biopolymer preparation could be considered as an integral part of a given EOR project. Formulation and conditioning of the raw products affect the characteristics of the resultant biopolymer. Starch is a naturally abundant biopolymer composed of two basic units: amylose (linear chain) and amylopectine (branched chain). Preparation methods can alter the ratio of these units and thus the characteristics of the resultant product.

Starch is widely distributed as the reserve carbohydrate in the leaves, stems, roots, and fruits of most land plants. Commercial sources are the seeds of cereal grains (corn, sorghum, wheat, and rice) and certain roots such as potato and cassava. Starch is a polysacharide which has favorable thickening, gelling, adhesive, and film-forming properties[6,7] .Therefore, low cost, controlled quality, and availability from numerous vegetal sources made starch a very attractive prospect for EOR processes.

Recent environmental regulatory laws, such as the Resource Conservation and Recovery Act (RCRA), make the biodegradable starch very attractive when compared to the non-biodegradable synthetic polymers.

Starch is insoluble in water at ambient temperature, but chemically gelatinizes in an alkaline medium. A second method of forming a gel is to change the temperature of the solution[7] . Starch granules swell in water at 140 °F [60 °C], expanding their volumes up to 250 times. Starch gel formation is characterized by a setting of the particles into a coherent structure. Whereas in a real coagulation process the dispersed particles form aggregates that settle down by gravity. A third method of forming gels is by cross-linking macromolecules. The crosslinking agents are Zirconium, Chromium Titanium or Aluminum compounds. These agents however, present serious environmental concerns[8] . Starch does not require cross-linking. Formation waters are at a sufficiently high temperature to cause starch swelling and lead to in-situ gel formation.

Selection of NMR Compatible Core Samples

Several artificially consolidated porous media with known chemical composition and almost free of paramagnetic substances were obtained. These samples were selected by: grain size, pore size distribution, permeability values, and compatibility with NMR.

The following is a description of the materials considered:

a. Polypropylene porous media suitable for NMR purposes was acquired. The inconvenience of this material is that the available rod diameters of the samples are 0.5 inches maximum. Testing equipment is mainly designed to handle only one inch in diameter samples. An adapter sleeve has been bought to overcome this problem and it has been successfully tested with the core. However, the NMR signal-to-noise ratio is not favored by this smaller sample size. These samples can be used with a modified core holder and NMR coil in a flowing experiment. Permeability can also be determined from non-flowing experiments and to that effect these samples have been cased in an epoxy resin. Permeability and porosity have been determined conventionally in all these samples.

b. Homogeneous glass porous media were also identified and purchased. This material is commonly used for filtering. Although there is no restriction on the diameter of the samples, the maximum depth is limited. These samples can only be cut in non-conventional sizes (1/2" by 3" rectangular parallelepipeds) and cast in a cylindrical shape with epoxy resins.

c. Aluminum oxide based materials are also being tested, although some of the agglutinates used in their preparation contain paramagnetic impurities which cause line broadening in the NMR signal.

d. Artificial samples composed of glass grains cemented by an epoxy mixture. Several grain sizes and sample sizes were purchased and analyzed.

e. Natural rock samples of sandstones and limestones.

Core Preparation and Results

Ten core samples of different natural rocks with permeabilities ranging from 40 md to 3,000 md were analyzed. The samples were saturated with distilled water. Line widths and T_1 measurements were performed on the saturated samples to determine their suitability to NMRI applications. The magnetic field is 40,000 Gauss (2 Tesla) and the maximum gradient used was 20 Gauss/cm, which for a sample of approximately 10 cm long amounts to changes in frequency no greater than 5,000 ppm. Hahn's spin-echo sequence was used to determine the line width and the inversion recovery sequence was used for measuring T_1 values.

On the basis of these measurements, six rocks were selected as being suitable for NMRI studies. The smaller the line width, the more suitable is the rock for NMRI. The selected samples were: Limestone 1 & 2, Elgin, Okesa, Heath well #2 formation, and Bentheim sandstones. From these six types of rock only the high permeability samples were used because the fluid velocity measurement was limited to a maximum of 20 micron per minute by the NMR instrument. We selected (1) Limestone #1 with a permeability of

250 md, line width of 171 Hz and a T_1 of 204 ms and (2) Elgin sandstone with a permeability of 2500 md, line width of 549 Hz and a T_1 of 208 ms.

The last set of samples were finally selected to perform polymer and study displacing mechanisms using NMR. The results are summarized in Table 2.

No.	Rock Name	Sample Name	Line Width (Hz)	T_1 (msec)
1	Limestone 1	LS-1	304.6	204.3
2	Limestone 2	LS-2	171.3	
3	Bentheim SS	G-9	228.1	
4	Heath well #2	H	386.6	173.8
5	Elgin SS	E-14	549.6	207.9
6.	Okesa SS	O-24	875.7	107.9
7	Berea SS	B-14	1098.7	
8	Berea SS	BS-2	974.8	
9	Carbon field	T	1561.3	
10	Cottage Grove SS	CG-6	1876.1	

Table 2. Line width and T_1 measurements of Limestones and Sandstones

Biopolymer Preparation and Process Evaluation

The ease of synthesis and the low overall cost of modified starch made it an attractive enhanced recovery agent. Its biodegradability makes it environmentally safe. In addition to favorable economics, our modified starch is devoid of problems such as microgel formation associated with protein present in commercial biopolymers such as Xanthan gums. We have used our in-house made product for all the polymer flood studies.

Starch was extracted from corn by steeping and wetmilling processes. Further purification was achieved by centrifugation and defattening processes, which remove the protein. The final moisture content of the starch after drying under vacuum was approximately 8-10%. Starch solutions of concentrations ranging from 0.2% to 5.0% were used in our studies. The solutions were prepared by suspending the powdered starch in distilled water and heated to 203 ^{o}F with continuous stirring. Starch begins to gelatinize at 158 ^{o}F and becomes fully gelatinized at 203 ^{o}F. After gelatinazation, the starch solutions are allowed to cool. The cooled solution can be stored at 39.2 ^{o}F for subsequent use. Starch solutions of concentrations ranging from 1% to 5% (by weight) were analyzed by a standard viscoanalyser to study the variation of viscosity with temperature.

Studies were conducted to investigate the properties of the biopolymer solution and its feasibility as an oil recovering agent. NMR properties such as line width, T_1 and T_2 of the polymer solutions, at different concentrations, were measured to determine the applicability of NMRI techniques. The measured properties proved the applicability of NMR techniques to our biopolymer solutions.

The use of a modified biopolymer, starch, as a method to enhance oil recovery was evaluated by analyzing: 1) changes in rock permeability caused by the macromolecular gel matrix of the polymer solution, 2) mobility reduction due to the higher viscosity of the polymer solution compared to that of water, 3) the chemical and mechanical stability of the biopolymer at reservoir conditions, 4) the effect of various polymer injection strategies, and 5) sweep efficiencies by Nuclear Magnetic Resonance Imaging (NMR/NMRI).

Artificially as well as naturally consolidated porous media with initial permeabilities ranging from 1,500 to 2,500 md were used. The average permeability reduction was from 1,500 to 500 md when a 1% by weight biopolymer was used. NMR/NMRI proved to be a very useful tool to evaluate the effectiveness of a starch biopolymer for rock permeability control.

Vertical sweep efficiencies measured by NMR means improved from 25% to 95% with the introduction of the biopolymer. Oil recovery was dramatically enhanced from 2% of the Original Oil in Place (OOIP) using brine as driving fluid to 98% when the in-house biopolymer was used during the displacement tests. Differential pressure (Dp) across 3-inch long samples continually increased from 10 to 130 psi. A xanthan-gum based commercial biopolymer yielded a recovery of only 58% of the OOIP when used under similar conditions. Displacement experiments were conducted at 1,000 psi and 160°F. The polymer solution exhibited moderate shear thinning viscoelastic behavior and pronounced shear thickening viscosity with increasing brine and polymer concentration.

NMR analyses were required to evaluate the ability of biopolymers used for permeability control and as relative mobility modifiers. A highly homogeneous and NMR compatible porous media is essential to study the permeability changes of the porous matrix and the changes in flow paths due to use of the polymers. The use of polymers as permeability modifiers is part of the plan of finding a method that would control and alter the permeability of a single porous sample. This dynamic change was quantified using NMRI techniques.

The maximum size of the samples to be used determines the NMR compatible core holder to be used. The two possibilities considered were: 1) samples of small diameter (less than one inch in diameter) and three inches in length and 2) conventional samples three inches long by one inch diameter.

An existing core holder compatible with NMR and able to withstand high pressure was modified. Pressure tests as well as flow tests were accomplished. Details of the construction and re-design of this core holder appear in the Perez[9] dissertation and in the Perez et.al. [10] article.

During preliminary experiments fluids were not circulated through the rock sample, and acquisition of T_1's were locally obtained to start developing image processing techniques.

Polymer Retention and Adsorption

Polymer flooding offers a significant economic potential over conventional water flooding techniques as it improves the efficiency of oil recovery by two principal means: 1) by decreasing the mobility of water and 2) by selective modification of the permeability in highly heterogeneous reservoirs by adsorption.

Concentrations as low as 0.2% were effective in permeability reduction by adsorption and thus expose low permeability paths to subsequent water flood. This property of polymer adsorption is generally desired where channeling and bypassing of oil are the main problems as in highly heterogeneous reservoirs. Polymer adsorption may also represent a substantial decrease in concentration and viscosity of the polymer flood. Therefore, substantial study of polymer adsorption in porous media has been conducted. Polymer adsorption measurements may be performed by two methods, namely from the use of (1) capillary pressure versus saturation data and (2) polymer retention measurements from a polymer material balance of conventional displacements.

Experiments were performed to determine the effect of polymer adsorption on capillary pressure curves. The difference in capillary pressure curves before and after polymer flooding indicates the degree of polymer adsorption in the porous media. A model was developed to compute the amount of polymer adsorbed in the porous media. A correlation was also developed to relate the adsorbed polymer thickness to the rock and the fluid properties. Elgin and Okesa sandstones were used to study adsorption of our biopolymer. All core samples were cut parallel to the bedding planes from the outcrop rock samples. Core plugs used for capillary measurements were one inch in length and one inch in diameter. Core plugs used in displacement studies were three inches long and one inch in diameter. An ultracentrifuge (model L8-60M/P) was used to obtain air brine displacement data for capillary pressure measurements. The core flooding apparatus consisted of a HPLC pump, a core holder and a fraction collector. Since the relative permeability to oil is slightly affected by the flow of polymer, all experiments were conducted at zero residual oil saturation. Centrifuge data was used to obtain pore entrance size distributions.

Figure 5 shows the capillary pressure versus saturation curves before and after a 50 PV flood of biopolymer solution for a variety of samples. Figure 6 indicates the difference in pore entrance size for an Elgin sandstone sample. All the samples studied exhibited a similar trend. Table 3 indicates the permeability reduction attained in all the analyzed cases. A trend of decreasing permeability was observed. Permeability reduction was higher in rock samples with lower initial permeabilities. The difference in the average pore entrance radii computed from these capillary pressure curves yield the average thickness of the polymer retained in the porous medium.

In the second method based on displacement experiments, known pore volumes of polymer were injected into a water saturated core sample. The polymer flood is followed by a water flood to displace all the polymer retained by the sample without being adsorbed. All the effluents are collected by a fraction collector. The concentration of the effluents are measured by a total starch analysis method developed by Technicon Industrial Systems, Inc. using an enzyme (amylase is used to convert gelatinized starch to glucose) digestion technique. By a mass balance, the amount of polymer adsorbed by the core sample is evaluated. This work is nearing completion and we plan to submit a paper including these results.

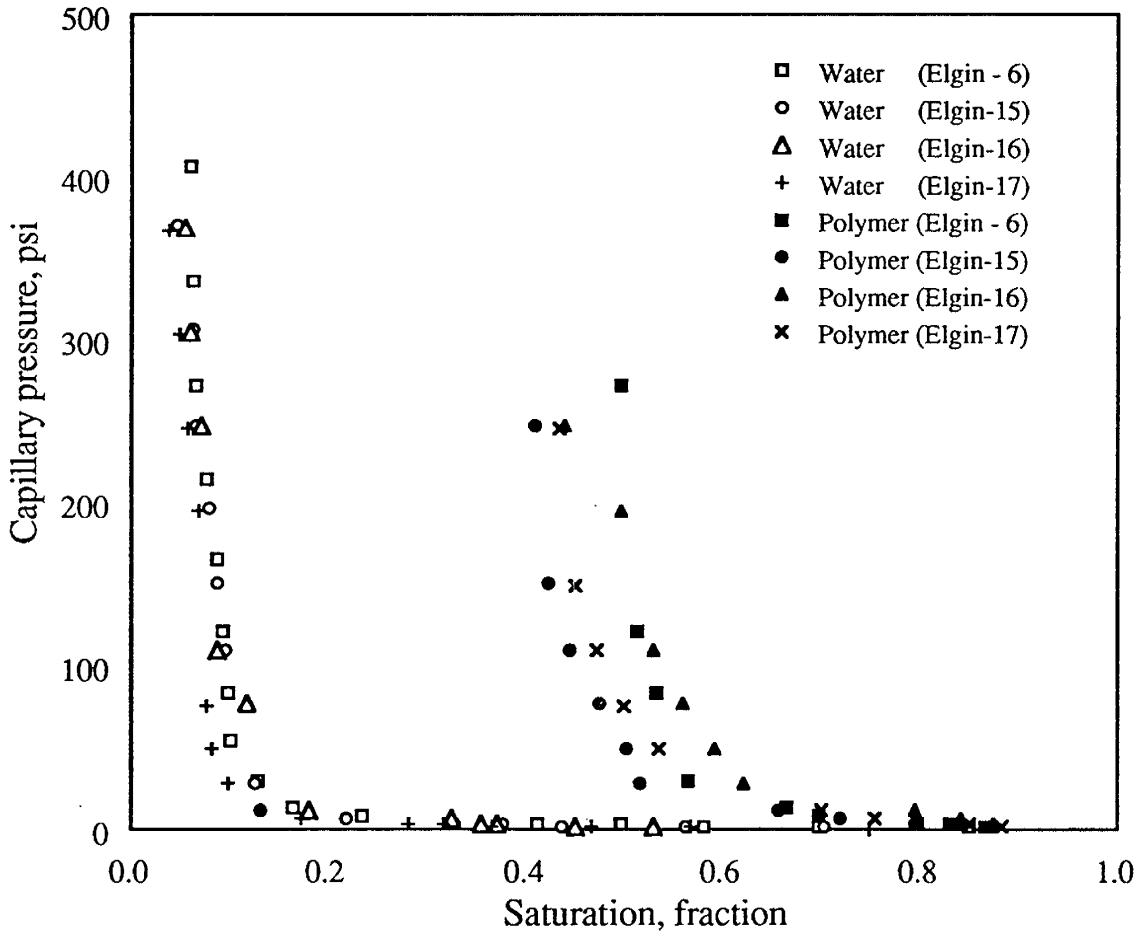

Figure 5. Comparison of water and biopolymer capillary pressure curves for Elgin sandstone.

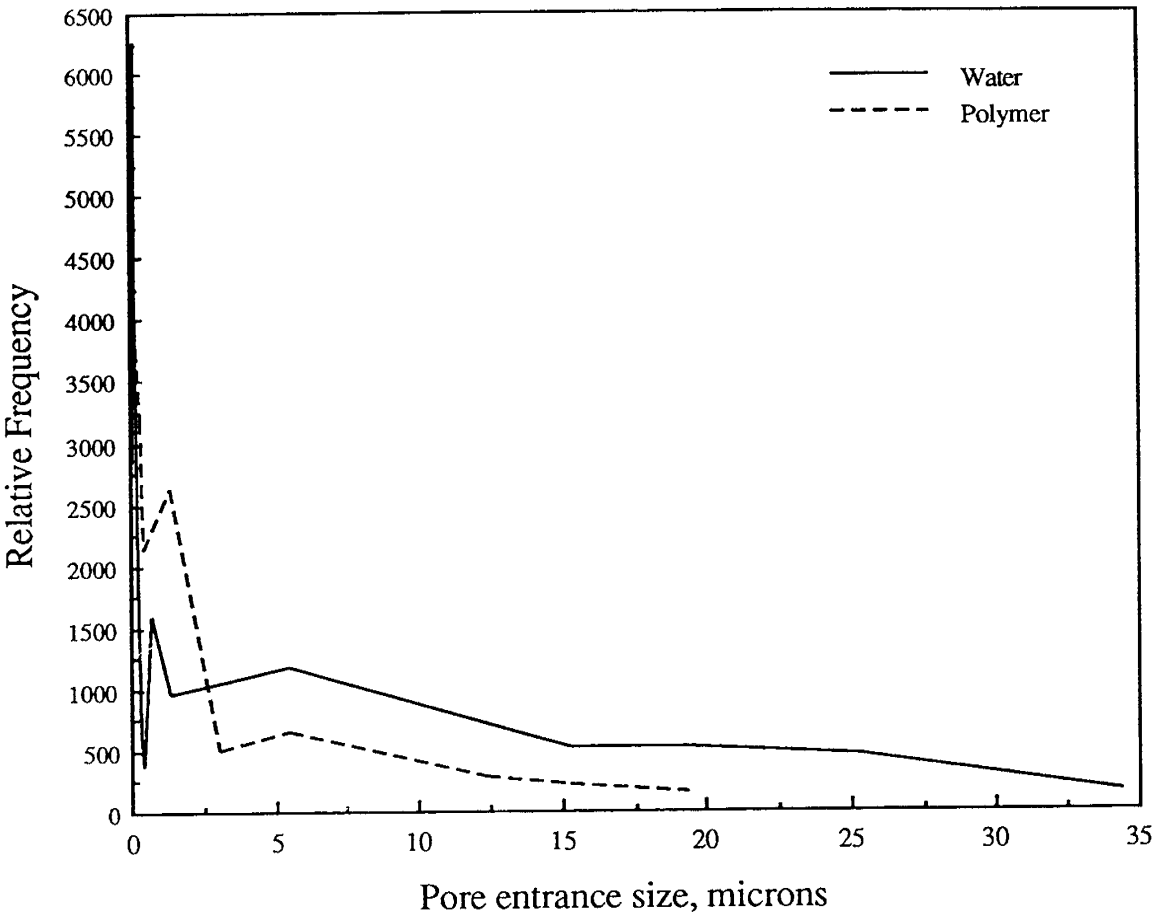

Figure 6. Pore entrance distribution before and after biopolymer flood for the Elgin - 6 sandstone.

Sample	Porosity, %	Initial k, (md)	Final k, (md)	k reduction, F_r
ELGIN - 6	23	1634	171	9.58
ELGIN-15	25	2072	258	8.04
ELGIN-16	25	2088	340	6.15
ELGIN-17	24	2396	496	4.83

Table 3. Rock properties and permeability reduction

Polymer Rheology

Information about the rheological behavior of polymer solutions in porous media is required to study the effective improvement on mobility control and permeability reduction due to the polymer flood. The bulk fluid viscosities were measured with a LVT Brookfield dial reading viscometer. The viscosities of the bulk polymer solution at several concentrations (0.2% to 2.0%) were measured. The presence of brine is known to have a detrimental effect on polymers used in the past. Salts cause a rapid structural degradation of the polymer chains. The chemical stability of our biopolymer under different saline environments was evaluated by performing rheological tests on starch solutions prepared with brines of different concentrations. Figure 7 shows biopolymer viscosity versus polymer concentration and salt concentration. The bulk polymer viscosities were measured for brine concentrations ranging from 0 to 20,000 ppm. The effect of brine on polymer viscosity was negligible for polymer concentrations less than or equal to 1.0%. For polymer concentrations higher than 1.0%, salinity increased the polymer viscosity. In contrast to currently available polymer products, our biopolymer reacts favorably in saline environments.

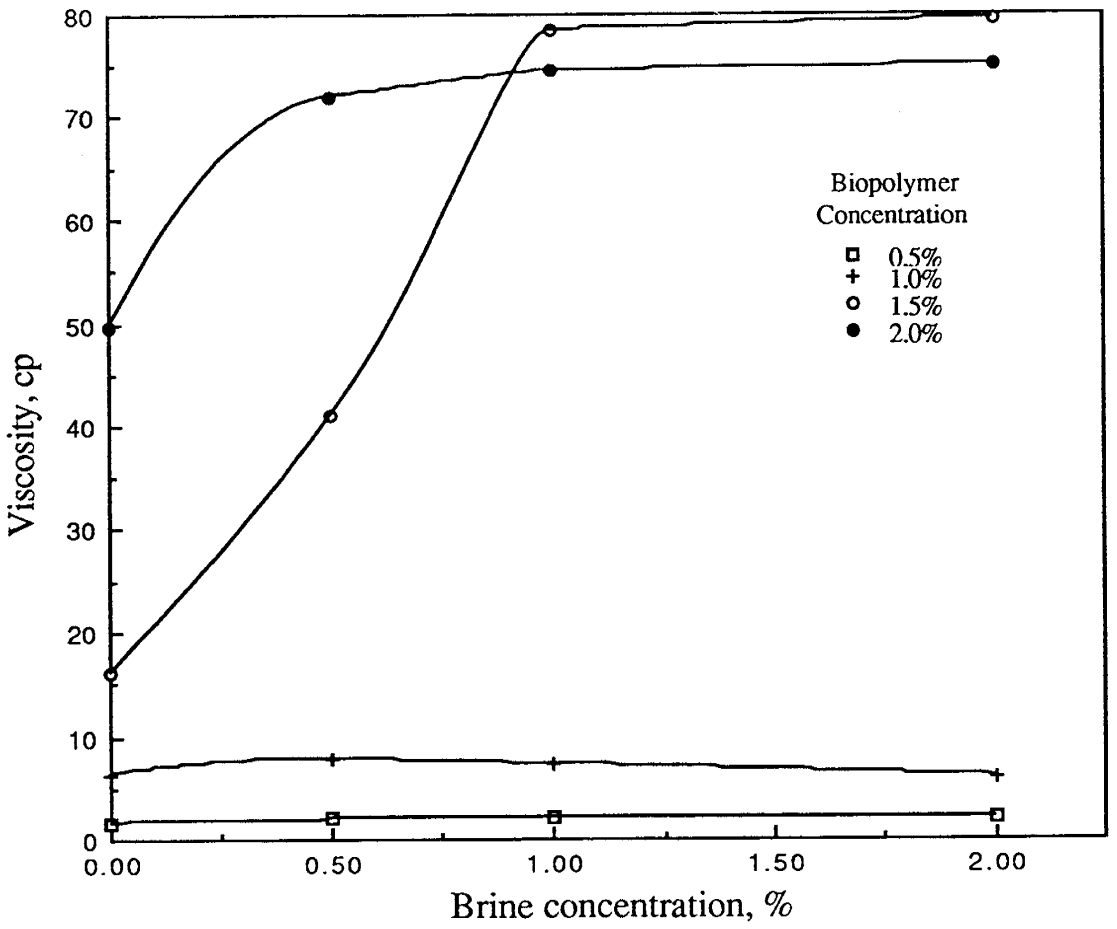

Figure 7. Effects of water salinity and starch concentration on viscosity of biopolymer solution.

Process Evaluation by NMRI and Conventional Techniques

Rock samples used to study the effects of biopolymer flooding as a permeability control agent were selected to have a high value of permeability to simulate the high permeability avenues that exist in highly heterogeneous reservoirs. Permeabilities measured around 2,500 md, with porosities close to 40 %. The samples were initially saturated with distilled water followed by oil injection to achieve an initial oil saturation. Austin Chalk oil from the Fazzino # 1 well was used for all the conducted studies. The oil had a 38.2 ^{o}API. Initial oil saturations were between 67 % and 78 %. Displacing liquids were pumped at a constant rate of 0.20 cc/min.

Biopolymer with a concentration of 10,000 ppm (1 % by weight) was used for the forced displacement studies. Measured amounts of polymer were combined and heated to a temperature of 95 ^{o}C. At this temperature the viscosity of the solution is perceptibly increased. Two cases of forced displacement of oil were designed to determine the applicability of the method: 1) a conventional waterflood followed by injection of biopolymer in the form of slugs, and 2) a continuous biopolymer flood without prior conventional flooding of water.

In order to combine NMRI techniques and pressure displacement studies conducted under elevated pressure (up to 2500 psia), an existing fiber-glass core holder was upgraded. Figure 8 shows the schematics for this core holder.

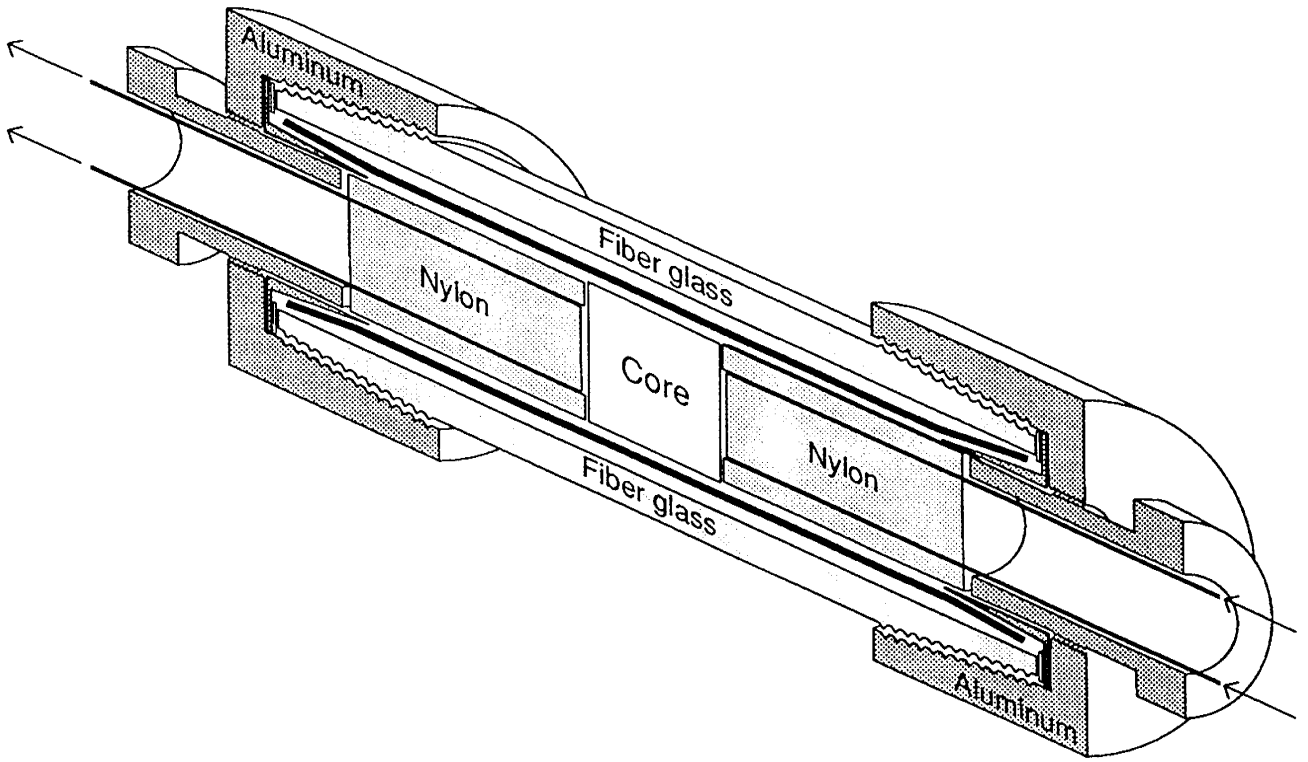

Figure 8. Modified NMR/NMRI fiber glass compatible core holder, with a working pressure of 2,500 psi.

Waterflood followed by biopolymer slugs

Maximum oil recovery due to waterflooding was only 2 % of the OOIP (S_{oi} = 78 %), with a differential pressure close to 10 psi. These results reflect serious fingering and bypassing of the oil in place by injected water. Two slugs of 0.5 PV were injected. The first slug increased oil recovery about one percent. A temporary increase in pressure was also observed. Pressure drop across the sample increased from 10 psi to 20 psi, but it diminished after a short time. A permanent increase in differential pressure of about 5 psi was observed. The second polymer slug, 0.5 PV, increased oil recovery to a maximum of almost 10 % of OOIP. Differential pressure was momentarily increased to 35 psi. An increased differential pressure remained over 20 psi. Figure 9 summarizes the results explained above.

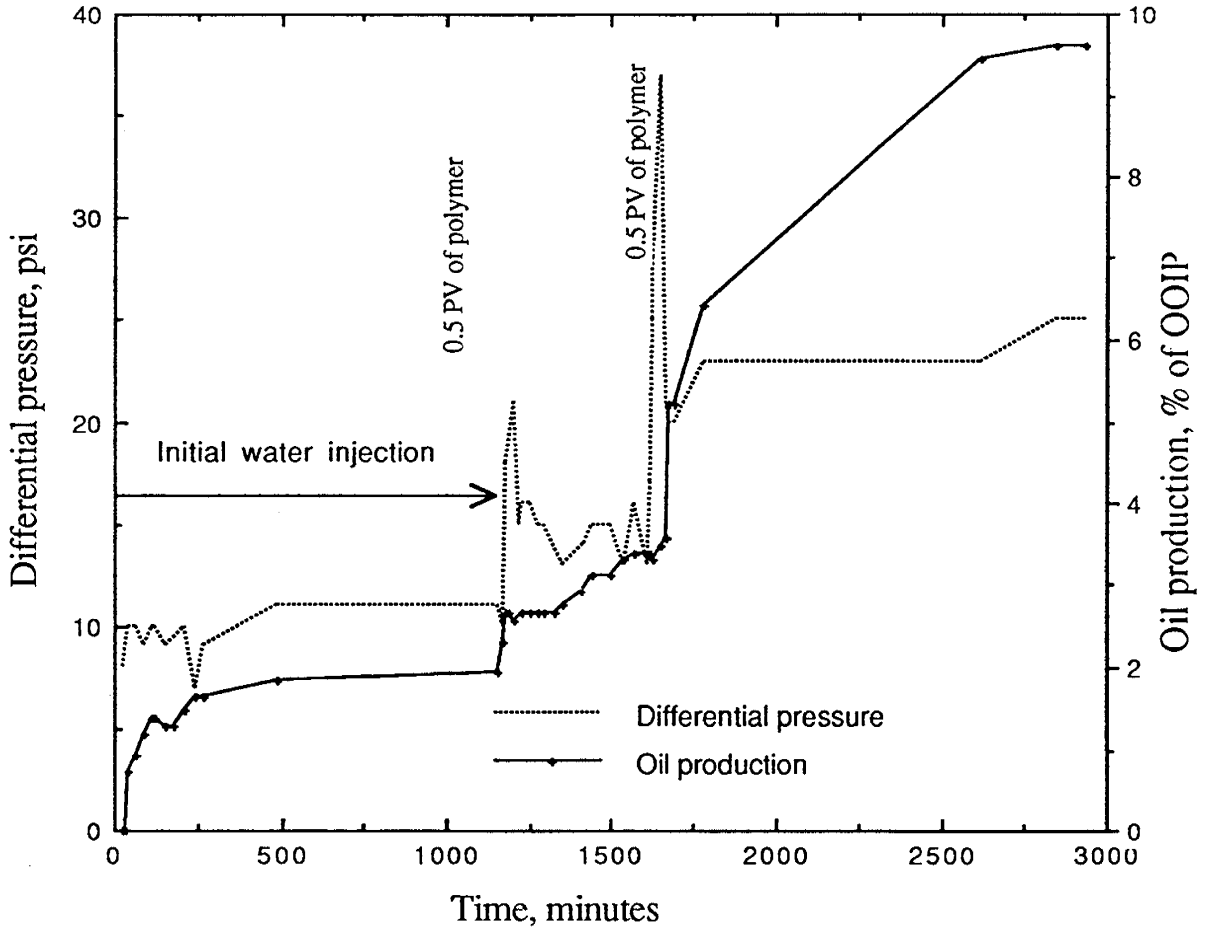

Figure 9. Oil recovery due to the injection of water and two 0.5 PV biopolymer slugs.

Complete biopolymer flood

The second case was attempted without prior waterflood. An oil recovery of nearly 100% was observed (Soi = 67%). Differential pressure across the sample increased to a maximum average of 120 psi. Figure 10 indicates these results.

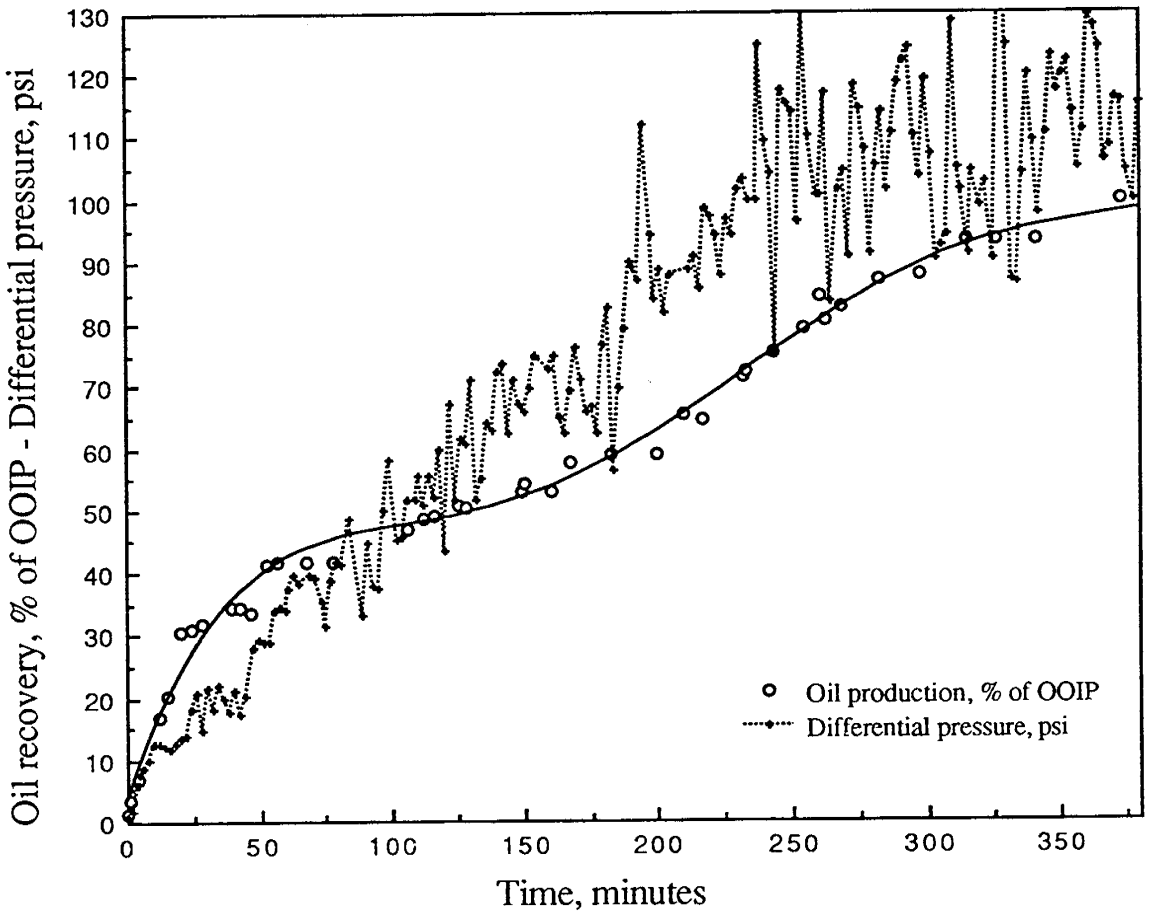

Figure 10. Oil recovery and changes in differential pressure caused by continuous biopolymer injection.

Injection of two 0.5 PV slugs of polymer increased the oil production from 2% of the OOIP obtained during waterflood, to nearly 10% of the OOIP. Differential pressure was increased from 10 psi for waterflooding to nearly 25 psi. Darcy's law expresses that oil flow is proportional to the pressure drop. Therefore, the observed increase in differential pressure could largely increase the oil recovery from adjacent oil bearing rock layers that would receive the same increase in applied pressure.

The same criteria yields very encouraging results when a complete polymer flood is analyzed. Not only was oil recovery complete (100% of OOIP), but also a tremendous

increase in differential pressure was achieved. Differential pressure increased to a maximum of 120 psi. A very significant increase in oil recovery could result by applying the increased pressure to adjacent reservoir layers.

Two intriguing phenomena were observed: 1) after a complete oil recovery was achieved, differential pressure decreased from 120 to 70 psi, and 2) pressure readings were more erratic as less oil remained inside the rock. These two effects point to an efficient oil displacement. NMRI studies revealed areal and volumetric sweep efficiencies. Displacement studies were also studied by non-invasive NMRI techniques.

The cores were selected from both natural and synthetic porous media with initial permeabilities ranging from 1,500 to 4,500 millidarcies. Table 4 shows the synthetic rock sample properties and the initial oil saturation used. A high oil recovery of about 95% was observed in all the experiments performed using the newly developed process as compared to 25% attained by other methods.

Average pore size of sample, m	Porosity, %	Initial k, (md)	Initial oil saturation, %
15	40	1600	77
40	34	2500	96
55	37	3200	96
90	33	4500	98

Table 4. Synthetic rock sample properties.

Figure 11 shows the oil recoveries obtained using a Xanthan-gum based commercial biopolymer and our starch-based biopolymer. The Xanthan-gum biopolymer yielded a recovery of only 58% when used under similar conditions.

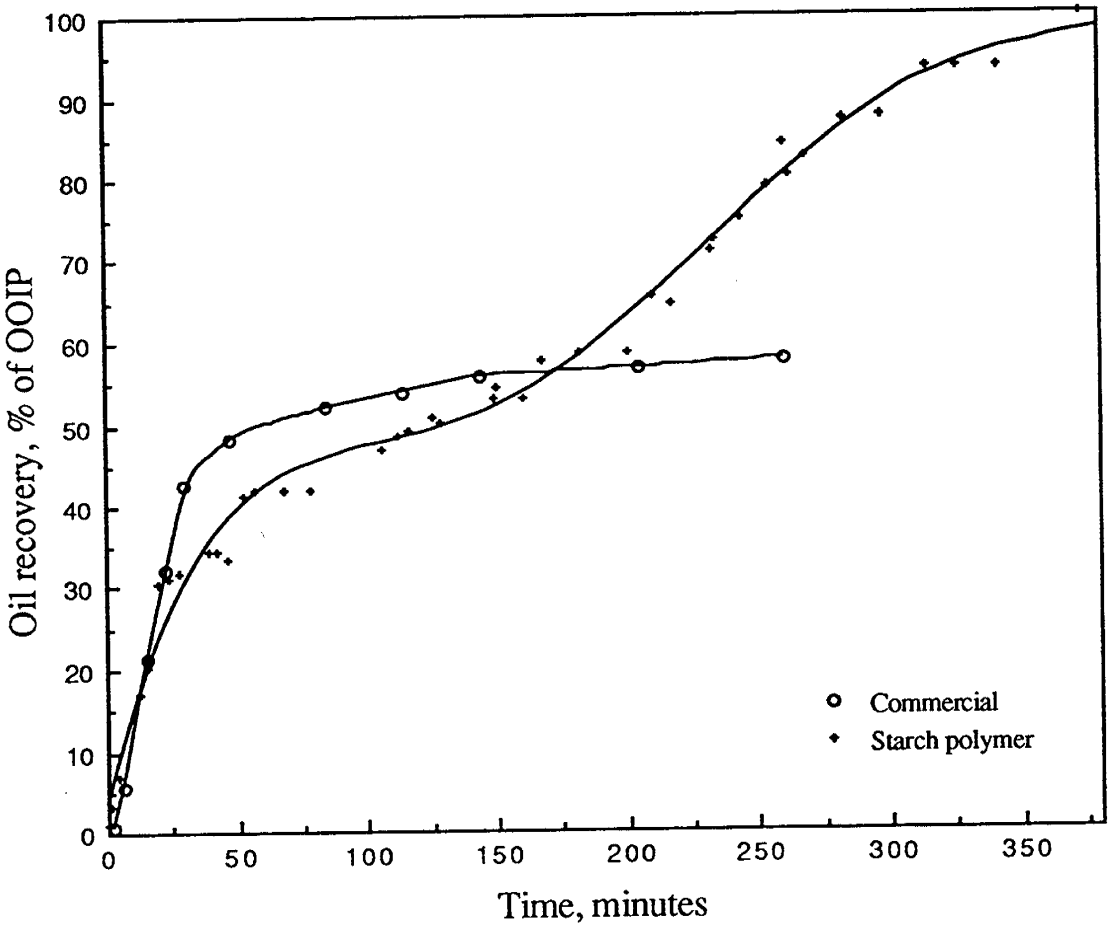

Figure 11. Comparison of oil recovery due to injection of a commercial and starch biopolymers.

Conventional core flood experiments yielded an average permeability reduction from 1,500 to 500 millidarcies. Application of NMRI to displacement processes resulted in two dimensional images taken parallel and perpendicular to the flow axis at different times of the displacement processes (Figures 12, 13 and 14). Sweep efficiencies were calculated from the longitudinal images (parallel to the flow direction) taken during the steady states conditions before and after the polymer flood. Saturation profiles derived from proton profiles (also called one dimensional images) were taken at different times during the displacement. They were useful in determining the changing saturation profiles during the displacement (Figure 15).

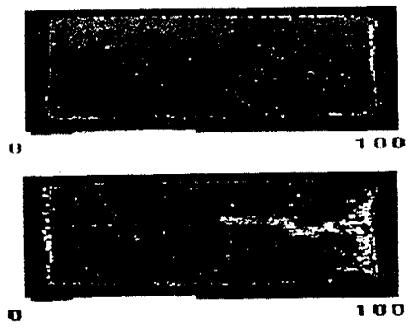

Figure 12. Oil saturation changes due to water injection. Water fingering is clearly visualized at early injection times. Initial and intermediate conditions are shown.

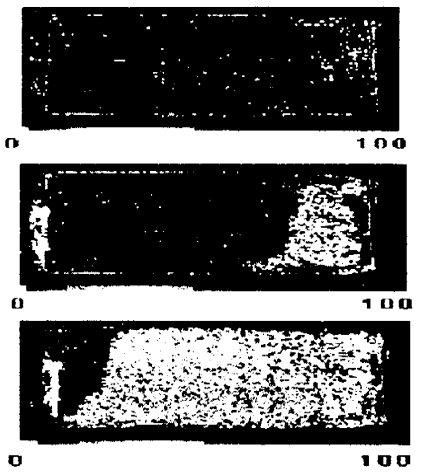

Figure 13. Oil saturation changes due to biopolymer injection. A more efficient displacement is observed. Initial, intermediate, and close to final conditions are shown.

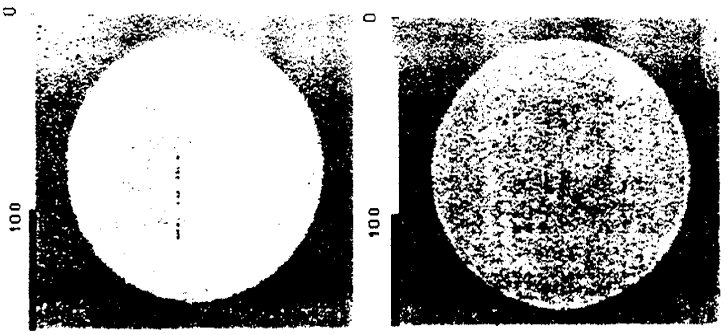

Figure 14. Cross sectional images before and after oil displacement by biopolymer injection.

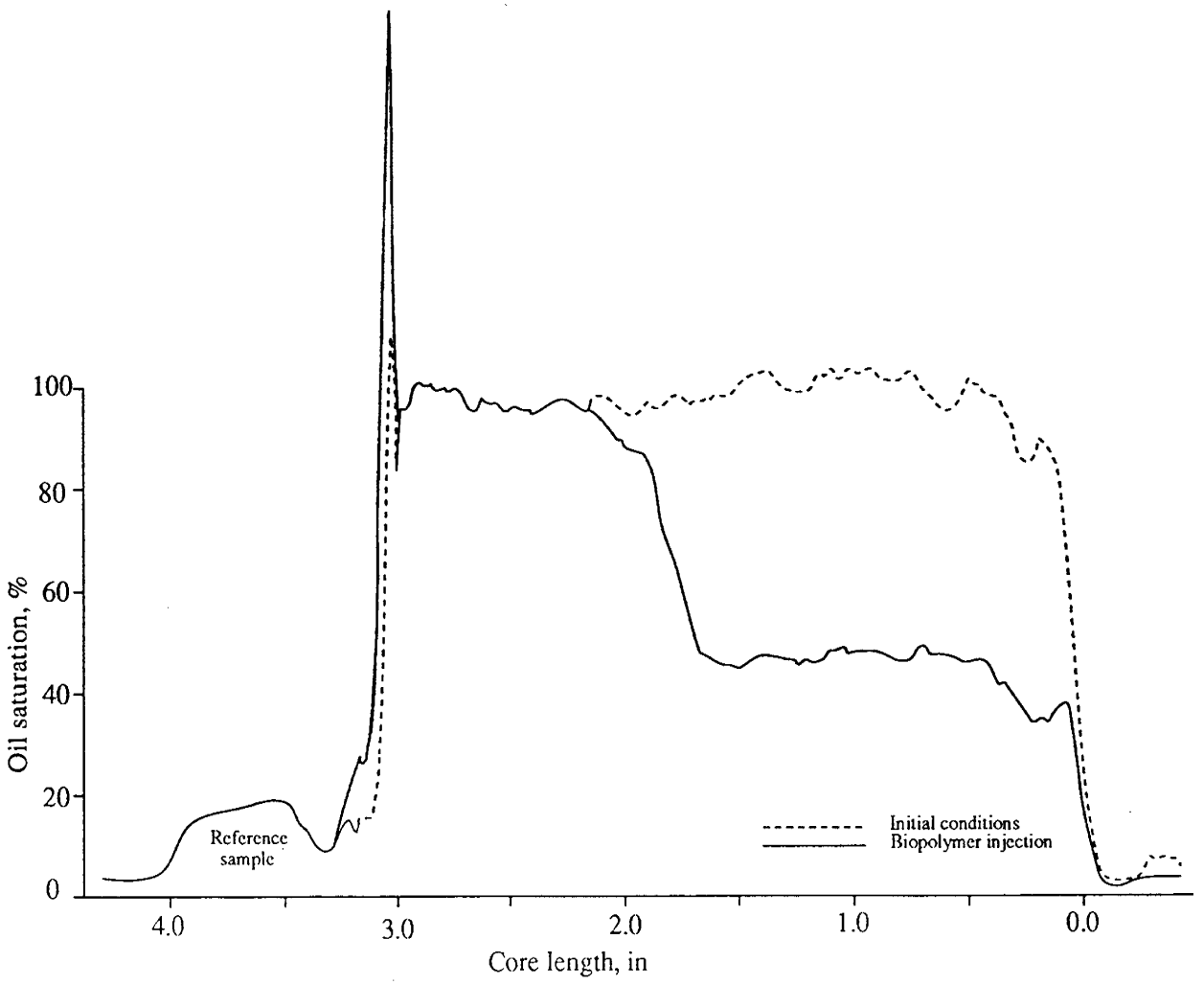

Figure 15. Oil saturation profiles, obtain from proton profiles, showing the efficiency of oil displacement by biopolymer injection.

A reference sample with a constant proton density was used to normalize the signal intensities obtained by NMR. The profiles were obtained in about 3 seconds and the two dimensional images were obtained in about 20 minutes. The obtained images clearly show the advantage of using biopolymers for effective mobility control resulting in high recoveries.

Determination of apparent diffusion coefficients by NMR techniques

An NMR technique to measure the apparent self-diffusion coefficients of fluids in porous media was developed. These coefficients can be used to obtain effective fluid viscosities during flow through porous media and also provide information of pore-size distributions of the porous media. As diffusion is highly temperature dependent, the temperature effect was also studied. Imaging techniques were tested to image fluid displacements through porous media to measure changes in fluid phase saturations and the effects of viscous fingering.

Four different radio frequency pulse sequences were developed and tested to measure fluid self-diffusion coefficients. As a result, a pulsed gradient stimulated-echo radio frequency pulse sequence was selected for use in porous media. The apparent self-diffusion coefficient of distilled water measured with the above sequence was validated by comparison with values given in the literature. For bulk biopolymer solutions of several concentrations the self-diffusion coefficients were measured. The measured coefficient values deviate from that of water for increasing polymer concentration.

The bulk diffusion coefficients measured by NMR/NMRI techniques can be correlated to the bulk fluid viscosities. The apparent diffusion coefficients are a measure of restricted diffusion in case of pore size reduction by adsorption. A potential use of this principle may be the prediction of instantaneous permeability of the porous media during the polymer flood. A correlation between the NMR-obtained diffusion coefficients and the polymer solution viscosities was obtained. The diffusion coefficients were obtained by a stimulated echo imaging technique using three mutually perpendicular phase encode gradients. Also, these measurements were made under conditions of unrestricted diffusion by applying appropriate diffusion times. Studies are under way to observe significant changes, if any, in the polymer solution viscosity during flow as a result of mechanical degradation or dilution.

As a result of this DOE sponsored project four publications have been produced under the direction of Dr. Maria A. Barrufet (references 10 to 14). Additionally, several new promising research areas emerged.

Simulation Studies

Sensitivity studies were conducted using a 3-D, 3-phase polymer/gel flow simulator obtained from DOE. A three dimensional, 3 phase simulator was used to study permeability modification due to polymer injection. This simulator allows study of the effects of many variables upon displacement processes. The variables being analyzed were: layered reservoirs with permeabilities ranging from 100 to 3,000 millidarcies. Different polymer concentration, injection strategy (slug/water/slug), and rheological properties for the polymer were used. The simulator was being scaled down to laboratory proportions. The use of the simulator would allow an optimum design of polymer floods to be conducted in the laboratory.

Several polymer properties are needed to simulate a polymer flood. These properties are still being measured. NMR experiments would confirm numerical results.

IV. References

1. Shivers, J. B., "The Development of MRI for the Determination of Porosity Distribution in Reservoir Core Samples, " Thesis, Texas A&M University. August (1991).
2. Da Costa E, and Silva A. J., "A New Approach to the Characterization of Reservoir Heterogeneity Based on the Geomathematica Model and Kriging Technique," SPE paper 14275. 60th Annual Technical Conference and Exhibition of Petroleum Engineers. Las Vegas, Nevada. September 22-25, 1985.
3. Sherman B. B., "The Development of Magnetic Resonance Imaging for the Determination of Porosity in Reservoir Core Samples," Thesis, Texas A&M University. May (1991).
4. Marek M., "The Development of MRI for the Determination of Fluid Saturation Distributions in Reservoir Core Samples," Thesis, Texas A&M University. August (1991).
5. Meister, J.J. and Li, C.T., "Complex Copolymers for Mobility Control, Water Purification, and Surface Activity," *ACS Symposium Series Oil-Field Chemistry - Enhanced Recovery and Production Stimulation*, John K. (ed.), (1989).
6. Hermans, J.J.: *Flow Properties of Disperse Systems*, North-Holland Publishing Company, New York (1953).
7. Gomez, M.H. and Aguilera, J.M., "A Physicochemical model for extrusion of corn starch," *J. Fd. Sci.* (1983) 48.
8. Prud'homme, R.K. and Uhl, J.T., "Kinetics of Polymer/Metal-Ion Gelation," paper 12640 SPE/DOE presented at the 1984 SPE/DOE Fourth Symposium on Enhanced Oil Recovery, Tulsa , April 15-18.
9. Perez-Cardoza J. M., "MRI Study of Imbibition Flooding Using Carbonated Water," Dissertation, Texas A&M University, August (1991).
10. Perez, J.M, Poston, S. W., and Barrufet, M.A., "Studies of Carbonated Water Imbibition Using MRI," Paper SCA 9221 presented at the Society of Core Analysts, SCA/SPWLA Joint Annual Conference, Oklahoma City, Oklahoma, June 14-17, 1992.
11. Perez, J.M, Barrufet, M.A., and Poston, S. W., "MRI Studies of Permeability Control Using Biopolymers," poster paper presented at the Society of Core Analysts, SCA/SPWLA Joint Annual Conference, Oklahoma City, Oklahoma, June 14-17, 1992.
12. Barrufet, M.A., Perez, J. M., Ali. L., Mandava S. and Poston, S. W., "MRI Studies of Permeability Control Using Biopolymers," SPE 24809, paper presented at the 67th Annual Technical Conference & Exhibition, October 4-7, 1992, Washington, D.C.
13. Ali, L., M.A. Barrufet, and S.W. Poston, "An Experimental Study of Profile Modification due to Polymer Adsorption in Reservoir Rocks, " paper accepted for presentation in the ACS Symposium on Enhanced Oil Recovery, Denver CO. , March 28 to April 2, 1993.
14. Ali, L., M.A. Barrufet, and M. Tantawy, "The Effect of an Adsorbed Polymer Layer on Relative Permeability Curves," paper accepted for presentation at the Ninth Wyoming Enhanced Oil Recovery Symposium to be held in Casper, Wyoming May 12-13, 1993.

SUBTASK 2: DEVELOPMENT OF NMRI AND CT SCANNING FOR CHARACTERIZING CONVENTIONAL MULTIPHASE DISPLACEMENT PROCESSES

Principal Investigator: A. T. Watson
Department of Chemical Engineering

I. Introduction

Most reservoir processes involve the flow of two immiscible fluid phases (e.g., oil and water) or three fluid phases (e.g., oil, water and gas). In spite of its fundamental importance for petroleum recovery, many aspects of multiphase flow in porous media are not well understood. Flow in macroscopically homogeneous porous media is normally described using relative permeability and capillary pressure functions. However, there are no reliable methods for predicting those quantities from microscopic observations, and no reliable relationships for predicting variations of that property with different conditions, such as wettability, flow velocity, surface chemistry and temperature. The lack of reliable methods for determining both two- and three-phase relative permeability functions from laboratory experiments has hindered the development of useful predictive methods.

Nuclear magnetic resonance spectroscopy and imaging (NMR and NMRI) techniques can provide unprecedented information about fluid states in porous media. To date, such information has largely been used in a qualitative fashion. We are developing NMR spectroscopic and imaging techniques to provide useful quantitative information for obtaining a better understanding of the storage and transport of multiple fluid phases in porous media.

The work has been divided into four tasks. In the first task we have developed new methods for quantitative determination of porosity and fluid saturation distributions under both static and dynamic (flowing) situations. A key feature of this work is the representation of transverse relaxation during signal acquisition for the interpretation of the imaging data so that accurate quantitation can be obtained. In the second task, a method was developed to obtain accurate, simultaneous estimates of two-phase relative permeability and capillary pressure functions from two-phase dynamic displacement experiments using saturation information obtained with NMRI. In the third task, pulsed field gradient NMR techniques were used to determine information regarding the self-diffusion process of fluids in porous media. Since pore boundaries restrict molecular diffusion in porous media, the diffusion measurements can be used to extract information concerning the microscopic structure of porous media. Several unconsolidated model porous media and consolidated sandstone samples were studied. Numerical analysis procedures for analyzing diffusion data to obtain pore structural information were also developed. In the final task, progress was made on revealing relations between fluid phase distributions in multiphase situations and NMR relaxation. Such information can be useful for characterizing pore structure. Also, the work has revealed a simple relation between saturation and NMR relaxation time that may prove useful for estimating saturation from relaxation measurements.

This project has resulted in a number of significant achievements in the application of NMR imaging technology to obtain various petrophysical information in static and dynamic experiments, particularly with regard to multiphase situations. The research has resulted in a number of publications, including papers published in *Mag. Reson. Imag., AIChE Journal,* and *J. of Applied Physics*. Also, one more paper was recently accepted for publication in *Mag. Reson. Imag.* and another was submitted to *AIChE J.* In addition, four conference publications were published and 13 conference papers were presented. A list of the publications and presentations are included in the Appendix.

II. Objectives

The objectives of this subtask are to: (1) demonstrate NMR imaging methods to determine porosity and saturation distributions during unsteady (transient) displacement experiments, (2) develop methods to estimate two- and three-phase relative permeabilities from dynamic displacement data, (3) use NMR restricted diffusion experiments for characterizing local fluid distributions and pore structures, and (4) develop a new approach for using NMR relaxation techniques to study fluid phase distribution at different saturation states and characterize saturation using relaxation analyses. The research work pertaining to each of the objectives is reported in separate sections below.

III. Determination of Fluid Saturations During Displacement Experiments

Introduction

Fluid saturations are the basic quantitative measures for describing the amount of fluid phases present within local regions and are essential for describing the storage and transport of fluids in porous media. Conventional methods provide measures only as bulk or average properties. Such measurements are not adequate for characterizing heterogeneous systems where the saturation may vary appreciably throughout the sample. In contrast, NMR imaging techniques can provide unprecedented information about fluid phase distributions in porous media during displacement processes, as well as information about rock structures corresponding to local regions within porous media.

Although there have been a number of applications of NMR imaging to observe the distribution of fluids in porous media[1-7], most of these studies provide qualitative, or at best semi-quantitative, measures of the amount of fluid phase observed at each location (or voxel). During the reporting period, we have developed a method for quantitative determination of the fluid saturation and porosity distributions from the NMR images. We have examined multi-exponential relaxation models for representation of transverse relaxation, and have developed a statistical approach to select the appropriate number of components in the multi-exponential model. This procedure can accurately estimate the intrinsic magnetization by evaluating the model for the magnetization evolution at zero echo time, which in turn is used to determine the porosity and saturation distributions of the samples.

To implement these developments, we performed static experiments with various core samples. In those experiments, core samples are fully saturated, and then NMR

images are conducted. In addition, we conducted a desaturation experiment with a limestone sample. In that experiment, a centrifuge was used to desaturate fluid in a fully saturated core sample to obtain various saturation profiles, and then NMR image data were collected.

For porosity and saturation measurements in the static and desaturation experiments mentioned above, the results obtained using NMR can be compared with those obtained gravimetrically for verification of the accuracy of our quantitative NMR imaging techniques. For obtaining saturation distributions during dynamic experiments, the gravimetric method can not be used; therefore, it is neccesary to develop a different approach in order to have an independent verification of the NMR results. Such verification is important in view of the fact that the transverse relaxation behavior at different saturations is different. In addition, it is also desirable to evaluate whether flow affects the accuracy of the estimates. In this task, we have developed a technique based on independent measurements of production during the displacement experiments. The new approach takes advantage of the fact the dielectric coefficient of oil is much less than that of water. By collecting the produced fluids and measuring the capacitance of the immiscible fluids containing oil and water, the relative amounts of oil and water in the collection device can be determined. We designed and fabricated a prototype electric capacitance device which can be used to determine the amount of the oil produced from core sample continuously during the two-phase displacement experiments. A displacement experiment was conducted in order to test the utility of the device.

Theory

The use of NMR profile imaging techniques to determine saturation is based on the fact that the intrinsic magnetization intensity is proportional to the number of proton spins in the region subject to NMR excitation. For longitudinal profiles with spatial resolution in the z direction,

$$M_0(\omega) = \kappa(z) N(z) \Delta z / \Delta\omega \tag{1}$$

where

$$N(z) = \iint_{A_{xy}} \rho(x,y,z) dx dy \tag{2}$$

is the proton linear density in the sample. In this technique, the spatial information is represented in the frequency domain since $\omega = \gamma G z$. The image resolution is determined by the size of applied gradient G and is subject to the NMR linewidth of the sample under study. For a selected applied gradient size and an image window, the image pixel size is determined from

$$\Delta Z = \frac{2\pi SW_{total}}{\gamma G N_p} = \frac{2\pi \Delta f_p}{\gamma G}, \tag{3}$$

where SW_{total} is the total spectral width, N_p is the number of pixels, and Δf_p is the spectral width corresponding to a single pixel. If the NMR linewidth $\Delta\nu$ is much smaller than Δf_p,

the image resolution is the pixel size determined in Eq. (3). This condition may not always be valid for fluids in porous media due to susceptibility-induced broadening. In those cases, the actual image resolution is determined by substituting the NMR linewidth $\Delta\nu$ for Δf_p in Eq. (3) and, consequently, the resolution would be reduced.

For thin slice cross sectional profiles with slice thickness Δz and spatial resolution in the x direction,

$$M_0(\omega) = \kappa(x) N(x) \Delta x / \Delta\omega \tag{4}$$

where

$$N(x) = \int_y \int_{\Delta z} \rho(x, y, z) dy dz \tag{5}$$

is the proton density in a slab. For simplicity, longitudinal profiles will be used for the description of the general formalism in the remainder of this section.

The calibration constant $\kappa(z)$ must be determined in order to obtain the linear density $N(z)$ from Eq.(1). If a reference is within the range where both rf and static field homogeneties are guaranteed, and any variation due to the sample is negligible, κ can be treated as a constant and determined from

$$\kappa = \frac{\int_{\Delta\omega_r} M_0^r(\omega) d\omega}{\int_{\Delta z_r} N^r(z) dz} \tag{6}$$

The fluid phase saturation distribution can be calculated by

$$S(z) = N(z) / N_i(z) \tag{7}$$

where $N_i(z)$ is the linear proton density measured when the sample is fully saturated. The porosity distribution $\phi(z)$ can be determined by

$$\phi(z) = N_i(z) / (\rho A_{xy}) \tag{8}$$

where ρ is the proton density of the observed fluid phase and A_{xy} is the cross sectional area.

The main difficulty in quantitation arises from the fact that the acquired profile intensity measured at finite echo times is not the intrinsic magnetization $M_0(\omega)$ due to relaxation effects. If the relaxation process were represented suitably by parameters T_1 and T_2, and the parameters were uniform throughout the medium, the relation between the observed and intrisic magnetization intensity could be expressed as follows[2] :

$$M(\omega, TE, TR) = M_0(\omega) f(T_1, TR) g(T_2, TE) \tag{9}$$

The effects of T_1 can be readily eliminated if sufficiently long delay time TR is used since the function $f(T_1, TR)$ approaches unity when $TR \geq 5T_1$ This condition was adhered to in all our experiments. If the T_2 relaxation in the sample were assumed to be uniform throughout the sample and was represented by a single exponential model using a single, average value of T_2, then Eq. (9) can be written as

$$M(\omega, TE, TR) = M_0(\omega)\exp(-TE/T_2) \tag{10}$$

Since the transverse relaxation depends on the sizes of pores in which the fluid resides, as well as on local surface composition, a single, average value may not accurately represent relaxation behavior in porous media which has a distribution of characteristic pore sizes. In addition, the distribution of pore sizes occupied by the observed fluid phase will change as saturation changes, resulting in the observed relaxation rate being a function of saturation. Therefore, a multi-exponential approch may be suitable for many situations:

$$M(\omega_i, TE) = \sum_{j=1}^{N_C} M_{0j}(\omega_i)\exp(-TE/T_{2ij}) \tag{11}$$

Single exponential relaxation is obtained for the special case of N_c=1. A different representation for the echo intensity is provided by the stretched exponential relaxation model [8,9]

$$M(\omega_i, TE) = M_0(\omega_i)\exp\left[-(TE/T_{2i})^{\alpha_i}\right]. \tag{12}$$

The stretched exponential was shown to arise from a distribution of single exponential relaxation times weighted towards short times.[8]

Estimates for the intensities and relaxation parameters were obtained by nonlinear regression through minimization of the following performance index for the *i*th pixel:

$$J_i = \sum_{l=1}^{n}\left[M^{obs}(\omega_i, TE_l) - M^{cal}(\omega_i, TE_l)\right]^2 \tag{13}$$

where the calculated values M^{cal} are provided by the representation in Eqs. (11) or (12). For the multi-exponential model, estimates would be obtained for $(M_{0j}(\omega_i), T_{2ij})$, j=1, N_c, for each pixel. The intrinsic intensity of magnetization for the pixel is the sum:

$$M_0(\omega_i) = \sum_{j=1}^{N_c} M_{0j}(\omega_i) \tag{14}$$

For the stretched exponential model, estimates for $M_0(\omega_i)$, T_{2i}, and α_i are obtained for each pixel.

A useful criterion for selection of the appropriate number of terms for the multi-exponential model is the *F*-test. One can test whether a more complete model is warranted by comparing a tabulated value with a statistic calculated using values of the residual sum of squares (*RSS*) obtained using the more complete model (with N_C components) with the simpler model (with N_C-1 components). The calculated statistic is

$$F = \frac{\left[RSS(N_c - 1) - RSS(N_c)\right]/q}{RSS(N_c)/(n-m)} \tag{15}$$

where n = number of observed data, $m = 2N_C$, and $q = 2$ is the difference between the number of components in the simpler and more complete models. If the tabulated value exceeds the calculated value, one concludes (at the specified level of significance) that the

available data do not warrant inclusion of the additional terms of the more complete model. For nonlinear regression, the confidence level is said to be approximate.

Experimental Work

Several static experiments, one desaturation experiment, and one displacement experiment have been conducted using several different types of rock samples, including Indiana, Texas Cream, and building block limestones. All the samples are prepared in cylindrical shape with 2.54 cm diameter but different lengths.

In the static experiments, distilled water was used to fully saturate the core samples, and then the average porosities of the core samples were determined gravimetrically. Subsequently, NMR profile images were obtained. In the desaturation experiment, a core sample was saturated with distilled water and then desaturated in air to various saturation states using a centrifuge. After each desaturation, the average saturation was determined gravimetrically, and NMR profile images were measured.

All NMR measurements were performed at 85 MHz with a GE 2 Tesla (85 MHz) CSI-II system. The imaging profiles were obtained using a standoard one dimensional profile imaging sequence[7] with a frequence-encoding gradient applied along the cylindrical axis of the core samples.

In the displacement experiment, refined oil was used as the oleic phase, and deuterium oxide (D_2O) was used as the aqueous phase. The core sample was mounted in a plexiglass core holder and sealed with an epoxy (Stycast 2651) sealant. The sample was initially evacuated and then saturated with the refined oil. A reference sample, consisting of a gel of agarose powder and 0.005M $CuSO_4$ solution, was taped on to the core holder as a reference standard for signal intensity calibration. Pressures at the core inlet and outlet were measured with pressure transducers. A schematic of the experimental apparatus is shown in Figure 1.

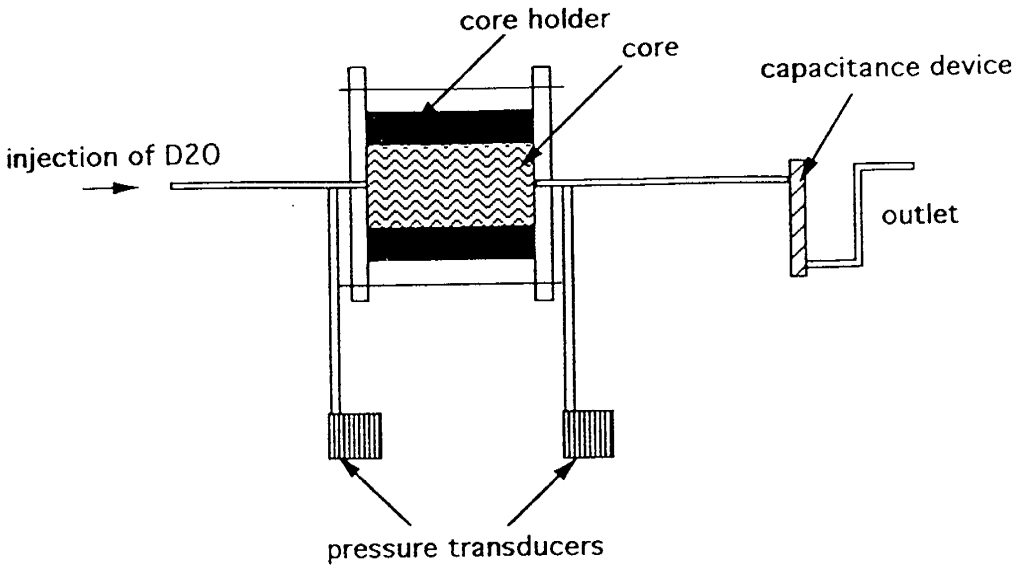

Fig. 1. Experimental flow apparatus.

The capacitance device was connected to the outlet of the core sample to measure the amount of oil in the effluent of the core sample. The capacitance was measured using GLC 1659 RLC Digibridger, which was interfaced with an IBM PC. Software was developed to control the Digibridger for measuring, transfering and storing data automatically during flow experiments. The fluid collecting device, designed as a parallel-plate type capacitor, is shown in Figure 2. The capacitance device was made with two electric printed boards affixed to either side of a plexiglass plane spacer of 1/8 inch in thickness with copper facing inward. The volume of the capacitance device is 30 ml. The inlet to the device is located at the top of the device, and the outlet is placed at the bottom. Initially the device and the conduit between the inlet of the device and the outlet of the core holder were fully filled with D_2O. During the displacement experiment, the oil is retained within the capacitance device since its density is less than that of D_2O. The amount of oil produced is determined through a calibration curve that relates the capacitance difference between the mixture of oil and D_2O and that of pure D_2O which was measured when the device was initially filled with D_2O. The calibration curve was prepared by pumping pure oil at a constant flow rate into the capacitance device which was initially filled with D_2O.

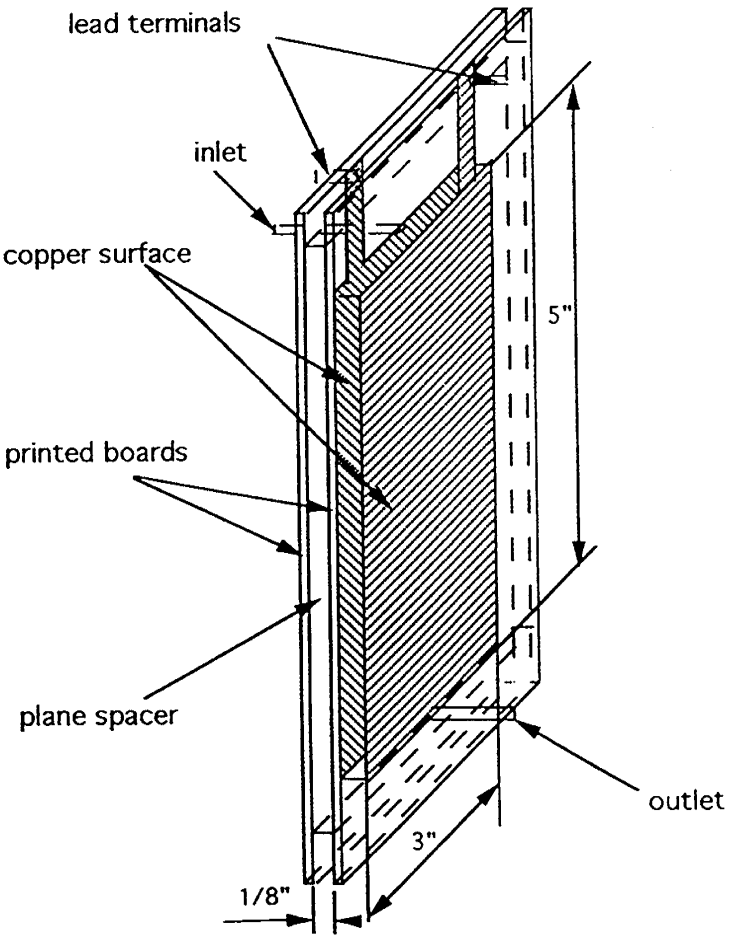

Fig. 2. Capacitance device for production measurements.

Results and Discussion

Quantitative Evaluation of Porosity and Saturation

We first demonstrate the role of model selection in making quantitative estimates using data obtained with samples that are fully saturated with a single fluid phase. In order to validate the quantitative estimates, we compared estimates of the average porosity with those values determined gravimetrically. First, the average values were computed using a simplified procedure in which the regression analysis was performed with the integrated signal. Using this method, possible variation of transverse relaxation with position is ignored. However, this assumption was checked by calculating relaxation parameters for selected models on a pixel-by-pixel basis, and comparing the average of the profile with gravimetric values. This latter approach does not require any assumptions regarding the spatial uniformity of transverse relaxation.

Regression results for the Indiana limestone sample are summarized in Table 1. A substantial reduction in the *RSS* was obtained when using a bi-exponential representation as compared to a single exponential. Little further reduction was obtained using a tri-exponential representation. The selection of the bi-exponential model is supported by the F-test shown in Table 1. The measured values of $M_0(\omega)$ are plotted with calculated values determined with single- and bi-exponential models in Figure 3. The latter model provides a much more precise fit of the data. The value estimated for the average porosity was 17.7%, which is within 5% of the value obtained gravimetrically (which is 16.9%). Neither the single exponential nor the stretched exponential provide accurate estimates. Errors in estimates obtained with those models were 19% and 13%, respectively.

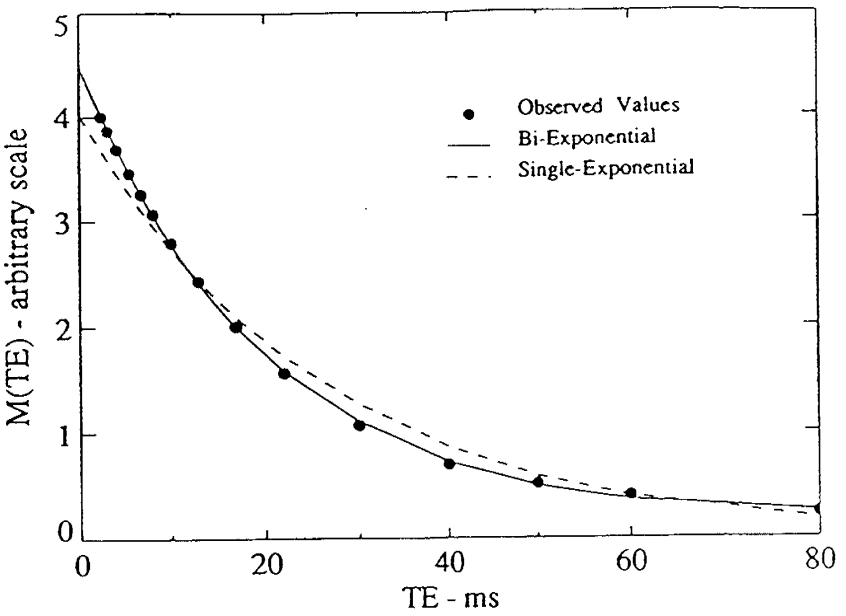

Fig. 3. Comparison of different models.

The calculated porosity distribution is shown in Figure 4. In these calculations, the model selection procedure to determine the appropriate number of components was first carried out for several selected pixels. Since for each case the bi-exponential model was chosen, that model was then used for each of the pixels. The readout gradient G=3.25 Gauss/cm (1350 Hz/mm for protons) was used in the experiment. The pixel size of 0.42mm corresponds to the resolution for this experiment since the frequency resolution of $\Delta\nu$=567 Hz/pixel is much larger than the overall NMR linewidth for this sample, which is approximately 200 Hz. An estimate of the noise level can be obtained by analyzing a region in the profiles which does not include the sample. The ratio between the standard deviations calculated in such a void region with that of a similarly sized region corresponding to a relatively uniform portion of the sample is approximately 1:8, indicating that much of the signal variation may well be due to variations in the local porosity. The average value for the porosity distribution is 17.5%, which compares well with the value calculated with the integrated signal and the gravimetric analysis (see Table 2).

Table 1. Regression Results for Indiana Limestone

N_c	*RSS* (scaled*)	R^2	F-value**	$F_{0.95}$ $(q, n-m)$
1	90.8	0.990		
2	1.29	1.000	450	3.81
3	1	1.000	1.8	3.89
* Scaled to unity for tri-exponential model ($N_c = 3$). ** Calculated with present and previous model.				

Table 2. Porosity Estimation Using Different Relaxation Models

Samples	Porosity (% - Error)				
	Gravimetric Method	Integrated Signal			Avg. Distribution (Bi-Exp.)*
		S-Exp.	Bi-Exp.	Stretch-Exp.	
Indiana Limestone	16.9	20.1(19%)	17.7(5%)*	19.1(13%)	17.5(3%)
Bldg Limestone A	18.9	21.4(13%)	19.1(1%)*	21.5(14%)	19.4(3%)
Bldg Limestone B	19.2	21.1(10%)	19.1(-1%)*	21.0(9%)	19.2(0%)
Texas Cream Limestone	24.2	25.5(5%)	25.0 (3%)*	25.1(4%)	24.9(3%)

* Selected model

Similar analyses were conducted with the two different samples of building limestones and Texas Cream limestone. For these samples, the bi-exponential model was again chosen by the model selection procedure. Average porosity values for these samples calculated using the bi-exponential model were within 1% of those obtained gravimetrically, while estimates using the single- and stretched-exponential models ranged from 9% to 14% as shown in Table 2.

The same procedure was applied for quantitatively evaluating the various saturations of a Texas Cream limestone core sample. For this sample, the bi-exponential model was selected as the most suitable model, and it provided the most accurate estimates as compared with the gravimetric values. Average saturation values for this sample calculated with different models are shown in Table 3. The average saturation values evaluated with the bi-exponential model are within 4% of those obtained gravimetrically, while errors in estimates using single- and stretch-exponential models range up to 15%. Figure 5 shows saturation profiles evaluated with bi-exponential model.

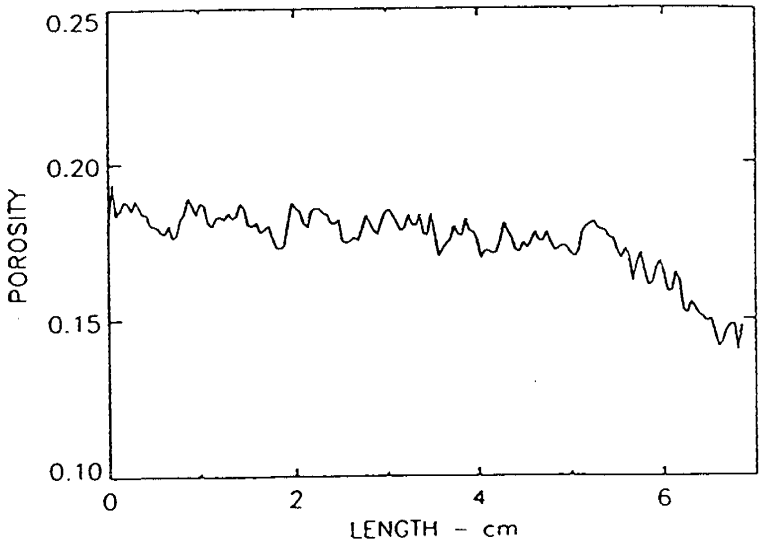

Fig. 4. Porosity profile for Indoana limestone.

Table 3. Saturation Estimation Using Different Relaxation Models

Gravimetric %	Pixel Average (% -Error)		
	S-Exp.	Bi-Exp.*	Stretch-Exp.
91.6	87.7 (4%)	88.8 (4%)	88.7 (3%)
85.1	81.9 (4%)	84.6 (1%)	85.7 (1%)
71.6	66.3 (8%)	72.1 (1%)	74.4 (4%)
63.4	56.7 (11%)	63.8 (1%)	67.0 (6%)
57.7	50.3 (13%)	57.8 (0%)	61.5 (7%)
47.5	40.4 (15%)	49.2 (4%)	53.6 (13%)

* Selected model

Production Measurements from the Displacement Experiment

Using the procedure described above, the porosity profile was determined from the fully-saturated profile image obtained before the displacement experiment. Also, the saturation profiles for several different times during the displacement experiment were determined, and are shown in Figure 5.

In the determination of production values with NMR data, material balances were performed using the NMR profiles corresponding to the fully-oil-saturated initial state and at various oil saturations. In our experiment, a random order of *TE* values was used in acquiring profiles; this can reduce the systematic errors caused by flow effects. The production values measured with the capacitor and those determined with data from NMR images are shown in Figure 6. The production curve acquired from capacitance measurements fairly well matches the values estimated with data from NMR measurements. However, it can also be seen that there are some systematic errors. Since the capacitance device is connected to outlet of core with a long conduit, the capacitance response to the oil displacement was delayed.

We intend to improve the production measurements by using a smaller capacitance device and shorter conduit in order to reduce the systematic errors during the experiments. In addition, we intend to estimate relative permeability and capillary pressure functions using the experimented data which include saturation profiles, pressure measurements and production measurements.

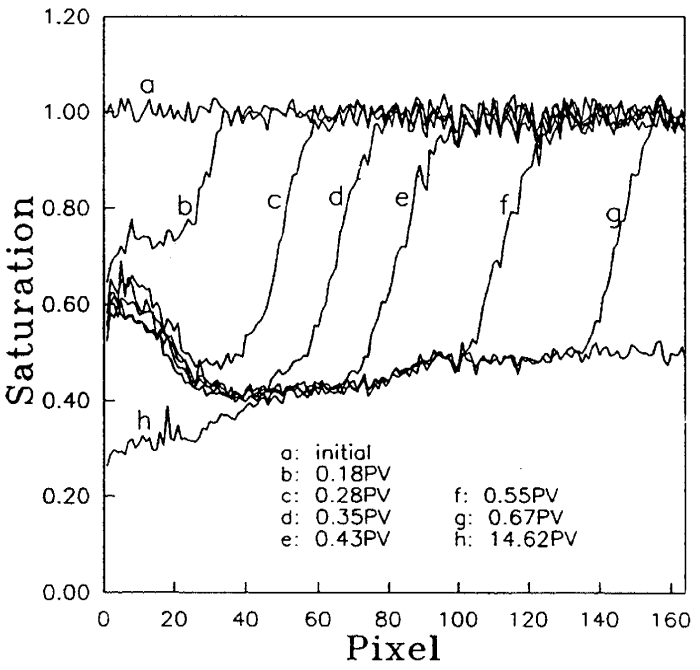

Fig. 5. Saturation profiles for Texas Cream limestone.

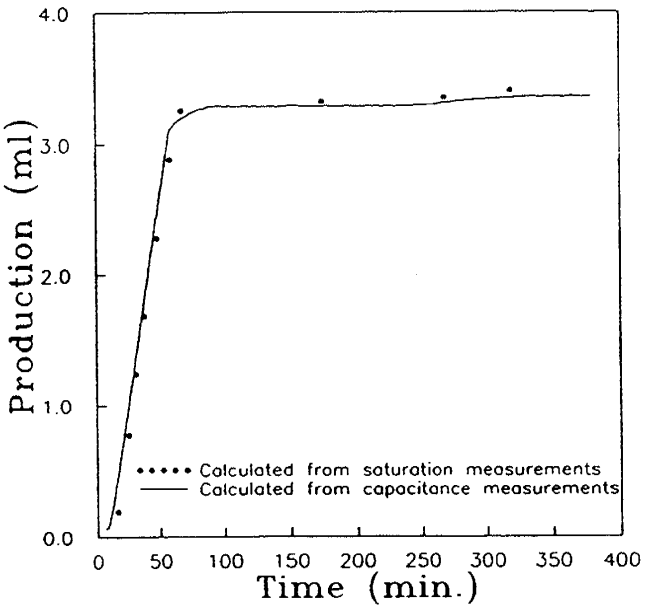

Fig. 6. Oil production profile.

IV. Estimation of Flow Functions from Displacement Experiments

Introduction

Accurate estimates of two and three-phase relative permeability and capillary pressure curves (flow functions) are critical to simulate multiphase flow through porous media. These functions are used in numerical simulators of oil fields to predict reservoir behavior and help make decisions about recovery methods, well locations, flow rates, etc. Since most oil recovery processes occur with the simultaneous flow of two or three phases, reliable methods for accurate determination of multiphase flow functions are very desirable. As part of this project, we are developing a parameter estimation method for estimating multiphase relative permeability and capillary pressure functions from laboratory displacement experiments.

Two-phase flow functions can be estimated from either steady-state or unsteady-state experiments. Production and pressure drop data are obtained from these experiments. In the steady-state procedure, the two phases should be injected simultaneously until a steady-state is attained. Pressure drop and production data are measured and then the injection rate is changed until another steady-state is reached. The values of relative permeability obtained at different steady-states in the experiment are assumed to correspond to an average value of saturation in the sample. In fact a range of these values of saturation may exist in the core, so assignment of the relative permeabilities to an average saturation value may lead to significant errors in the estimates. Besides, the steady-state experiment is very long and tedious to carry out, and

the very few values of relative permeability determined from such experiments do not allow for adequate resolution of the relative permeability curves.

The unsteady-state displacement experiment is fast and a great deal of data are collected. For this reason it is usually the preferred experiment. However, the process of estimating the flow functions is more complex. In this experiment, the core is flooded with one of the fluids and then this fluid is displaced by injecting the other phase. Data are collected during the dynamic displacement. Usually the Johnson-Bossler-Naumann (JBN) method[10] is used to estimate two-phase relative permeability functions using production and pressure drop data. This method is based upon Buckley-Leverett[11] displacement which, in particular, neglects capillary pressure effects. In an attempt to achieve this condition, experiments are performed at high flow rates that greatly exceed fluid velocities encountered in reservoir production. Great inaccuracies in the estimates of relative permeabilities may be obtained when the capillary pressure is neglected[12]. To simulate fluid displacement using the functions estimated with the JBN analysis, the capillary pressure curve must be obtained from an independent experiment.

Watson and coworkers[13] developed a regression-based parameter estimation procedure to estimate simultaneously two-phase relative permeability and capillary pressure functions. In this method, the relative permeability and capillary curves are adjusted within a numerical simulation of the laboratory experiment in such a way that the calculated quantities match, in a weighted least squares sense, data measured during the experiment. The simulation can include all the important physical effects, such as capillary pressure. In addition to the use of measured values of the pressure drop and production, the parameter estimation approach can incorporate other data, such as saturation distributions measured during the displacement experiments.

In this work we have extended the regression-based parameter estimation technique for obtaining estimates of three-phase relative permeability and capillary pressure functions from dynamic displacement experiments. Full development of this method should provide the first reliable method for obtaining three-phase relative permeability functions. Previously, three-phase relative permeabilities have been obtained from models based on measurement of two-phase relative permeabilities. However, various methods give different results, and sufficient data have not been available to evaluate these methods. The only method currently used to estimate three-phase relative permeabilities from dynamic displacement experiments is a method developed by Sarem[14]. This method is an extension of JBN method and, consequently, it is subject to the same assumptions. In particular, it neglects capillary pressure effects and assumes linear isoperms. It is not likely that accurate estimates of the relative permeability curves can be obtained when those assumptions are used. Several works have shown that the isoperms may be concave or convex[15-21]. A reliable method for estimating accurate three-phase relative permeability and capillary pressure functions is critical for accurate description of three-phase flow through porous materials.

Theory

In this section we present the mathematical model used to describe two and three-phase flow through porous media. We then discuss the estimation procedure and the Monte Carlo method for computing confidence intervals for the estimated functions.

Mathematical Model of Displacement Process

To estimate multiphase flow functions, we need a model capable of describing unsteady-state multiphase flow through a core sample. The experiments considered for the two-phase case are imbibition or drainage for which a single fluid phase is injected. These are the standard experiments used to analyze multiphase flow through porous media. The three-phase experiment is more complex than the two-phase experiment, and further work on designing the experiment is desired. At this time we are considering injecting one or two phases. However, the computer code for solving the model is flexible so that future changes can be readily incorporated.

We are using the following equations which form the standard model for simulating multiphase flow in porous media[22]:

$$\nabla\cdot\left(\frac{Kk_{rw}\rho_w}{B_w\mu_w}\left(\nabla P_w+g\nabla z\right)\right)=\frac{\partial\left(\phi\rho_w S_w/B_w\right)}{\partial t}+q_w \tag{16}$$

$$\nabla\cdot\left(\frac{Kk_{ro}\rho_o}{B_o\mu_o}\left(\nabla P_o+g\nabla z\right)\right)=\frac{\partial\left(\phi\rho_o S_o/B_o\right)}{\partial t}+q_o \tag{17}$$

$$\nabla\cdot\left(\frac{Kk_{rg}\rho_g}{B_g\mu_g}\left(\nabla P_g+g\nabla z\right)\right)=\frac{\partial\left(\phi\rho_g S_g/B_g\right)}{\partial t}+q_g \tag{18}$$

$$P_{cow}=P_o-P_w \tag{19}$$

$$P_{cgo}=P_g-P_o \tag{20}$$

$$S_o+S_w+S_g=1 \tag{21}$$

where

ϕ = porosity of the porous medium
S_i = saturation of phase i
ρ_i = density of phase i
μ_i = viscosity of phase i
K = absolute permeability of the porous medium
k_{ri} = relative permeability of phase i
P_i = pressure of phase i
P_{cij} = capillary pressure between phases i and j
q_i = sink of phase i
B_i = formation volume factor of phase i
g = gravitational constant

The subscripts o, w, and g refer to oil, water, and gas.

These equations can be simplified to represent the two-phase case. With this model we have greater flexibility than with the Buckley-Leverett model since we can specify in

different sections of the core permeability, porosity, and initial water saturation. To solve this model, the relative permeability and capillary pressure curves are represented as functions of saturation. We propose the use of B-splines to represent these curves due to their ability to represent an arbitrary smooth function[23,24]:

$$k_{ri}(S_w,S_o)=\sum_{j=1}^{n_i} a_j^i N_j^m(S_w,S_o) \tag{22}$$

$$P_c(S_w,S_o)=\sum_{j=1}^{n_i} a_j^i N_j^m(S_w,S_o) \tag{23}$$

where

$N_j^m(S_w,S_o)$ = bivariate B-spline

a_j^i = coefficients to be estimated

n_i = dimension of the spline

m = total order of the spline

Several finite difference methods have been proposed to solve these equations. We solved them using an implicit approach for one or two saturations and one pressure depending if it is a two or three-phase case. This is a variation of the simultaneous solution method reported by Aziz and Settari[22]. To validate the computer program, results of this program were compared with results of previous study cases at Texas A&M University[26] and with results of simulators at Arco Oil and Gas Co. The computer program was designed to be run on the Cray supercomputer. Using this computer we can estimate the flow functions fast and efficiently.

Estimation Procedure

When the relative permeability and capillary pressure functions are represented using B-splines with a chosen partition, the functions are specified by the set of coefficients a_j^i in Eqs. 22 and 23. The relative permeability and capillary pressure functions can then be estimated by choosing the coefficients so that values calculated with the numerical simulation of the experiment "match" the measured data. This can be accomplished by determining the coefficients that minimize the weighted sum of squared differences between the measured and calculated quantities:

$$Q(\vec{\beta})=(\vec{y}-\vec{f}(\vec{\beta}))^T W(\vec{y}-\vec{f}(\vec{\beta})) \tag{24}$$

where

$Q(\vec{\beta})$ = objective function

$\vec{y}$ = vector of experimental data

$\vec{f}(\vec{\beta})$ = vector of predicted values

W = weighting matrix

In this expression, the vector of parameters to be estimated is:

$$\vec{\beta} = \left[a_1^w, \ldots, a_{N_w}^w, a_1^o, \ldots, a_{N_o}^o, a_1^g, \ldots, a_{N_g}^g, a_1^{p_1}, \ldots, a_{N_{p_1}}^{p_1}, a_1^{p_2}, \ldots, a_{N_{p_2}}^{p_2}\right]^T \quad (25)$$

where w, o, and g represent water, oil and gas respectively; p_1 and p_2 represent the two capillary pressures. The number of parameters to be estimated may be increased to find an appropriate representation for the flow functions[25]. The matrix W should be chosen as the inverse of the variance-covariance matrix for measurement errors. The vectors of experimental and predicted data include the pressure drop, production, and in situ data. We included linear inequality constraints in the estimation process since we desire that the functions be monotonic:

$$G\vec{\beta} \geq \vec{g} \quad (26)$$

where

$\vec{g}$ = right hand side of inequality constraints

G = matrix of inequality constraints

The form of the inequality matrix and the right hand side vector has been discussed in detail by Richmond[13].

Accuracy of Estimates

Approximate pointwise confidence intervals for the estimated functions can be obtained using constrained Monte Carlo simulation[25]. The solution of the following minimization problem gives parameter errors that correspond to a specific error vector:

$$min\ L(\delta\vec{\beta}) = \left[\vec{\varepsilon} - A_t\delta\vec{\beta}\right]^T W^{-1}\left[\vec{\varepsilon} - A_t\delta\vec{\beta}\right] \quad (27)$$

$$subject\ to: \quad G\delta\vec{\beta} \geq \vec{g} - G\vec{\beta}$$

where

$L(\delta\vec{\beta})$ = objective function

$\delta\vec{\beta}$ = vector of variations in parameters

$\vec{\varepsilon}$ = vector of residuals

A_t = sensitivity matrix

Using a pseudo-random number generator, N_{mc} sets of random errors are generated. With these random errors and the variances of the pressure drop, production, and in situ data, we generate N_{mc} different vectors of residuals. Solving Eq. 18 for each vector of residuals we find N_{mc} vectors of variations in the parameters. With these vectors and the

vector of the specified parameters we can compute N_{mc} different relative permeabilities and capillary pressure curves. For example, for the two-phase case, ordering values for these functions at any given saturation S_w, we can approximate 95% confidence intervals by discarding the outer 5% of these calculated values:

$$
\begin{aligned}
&k_{rn}\left(S_w, \vec{\beta}_{i1}\right) \le k_{rn}\left(S_w, \vec{\beta}_{i2}\right) \le \ldots \le k_{rn}\left(S_w, \vec{\beta}_{iN_{mc}}\right) \\
&k_{rw}\left(S_w, \vec{\beta}_{j1}\right) \le k_{rw}\left(S_w, \vec{\beta}_{j2}\right) \le \ldots \le k_{rw}\left(S_w, \vec{\beta}_{jN_{mc}}\right) \\
&P_c\left(S_w, \vec{\beta}_{k1}\right) \le P_c\left(S_w, \vec{\beta}_{k2}\right) \le \ldots \le P_c\left(S_w, \vec{\beta}_{kN_{mc}}\right)
\end{aligned}
\tag{28}
$$

The same ordering can be done to approximate confidence intervals for three-phase flow functions at any given values of saturation. Analyzing the shape of the confidence intervals obtained, we can study the influence of the data in the accuracy of the estimated flow functions.

Results and Discussion

At this time we have obtained results for simulated two-phase cases at low and high flow injection rates. In these cases, we assumed "true" flow functions of typical reservoir samples. With these functions we simulated experiments and collected predicted data. Then, we added random errors to the data to obtain "simulated" data. As an example of the improvement in accuracy of the estimated relative permeability and capillary pressure functions when in situ data are included in the parameter estimation process, we discuss the estimated functions obtained using simulated data for two-phase flow. This example was presented by Richmond[26]. The core was initially flooded with water at residual oil saturation. Oil was injected at a low flow rate to displace the water from the core and production and pressure drop data were collected. The initial water saturation was 0.80 and the lowest value of saturation reached was around 0.425. Starting with an initial guess of the parameters, Richmond estimated the flow functions using the parameter estimation procedure. He found that sometimes incorrect estimates of the flow functions could be obtained if too few parameters were used in the B-spline representation of the flow functions. These incorrect estimates corresponded to local (nonglobal) minima encountered in minimizing the objective function defined by Eq. 24. We considered the same case but now we included in situ data in the estimation process. We estimated the flow functions by solving a sequence of estimation problems in which the number of parameters in the B-spline representation were increased until significant reductions in the residual value of the objective function were no longer achieved. The results obtained in all runs using in situ data did not show incorrect estimates of the flow functions corresponding to nonglobal minima, and more accurate estimates were obtained. Using the constrained Monte Carlo procedure, we computed confidence intervals for the "true" flow functions. These confidence intervals were computed using three equally spaced interior knots in the region of water saturation between 0.25 and 0.80.

Figs. 7 and 8 show the estimated functions using production and pressure drop data (case 1) in the parameter estimation procedure. Figs. 9 and 10 show the results including in situ data (case 2). Clearly, we obtained better accuracy for the estimated flow functions when we included in situ data in the estimation procedure. This shows the great sensitivity that our estimation procedure has for the in situ data. Figs. 7 and 8 show good estimates of the relative permeability and capillary pressure functions but the accuracy is poor. Since the lowest value of water saturation reached was around 0.425, we could not obtain accurate estimates of the flow functions below this value. Hence, the estimated functions have large confidence intervals in the region of water saturation below this value in both cases. The bottleneck in the confidence intervals for the capillary pressure in Fig.8 corresponds to the region of water saturation reached after the breakthrough time. This region of saturation corresponds to the steady-state where we collected half of the production and pressure drop data (400 values). Since a great amount of data were available for estimating the flow functions in this region of saturation, great accuracy in the estimated capillary pressure was obtained.

This summer our estimation procedure was used to analyze experimental production, pressure drop, and in situ data at ARCO Oil and Gas Co. in Plano, Texas. The in situ saturation data were obtained using X-ray CT scanning. The data analyzed corresponded to two core samples. For one core, in situ saturation data were obtained at both low and high flow rates. These data, together with production and pressure drop data, were used in our parameter estimation method to estimate simultaneously relative permeability and capillary pressure functions. The production and pressure drop data calculated using our estimated functions showed a better match of the experimental data than the values calculated using the estimates obtained with the JBN analysis. The second core was composed of two different samples of rock. We estimated the flow functions using production, pressure drop, and the available in situ saturation data. The results predicted with our estimated functions showed great improvement compared with the results predicted using the estimated flow functions obtained with the JBN analysis. The results and discussion of the work at ARCO will be presented or published in the near future.

At this time, we have estimated three-phase relative permeability and capillary pressure functions for a simple simulated case. The results obtained show great accuracy in the estimated flow functions. Details about these results and the proposed solution of the three-phase flow model is available in Dr. Mejia's Ph.D. dissertation.

V. Characterization of Local Fluid Distribution by NMR Restricted Diffusion Measurements

Introduction

An important aspect of the oil-recovery research is to understand fluid flow behavior in porous media at the microscopic level. Since microscopic events control displacement processes in porous rocks, studies of properties that characterize local pore structures are expected to yield important information for understanding macroscopic flow behavior. In addition, a comprehensive theory for predicting the

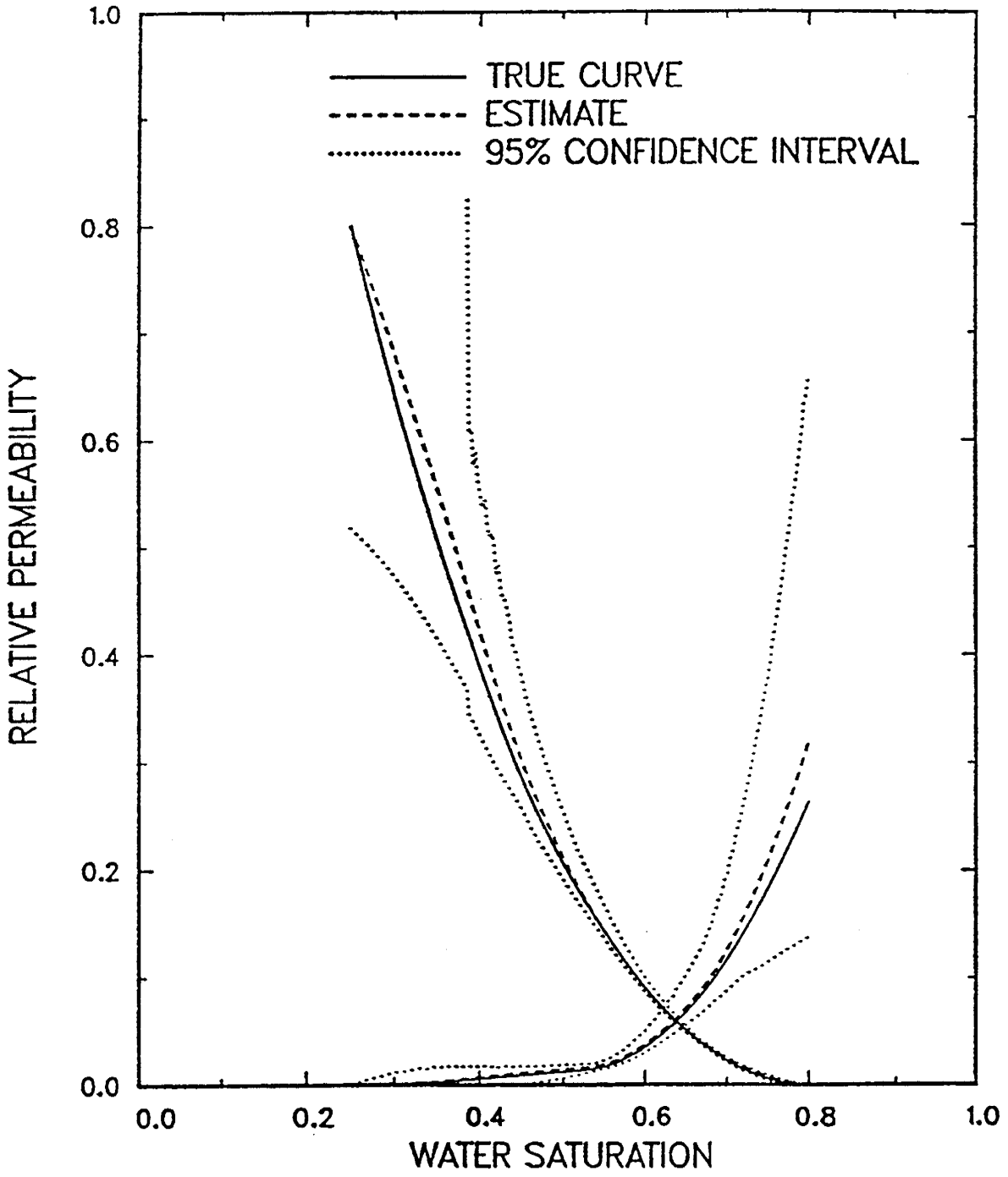

Fig. 7. Relative permeability curves for Case 1.

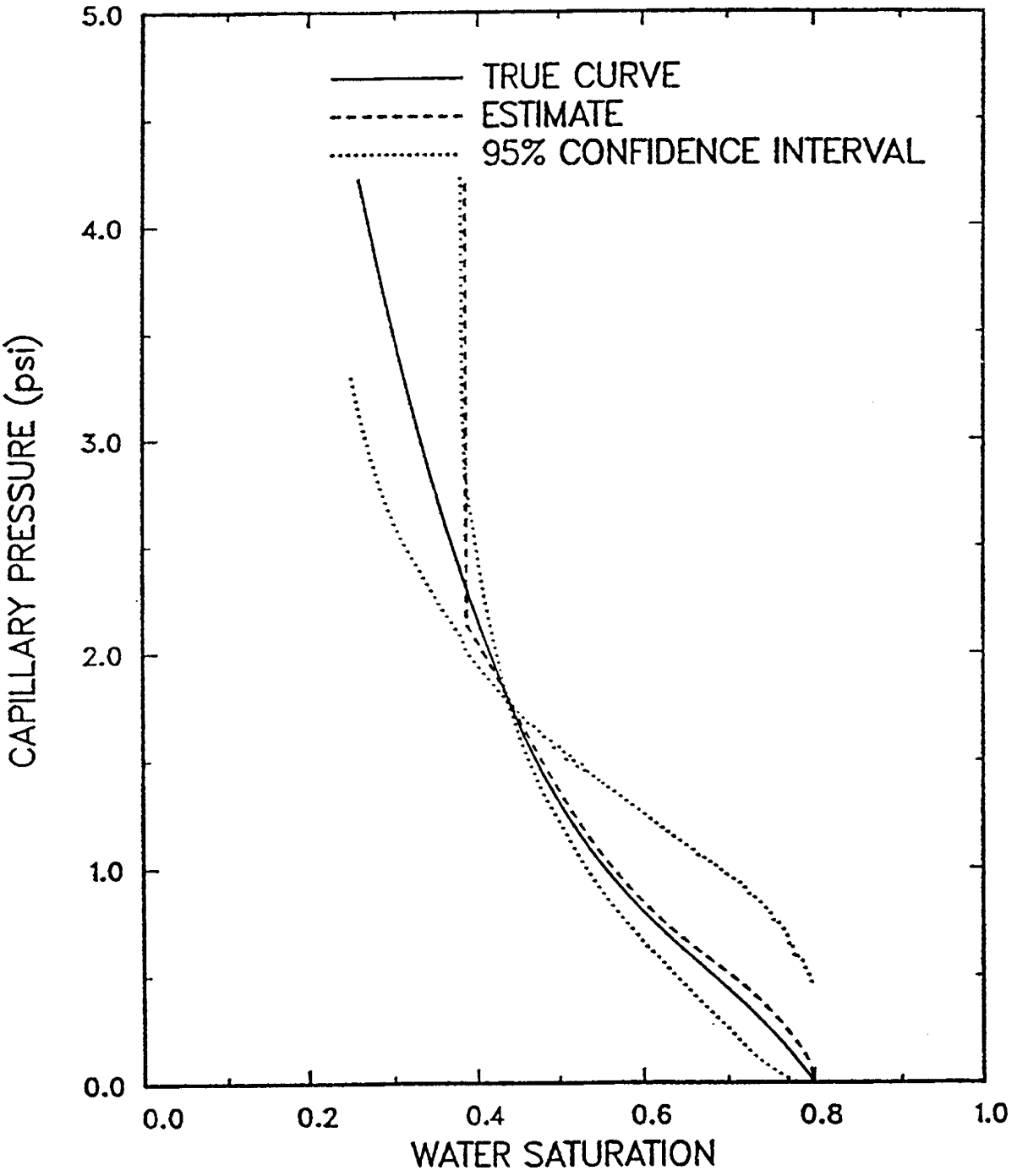

Fig 8. Capillary pressure curvs for Case 1.

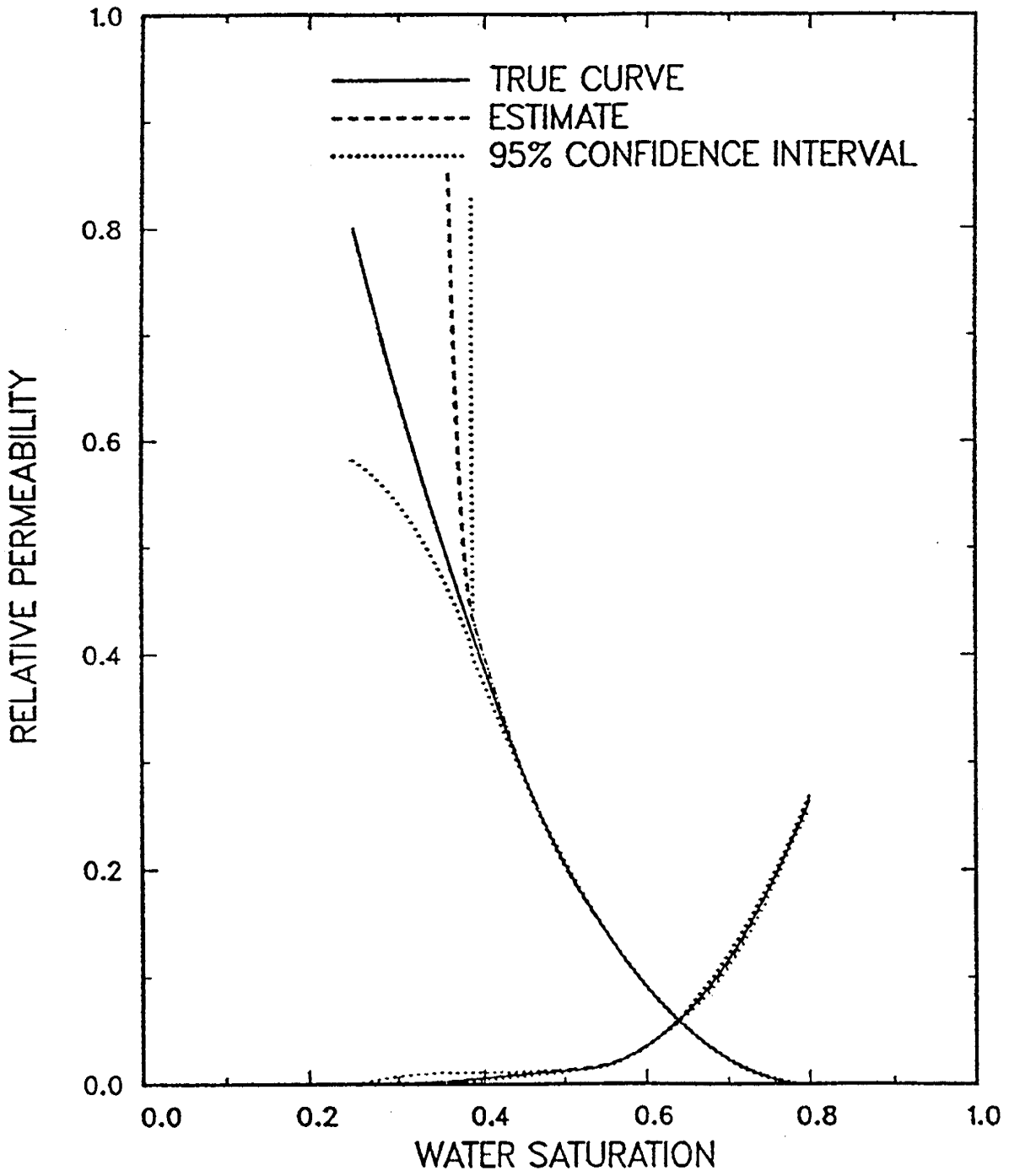

Fig. 9. Relative permeability curves for Case 2.

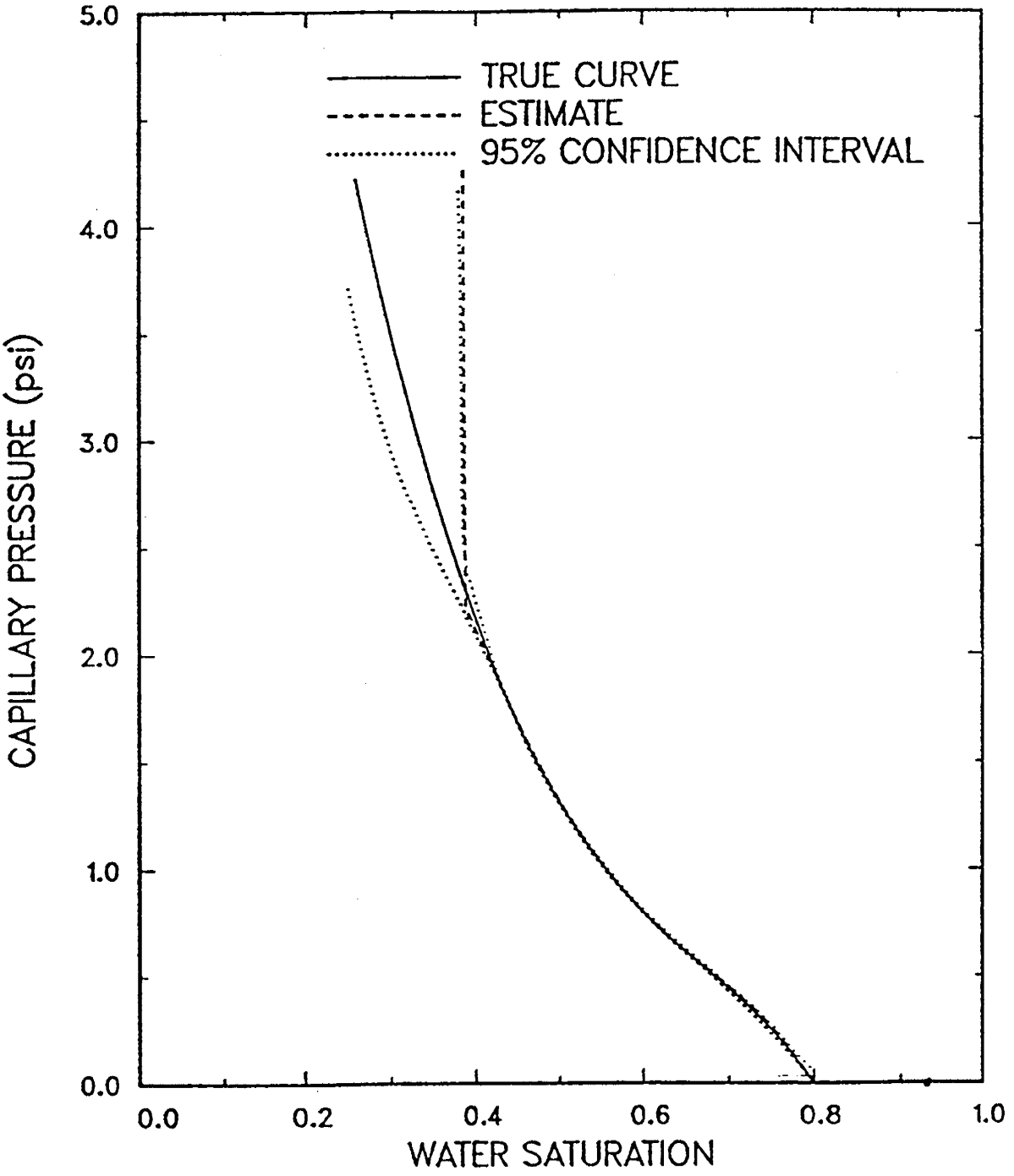

Fig. 10. Capillary pressure curves for Case 2.

properties on the basis of microscopic experimental results is desired in order to better understand and predict oil recovery processes.

NMR techniques can detect the changes in the local structural arrangements and interactions in the vicinity of the resonating nuclei. Consequently, NMR can provide an excellent means for elucidating pore structure and fluid transportation in reservoir rocks at a microscopic level.

The new method of using NMR for characterizing pore structure is based on the fact that molecular self-diffusion in a porous medium is hindered by the presence of pore boundaries. Thus, it is conceivable that the study of restricted diffusion may provide information leading to pore structure characterization. In particular, the measured apparent diffusivity will be smaller in a geometrically confined system such as porous media, and will be time dependent, with apparent diffusivity decreasing with the diffusion time.

Pulsed field gradient (PFG) NMR techniques can be used to study restricted diffusion in porous media. The capability for measuring diffusivity values over a large interval of diffusion times by PFG NMR makes it unique for studying restricted diffusion. In our work, restricted diffusion measurements have been conducted in un-consolidated model porous media including several different sized glass bead packs as well as in porous rock samples. We observed apparent diffusivity as function of pore size, fluid saturation, and the experimental diffusion times during which molecular diffusion is probed. We developed computational procedures for explaining the experimental observations and for obtaining pore structural information using experimental data.

Theory

PFG NMR Restricted Diffusion Measurements

There are several PFG NMR pulse sequences[27] available for diffusion measurement. For specific application to our porous systems, we found that the PFG stimulated echo sequence[11] is the most favorable choice. This sequence allows a relatively large dynamic range of diffusion time for measuring the apparent diffusivity for systems such as fluids in porous media that characteristically exhibit larger spin-lattice relaxation time (T_1) than spin-spin relaxation time (T_2). Using this pulse sequence, the measured stimulated echo amplitudes are represented by[28]:

$$M = \frac{M_0}{2}\exp\left[-\frac{2\tau_1}{T_2}-\frac{\tau_2-\tau_1}{T_1}\right]\exp\left[-\gamma^2 D\left(a\boldsymbol{g}^2+bg_0^2+c\boldsymbol{g}\cdot\boldsymbol{g}_0\right)\right] \tag{29}$$

where $\boldsymbol{g}$ and $\boldsymbol{g}_0$ are the applied and internal gradients, respectively. The coefficients

$$a=\delta^2\left(\Delta_d-\frac{\delta}{3}\right),\ b=\tau_1^2\left(\tau_2-\frac{\tau_1}{3}\right),\ c=-\delta\left[t_1^2+t_2^2+\delta\left(t_1+t_2\right)+\frac{2}{3}\delta^2-2\tau_1\tau_2\right] \tag{30}$$

consist of timing parameters which are defined in the pulse sequence illustrated in Fig. 11.

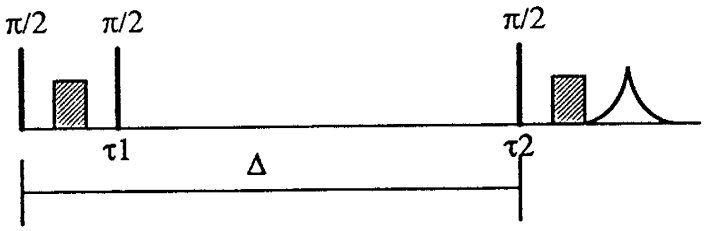

Fig. 11. PFG stimulated echo sequence.

From this expression, we see that both the relaxation effect (T_1 and T_2) and the diffusion effect (D) contribute to the echo decay. By measuring the stimulated echo amplitude at $g = 0$ and at a finite value of g, the relaxation effect can be canceled since

$$\Phi = \frac{M}{M_0}\exp\left[-\gamma^2 D\left(ag^2 + cg\cdot g_0\right)\right], \tag{31}$$

where

$$M_0 = \frac{M_0}{2}\exp\left(-\frac{2\tau_1}{T_2} - \frac{\tau_2 - \tau_1}{T_1} - \gamma^2 D b g_0^2\right) \tag{32}$$

is the echo amplitude for $g = 0$.

In porous media the internal gradient g_0 mainly arises from the variation of magnetic susceptibility χ and the structural heterogeneity. If the g_0 effect is negligible, the above equations are simplified to

$$\Phi = \frac{M}{M_0}\exp\left(-\gamma^2 D a g^2\right) \tag{33}$$

and

$$M_0 = \frac{M_0}{2}\exp\left(-\frac{2\tau_1}{T_2} - \frac{\tau_2 - \tau_1}{T_1}\right). \tag{34}$$

Calculation of Apparent Diffusivities

Due to distributions of pore sizes and the heterogeneous nature of the pore structure, as well as the pore connectivity, there may exist a distribution of apparent diffusivities for fluid in porous media. We focused on the development of computational procedures for estimation of such distributions, and the methods of approximating the distribution with different mathematical models.

Single-Component Diffusivity: Simplified procedures can be used for calculating a single value for the apparent diffusivity. This case would be valid if there is a single diffusional process, such as in cases with a narrow distribution of pore sizes, or in cases for which data are measured with short diffusion times such that only a narrow distribution of diffusivities is observed. In these cases, if the internal gradient is neglected, linear regression may be used to determine the apparent diffusivity D_{app} from

$$\ln \Phi_i = -\gamma^2 D_{app} a g_i^2, \tag{35}$$

where values of Φ_i are measured echo decays using various values of applied gradient g_i. In this case, the data will appear linear with g^2 on a semilog scale when a single value of D_{app} is appropriate. In cases for which the internal gradient is not negligible, D_{app} can be calculated using nonlinear regression by determining the values of the diffusivity and internal gradient that minimize the following objective function:

$$J = \sum_{i=1}^{n} \left\{ \Phi_i^{obs} - \Phi_i^{cal} \right\}, \tag{36}$$

where Φ_i^{obs} are measured values and Φ_i^{cal} are values calculated using Eq. (32).

Diffusivity Distributions: In more general cases for dealing with diffusion in porous media, we found that the single-diffusivity estimation can not represent the echo decay satisfactorily. We developed two computational approaches for situations not suitably described with a single component D_{app}. In one method, we used an orthogonal set of B-spline functions[29] to represent diffusivity distribution functions and in another method we used multiple discrete components to approximate the diffusivity distributions.

In the first method, the continuous distribution of diffusivity is represented by B-spline functions:

$$m(D) = \sum_{j=1}^{N} C_j B_j^k(D). \tag{37}$$

The echo decay can then be described using the decay function of a single diffusional process weighted by the distribution function:

$$\Phi(D) = \int_{D_1}^{D_2} m(D) \exp\left(-\gamma^2 D a g^2\right) dD, \tag{38}$$

where the internal gradient effect is neglected. Our computational procedures are to determine the set of coefficients C_j with a given B-spline dimension N. A computational routine was developed to obtain these coefficients with the non-negative least squares[30] method.

A second approach we used is to represent the distribution as a set of discrete components. The echo attenuation would be given as a sum of the contributions from each component:

$$\Phi = \sum_l \Phi_l = \sum_l \varphi_l \exp\left[-\gamma^2 D_l \left(ag^2 + cg \cdot g_0\right)\right], \tag{39}$$

where $\sum_l \varphi_l = 1$.

Experimental Work

Diffusion measurements were conducted in model porous media made of 8 different size ranges of closely-packed glassbead packs and porous rocks. The bead size range of these 8 samples are 1-38, 45-63, 63-90, 90-125, 125-180, 180-250, 250-355, 500-710 mm, respectively. These beads were obtained from a commercial source. We sieved the sizes, cleaned using 0.06M NaOH first, rinsed with distilled water to neutral acidity, cleaned again using 6M HCl solution, and rinsed thoroughly with distilled water. Fluid saturated beads packs were centrifuged to ensure close-packing before performing the NMR measurements. Excessive amounts of fluid were carefully removed from the tops of the bead packs. Two Bentheimer and one Berea sandstone samples, and one Texas Cream limestone sample were used in the experiments. These rocks have different characteristic pore sizes and permeabilities. One Bentheimer sandstone was studied extensively at different water saturation states obtained by a gas-liquid drainage process.

Results and Discussion

Diffusion in Model Porous Media

In the last annual report, results were presented in which the data measured using model porous media were analyzed with a single-component diffusivity. Using stimulated echo measurements, restricted diffusion was observed in the eight different sized glass bead packs. The echo attenuation, as a function of the applied gradient, showed strong dependence on the bead size (Fig. 12). The measured apparent diffusivity depends on bead sizes as well as on the diffusion times. To quantitatively relate the bead sizes with pore sizes, we assumed each bead pack had a uniform size and an ideal packing structure (i.e. either f.c.c. and h.c.p. structures). Using this approach, we obtained the pore-volume-to-pore-surface ratio of a bead pack to be

$$\xi = \frac{V_{\text{pore}}}{S_{\text{pore}}} = \frac{\sqrt{2} - \pi/3}{\pi} d, \tag{40}$$

where d is the bead size, and ξ is defined as the characteristic pore size. With this approximation, we obtained the relationship between the bead size d and the apparent diffusivity D_{app} shown in Fig. 13. The single-component diffusivity model was used for estimating the values of D_{app} for each bead pack. Two methods were used for estimation: one incorporated the effects of the internal gradient, while the other neglected it. It can be seen that the values obtained using the two approaches are quite similar, indicating that the g_0 effects are not very significant. It is noted that the pore sizes defined in Eq. (40) are approximations even for sieved bead packs, since even a narrow distribution may result in a sizable departure from the ideal packing.

The linear dependency of Eq. (36) is not observed for relatively long experimental diffusion times. Figure 14a shows curves for Φ_i as a function of g_i^2 for beadpacks with d = 125-180 mm, measured at Δ_d = 400 ms with 22 g_i values ranging from 0--16 G/cm and with δ = 3 ms and τ_1 = 5 ms. Since we found that the echo decay changes more rapidly in the smaller g_i regions, more experimental g_i values were chosen in this region. For this longer diffusion time, even for these smaller values of g_i and δ, a nonlinear dependence can not be explained satisfactorily by considering the effects due to g_0 with a single apparent diffusivity. Thus we considered reconciliation of the data using a distribution of diffusivities.

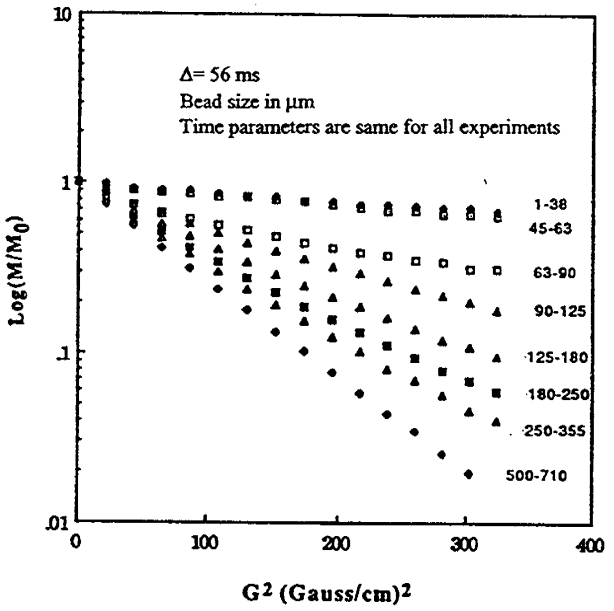

Fig. 12. Echo attenuation vs. g^2 in different sized bead packs.

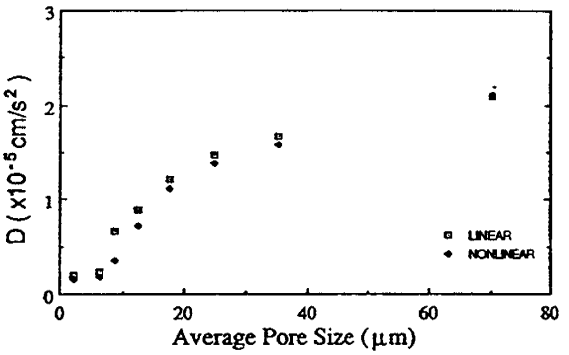

Fig. 13. Pore size dependency of D_{app}.

We used the procedure described in the *Theory* section to estimate the diffusivity distributions. The validity and stability of the computational procedure have been tested by recovering the spectra from both exact and error corrupted data. Also, more experimental data (22 points) were acquired to improve the accuracy of the calculation. Using this procedure, we obtained the diffusivity spectra (Fig. 14b) corresponding to the experimental echo decay data shown in Fig. 14a. The number of splines was selected from a plot of residual sum of squares vs. the number of splines (Fig. 14c). In this case, seven splines were selected which corresponds to the fewest degrees of freedom that attains essentially the smallest RSS. We also calculated the diffusivity distribution using discrete component models represented by Eq. (39) but dropping the term involving the internal gradient g_0. In particular, the estimated curves for l = 1 and 2 components are shown in Fig. 14a. It is obvious that the single component model fits the experimental data poorly while the continuous model provides the best fit. The fitting quality of the three models

can be more easily examined by comparing the residual sum of squares (RSS) values computed using different models. We obtained RSS=$1.0\text{x}10^5$, $1.6\text{x}10^2$, and $8.1\text{x}10^5$ for continuous, single, and two discrete component analyses, respectively. We see that the RSS of the continuous model is approximately one order of magnitude better than the two-component model, and is three orders of magnitude better than the single-value diffusivity model. We see clearly in this case the single-diffusivity analysis will not be valid but the two-discrete-component model is approximately valid. We computed that the values of two diffusivities for the two discrete component model are $3.3\text{x}10^6$ cm^2/s and $1.6\text{x}10^5$ cm^2/s with percentages of the two components to be 32% and 68%, respectively. The average diffusivity value calculated from two-component model is $1.18\text{x}10^5$ cm^2/s. By comparison, the average diffusivity calculated by

$$\langle D_{app} \rangle = \frac{\int_{D_{min}}^{D_{max}} m(D) D dD}{\int_{D_{min}}^{D_{max}} m(D) dD} \tag{41}$$

using the distribution function $m(D)$ in Fig. 14b is $1.15\text{x}10^5$ cm^2/s, which is in excellent agreement with that for the two-component model.

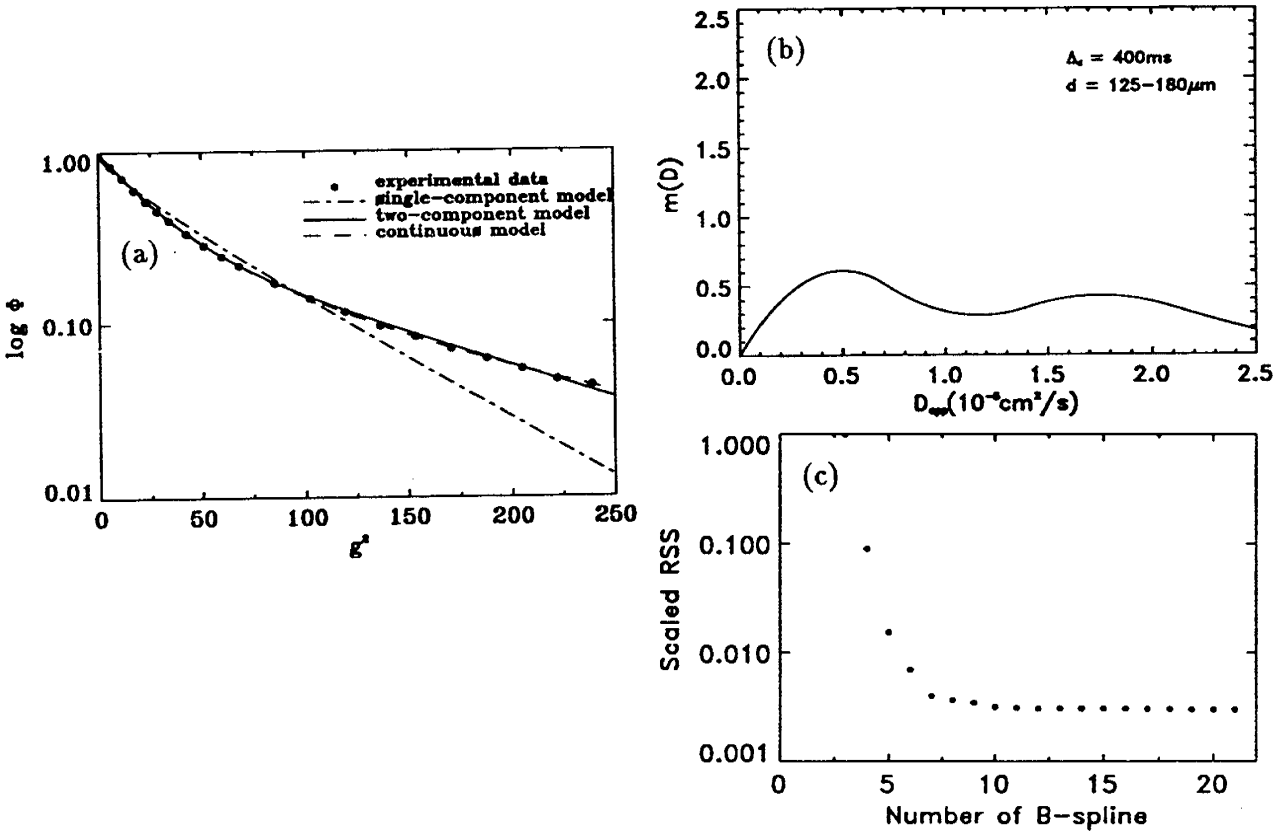

Fig. 14. (a) Nonlinear dependence of log F vs. g2. (b) Calculated diffusivity spectrum. (c) Scaled RSS values for different number of B-splines

In order to investigate the effects of bead sizes and experimental parameters on observed diffusivity distributions, a number of experiments with various diffusion times were performed in several different sized bead packs. First, we discuss the pore size dependence by examining the results obtained using different sized beads but measured with a single, relatively long diffusion time. Figures 15a-e show the calculated apparent diffusivity spectra corresponding to five beadpacks with bead sizes d = 45-63, 90-125, 125-180, 180-250, and 250-355 μm, measured at Δ_d = 400 ms. Again, 22 different g_i values with $\delta = 3$ ms and $\tau_1 = 5$ ms, which are the same as those for obtaining data in Fig. 11a, were used in these measurements. At this relatively long diffusion time, molecular diffusion should experience strong restrictions in all these samples, as the mean pore sizes in the sample are smaller than the free diffusion length scale determined by $\langle x^2 \rangle = 2D\Delta_d$.

The double-peak pattern for the diffusivity spectra is observed for smaller sized bead packs (see Fig. 15), while for the larger sized bead packs only a single peak was observed. It must be emphasized that a single-peaked diffusivity distribution is not equivalent to a single value of diffusivity. In fact, we found that single-valued diffusivity analyses gave very poor fits for those cases.

In Fig. 15, we see that for those spectra showing two peaks, the proportion of the area under the two curves corresponding to the two characteristic regions changes for the different sizes of bead pack. Generally speaking, the peak corresponding to the lower values of the diffusivity results from molecules that have experienced significant restrictions. Presumably, a significant fraction of those have initial positions near to boundaries. In the smaller bead packs, a relatively larger number of molecules may correspond to these positions. In the large bead packs, relatively little of the volume corresponds to the "near boundary" regions. Thus, the spectra of the large sized beadpacks only exhibit single-peaked distributions which may correspond to a merging of interpore and intrapore phenomenon in the larger bead packs. Because of the merging, the diffusivity values corresponding to the single peak for the large bead packs appear smaller than that of the right hand peak in the diffusivity spectra of smaller sized bead packs. We found that the average diffusivity decreases with bead size as would be expected. The values calculated for increasing bead size are $D_{app} = 0.85$, 1.1, 1.2, 1.2, 1.3 cm^2/s, respectively.

Diffusion Measurements in Rocks

Similar diffusion measurements were performed in Bentheimer sandstone rock samples. The two rocks we chose differ in permeability by more than a factor of 2 with k = 1,200 mD for the Bentheimer and k < 500 mD for the Berea sandstone. This difference may reflect a difference in characteristic pore sizes which are distinguishable by PFG NMR diffusion measurements. An advantage of sandstone is that the main chemical composition of sandstones (quartz) is similar to that in glassbeads (SiO_2), and they should thus have similar χ values which will facilitate comparisons with the model porous media.

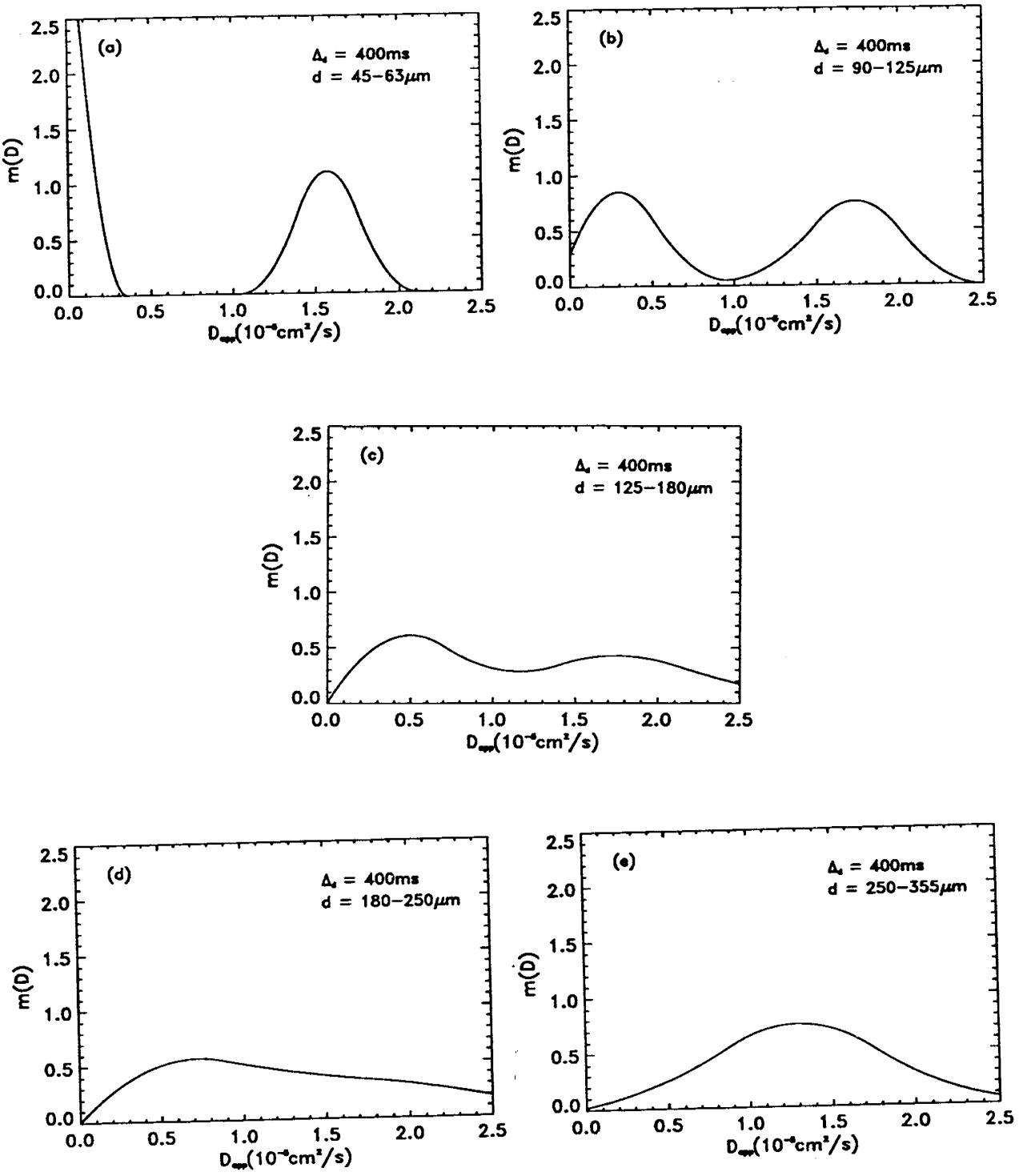

Fig. 15 (a-e) Diffusivity spectra corresponding to different sized bead packs measured with same experimental conditions.

Figure 16 shows the echo attenuation measured with $\Delta_d = 56\text{ms}$ and $\delta = 4\text{ms}$ for the two samples using 23 g_i values. We see that the echo attenuation dropped much faster for Bentheimer than for Berea, i.e., fluid diffusion in the Berea sandstone experiences more restriction, which is consistent with the fact the Berea sample has the lower permeability. It is also noticed that even at this relatively short diffusion time, linear dependence with g^2 on the semilog scale is not observed. This nonlinearity may also be attributed to multiple components of diffusivities. Nevertheless, for the purpose of estimating a characteristic pore size, we used the relatively linear portion of the curve (the first 11 data points corresponding to the lower values of g_i) with nonlinear regression (using Eq. (36)) to calculate the apparent diffusivities. Values obtained for the Berea and Bentheimer samples were $3.4\text{x}10^{-6}$ cm^2/s and $8.6\text{x}10^{-6}$ cm^2/s, respectively. Thus we demonstrated that NMR diffusion measurements can be used to detect differences for rocks with different permeabilities associated with different pore sizes.

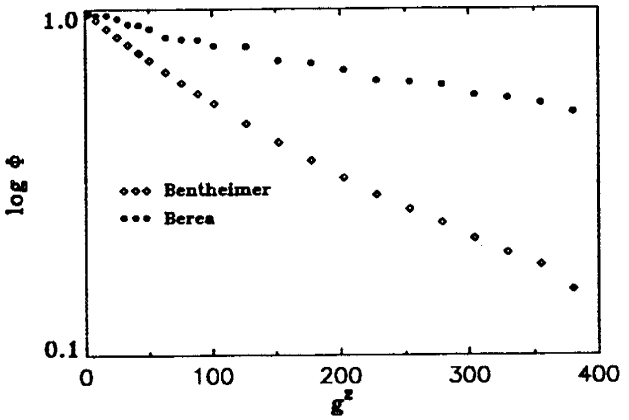

Fig. 16. Echo attenuation measurements in sandstones.

Restricted diffusion measurements were also conducted in a Bentheimer sandstone at various wetting phase (water) saturation states for a drainage experiment involving gas-liquid phases. The purpose of this experiment is to investigate the fluid distribution in different sized pores at different fluid saturations. Figure 17 shows the echo decay curves measured at several saturation states. It is observed that the slope of the echo attenuation becomes less as the saturation is lowered, corresponding to a stronger restricted diffusion effect. Thus the values of D_{app} will be smaller at low saturations, which is interpreted as the water phase being distributed in smaller sized pores. Table 4 lists the values of D_{app} at different saturations. This observation is consistent with the fact that for a drainage process, the wetting phase is distributed in smaller and smaller sized pores as saturation decreases. Saturation dependent studies were also carried out using relaxation measurements and more detailed description of the relaxation study is carried out in the next section.

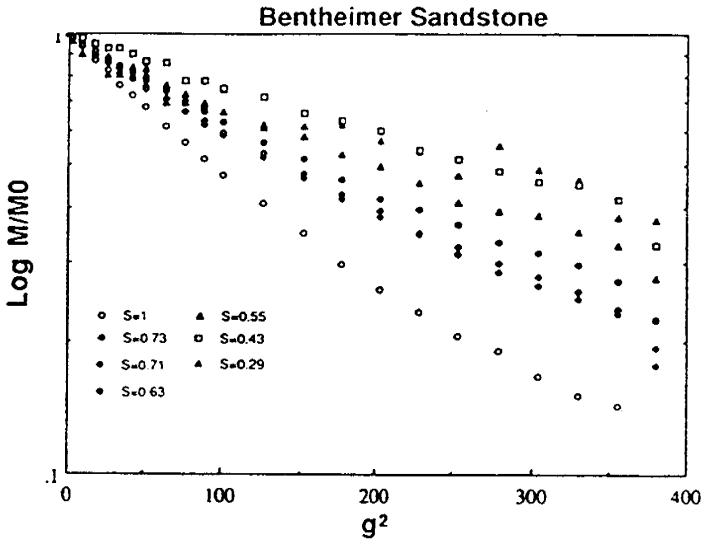

Fig. 17. Saturation-dependent echo attenuation in Bentheimer sandstone

Table 4. Relationship between S_w and D_{app} using single component analysis

S_w (%)	$D_{app}(\times 10^{-5}cm^2/s)$
100	0.68
71.4	0.48
62.8	0.41
54.6	0.32
43.3	0.31
28.8	0.10

VI. Characterizing Saturation and Pore Structure by NMR Spin-Lattice Relaxation Measurements

Introduction

Fluid saturation in porous media is a macroscopically defined quantity that is a measure of the relative amounts of fluid phases. Saturation is controlled by capillary pressures, and thus is related directly with the microscopic pore structures of a porous medium. Detailed information about the relationship between pore structures, fluid distributions and saturations could be useful for a better understanding of displacement processes in such areas as petroleum production, chemical reactors, and environmental remediation.

NMR spin-lattice relaxation measurement has been used as an approach to characterize pore size distributions of porous media based on the fact that surface relaxation dominates the relaxation process and the observed relaxation rate is proportional to the pore surface-to-volume ratio, which can be regarded as a characteristic quantity representing the pore size.

In this study, the NMR relaxation dependence on fluid saturation in porous media is investigated. A gas-fluid two phase drainage process was used to obtain partial water saturation states. The spin-lattice relaxation measurements were carried out at various fluid saturation levels, from which different wetting fluid phase distributions with respect to different saturation levels are obtained. The observed relaxation times decrease monotonically with decreasing wetting fluid saturation. This observation can be explained by considering the fact that the NMR relaxation time is proportional to the characteristic pore size, which decreases as water is drained from the porous medium. The observed relaxation curves also exhibit non-single-exponential decay at all saturation levels, which can be understood by considering a distribution of pore sizes. Stretched exponential and multiple discrete component relaxation functions are used to represent the relaxation decay curves. In these analyses, the effects due to bulk relaxation were separated from the observed relaxation times. The relaxation-saturation relationship was found to fit well with a simple power-law dependence, which provides a basis for a possible new approach for characterizing fluid saturation in porous media.

Theory

The spin-lattice relaxation rate of fluid in porous media can be expressed in terms of a relaxation rate of bulk-like fluid corresponding to regions of fluid away from the pore boundaries, and a relaxation rate of surface-fluid corresponding to a thin layer near the pore boundaries. In the fast diffusion limit[31] the T_1 relaxation rate for fluid in each individual pore can be written as[32]

$$\frac{1}{T_{1_i}} = \frac{1}{T_{1b}} + \frac{\lambda}{T_{1s_i}} \frac{m}{r_i} \tag{42}$$

where r_i is the characteristic pore "radius" and $m/r_i = S_i/V_i$ is the ratio of pore surface to pore volume. The parameter λ is the thickness of surface fluid layer and is equal to a few molecular sizes.

For T_1 measurements using the inversion-recovery sequence, the observed relaxation decay can be represented by a model of multiple discrete exponential components

$$M(t) = \sum_i \left\{ M_{0i} \left[1 - 2\exp\left[-t \left(\frac{1}{T_{1b}} + \frac{\lambda m}{T_{1s_i} r_i} \right) \right] \right] \right\} \tag{43}$$

For a porous medium with a relatively homogeneous mineral composition, the surface relaxation rate, T_{1s}, is relatively uniform. On the other hand, the bulk fluid relaxation time T_{1b} is not pore size dependent. Thus, the above equation can be rewritten as

$$\left(M(t)-M_0\right)\exp\left(\frac{t}{T_{1b}}\right)=\sum_i\left(-2M_{0i}\right)\exp\left(-\frac{t}{\tau_{1i}}\right) \tag{44}$$

where $M_0=\Sigma_i M_{0i}$ and

$$\frac{1}{\tau_{1i}}=\frac{1}{T_{1_i}}-\frac{1}{T_{1b}}=\frac{\lambda}{T_{1s}}\frac{m}{r_i} \tag{45}$$

Clearly, the quantity τ_1 is proportional to the characteristic pore size. The evaluation of the average τ_1 yields the average pore size of the porous medium:

$$\langle\tau_1\rangle=\sum_i f_i\tau_{1i}=\sum_i f_i\frac{T_{1s}r_i}{\lambda m}=\frac{T_{1s}}{\lambda m}\langle r\rangle \tag{46}$$

where f_i is the density-weighted coefficient of the ith component.

If we consider a distribution of relaxation times $P(\tau_1)$ corresponding to pore size distribution $Q(r)$, the relaxation decay function for the inversion recovery sequence is

$$\tilde{M}(t)=\frac{M(t)-M_0}{-2M_0}\exp\left(\frac{t}{T_{1b}}\right)=\int_0^\infty P(\tau_1)\exp\left[-\frac{t}{\tau_1}\right]d\tau_1 \tag{47}$$

where the contribution of T_{1b} has been removed from the integral. A parametrization for the relaxation decay function which has been used with some success in the past is the stretched exponential function:

$$\tilde{M}(t)\approx\exp\left[-\left(\frac{t}{\tau_{1,\alpha}}\right)^\alpha\right] \tag{48}$$

where α is a stretch exponent related to the distribution of relaxation times, and a symbol $\tau_{1,\alpha}$ is used to distinguish values from those obtained using multi-component analyses. It has been shown[33] that this function nearly approximates Eq. (47) when a certain exponential representation is used for the relaxation time distribution; in particular, a value of $\alpha=2/3$ arises when the distribution is represented by a half Gaussian function.

Experimental Work

A cylindrical Bentheimer sandstone sample, 2.54 cm in diameter and 3.25 cm in length, was used in the experiments. The porosity of this sample is 23%. A desaturation device (Fig. 18) was used for obtaining each equilibrium water saturation level. The sample was sealed in a Teflon core holder to ensure one-dimensional displacement in the drainage process. For each process, the sample was fully saturated

with deionized water initially, and then was placed in the desaturation device. The inlet of the device was connected to pressurized N_2 gas and the outlet connected to deionized water. Hydrophobic and hydrophilic membranes were used at the interfaces of the inlet and outlet of rock sample, respectively, to ensure continuity of the gaseous or aqueous phase at the respective ends of the sample. Different pressures were applied to obtain different saturations. Each time the drainage process was performed for a sufficiently long time to ensure a capillary equilibrium was obtained, and then NMR experiments were performed immediately to avoid any fluid redistribution. No significant weight change between the beginning and end of the NMR measurements was observed. Upon completion of measurements for one saturation state, the sample was thoroughly dried in an oven, and then resaturated with deionized water for the next desaturation experiment. By doing so, we preserved a well defined and repeatable initial state.

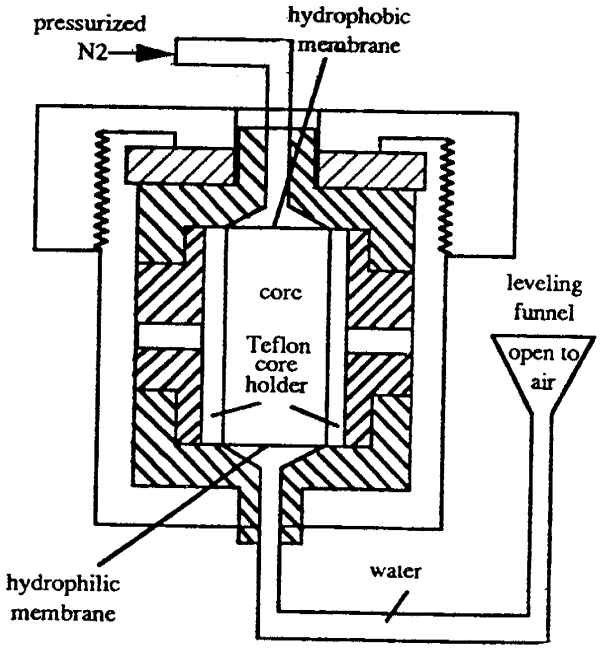

Fig. 18. Water desaturation device used for dainage experiments.

Results and Discussion

Figure 19 shows the variation of τ_1 and the relative fluid intensities at different values of water saturation. The three component multi-exponential function described in Eq. (44) was selected for analyzing the relaxation evolutions corresponding to all values of saturations. The number of components for the multi-exponential representation was chosen from the analysis of the data collected for the fully saturated case. In Fig. 19, the vertical axis represented $f_{0ij} \cdot S_{wj}$, where the subscript j indicates the jth saturation level, and the horizontal axis represents the values of three components of τ_{1ij}. The quantity $f_{0ij} \cdot S_{wj}$ is proportional to the absolute water quantity corresponding to the ith relaxation component. We see that the τ_{11} values, corresponding to the longest component, decrease monotonically with decreasing water saturation for all saturation levels in our study, while the relaxation values of the two shorter components, τ_{12} and τ_{13}, do not vary significantly with saturation. The above features are explained by considering that water is drained from different sized pores at different saturation levels. When saturation decreases, the wetting phase (aqueous phase) has been displaced by the nonwetting phase (gaseous phase) from the largest pores at low capillary pressure (high saturation). With the increase of capillary pressure (at low saturation), the wetting phase is displaced from the next largest pores. From the multi-component analyses, one can evaluate the amount of fluid distributed in different pore size ranges since the different pore size ranges are represented by the relaxation time components and the percentage index f_i is proportional to the amount of fluid corresponding to each pore size range. This approach requires that the factor m in Eq. (46) is not significantly different at different saturations and the values of T_{1s} are approximately independent of pore size, which should be valid for rocks with relatively homogeneous compositions. With these approximations, the relation

$$\frac{\tau_{1,S_{w_j}}}{\tau_{1,S_w=1}} = \left[\frac{m_{S_w=1}}{m_{S_{w_j}}}\right] \frac{r_j}{r_{S_w=1}} \approx \frac{r_j}{r_{S_w=1}} \tag{49}$$

becomes valid.

The relationship between saturation and relaxation is investigated in Fig. 20, for which the average $<\tau_1>$ values for the different saturation levels are plotted. The curve on this figure results from least squares fit of the data corresponding to the largest eight saturation levels for $<\tau_1>$ with a power-law model

$$\tau_1 = aS_w^{\ b} \tag{50}$$

where S_w is the water saturation. It can be seen from the figure that the power-law relation fits the relaxation-saturation dependence satisfactorily with a broad range of saturations using $<\tau_1>$. It has been reported theoretically that either a grain-consolidation[34] or a shrinking-bond[8] porous medium model can yield a power-law dependence between the relaxation and saturation. Without including possible variations in pore shape for different sized pores, i.e., treating m as a constant, the power factor b is predicted to be between the values of 1 and 2 for the grain-consolidation

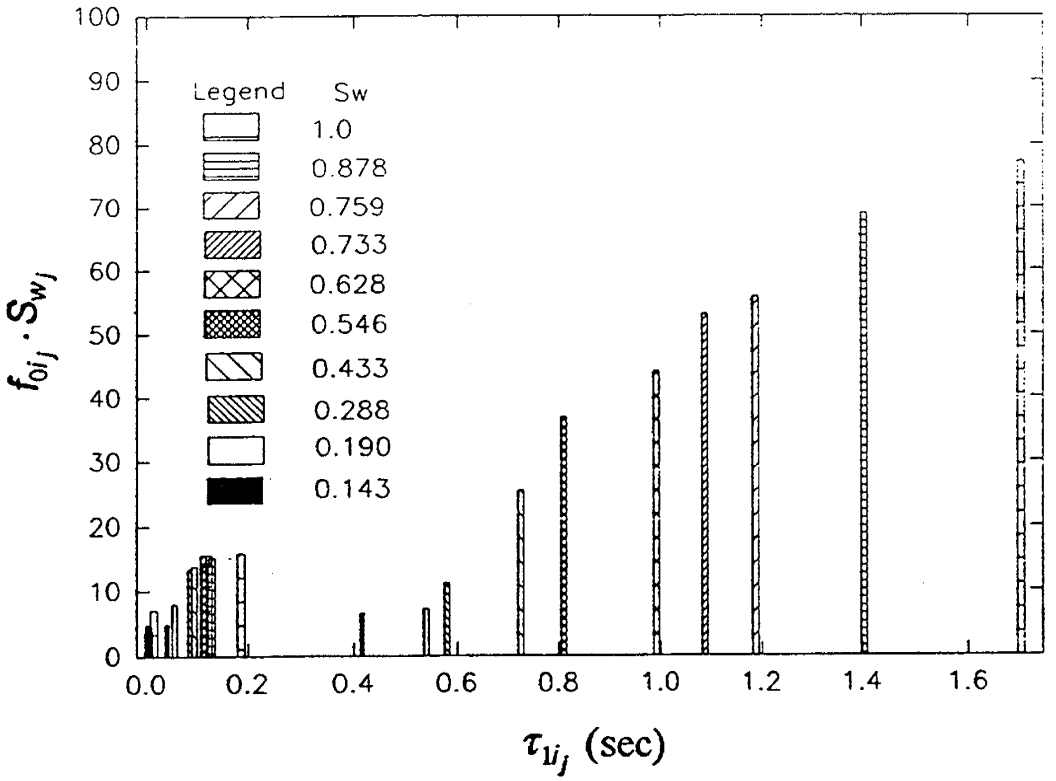

Fig. 19. Three component analysis of relaxation parameters corresponding to different saturations. The vertical axis represents the relative water quantity in percentages compared to the total amount of water at the fully-saturated state.

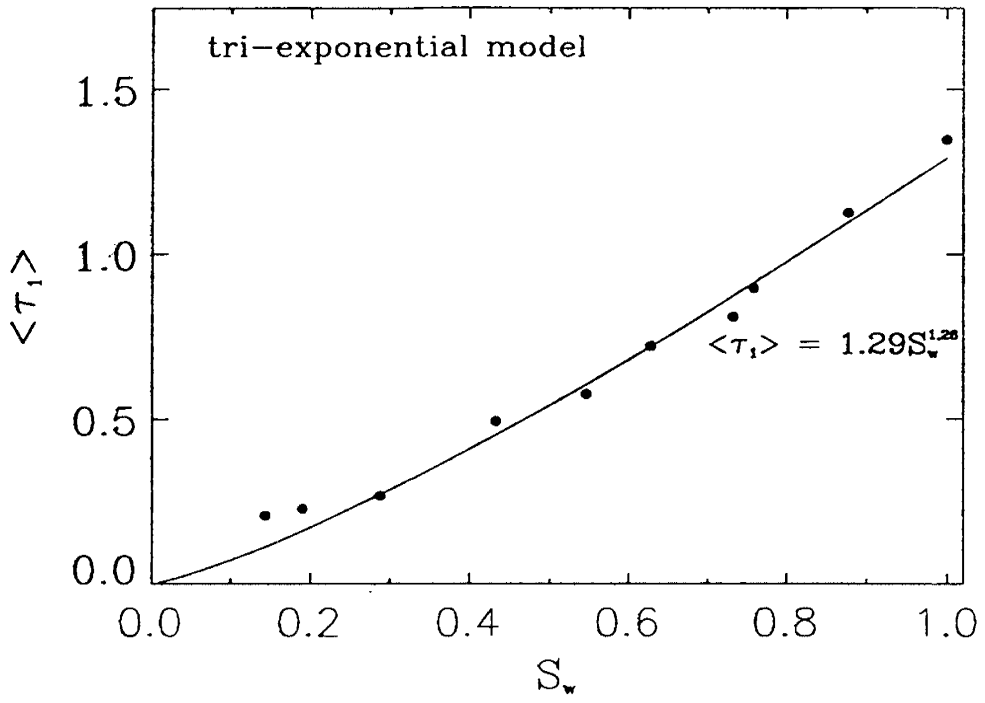

Fig. 20. The saturation dependence of $\langle \tau_1 \rangle$ for tri-exponential analysis.

model, with $b = 1$ corresponding to the fast diffusion limit and $b = 2$ the slow diffusion limit. On the other hand, for the shrinking-bond model, it is predicted that b is between the values of 1/3 and 2/3 for all cases. The values obtained from the power-law model, $<\tau_1> = 1.29 S_w^{1.26}$ sec, are in general agreement with those expected for the grain-consolidation model. The departure from $b = 1$ (fast diffusion limit) may not be regarded as simply due to the mixture of fast and slow diffusion. Instead, it may well be due to the simplified nature of the model. A power-law representation of the experimental data is very attractive since the behavior is predicted with just a few parameters.

The stretched exponential relaxation function (Eq. (48)) provides a fit that is nearly as precise as that of the tri-exponential function for this sandstone, as measured by the residual sum of squares. A comparison of the fits using the two functions is shown in Fig. 21 for data obtained at $S_w = 0.29$. Using the relaxation parameters obtained with the stretched exponential model, similar power-law behavior can also be obtained. Figure 22 shows $\tau_{1,\alpha}$ as a function of S_w. A least squares fit using Eq. (50), after exclusion of the data corresponding to the two lowest saturations, yields $\tau_{1,\alpha} = 1.30 S_w^{1.59}$. The $\tau_{1,\alpha}$ saturation dependence imitates the features observed by the multiple discrete-component analysis, except that the power factor is larger. On the other hand, the values of the stretch exponent, α, obtained at different saturation values are shown in Fig. 23. The α values corresponding to the six largest saturation levels differ little (they are between 0.61 and 0.65), but decrease as saturation is further lowered. We note that if the α values are at substantially different saturations, we can not simply compare the values of $\tau_{1,\alpha}$ at different saturations, since the calculated $\tau_{1,\alpha}$ value is subject to the value of α.

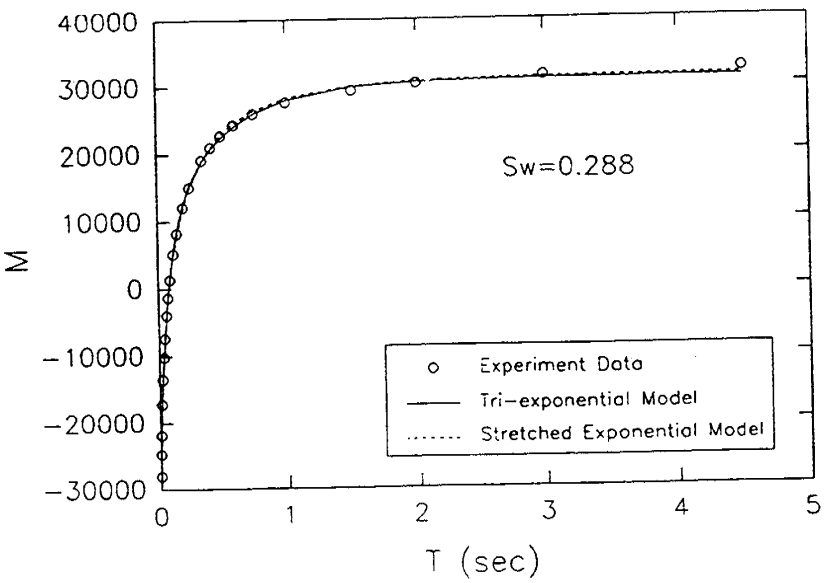

Fig. 21. The comparison of fitting quality using the tri-exponential and stretched exponential analysis.

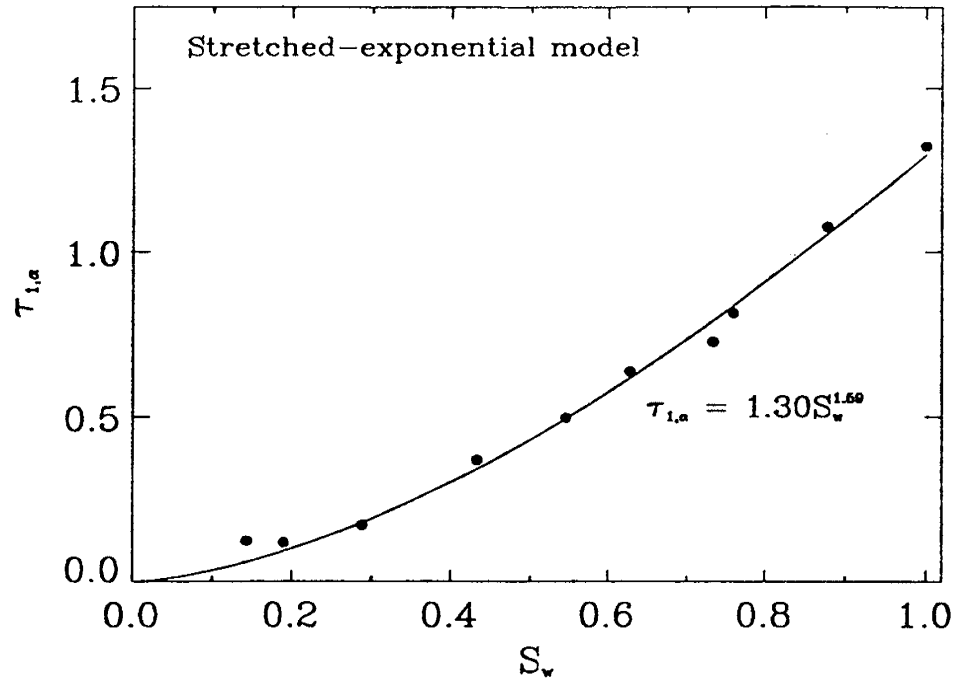

Fig. 22. Saturation dependence of $\tau_{1,\alpha}$ for the stretched exponential model.

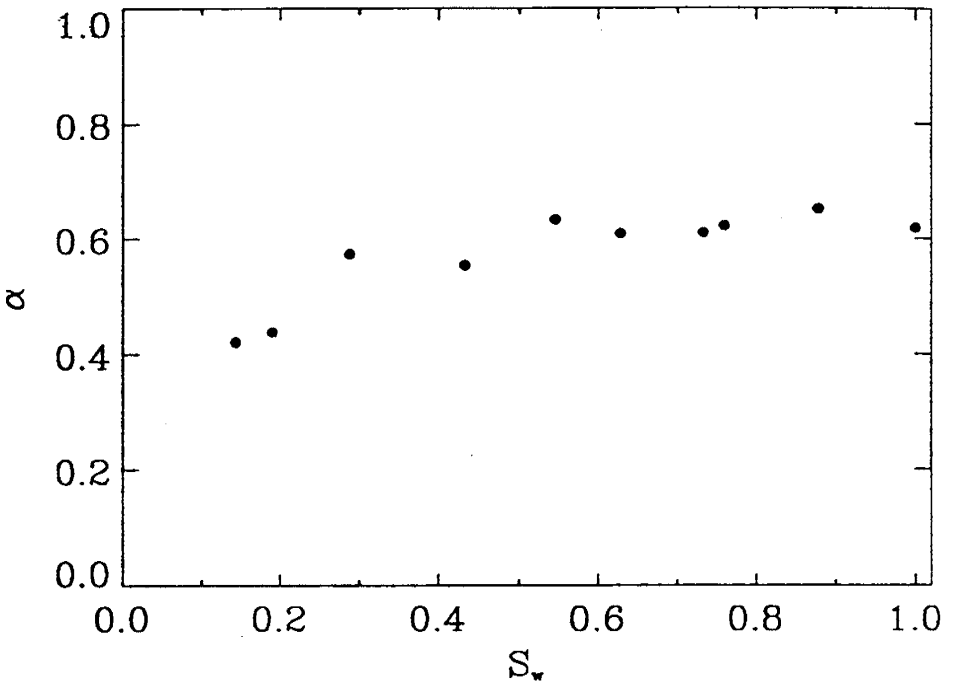

Fig. 23. The calculated stretched exponent α values at different saturation levels.

In the above analysis, both the tri-exponential and stretched exponential analyses show that the relaxation times fit a simple power-law dependence with saturation. Though stretched exponential analysis has a simplicity of having relatively few numbers of parameters, its validity appears to be limited to the cases where α is near 2/3. We generally favor using the multi-exponential analysis and using the parameter $<\tau_1>$ as a unique representation of the average pore size corresponding to each saturation level.

VII. Conclusions

Nuclear magnetic resonance spectroscopy and imaging (NMR and NMRI) techniques have been applied in porous media research. Experimental methods were developed for acquiring fluid phase distributions during two-phase immiscible fluid displacement experiments. Computational procedures were developed for analyzing imaging data so that porosity and saturation distributions can be estimated with great accuracy. Other computational procedures were developed for estimating two- and three-phase relative permeability functions from displacement data that includes those measures of the saturation distribution. New approaches for characterization of fluid distributions and pore structures using NMR relaxation and restricted diffusion measurements were investigated and significant progress was achieved. In particular, apparent diffusivities were introduced for characterizing pore sizes in different sized model porous media. Methods for analyzing diffusivity distributions arising from diffusional processes in different compartments of fluids were developed. In addition, saturation-dependent relaxation measurements were carried out to study fluid distributions corresponding to different saturation levels. Computational procedures for obtaining those distributions were developed.

VIII. References

1. Edelstein, W.A, Vinegar, H. J., Tutunjian, P. N., Roemer, P.B., Mueller, O.M.: "NMR Imaging for Core Analysis" *Soc. Petroleum Eng. Annual Tech. Conf.* SPE paper #18272, (Oct. 2-5, 1988).
2. Mandava, S.S., Watson, A.T., Edwards, C.M.: "NMR Imaging of Saturation during Immiscible Displacements", *AICHE J*, **36**, 1680 (1990).
3. Osmemt, P.A., Packer, K.J., Taylor, M.J., Attard J.J., Carpenter, T.A., Hall, L.D., Herrod, N.J., and Doran, S. J.,: "NMR Imaging of Fluids in Porous Solids", *Phi. Trans. R. Soc. Lond.* A**333**, 441 (1990).
4. Chen, J., Dias, M.M., Patz, S., Schwartz, L.M.: "Magnetic Resonance Imaging of Immiscible Fluid Displacement in Porous Media", *Phys. Rev. Lett.* **61**(13), 1489 (1988).
5. Baldwin, B.A., Yamanashi, W.S.: "Detecting Fluid Movement and Isolation in Reservoir Cores Using Medical NMR Imaging Techniqures", *Soc. Petroleum Eng. Annul Tech. Conf.* SPE paper #14884, 39 (1986)
6. Blackband, S., Mansfied, P., Barnes, J.R., Clague, A.D., Rice, S.A.: "Discrimination of Crude Oil and Water in Sand and in Bore Cores with NMR Imaging," *SPE Form. Eval.* **1**, 31 (1986)
7. Chen, S., Kim, K.-H., Qin, F., Watson, A.T.: "Quantitative NMR Imaging of Multiphase Flow in Porous Media", *Mag. Reson. Imag.*, **10**(5), pp. 815-826 (1992).
8. Banavar, J.R., Schwartz, L.M.: "Probing Porous Media with Nuclear Magnetic Resonance," In: J. Klafter, J.M. Drake (Eds). Molecular Dynamics in Restricted Geometries. (John Wiley & Sons, New York, 1989) pp. 273-310.
9. Kenyon, W.E., Day, P.I., Straley, C., Willemsen, J.F.: "A Three-Part Study of NMR Longitudinal Relaxation Properties of Water-Saturated Sandstones," *SPE Form. Eval.* **3**, 622 (1988).
10. Johnson, E. F., Bossler, D. P. and Newman, V. O.: "Calculation of Relative Permeability from Displacement Experiments," *JPT Trans.* AIME , **216**, 61 (1959).
11. Buckley, S. E. and Leverett, M. C.: "Mechanism of Fluid Displacement in Sands," *Trans.*, AIME, **146**, 107 (1942).
12. Tao, T. M. and Watson, A. T.: "Accuracy of JBN Estimates of Relative Permeability: Part 1 - Error Analysis," *Soc. Pet. Eng. J.*, 209 (April, 1984).
13. Watson, A. T., Richmond, P. C., Kerig, P. D., Tao, T. M.: "A Regression Based Method for Estimation of Relative Permeabilities from Displacement Experiments," *SPERE,* 953 (August 1988).
14. Baker, L. E.: "Three-Phase Relative Permeability Correlations," presented at the *Enhanced Oil Recovery Symposium*, Tulsa, OK, SPE Paper 17369 (April 17-20, 1988).
15. Sarem, A. M.: "Three-Phase Relative Permeability Measurements by Unsteady-State Method," *Soc. Pet. Eng. J.*, 199 (Sept. 1969).
16. Levered, M. C. and Luis, W. B.: "Steady Flow of Gas-Oil-Water Mixtures through Unconsolidated Sands," *Trans.* AIME **207**, 107 (1941).
17. Caudle, B. H., Slobod, R. L., and Brownscombe, E. R.: "Further Developments in the Laboratory Determination of Relative Permeability," *Trans.* AIME **192**, 145 (1951).

18. Corey, A. T., Rathjens, R. J., Henderson, J. H., and Wyllie, M. J.: "Three-Phase Relative Permeability," *Trans.* AIME **207**, 349 (1956).
19. Snell, R. W.: "The-Phase Relative Permeability in an Unconsolidated Sand," *J. Inst. Pet.* **84**, 80 (1962).
20. Schneider, F. N. and Owens, W. W.: "Sandstone and Carbonate Two and Three Phase Relative Permeability Characteristics," *Soc. Pet. Eng. J.* 75 (March, 1970).
21. Donaldson, E. L. and Dean, G. W.: "Two- and Three-Phase Relative Permeability Studies," RI 6826, U. S. Bureau of Mines (1966).
22. Spronsen, E. V.: "Three-Phase Relative Permeability Measurements Using the Centrifuge Method," presented at the *Third Joint Symposium on Enhanced Oil Recovery*, Tulsa, OK, April 4-7, SPE Paper 10688 (1982).
23. Aziz, K. and Settari, A., *Petroleum Reservoir Simulation*, Applied Science Publishers LTD, London, 1979.
24. Schumaker, L. L., *Spline Functions: Basic Theory*, John Wiley & Sons, New York, 1981.
25. de Boor, C., *A Practical Guide to Splines*, Springer Verlag, New York , 1978.
26. Richmond, P. C.: "Estimating Multiphase Flow Functions in Porous Media from Dynamic Displacement Experiments," Texas A&M University Dissertation, College Station, 1988.
27. Karger J., Pefeofer H., and Heink W.: "Principles and Application of Self-Diffusion Measurements by Nuclear Magnetic Resonance," *Adv. in Mag. Reson.* **12**, 1 (1988).
28. Tanner, J. E.: "Use of Stimulated Echo in NMR Diffusion Studies," *J. Chem. Phys.*, **52**(5), 2523 (1970).
29. Abranowitz, M.: *Handbook of Mathematical Functions, with Formulas, Graphs, and Mathematical Tables*, Dover Publications, 1965.
30. Lawson, C. L. and Hanson, R. J.: *Solving Least Squares Problems,* Prientice-Hall, Englewood Cliffs, NJ, 1974.
31. Halprin, W. P., D'Orazio, F., Bhattacharja, S., and Tarczon, J. C., in *Molecular Dynamics in Restricted Geometries*, edited by J. Klafter and J. M. Drake, Ch. 11, 311, John Wiley, New York 1989.
32. Brownstein, K. R., and Tarr, C. E.: "Importance of Classical Diffusion in NMR Studies of Water in Biological Cells," *Phys. Rev. A.* **19**, 2446 (1979)
33. Kenyon, W. E., Day, P. I., Straley, C., and Willemsen, J. F., Compact and Consistent Representation of Rock NMR Data for Permeability Estimation, *Soc. Petroleum Eng.* paper #15643, 1986.
34. Roberts, J. N. and Schwartz, L. M.: "Grain Consolidation and Electrical Conductivity in Porous Media," *Phys. Rev. B* **31**, 5990 (1985).

Appendix
List of Publications and Presentations

Refereed Journals

S. S. Mandava, A. T. Watson, and C. M. Edwards: NMR Imaging of Saturation During Immiscible Displacements, *AIChE J.* **36**, pp. 1680-1686 (1990).

S. Chen, K.-H. Kim, F. Qin, and A. T. Watson: Quantitative NMR Imaging of Multiphase Flow in Porous Media, *Mag. Reson. Imag.*, **10** (5) pp. 815-826 (1992).

S. Chen, F. Qin, K.-H. Kim, and A. T. Watson: NMR Imaging of Multiphase Flow in Porous Media, *AIChE J.*, **39**, 925-934 (1993).

S. Chen, H.-K. Liaw, and A. T. Watson: Fluid Saturation Dependent NMR Spin-Lattice Relaxation in Porous Media and Pore Structure Analysis, *J. Appl. Phys.*, **74** (3), pp. 1473-1479 (1993).

S. Chen, H.-K. Liaw, and A. T. Watson: Measurements and Analysis of Fluid Saturation Dependent NMR Relaxation and Linebroadening in Porous Media, *Mag. Reson. Imag.*, in press.

C. T. Chang, A. T. Watson, S. Mandava, S. Sarkar, and C. M. Edwards: The Use of Agarose Gels for Quantitative Determination of Fluid Saturations in Porous Media, *Mag. Reson. Imag.* **11**, 717-725 (1993).

Conference Publications

K.-H. Kim, S. Chen, F. Qin, and A. T. Watson: Use of NMR Imaging for Determining Fluid Saturation Distributions During Multiphase Displacement in Porous Media, *Proceedings of SCA/SPWLA Joint Conference*, SCA paper 9219, Oklahoma City, OK, June 14-17, 1992.

S. Chen, P. Miao, and A. T. Watson: Characterization of Pore Structures Using NMR Proton Restricted Self-Diffusion Measurements, *Proceedings of 67th Annual Fall Technical Conference of Soc. of Petroleum Engineers*, SPE paper 24812, pp. 477-489, Washington D. C., Oct 4-7, 1992.

S. Chen, F. Qin, K.-H. Kim, and A. T. Watson: NMR Imaging of Multiphase Flow in Porous Media, *Proceedings of 67th Annual Fall Technical Conference of Soc. of Petroleum Engineers*, SPE paper 24760, pp. 1013-1026, Washington D. C., Oct. 4-7, 1992.

S. Chen, J. Qiao, H.-K. Liaw, and A. T. Watson: Studies of Rock Pore Structures Using NMR Restricted Diffusion Measurements and Analyses, SCA paper 9313, Houston, Texas, Aug. 9-11 (1993).

Presentations

S. S. Mandava, C. M. Edwards, and A. T. Watson: NMR Imaging of Saturation During Immiscible Displacements, *AIChE* Spring Meeting, March, 1990.

S. Chen, K.-H. Kim, F. Qin, and A. T. Watson: Quantitative NMR Imaging of Multiphase Flow in Porous Media, presented at 1st Forum AMPERE, *Magnetic Resonance New Methodologies: Impact on Industrial Research*, Rome, Italy, Nov. 21-24, 1991.

S. Chen, A. T. Watson, and K.-H. Kim: MRI Evaluation of Flow Through Structurally Heterogeneous Porous Media, presented at March Meeting of the *Am. Phys. Soc.*, Indianapolis, ID, March 16-20, 1992.

A. T. Watson, S. Chen, and P. Miao: Characterizing Porous Medium Structures Using Pulsed Field Gradient NMR Restricted Diffusion Measurements, presented at March Meeting of the *Am. Phys. Soc.*, Indianapolis, ID, March 16-20, 1992.

K.-H. Kim, S. Chen, and A. T. Watson: NMR Imaging For Quantitative Determination of Fluid Saturation During Flow in Porous Media, presented at March Meeting of the *Am. Phys. Soc.*, Indianapolis, ID, March 16-20, 1992.

A. T. Watson: NMR Imaging of Multiphase Flow in Porous Media, presented at *66th Colloid and Surf. Sci. Symp.*, Morgantown, WV, June 14-17, 1992.

A. T. Watson: NMR Studies of Restricted Diffusion in Porous Media, presented at *66th Colloid and Surf. Sci. Symp.*, Morgantown, WV, June 14-17, 1992.

A. T. Watson: Characterizing Fluid Distributions in Porous Media Using NMR Imaging, presented at *Gordon Research Conference*, Aug. 10-14, 1992.

S. Chen, P. Miao, and A. T. Watson: Characterization of Pore Structures Using NMR Proton Restricted Self-Diffusion Measurements, presented at *67th Annual Fall Technical Conference of Society of Petroleum Engineers,* Washington D. C., Oct. 4-7, 1992.

S. Chen, F. Qin, K.-H. Kim, and A. T. Watson: NMR Imaging of Multiphase Flow in Porous Media, presented at *67th Annual Fall Technical Conference of Society of Petroleum Engineers,* Washington D. C., Oct. 4-7, 1992.

S. Chen, H.-K. Liaw, and A. T. Watson: Measurements and Analysis of Fluid Saturation Dependent NMR Relaxation and Linebroadening in Porous Media, presented at *2nd International Conference on the MR Applications to Porous Media*, Canterbury, U. K., April, 1993.

S. Chen, F. Qin, and A. T. Watson: Determination of Saturation Distributions During Multiphase Displacement in Porous Media by NMR Imaging, presented at *AIChE Spring Conference and Exhibitions*, Houston, TX, March 29-April 1, 1993.

S. Chen, J. Qiao, H.-K. Liaw, and A. T. Watson: Studies of Rock Structures Using NMR Restricted Diffusion Measurements, presented at *The 8th Annual Soc. of Core Analysts Conference*, Houston,, TX, Aug. 9-11, 1993.

SUBTASK 3. DEVELOPMENT OF NMR AND CT SCANNING FOR CHARACTERIZING DISPERSED PHASE PROCESSES

Principal Investigator: R. W. Flumerfelt

Department of Chemical Engineering

I. Objectives

The objective of this subtask is to obtain a detailed understanding of the behavior and mechanisms of dispersed phase systems in porous media using advanced NMR and CT imaging methods. Three different projects are designed to achieve the overall objective: 1) characterization of fractional wettability of porous media using NMR relaxation methods; 2) study of a surfactant based imbibition and solution gas drive process (foam) displacement using NMR imaging methods; and 3) study of the dynamic process of dispersed phase flow in porous media using CT imaging methods. These three projects will be discussed separately below.

II. Characterization of Fractional Wettability

Background

Wettability is defined as "the tendency of one fluid to spread on or adhere to a solid surface in the presence of the other immiscible fluids".[1] In rock/oil/water systems, wettability is a measure of the preference of rock to either oil or water. The internal surfaces of reservoir rock may be water-wet, oil-wet, or neutrally wet. Strongly water-wet surfaces and strongly oil-wet surfaces can also exist in different parts of the same rock to produce "fractional wettability". A special type of fractional wettability is when the oil-wet surfaces form continuous paths through the larger pores, while the smaller pores remain water-wet. This special case of fractional wettability is known as "mixed wettability".

Wettability is an important concept in the characterization of oil reservoirs. Wetting characteristics of the rock matrix greatly affects the distribution of oil and water in a reservoir. The oil recovery processes and the total amount of recoverable oil are also influenced by the rock wettability. Knowledge of reservoir wettability is essential to efficient secondary and tertiary oil recovery processes.

Various methods for determining wettability of porous media were reviewed by Anderson [2]. Among these methods, the Amott method and the USBM method are accepted quantitative methods and are widely used by core analysts. Both methods provide certain rock wettability indices; however, they are time consuming and require a degree of interpretation. Moreover, they are not suitable for determination of fractional wettability or mixed wettability.

NMR relaxation methods promise fast and convenient tools in the measurement of rock wettability. This method is based on the observation that the surfaces of porous media contribute greatly to the NMR relaxation rates of fluids in the porous media. The strong intermolecular interactions between solid surfaces and the nearby fluids have significant influences on the thermal motion of the liquid molecules and cause their NMR relaxation times to be shorter than that of bulk liquid. Furthermore, the strength of the intermolecular forces between a given fluid and a wetting surface is very different from that between this

fluid and a non-wetting surface. For example, the relaxation times of water, H_2O or D_2O, in a water-wet porous media are expected to be shorter than in an oil-wet porous media. We thus anticipate that different values of NMR relaxation times will give us measures about different wettabilities of porous media.

The measurements of NMR relaxation times T_1 and $T_{1\rho}$ of both H_2O and D_2O in various bead packs and sand packs were reported by several groups [3-5]. However, the studies by different investigators gave seemingly conflicting results. Brown and Fatt [3] used uncoated sand packs as water-wet porous media, and Dri-film treated sand packs as oil-wet porous media; they measured proton spin-lattice relaxation time T_1 of water (H_2O) in each of these systems. They found that water relaxed faster in the water-wet system than in the oil-wet system. They also found that for mixtures of oil-wet and water-wet sands the relaxation rate ($1/T_1$) varied linearly with the percentage of oil-wet sand. Later, Saraf et al.[4] observed similar behavior of water spin-lattice relaxation times in glass beads (water-wet) and polymer beads (oil-wet) systems. These observations were consistent with original expectations. However, more recent studies by Williams and Fung[5] showed an opposite behavior. The latter investigators measured spin-lattice relaxation times in laboratory (T_1) and in rotating frames ($T_{1\rho}$) of both H_2O and D_2O, using uncoated glass beads as water-wet systems and commercial coated glass beads as oil-wet systems. Their measurements showed that proton relaxation times, T_1 and $T_{1\rho}$, were shorter in oil-wet bead packs than in water-wet bead packs. However, their deuteron $T_{1\rho}$ measurements showed similar behavior as that of proton T_1 measured by Brown and Fatt, although with much less sensitivity. Williams and Fung interpreted the abnormal proton relaxation times as the influence of the methyl group in the coating material on proton relaxation. Since such methyl group components exist in most reservoir oil-wet surfaces, they concluded that proton relaxation times could not be used to characterize wettability of oil-wet porous media.

These contradictory results prevented application of NMR relaxation methods in characterizing wettability of porous media. To understand the phenomena and to investigate the possibility of applying such methods in reservoir rock characterization, we have conducted extensive and systematic studies.

Our research consisted of two parts. In the first stage of the program we used various bead packs with different wetting characteristics as model porous media, and investigated the effects of different wetting surfaces on water NMR relaxation times in those systems. After the extensive studies on model systems we further applied the technique on rock samples and investigated the behavior of water NMR relaxation times in rocks with different wettabilities. These studies will be discussed below.

NMR Relaxation Times in Model Porous Media

Model Porous Media

Five groups of beads were used to make up the model porous media in this part of the study. Each group contains water-wet and oil-wet beads (Table 1). Bead packs were made from 100% water-wet beads, or 100% oil-wet beads, or mixtures of water-wet and oil-wet beads at different percentages. All beads were shivered such that their sizes were between 44 and 62 micron. Group A is the same type of beads used by Williams and Fung, and contains commercial coated (oil-wet) and uncoated (water-wet) glass beads. The oil-wet beads in Group B were obtained in our laboratory by treating cleaned uncoated glass beads with a silicone fluid, SF99 (GE Co.), at 400°F for several hours. The polymer beads in

Group C, made of polydivinylbenzene, were obtained from Bangs Laboratory Inc. These beads were water-wet when purchased, and could be treated to obtain oil-wet surfaces[6]. Two crude oils, Syncrude Coker bitumen and Kuparuk crude oil, were used to prepare oil-wet beads through the deposition of asphaltene and other polar compounds from the crude oil onto uncoated glass bead surfaces (Group D and Group E). The general procedures to deposit asphaltene on surfaces of the glass beads were similar to the methods described elsewhere[7]. After such treatments, the glass beads were preferentially oil-wet.

In the NMR relaxation measurements, the closely packed bead pack sample was saturated with either H_2O or D_2O before being put into the NMR apparatus. The spin-lattice relaxation time in the laboratory frame, T_1, was measured using the inversion recovery method. The spin-lattice relaxation time in the rotating frame, $T_{1\rho}$, was measured using the spin-lock method. A General Electric CSI imager was used for the NMR measurement. The constant magnetic field was 2 Tesla which corresponded to a proton resonance frequency of 85.54 MHz and a deuteron resonance frequency of 13.13 MHz.

Bead Pack	Water-Wet	Oil-Wet
Group A	uncoated glass beads	coated glass beads
Group B	uncoated glass beads	uncoated glass beads treated with SF99
Group C	polymer beads with silica layer	polymer beads with silica layer removed
Group D	uncoated glass beads	uncoated glass beads treated with Syncrude bitumen
Group E	uncoated glass beads	uncoated glass beads treated with Kuparuk crude oil

Table 1. Model porous media of different wetting characteristics

Results and Discussion

In Table 2 we show the NMR relaxation times obtained for H_2O and D_2O, measured in various bead pack groups. Also listed in Table 2 are the corresponding relaxation times of bulk water. To observe the effects of the porous medium surface on NMR relaxation time, we would compare relaxation times of water in water-wet beads with those in oil-wet beads of each group.

On the basis of wetting considerations, the relaxation times of water in an oil-wet bead pack should be longer than that in a water-wet bead pack. However, Williams and Fung reported opposite results in their measurements of proton (H_2O) relaxation times. We observed similar behavior in our measurements of proton relaxation times in bead Group A, which was the same type of beads as those used by Williams and Fung. This indicated that some mechanisms other than wettability dominated the proton relaxation in these bead packs. Williams and Fung attributed this additional mechanism to the dipole-dipole interaction between the methyl groups in the coating surface and the water that enhanced the relaxation of protons.

Group	Beads	$T_1(H_2O)$ (sec)	$T_{1\rho}(H_2O)$ (sec)	$T_1(D_2O)$ (sec)	$T_{1\rho}(D_2O)$ (sec)
	Bulk Water	2.92	2.75	0.39	0.40
A, B, D, E (water-wet)	Cleaned Uncoated Glass Beads	1.15	0.33	0.38	0.17
A (oil-wet)	Cleaned Coated Glass Beads	0.62	0.17	0.38	0.18
B (oil-wet)	Uncoated Glass Beads Treated with SF99	2.70	0.84	0.40	0.36
C (water-wet)	Polymer Beads *with* Silica Layer	1.44	0.43	0.40	0.22
C (oil-wet)	Polymer Beads *without* Silica Layer	2.00	0.56	0.40	0.32
D (oil-wet)	Uncoated Glass Beads Treated with Syncrude Oil	0.34	0.17	0.39	0.25
E (oil-wet)	Uncoated Glass Beads Treated with Kuparuk Oil	2.15	0.60	0.37	0.24

Table 2. Relaxation times of model porous media saturated with water (H_2O or D_2O). The locking frequency for H_2O $T_{1\rho}$ measurements was 5.0 KHz, and that for D_2O $T_{1\rho}$ measurements was 4.2 KHz.

In order to check this claim, we studied the relaxation behavior of water in bead pack Group B, where the oil-wet beads were generated by treating cleaned, uncoated glass beads with SF99. The chemical properties of the silicon fluid SF99 are very similar to the commercial coating material used in Group A. If the additional relaxation mechanism was indeed caused by the methyl groups in the coating material, we would expect to observe the same relaxation behavior of water in this group of beads. However, as shown by the data in Table 2, all proton relaxation times measured in oil-wet beads of this group were considerably higher than those measured in water-wet beads. These results dismissed the explanation given by Williams and Fung regarding the additional relaxation mechanism. Instead of the dipole-dipole interaction between the methyl group in the coating surface and water molecules, we believe that the enhanced relaxation was caused by the magnetic impurities left on the glass bead surfaces during the commercial manufacturing processes. As we observed during the process of cleaning the uncoated glass beads, large amounts of magnetic impurities were dissolved from the bead surfaces by the acid solution. If these impurities were not completely removed during the commercial coating process, they would have great effects on the water relaxation in bead packs. Such magnetic impurities were carefully cleaned during the process of generating oil-wet beads of Group B, hence were not a factor in the water relaxation experiments.

The measurements on the polymer beads, Group C, also confirmed that the proton and deuteron relaxation times for oil-wet systems were higher than those for water-wet systems, as shown by the data in Table 2. The similar relaxation behavior of water in Group B and C, which had totally different surface compositions, suggested that water relaxes faster in water-wet porous media than in oil-wet media.

Table 2 also lists the relaxation times of deuterons (D_2O) in these bead packs. It can be seen that deuteron relaxation behavior was quite different from that of protons. The deuteron T_1 values were almost the same in water-wet bead packs, oil-wet bead packs, and bulk D_2O. On the other hand, the deuteron $T_{1\rho}$ values were always larger in oil-wet systems than in water-wet systems, although the magnitudes of the differences were small.

The different behavior of proton relaxation and deuteron relaxation can be attributed to their different relaxation mechanisms and the nature of T_1 and $T_{1\rho}$. After absorbing energy from the magnetic field during a NMR experiment, protons relax through magnetic dipole-dipole interactions that can be either intra-molecular or inter-molecular. Hence the proton relaxation can be affected by the external magnetic impurities. On the other hand, deuteron relaxes mainly through intra-molecular electrical quadrupole interaction. They are less affected by the external magnetic impurities. The different relaxation mechanisms of protons and deuterons also may cause the number of deuterons affected by surfaces to be less than that of protons. As a result the measured deuteron T_1 was dominated by the contribution from portions of D_2O which were not affected by the surfaces. The change in deuteron $T_{1\rho}$ in different bead packs was due to the fact that $T_{1\rho}$ was very sensitive to the slowly moving molecules near the surfaces. A more complete discussion of the different relaxation behavior is given in our papers.[8-9]

We studied these effects further through tests on beads of Group D and Group E. These two groups of beads resembled reservoir rocks in that the oil-wet surfaces were generated by depositions of asphaltenes from crude oil. Tests on these groups of beads would reveal the validity of applying NMR relaxation methods to determine reservoir rock wettability. As shown by the data in Table 2, H_2O relaxed faster in the treated bead pack (oil-wet) of Group D than in the uncoated bead pack (water-wet), which was different from that expected according to wettability considerations; the changes of D_2O $T_{1\rho}$ agreed with the expectation. Nevertheless, both proton and deuteron relaxation times measured in bead packs of Group E agreed with expectations from wettability considerations.

The different behaviors exhibited by Groups D and E could be attributed to the effects of ferro- and paramagnetic trace metals in the crude oils. The effects of ferromagnetic (Fe, Co, Ni) and paramagnetic (Mn, V, etc.) impurities on proton T_1 and $T_{1\rho}$ were significant. If trace metals existed in the crude oil, they would also be contained in the deposited asphaltene layer on the glass surface. The relaxation due to the dipolar interactions between the ferro- and paramagnetic ions and the H_2O molecules would be the dominant mechanism of the system. The trace metal contents in these crude oils (Syncrude Coker bitumen used in coating beads in Group D, and Kuparuk crude oil used in coating beads in Group E) were analyzed by the inductively coupled plasma (ICP) methods (Table 3). The Syncrude Coker bitumen showed very high concentrations of these impurities, while the Kuparuk crude oil contained only small amounts of these ions. The ICP tests confirmed our suspicion on the effects of trace metal on the NMR relaxation measurements.

	Co	Ni	Fe	V	Mn	Cu
Syncrude	0.817	11.10	269.6	106.7	6.495	1.925
Kuparuk	~0	15.5	1.2	49.3	0.14	~0
ICP Limit	0.005	0.009	0.003	0.004	0.0008	0.003

Table 3. ICP analysis of Syncrude Coker bitumen and Kuparuk crude oil (in ppm).

The relaxation measurements on mixed oil-wet and water-wet bead packs were performed for bead Groups B, C, and E. Linear relations between the relaxation rates ($1/T_1$ or $1/T_{1\rho}$) and the percentages of oil-wet beads were observed for H_2O or D_2O in all the mixed-wet bead packs. The relation was shown by the following equation,

$$\frac{1}{T_i} = \frac{X_{\text{oil-wet}}}{T_{i,\text{oil-wet}}} + \frac{1 - X_{\text{oil-wet}}}{T_{1,\text{water-wet}}}$$

where T_i can be proton T_1, $T_{1\rho}$ or deuteron $T_{1\rho}$, and X is the fraction of oil-wet beads in the sample.

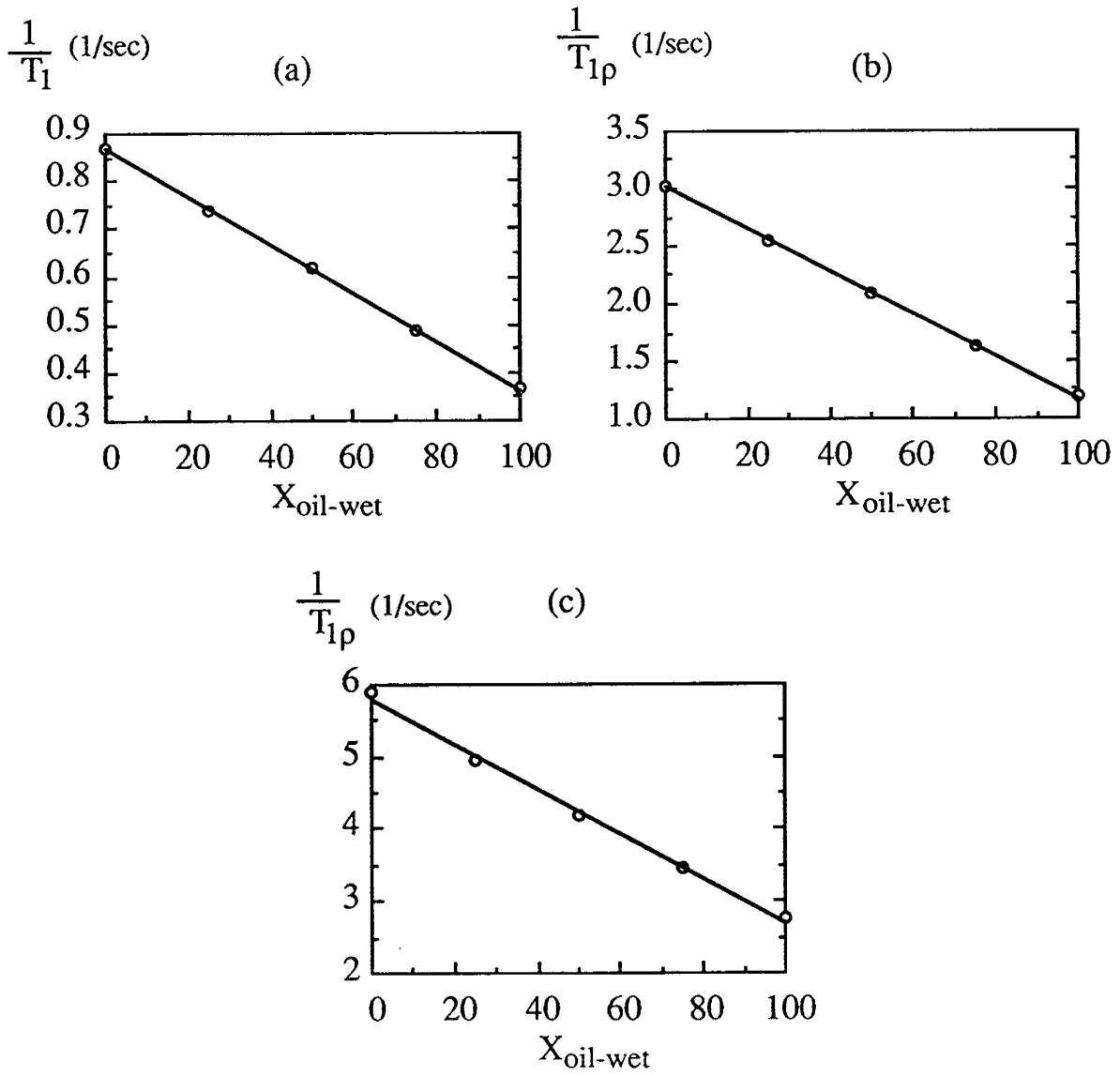

Figure 1. Relaxation rates of water in mixed beads of Group B versus percentage of oil-wet beads. (a) proton T_1^{-1}; (b) proton $T_{1\rho}^{-1}$; (c) deuteron $T_{1\rho}^{-1}$

The observed linear relations are demonstrated in Figure 1(a-c) for the Group B of beads. These results suggest that NMR proton and deuteron relaxation time measurements can be used to estimate the fractional wettability of porous media if relaxation times of 100% oil-wet and 100% water-wet are known.

In conclusion, we gave proper explanation to the previous contradictory results through our extensive experimental study on model porous media using NMR relaxation methods. Our study confirmed the expectation that the proton and deuteron relaxation times can be used to characterize the wettability of porous media. When such systems are free from ferro- or paramagnetic impurities, proton T_1 appears to give the best sensitivity among the relaxation methods tested. With the presence of magnetic impurities, deuteron $T_{1\rho}$ is recommended since impurities have much less influence on deuteron $T_{1\rho}$ than the other relaxation processes. Linear relations between relaxation rates and fractional wettability have been established for all of the NMR relaxation methods. This study provides the foundations for the application of NMR relaxation in the determination of wettability of reservoir rocks.

NMR Relaxation Times in Carbonate Rock Samples

Our studies on model porous media wettability demonstrated the capability of NMR relaxation methods in characterizing wettability of porous media. However, actual rock systems are much more complex than model systems. Factors that affect NMR relaxation measurements, such as surface chemical composition and pore size distribution, can be quite different in a wide range of different rock samples. It is therefore necessary to test the techniques on actual consolidated rock samples to completely establish the methods.

Experimental Work

In order to determine the wettability of rock samples by the NMR relaxation, we have designed the following experimental procedures. A rock sample would first be treated to achieve a water-wet state, and then saturated with water or deuterium (H_2O or D_2O). The NMR relaxation times of the water would then be measured. After these measurements were made for the water-wet state, the same rock would be treated to be oil-wet, and similar measurements conducted. These measurements provided the NMR relaxation times of the wettability extremes. The final step of the experiment would consist of creating a rock sample with mixed wettability, measuring the relaxation times of the waters in this sample, and comparing the measured relaxation times with those of the extreme cases to determine the degree of wettability of the sample.

The rocks used in our experiments included Indiana limestone outcrops (obtained from Cleveland Quarries Company) and reservoir dolomite cores (obtained from Marathon Oil Company and cleaned by conventional extraction methods). All rock samples were cut into core plugs of one inch in diameter and one inch in length. The porosities and the permeabilities of the cores were measured by the saturation method and by a TEMCO gas permeameter, respectively (Table 4). To prepare 100% water-wet samples, core samples L4, C2, and D2 were fired in a muffle furnace at 400°C for six hours. This procedure removed any hydrocarbon film on the rock surfaces and made the rocks strongly water-wet.

Two methods were used to prepare oil-wet carbonate samples. In the first method, the carbonate cores were flushed with 30 PV of 10% naphthenic acid in benzene solution, then dried in a vacuum oven at room temperature. In the second method, the cores were refluxed in the same solution at 80°C for four hours and then dried in the vacuum oven at

room temperature. The naphthenic acid was believed to be chemisorbed and formed calcium naphthenate at the carbonate rock surfaces. The treated cores were considered to be oil-wet.[10]

Core Samples	Porosity (%)	Permeability (mD)
L1 (Indiana limestone, *unfired*)	19.1	30
L2 (Indiana limestone, *unfired*)	18.3	29
L4 (Indiana limestone, *fired*)	21.1	40
C2 (reservoir dolomite, *fired*)	28.1	726
D2 (reservoir dolomite, *fired*)	28.4	625

Table 4. Porosities and permeabilities of limestone and dolomite cores

To prepare rock samples for NMR relaxation measurements, the cores were put in vacuum for eight hours before deionized distilled water, H_2O, (or deuterium oxide, D_2O) was introduced into the evacuated container to saturate the cores overnight. These cores were taken out of the water just before the NMR measurements. Excess water on the outer surface of the cores was wiped clean with a tissue, and the core was wrapped tightly by PARAFILM laboratory film to prevent any evaporation of water.

NMR relaxation times are affected by both the wetting characteristics of the media as well as the pore geometry. In the tests here, the pore geometry was held fixed by conducting comparative tests on the same rock sample. Each sample was first treated to be strongly water-wet. NMR relaxation measurements were performed on the water-wet sample. After the measurements, the same sample was treated with naphthenic acid to obtain oil-wet surface. NMR relaxation measurements were then performed on the oil-wet sample.

Results and Discussion

Unlike in bead packs, the relaxation data measured in rock samples could not be fit with single exponential function to obtain relaxation times. This was because core samples have much wider pore size distributions and water in different pores with different pore sizes would relax at very different rates. Since the overall relaxation rate was observed in the experiments, a single exponential function was often not enough to express the total relaxation behavior. Among the various relaxation times measured, only deuteron $T_{1\rho}$ could be determined by fitting relaxation data with a single exponential function. All other relaxation times, proton T_1 and $T_{1\rho}$, and deuteron T_1, were obtained by fitting the relaxation data with the stretched exponential function given by

$$M(t) = M_o(1 - (1 - Z)\exp(-\frac{t}{T_{1_\alpha}})^{\alpha_\rho})$$

for T_1, where Z is used to correct for an inhomogeneous H_1 field that produces incomplete inversion by the 180 degree pulse, and

$$M(t) = M_o \exp(-\frac{t}{T_{1\rho_\alpha}})^{\alpha_\rho}$$

for $T_{1\rho}$. The residual errors of the stretched exponential model in fitting rock relaxation data were usually at least five times smaller than those of single exponential model.

The measured proton and deuteron relaxation times are listed in Table 5 and Table 6 respectively. The proton T_1 and $T_{1\rho}$ relaxation rates for oil-wet cores were about 50% less than for water-wet cores. This trend matched our expectations, i.e., water molecules next to the oil-wet surfaces are less bound than those next to water-wet surfaces, and thus have longer relaxation times. The carbonate rocks fired at 400°C have the most water-wet inner surfaces and therefore the fastest relaxation rate. Furthermore, the naphthenic acid refluxed carbonate rocks had higher relaxation times compared with the flushed cores. This indicated that the reflux treatment at the boiling point of benzene (80°C) produces a more oil-wet sample than the flush method at room temperature.

As expected, the deuteron $T_{1\rho}$ in oil-wet rock samples was longer than that in water-wet samples. However, the deuteron T_1 in oil-wet samples also showed slight increases from that in water-wet samples. Such increases were not observed in the bead packs studied earlier, nor was it reported by Williams and Fung in their bead pack studies. Considering the wide variety of bead packs and different surface properties studied, it is reasonable to believe that the observed difference in deuteron T_1 between oil-wet and water-wet systems is at least partially caused by the broad pore size distribution of the rock samples.

A paper was presented at the 67th SPE annual meeting in Washington, DC, October 4-7, 1992, summarizing this work.[8]

core samples	Wetness	T_{1_α}, sec	α	$T_{1\rho_\alpha}$, sec	α_ρ
limestone L1	WW	0.65	0.69	0.13	0.41
naphthenic acid flushed L1	OW	0.83	0.72	0.16	0.45
limestone L2	WW	0.61	0.65	0.14	0.42
naphthenic acid flushed L2	OW	0.85	0.73	0.20	0.47
fired limestone L4	WW	0.42	0.63	0.16	0.46
naphthenic acid refluxed L4	OW	1.06	0.72	0.27	0.52
fired dolomite C2	WW	0.46	0.57	0.13	0.45
naphthenic acid refluxed C2	OW	0.89	0.70	0.30	0.57
fired dolomite D2	WW	0.32	0.61	0.10	0.49
naphthenic acid refluxed D2	OW	0.67	0.72	0.24	0.59

Table 5. Proton* relaxation times T_{1_α} and $T_{1\rho_\alpha}$ ** for water-wet and oil-wet cores

(* Proton T_1 at 85.54 MHz; ** Spin-locking at 5000 Hz)

core samples	Wetness	T_1, sec	$T_{1\rho_\alpha}$, sec	α_p
limestone L1	WW	0.31	0.12	0.65
naphthenic acid flushed L1	OW	0.33	0.13	0.74
limestone L2	WW	0.32	0.13	0.67
naphthenic acid flushed L2	OW	0.33	0.15	0.70
fired limestone L4	WW	0.32	0.13	0.67
naphthenic acid refluxed L4	OW	0.35	0.18	0.76
fired dolomite C2	WW	0.28	0.12	0.64
naphthenic acid refluxed C2	OW	0.33	0.20	0.80
fired dolomite D2	WW	0.27	0.08	0.61
naphthenic acid refluxed D2	OW	0.31	0.18	0.80

Table 6. Deuteron* relaxation times T_1 and $T_{1\rho_\alpha}$ ** for water-wet and oil-wet cores

(* Deuteron T_1 at 13.13 MHz; ** Spin-locking at 4167 Hz)

Achievements

For quite some time investigators have realized the potential of using NMR relaxation methods to characterize porous media wettability, and have been talking about it in papers and textbooks. However, insufficient knowledge about the associated techniques plus the previous contradictory observations prevented application of the method. We have conducted a comprehensive and thorough investigation on this subject. Our studies demonstrated that NMR relaxation methods can indeed be used to determine wettability of porous media. It is much faster and more convenient than the currently available methods (Amott, USBM). We have applied the method not only to model porous media, as most other investigators have done, but also to carbonate rock samples. The validity of the method in rock samples as demonstrated by our study is a major step towards applying the method as part of general rock characterization measurements. Two of the major problems associated with this technique are the possible effects of magnetic impurities in rock samples and the effects of different pore size distributions of various rocks. The former problem can be partially solved by using deuteron relaxation methods. The latter problem causes the NMR relaxation measurements to be rock dependent. Further research is necessary to improve the technique and to provide an objective wetting index for porous media.

III. Imbibition and Solution Gas Drive Processes

Background

Conventional oil recovery methods, such as water flooding and other methods, are of limited effectiveness in low permeability, fractured reservoirs. While these methods tend to recover oil in fractures and in the immediate neighborhood of the fractures, they leave the majority of oil in the low permeability rock almost untouched. A small portion of this remaining oil can be recovered through a water soak imbibition process; however this process is very slow and only marginally economical.

Recent studies of a carbonate water imbibition process have shown promising results.[11] The inclusion of CO_2 in water has several important effects. It alters the interfacial properties between water and rock as well as between water and oil. It also causes significant swelling of the oil phase and decreases the oil viscosity. The acidic nature of the carbonated water can also clean up acid-soluble clay contamination in the pore space and widen pore throats in carbonated rocks. All these changes are believed to be beneficial for increasing imbibition rate and oil production. Furthermore, a gas drive process can be induced during the production phase of the process (when reservoir pressure is decreasing) to increase further the total amount of recovered oil.

The effectiveness of the solution gas drive associated with this carbonated water imbibition/gas drive process was limited due to the high mobility of CO_2 gas relative to the oil and connate water. The gas drive arises when the pressure is decreased during production below the bubble point pressure of the CO_2 in the water. With further reductions in pressure, the gas expands and pushes the liquid phases, both oil and water, out of the rock. If carbonated water is used alone in the process, the escape rate of the gas phase can be very high and thus make the process less efficient. Furthermore, since most reservoir rock is more oil-wet than water-wet, the imbibition rates, although enhanced over those of pure water imbibition, are still low.

The carbonated water imbibition/gas drive process can be improved by adding surface active agents to the carbonated water. Surfactants will greatly enhance the solution gas drive process by 1) promotion of gas nucleation and evolution, and 2) reduction of gas phase mobility through the in situ formation of a foam system. As a result of the process, the evolved CO_2 gas will provide a low mobility, highly efficient, solution gas drive mechanism. Furthermore, the use of proper surfactants can alter the rock surface wettability and make the system more water-wet and which in turn increase the imbibition rate.

Experimental Work

The experiments were designed to observe the oil recovery mechanisms in reservoir rock associated with this imbibition and solution gas drive process. Nuclear magnetic resonance imaging was used to monitor the spatial and temporal variation of oil saturation within the rock samples during the process. The NMRI measurements were conducted in a General Electric CSI imager with a two Tesla magnetic field corresponding to a proton resonance frequency of 85.5 MHz. A field of view about 4 inches long was generated by a readout field gradient of 1400 Hz/cm. All measurements were conducted under reservoir conditions of pressure (2000 psi) and temperature (50°C). During the experiment, imbibition fluids invaded the rock to displace the oil phase that was originally in the sample. The imbibition was allowed to take place until no more changes in oil saturation were

observed. The solution gas drive was then conducted by decreasing the system pressure from 2000 psig to 0 psig. By analyzing the recorded NMRI data, the effectiveness of the process was evaluated.

Typical oil saturation profiles within a rock sample during experiment are shown in Figure 2. The NMRI intensity is proportional to the number of protons within the rock. D_2O, as they displaced oil during the experiment, were not detected by NMRI when the resonance frequency was set at that of protons. Three profiles are shown in Figure 2. Initial oil profile shows oil saturation distribution within the sample before the experiment took place, The second curve shows the oil saturation distribution after the imbibition process and before the solution gas drive. The third curve shows the oil saturation distribution after the solution gas drive. The changes of oil saturation at various stages of the experiment is clearly observable. These profiles demonstrate that NMRI is a direct and convenient tool in detecting oil saturation changes within rock samples. The reference sample is a 1/4 inch rock with known oil saturation, cased by epoxy. Using the known oil saturation of the reference sample, the absolute oil saturation within the experimental rock sample can be calculated.

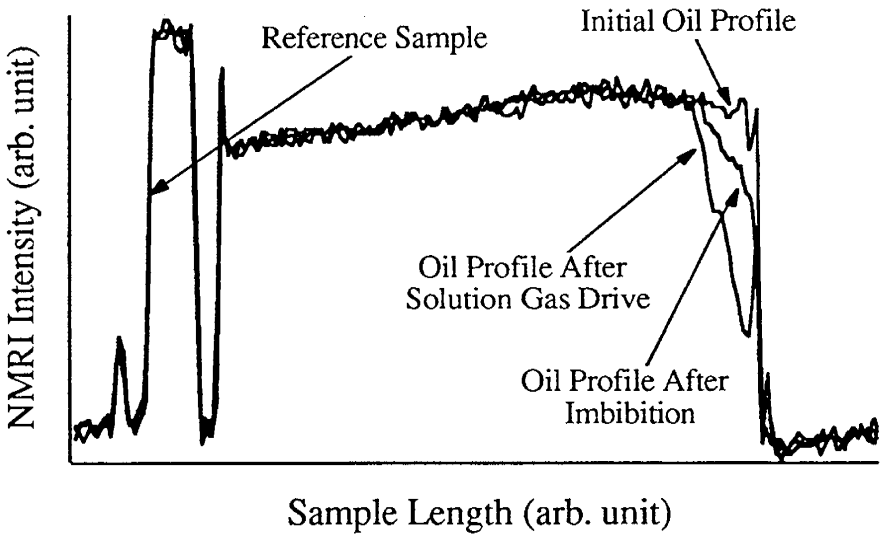

Figure 2. Typical oil saturation profile within rock sample recorded by NMRI method.

A specially designed Hassler sleeve type core holder was constructed (Figure 3). The high pressure and high temperature conditions were achieved by flowing high temperature water, doped with $MnCl_2$, through the outer jacket of the core holder at high pressure.

Dolomite outcrop rock was cut into core samples of 1 inch in diameter and 2.5 inches in length. To obtain the initial oil saturations corresponding to end-drainage saturation, the cores were first saturated with D_2O and placed in the core holder. Oil was then flushed through the samples under pressure to displace the D_2O. An initial oil saturation of about 60% was usually obtained using this method.

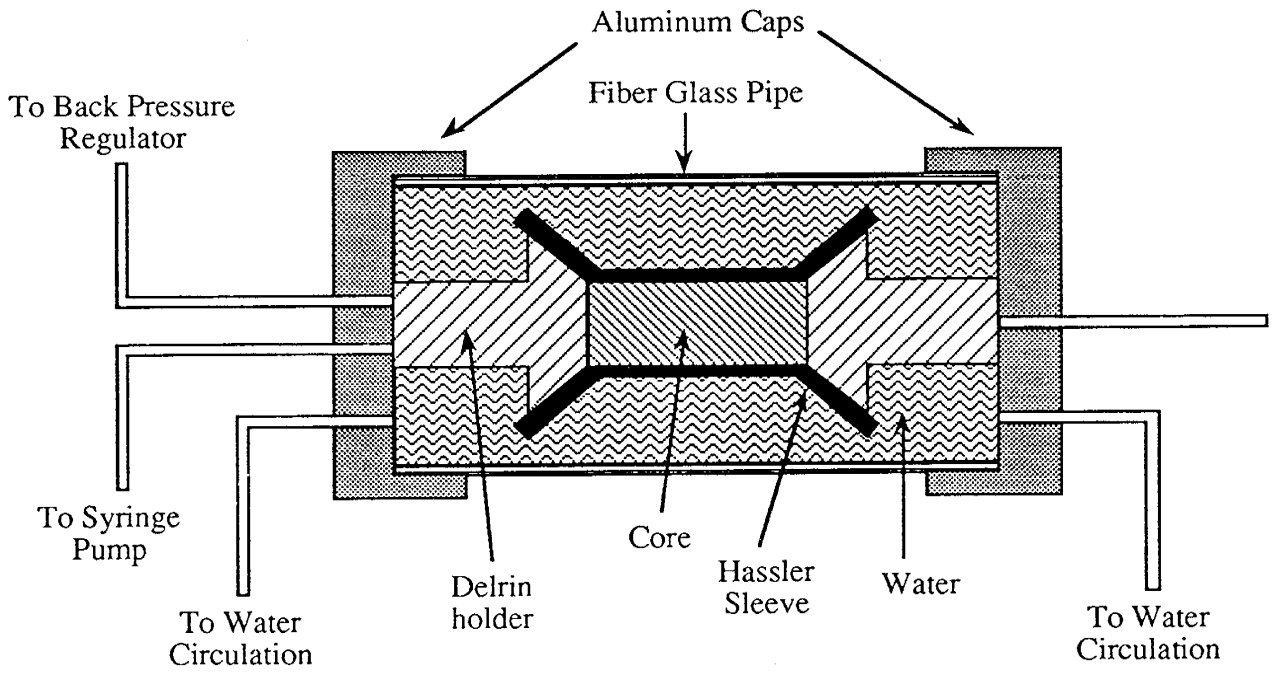

Figure 3. Core holder diagram.

To compare the effects of different imbibition fluids, three groups of imbibition fluids were used: 1) pure D_2O; 2) carbonated D_2O; and 3) carbonated D_2O with surfactant.

Two types of oil were used in the experiments -- kerosene and crude oil. Kerosene has a simple composition compared to crude oil, and was used in the initial studies to observe the effects of different imbibition fluids on the imbibition and solution gas drive processes. Later studies employed crude oil as the oil phase.

Two commercial surfactants were used in the experiments. Both belong to the Chevron surfactant series which is promoted for use in CO_2-foam processes. CD1050 was used in the experiments using kerosene as the oil phase, and CD1045 was used in the experiments using crude oil as the oil phase.

Results and Discussion

Surfactants

Chemical analyses of CD1050 and CD1045 were not available from the manufacturer, nor were we allowed to analyze these samples as per our use agreement. However, CD1050 is a non-ionic surfactant which has demonstrated effectiveness in CO_2-foam processes. CD1045 is a later generation product made up of a mixture of non-ionic and anionic surfactants. It has been shown to produce more stable foams than obtained with CD1050. The surface tensions of these surfactants were measured at different concentrations, and the critical micelle concentration (CMC) was determined (Figure 4).

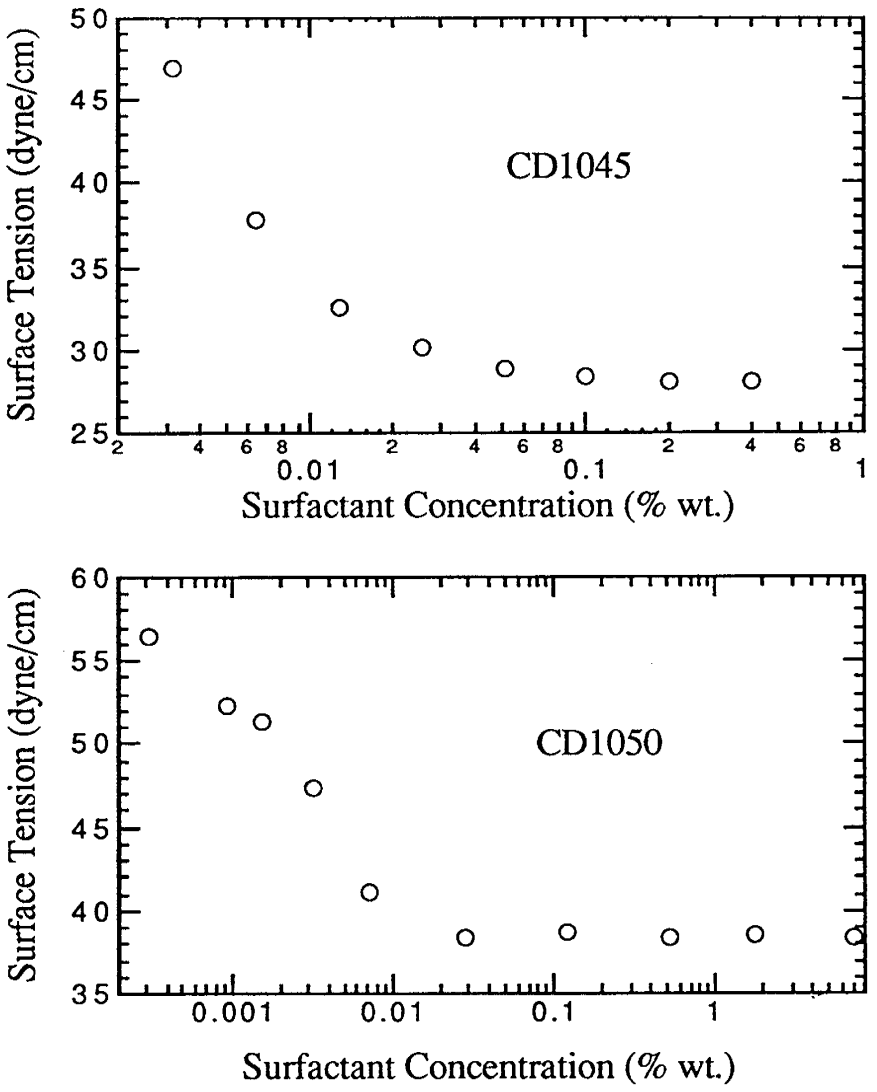

Figure 4. Surfactant surface tension as a function of surfactant concentration.
Top --- CD1045 Bottom --- CD1050

Kerosene as Oil Phase

The three figures on the left side of Figure 5 show the overall kerosene saturation in the cores as functions of time during the three processes using different imbibition fluids (pure D_2O, carbonated D_2O, or carbonated D_2O/CD1050, respectively). Among the three processes, carbonated D_2O exhibits the largest imbibition rate, while the carbonated D_2O/CD1050 solution has the lowest. This is seen by the fact that during the same amount of time the process using carbonated D_2O as the imbibition fluid produced the most oil through imbibition alone. The slower imbibition rate with the surfactant system is due to the lower interfacial tension between the oil and water phase, which lowered the effective capillary force that drives imbibition. However, the solution gas drive was most effective with the carbonated D_2O/CD1050 solution, as indicated by the larger jump in oil saturation

when the system pressure was released at the end of imbibition. This observation confirmed our expectation that the existence of surfactant in the imbibition fluid can greatly increase the efficiency of the solution gas drive mechanism.

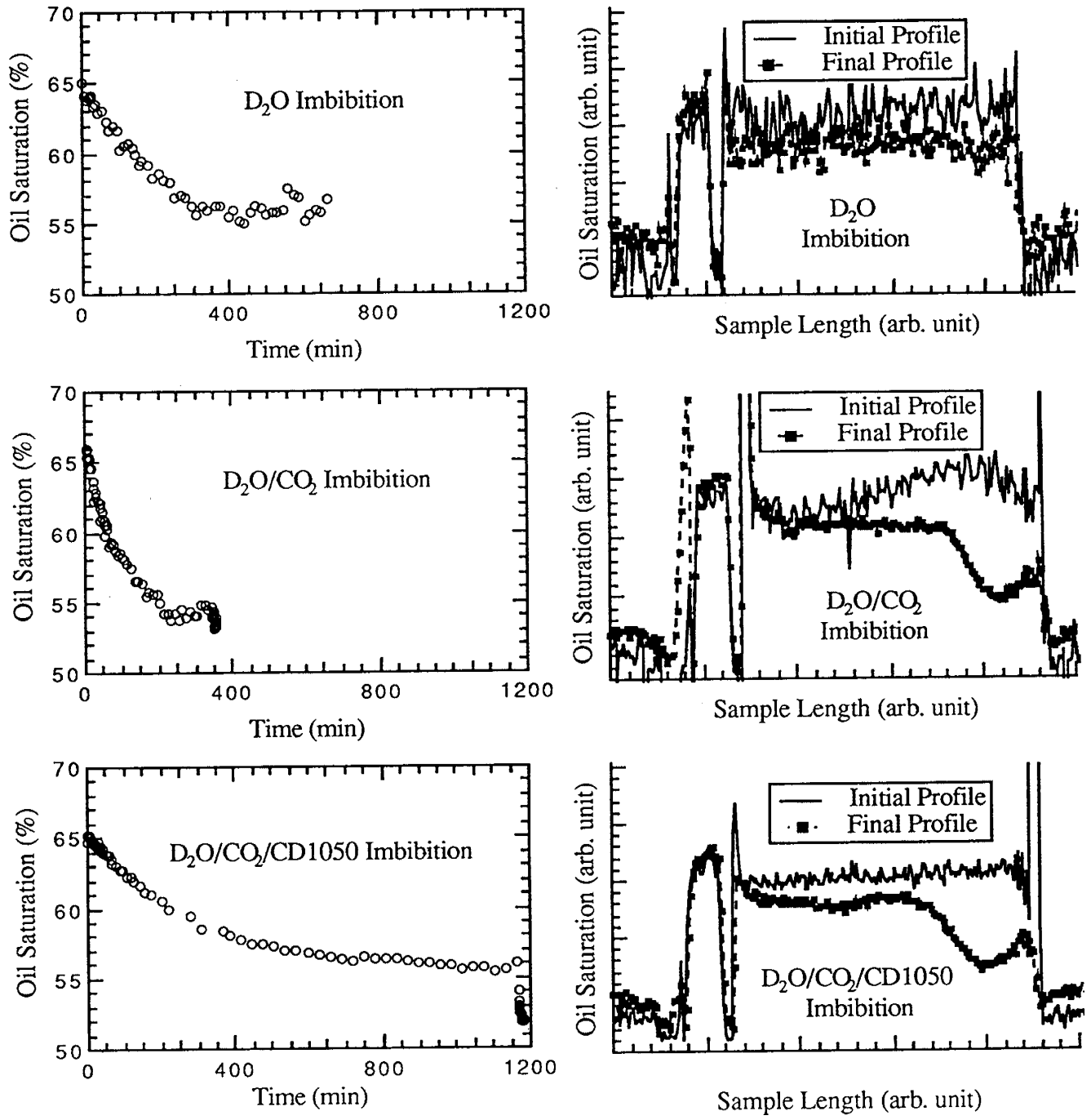

Figure 5. Kerosene saturations during the imbibition/solution gas drive process :
Left side --- oil saturation as function of time
Right side --- initial and final oil saturation profiles.

The three figures on the right side of Figure 5 are the oil saturation profiles within rock samples (see Figure 2) during the three experiments, respectively. Only the initial and final oil saturation profiles are shown. These profiles demonstrate the dramatic changes of oil saturation during the processes.

Crude Oil as Oil Phase

The imbibition process in reservoir rock is affected not only by the interfacial tension between the different liquid phases, but also by the wetting characteristics at the liquid/solid interfaces. The kerosene experiments were performed on presumably water-wet rocks with a fluid (kerosene) that would not alter the rock surface wettability. Such systems are not realistic since the crude oil in reservoir rock can alter wettability. The majority of reservoirs have mixed wettability. The ordinary imbibition process becomes less effective in oil-wet systems. Since surfactants have the ability to alter surface wetting characteristics, increased imbibition rates are possible with such additives, particularly for oil-wet rock systems.

In further experiments, crude oil was used as the oil phase instead of kerosene. The deposition of the asphaltene components from the crude oil onto the water-wet rock surfaces during the experiments can alter the rock surface from water-wet to oil-wet or partially oil-wet. A crude oil from West Texas was filtered to remove particles larger than 0.5 micron. The filtered oil had a viscosity of 12.79 centipose. Before the imbibition experiment, the dolomite rock sample was first saturated with D_2O. End-drainage oil saturations were then obtained by flowing crude oil through the rock sample. After saturation, the rock was allowed to sit at room temperature for about 10 hours. It then took about 3~4 hours to warm the whole system from room temperature to experimental temperature (50°C) before the imbibition process was initiated. Again, three D_2O solutions were used respectively to displace oil from the rock samples. These were water alone, carbonated water, and carbonated water with surfactant. The surfactant solution contained 0.3% wt. of CD1045.

The oil saturation of these rock samples as functions of time during the different processes are shown by the three figures on the left side of Figure 6. The three figures on the right side in Figure 5 are the corresponding initial and final oil saturation profiles of each experiment. The imbibition rates of all processes are considerably lower than those of kerosene tests. This is probably due to 1) the viscosity of crude oil was much larger than that of kerosene (~2 centipose), and 2) the deposition of asphaltene onto the rock surfaces slowed down the imbibition. It was also observed that the imbibition rate of the carbonated D_2O/CD1045 system was higher than that of the carbonated D_2O process. As in the kerosene tests, the surfactant greatly enhanced the solution gas drive mechanism.

Again, the three figures on the right side of Figure 6 are the oil saturation profiles within rock samples (see Figure 2) during the three experiments, respectively.

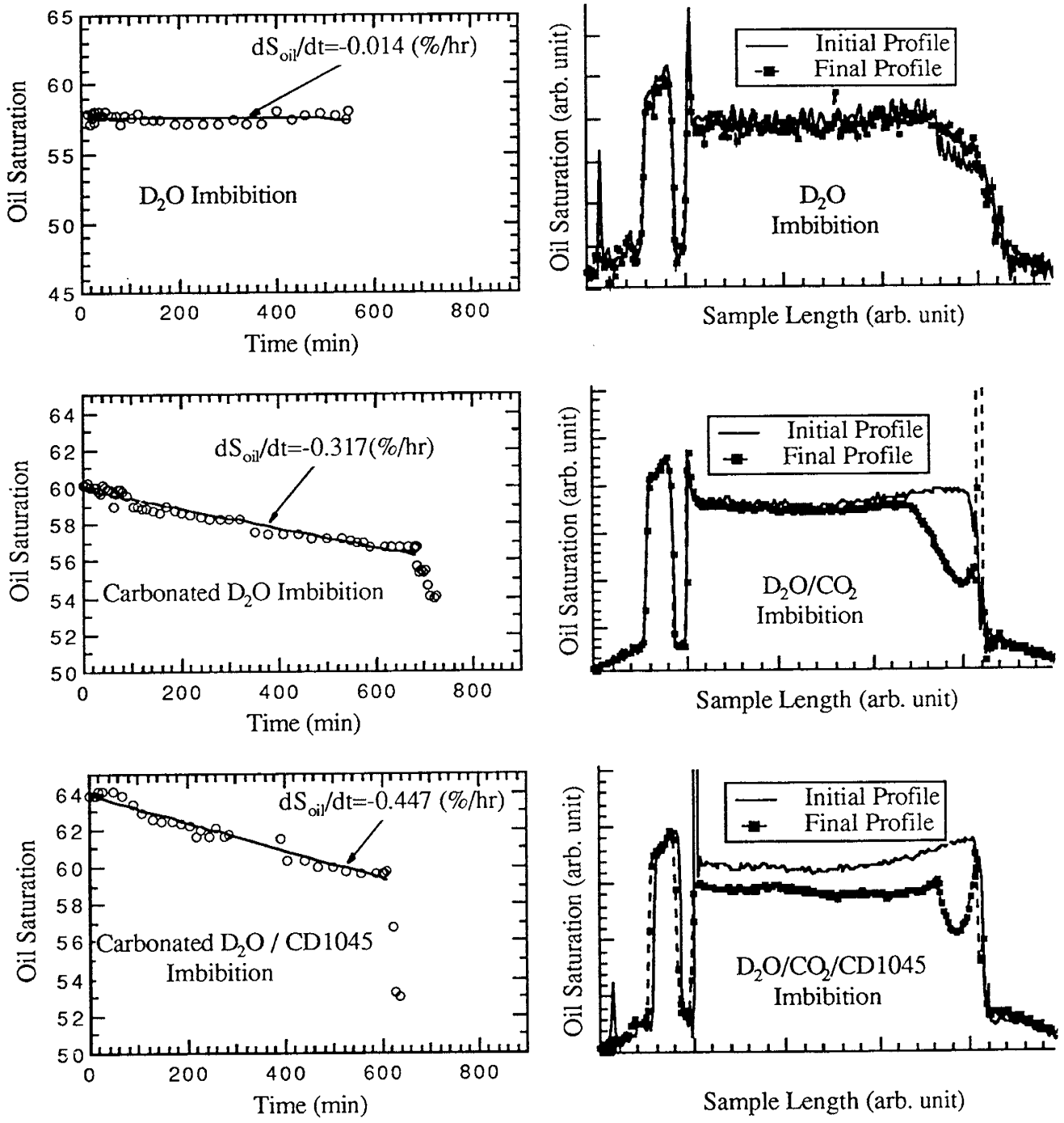

Figure 6. Crude oil saturation during the imbibition/solution gas drive process :
Left side --- oil saturation as function of time
Right side --- initial and final oil saturation profiles.

The effects of multiple imbibition/production cycles were also investigated. During these processes the imbibition and solution gas drive processes were used repeatedly every three hours on the same sample to recover as much oil as possible. The oil saturations as functions of time are shown in Figure 7. The final pressures of the solution gas drives were atmosphere pressure except for the first gas drive of the surfactant system where the final pressure was 300 psi. Another experiment with more cycles is shown in Figure 8. When the surfactant was present, the oil production due to the solution gas drive was significant, with the production being effect over the three cycles tested. These measurements show that the surfactant may greatly increase the total oil production when imbibition and production phases of the process are cycled.

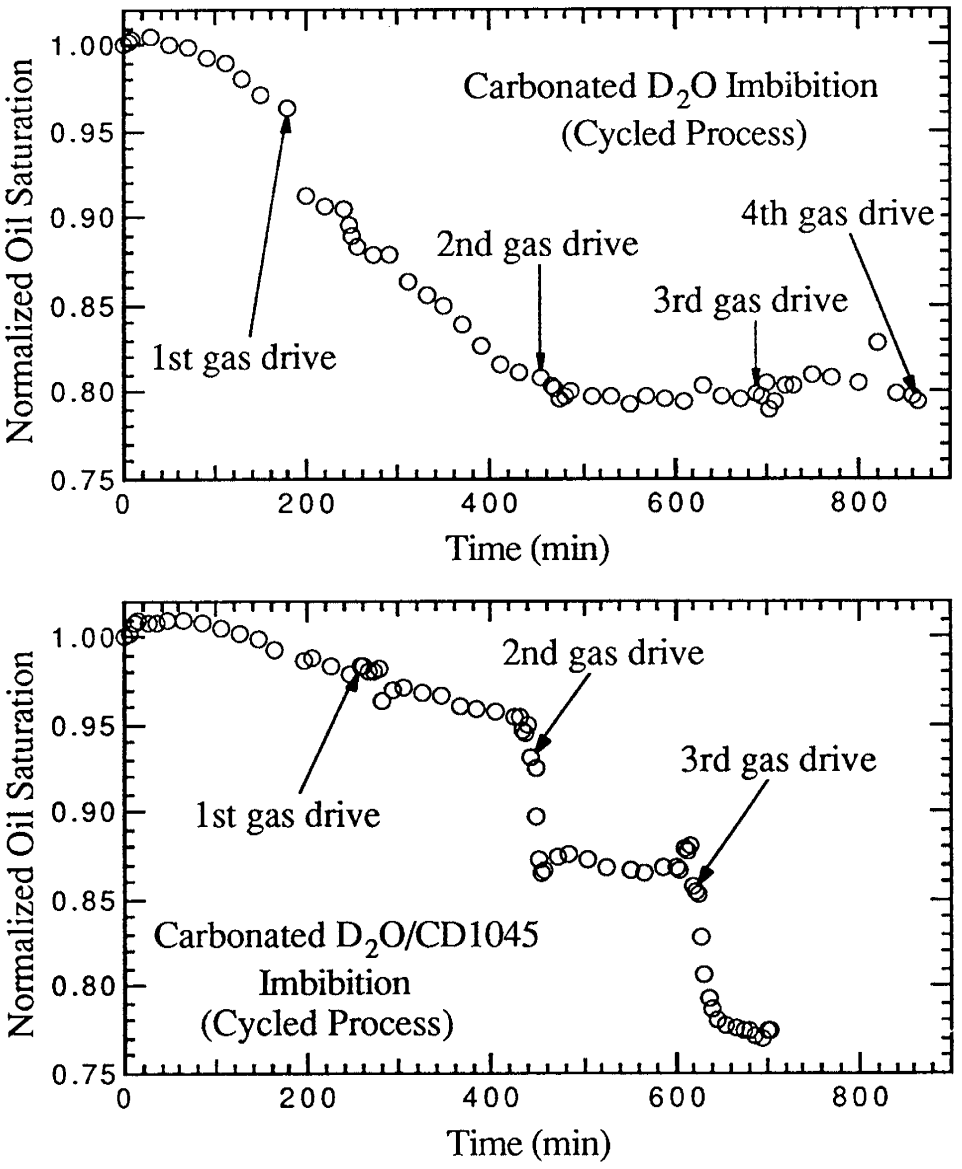

Figure 7. Crude oil saturations during multi-cycle experiments (I):
Top --- carbonated D_2O as imbibition fluid
Bottom --- carbonated D_2O/CD1045 solution as imbibition fluid.

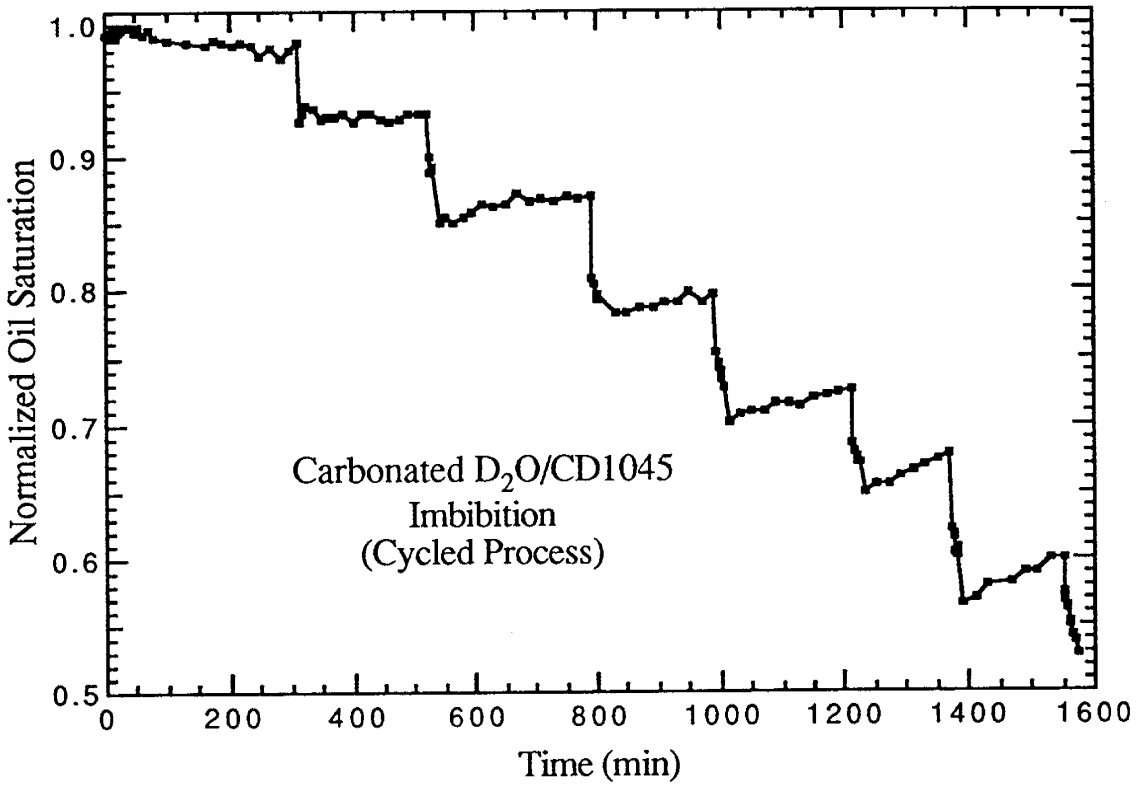

Figure 8. Crude oil saturations during multi-cycle experiments (II): carbonated D_2O/CD1045 solution as imbibition fluid.

Pressure Release Rate

We also investigated the effects of different pressure release rates on the solution gas drive mechanism. In these tests, a rock sample was flushed and saturated with carbonated water/surfactant solution under normal high pressure and high temperature conditions. At the end of the saturation, the system pressure was released from 2000 psi to 0 psi at different rates ranging from 0 to 10 minutes. The proton profiles of water within the rock during the process were recorded by NMRI. It was observed that when the pressure was released from 2000 to 0 psi within 0 to 5 minutes, the pressure release rate did not have great effect on the total amount of recovered oil, although the recovery rate became lower as the pressure release rate was decreased. However, when the pressure release rate was further decreased, the total amount of the recovered oil also became lower. It was also observed that under our experimental conditions most of the gas evolution occurred when pressure was released below 300 psi. These tests indicated that the solution gas drive process would be most effective when applied to reservoirs where low down hole pressures could be achieved.

Achievements

A new CO_2/water/surfactant process has been investigated for the recovery of oil from low permeability media. The tests show that using carbonated surfactant solutions in an imbibition/solution gas drive process can significantly improve the overall recovery efficiency, with the mechanisms being enhanced imbibition rates and enhanced solution gas drive. The initial success of our laboratory test suggested the potential utilization of this technique as a single well soak treatment for low permeability, fractured reservoir environments. Significant decreases in oil saturation (or increases in oil production) are particularly pronounced when the process is used in multi-cycle tests.

IV. Dispersed Phase Processes

Introduction

The use of fractional flow theory where relative permeabilities are expressed in terms of fluid saturations is appropriate for conventional multiphase oil and gas displacement processes in porous media. However, such representations are totally inadequate for describing chemically stabilized dispersed phase displacements, the latter arising when multiple phases move through a porous media in the presence of film stabilizing surface active agents. The most common examples of such displacements are those encountered with foam and emulsion systems.

The key elements in describing and simulating dispersed phase flows and displacements in porous media are:

(1) The identification and description of the phase dispersion and re-connection processes and the transient variations in the number and size distributions of the dispersed phase bodies.

(2) The determination of the mobilization and trapping conditions for the dispersed phase. This requires accurate determinations of the threshold and capillary pressure curves (functions) for dispersed phase systems, which heretofore had not been obtained.

(3) The specification of suitable mobility relations for the dispersed phase with closure achieved through appropriate displacement tests (analogous to relative permeability determinations in conventional non-dispersed multi-phase flows).

(4) The integration of the above descriptions in a comprehensive dispersed phase flow/displacement simulator with the ability to predict the superficial phase velocities and the phase saturation (trapped and flowing) under prescribed conditions and over reservoir length scales.

It is believed that NMR and CT X-ray imaging techniques can provide information on such systems, particularly temporal and spatial phase distributions, in-situ phase texture, dispersed phase stability, and relative phase mobility. When coupled with other indirect observations and data, as well as appropriate pore level analyses, such information can provide the basis for the development of new dispersed phase mobility representation.

Several experiments have been conducted under the current project to study dispersed phase systems. These have included the determination of dispersed phase texture by NMR restricted diffusion measurements and various dynamic displacement tests on dispersed phase systems using CT scanning methods.

Dispersed Phase Texture

Theory

Self diffusion of molecules having nuclear magnetic moments can be detected by NMR in the presence of various magnetic field gradients. Diffusion of such molecules in a magnetic field gradient causes the intensity of the NMR responses to be different from the responses in the absence of gradients. NMR attenuation, normally used to describe the effect of molecular self-diffusion, is defined as the ratio of the pulsed NMR signal intensities with and without external field gradients,

$$R = \frac{I_{\text{with gradient}}}{I_{\text{without gradient}}}$$

In particular, when a spin echo pulse sequence (Figure 9) is used together with two pulsed field gradients on a bulk liquid sample, a simple relation exists between the NMR attenuation R and the diffusion coefficient D :

$$\ln R = -\gamma^2 g^2 \delta^2 (\Delta - \tfrac{1}{3}\delta) D \qquad (1)$$

where g is the external field gradient, δ the gradient pulse width, and Δ the interval between the two gradient pulses during which the diffusion can be observed. The diffusion coefficient D can be easily determined from such measurements.

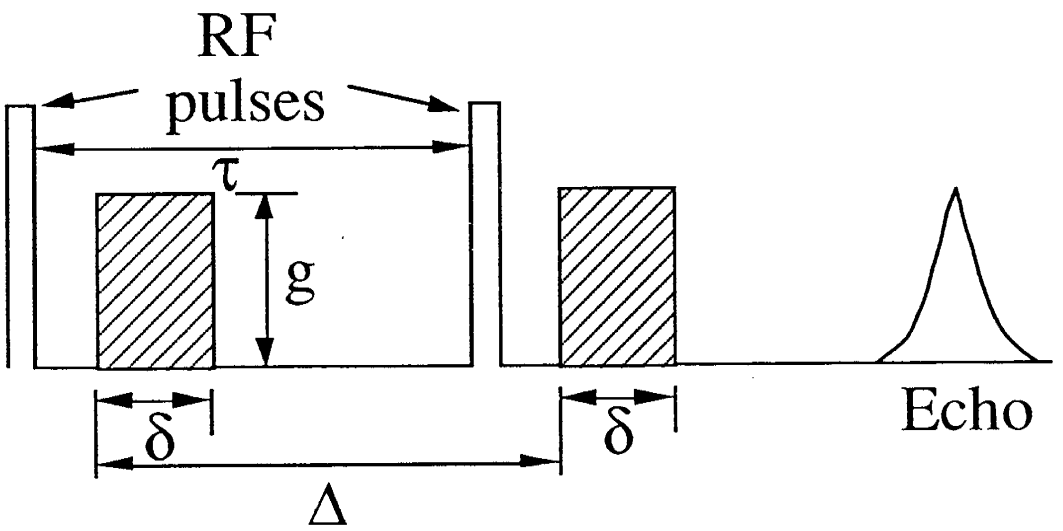

Figure 9. Diagram of a spin-echo sequence with two pulse gradients.

However, in dispersed systems, where the diffusion of molecules in the dispersed elements is restricted by the phase boundaries, such a simple relation is not applicable. The attenuation R will in general depend not only on g, Δ, δ and D, but also on the geometry of the dispersed phase. For example, the NMR attenuation due to the diffusion of protons in a sphere of diameter $2a$ can be calculated as[12]:

$$R(\Delta,\delta,a) = \exp[-2\gamma^2 g^2 \sum_{m=1}^{\infty} \frac{1}{\alpha_m^2(\alpha_m^2 a^2 - 2)} \{\frac{2\delta}{\alpha_m^2 D} - \frac{2 + e^{-\alpha_m^2 D(\Delta-\delta)} - 2e^{-\alpha_m^2 D\Delta} - 2e^{\alpha_m^2 D\delta} + e^{-\alpha_m^2 D(\Delta+\delta)}}{(\alpha_m^2 D)^2}\}] \quad (2)$$

where α_m is the mth positive root of the Bessel function equation

$$\frac{1}{\alpha a} J_{3/2}(\alpha a) = J_{5/2}(\alpha a) \ .$$

Eq.(2) relates the NMR attenuation with the size of the dispersed phase, a. This important fact suggests that information about the dispersed phase size distribution can be obtained from NMR restricted diffusion measurements.

NMR restricted diffusion measurements can be used to determine size distributions of bulk liquid emulsions, where the dispersed phase are spherical in shape. During the measurement, NMR attenuation can be recorded for various values of the observation time Δ and the gradient pulse duration δ. The measured NMR attenuation $\langle R(\Delta,\delta)\rangle$ is the combined effects of restricted diffusion of molecules in all the droplets of the emulsion sample and can be expressed in terms of a droplet size distribution, $P(a)$, and the calculated NMR attenuation $R(\Delta,\delta,a)$ (Eq. 2)[13]:

$$\langle R(\Delta,\delta)\rangle = \frac{\int_0^{\infty} a^3 P(a) R(\Delta,\delta,a) da}{\int_0^{\infty} a^3 P(a) da} \quad (3)$$

where the factor a^3 reflects the fact that NMR intensity is proportional to the number of protons. The choice of the distribution function is not unique. A commonly used size distribution function for a bulk emulsion system is the log-normal function:

$$P(a) = \frac{1}{2a\sigma(2\pi)^{1/2}} \exp\left[-\frac{(\ln 2a - \ln \xi)^2}{2\sigma^2}\right] \quad (4)$$

By fitting Eq.(3) and Eq.(4) with experimental data, the distribution parameters σ and ξ can be obtained.

Results and Discussion

In this experiment, the NMR restricted diffusion measurement was used to determine the droplet size distribution of bulk oil-in-D_2O emulsions. An optical method was also used to verify the results of NMR measurements. D_2O has very similar chemical properties as H_2O. It was used because the NMR resonance frequency of deuterons in D_2O is very different from that of protons in oil. The experimental parameters were set such that only the NMR signals from oil molecules could be observed. The emulsion samples were generated by adding oils, either hexadecane or n-octane, to D_2O containing the surfactant Alpha Olefin Sulfonate (AOS).

The diffusion coefficients D of both oils were measured from bulk oil samples using the spin echo method described previously (Eq.(1)). The NMR relaxation time T_1 of oil phase were measured for emulsion samples using the inversion recovery method. Both D and T_1 are listed in Table 7. The NMR attenuations were measured by means of spin echo method for short observation time Δ (<150 ms), and by means of stimulated echo method for long observation time.

	n-Hexadecane	n-Octane
D (cm^2/sec) (bulk oil)	3.74×10^{-6}	2.33×10^{-5}
D (cm^2/sec) (literature value)	3.92×10^{-6}§	2.00×10^{-5}†
T_1 (sec) (emulsion)	0.68	2.05

Table 7: Diffusion coefficients of the pure oils and the spin-lattice relaxation times of the oil-in-D_2O emulsion samples at room temperature.
(§ Ertl, H. and Dullien, F. A. L., 1973 ; † Douglass, D. C., and McCall D. W., 1958)

The measured NMR attenuations for a n-octane emulsion sample were shown in Figure 10 by discrete symbols as functions of observation time Δ and gradient pulse width δ. Effects of restricted diffusion were reflected by the nonlinear behavior of the data. The data was then fitted with Eq.(4-5) to obtained distribution parameters σ and ξ. The corresponding distribution function $P(a)$ is plotted in Figure 11 as a solid line, and the calculated NMR attenuation using Eq.(4) is plotted in Figure 10 as solid lines for comparison with experimental data.

The emulsion droplet size distribution of the same n-octane sample was also measured using an optical system, which consisted of a microscope, a video camera, a personal computer and image analysis software. The two dimensional projection of the emulsion sample was captured by the camera and stored in the computer. These data were later analyzed to obtain a size distribution which is represented in Figure 10 by discrete symbols. It can be seen that the distribution obtained by NMR restricted diffusion and by optical method match very well.

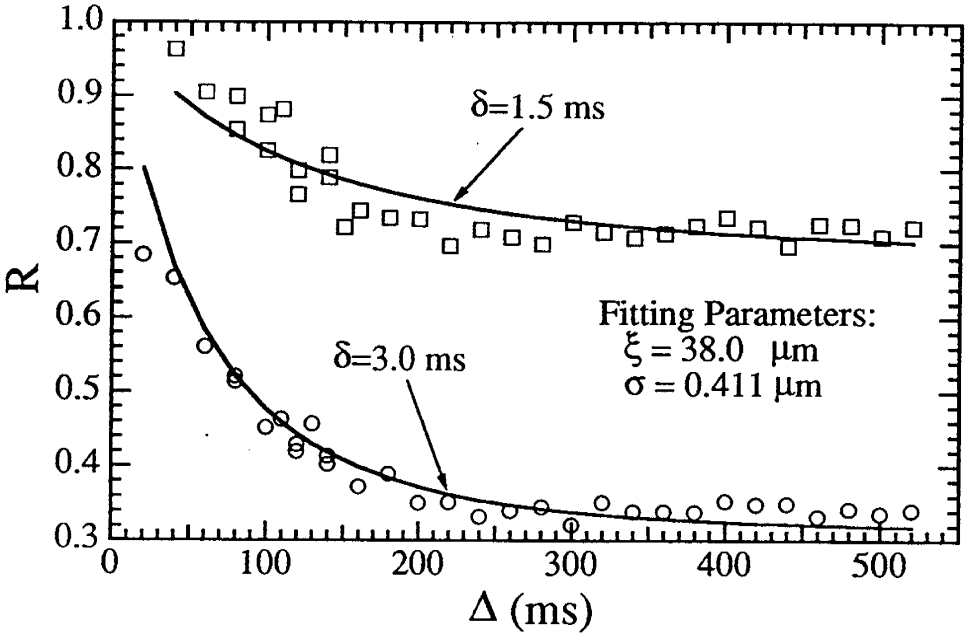

Figure 10. Measured and calculated NMR attenuation of a n-octane in D_2O emulsion.

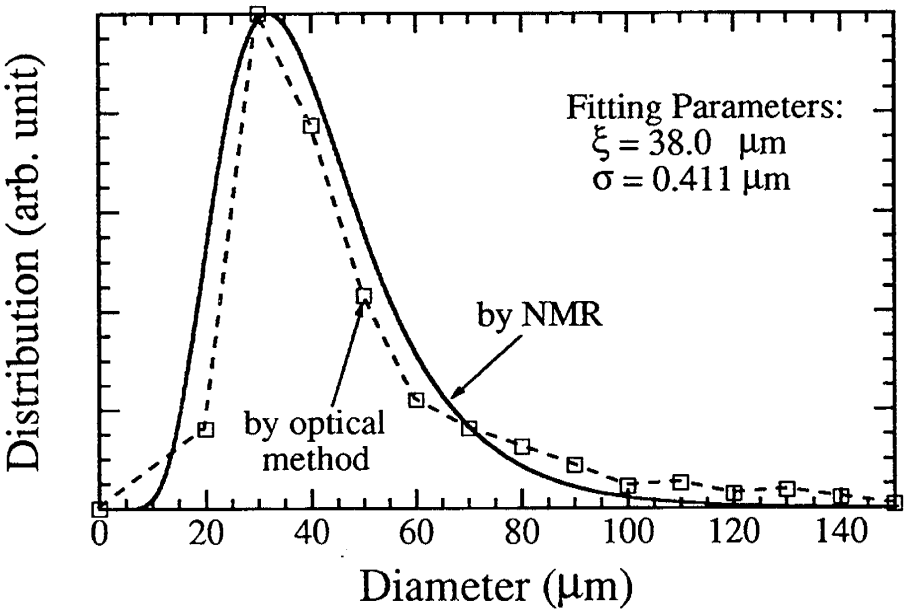

Figure 11. The droplet size distribution of a n-octane in D_2O emulsion, measured by NMR restricted diffusion and an optical method.

This experiment [14] showed that the bulk emulsion droplet size distribution obtained from NMR restricted diffusion measurements quantitatively reflects the real droplet size distribution. The effectiveness of this method depends on the average droplet size and the magnitude of the dispersed phase diffusion coefficient, D. The effects of the relation between D and the size of the dispersed phase need to be considered when applying this method on other dispersed phases.

Dynamic Displacement of Dispersed Phase Systems

Experiment

In this study we are interested in the effects of foam texture and foam stability on the dynamic displacement of dispersed systems in porous media. These experiments will provide information for developing simulation models of dispersed phase flow and displacement in porous media.

The displacement cell setup is shown in Figure 12. The main cell is made of aluminum and is cylindrical in shape with a diameter of 1 inch and a length of 5 inches. Aluminum has a very low X-ray absorption coefficient, and thus may be represented as being transparent to X-ray. Four pairs of pressure transducers are mounted symmetrically on the main cell, facing each other. The specially designed setup of these pressure transducers enables us to measure pressures in the liquid phase and gas phase, respectively. The body of the viewing cell is made of stainless steel with two high pressure glasses on the top and bottom of the cell. During the experiment, light can be shined through the cell from the bottom, and the images of passing foams can be recorded by a camera at the top of the cell. The captured foam images are recorded by a computer and analyzed at a later time.

For the CT scanning measurements, a Delta-Scan 100 scanner was used. A 256x256 cross-section image of a 7 mm thick slice can be obtained with an acquisition time of 2 minutes. Multiphase saturations within the porous media can be measured using dual X-ray power (high 120 kV, low 90 kV).

The porous media samples used in these experiments were Ottawa sands (90~125 micron in size) packed in the main cell. During the experiments, surfactant solution was injected into the sample cell together with nitrogen gas to generate the foam in situ in the sand pack. The specially designed high pressure sampling system enabled us to measure both liquid and gas pressures along the flow path. Dynamic capillary pressures at different locations in the system were then obtained from the measured pressures. The spatial and temporal distributions of separate phases during different flowing processes were determined by CT X-ray imaging methods.

Another unique feature of the system was its capability to measure bubble size distributions of the in situ foam (the foam texture). Previously, foam textures had been obtained by flushing foam out of the porous media and measuring the size distribution of the dispersed phase exiting from the cell. However, due to snap-off processes at the exit boundary of the porous media, the measured foam size distribution may not be the same as the original insitu foam size distribution. In our experiments, the in situ texture is determined by stopping the displacement, increasing the system pressure, and flushing the small foam bubbles from the media. The size distribution is then determined by passing the mixture through the viewing cell. Statistical measurements then provide the effluent bubble size distribution. The original insitu bubble size distribution can be obtained by back calculating the volume associated with the pre-pressured condition.

Results and Discussion

The displacement processes were studied with both non-dispersed phase and dispersed phase systems. In the studies of non-dispersed phase systems, pure water was injected with nitrogen gas with different liquid/gas ratios. From these studies the relative permeabilities of both liquid and gas phases were determined for drainage and imbibition displacements. Viscous fingering was observed in the non-dispersed phase displacement. Such fingering effects were reduced by an improved method of packing the sand pack.

To generate the dispersed phase, a surfactant solution containing Chevron surfactant CD1050 was injected simultaneously with nitrogen into the sand pack. Studies were conducted with different liquid/gas ratios. Various characteristic data, such as capillary pressure as a function of liquid saturation, the relative permeabilities of both liquid and gas phases, etc., can be determined from our measurements.

Figure 13 shows typical bubble size distributions measured during a dispersed phase displacement. In these measurements, the initial system pressure was 150 psi. The bubble size distribution under such condition can be determined by measuring the flowing bubbles in the viewing cell. The bubble size distribution under this normal system pressure is shown in Figure 13 by the dashed line. However, as discussed previously, this distribution may not be the same as the original in situ bubble distribution due to the snap-off effect at the exit boundary. The pressure was then raised to 750 psi and the effluent bubble size distribution of the foam was measured with the viewing cell. The bubble size distribution under high pressurization is shown in Figure 13 by the solid line. An image of bubbles passing through the viewing cell is shown in Figure 14. Many such images were collected and analyzed to determine the size distribution.

It was also observed that the foam quality was greatly affected by the total flow rate of the dispersed phase. Weak foams were formed during slow displacement. A critical velocity is suggested above which a strong foam can exist. Such a critical velocity needs to be determined in future experiments.

We have made significant progress in understanding the complicated dynamics of foam flow in porous media through the studies of this project. A wide range of detailed information can be obtained with our experimental setup. At the time of this report, we are still in the process of taking data on dispersed phase systems under various experimental conditions. We will be able to achieve better understanding of such processes at the completion of these extensive and systematic studies.

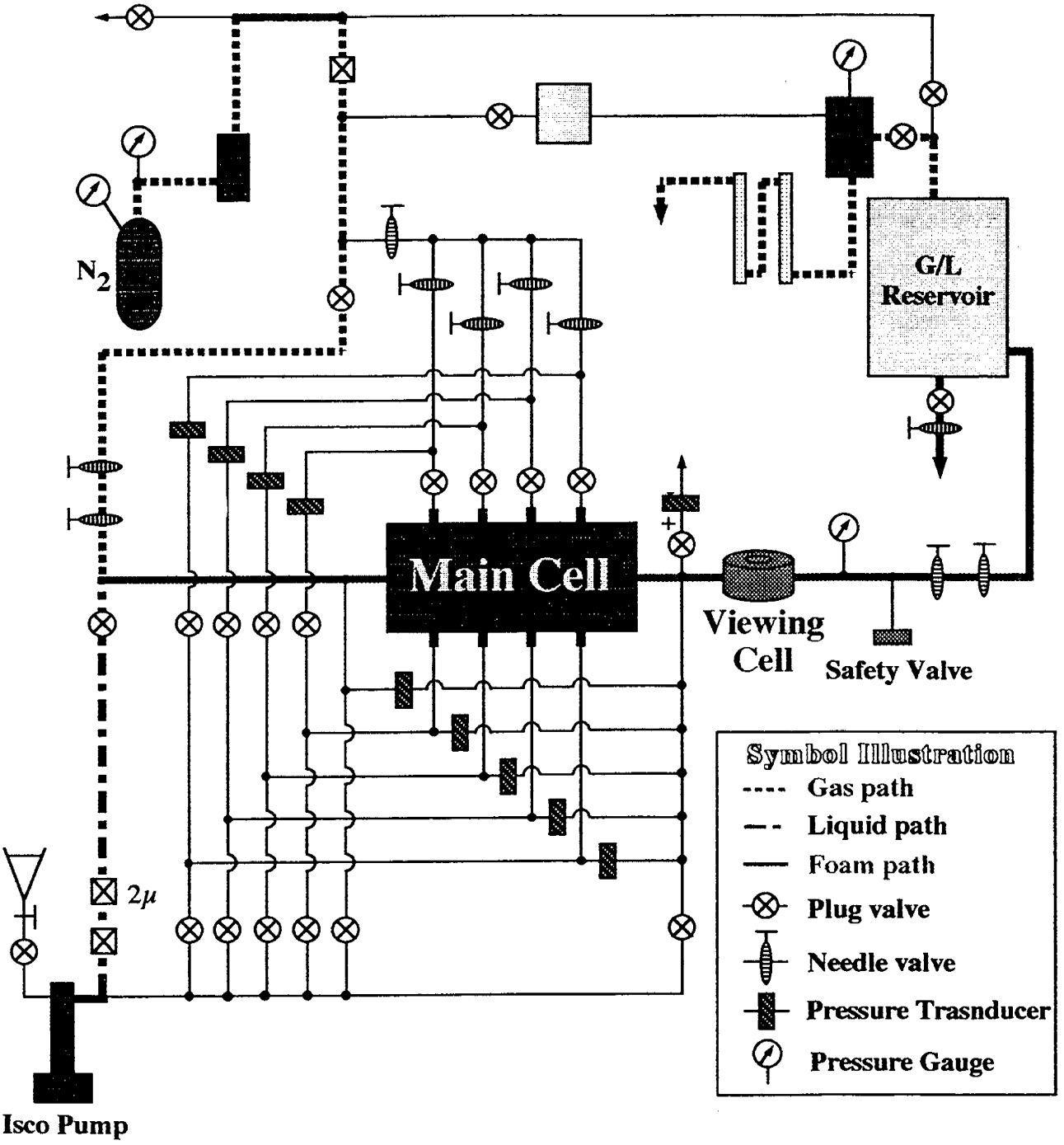

Figure 12. Experimental setup of the dynamic displacement of dispersed phase in porous media.

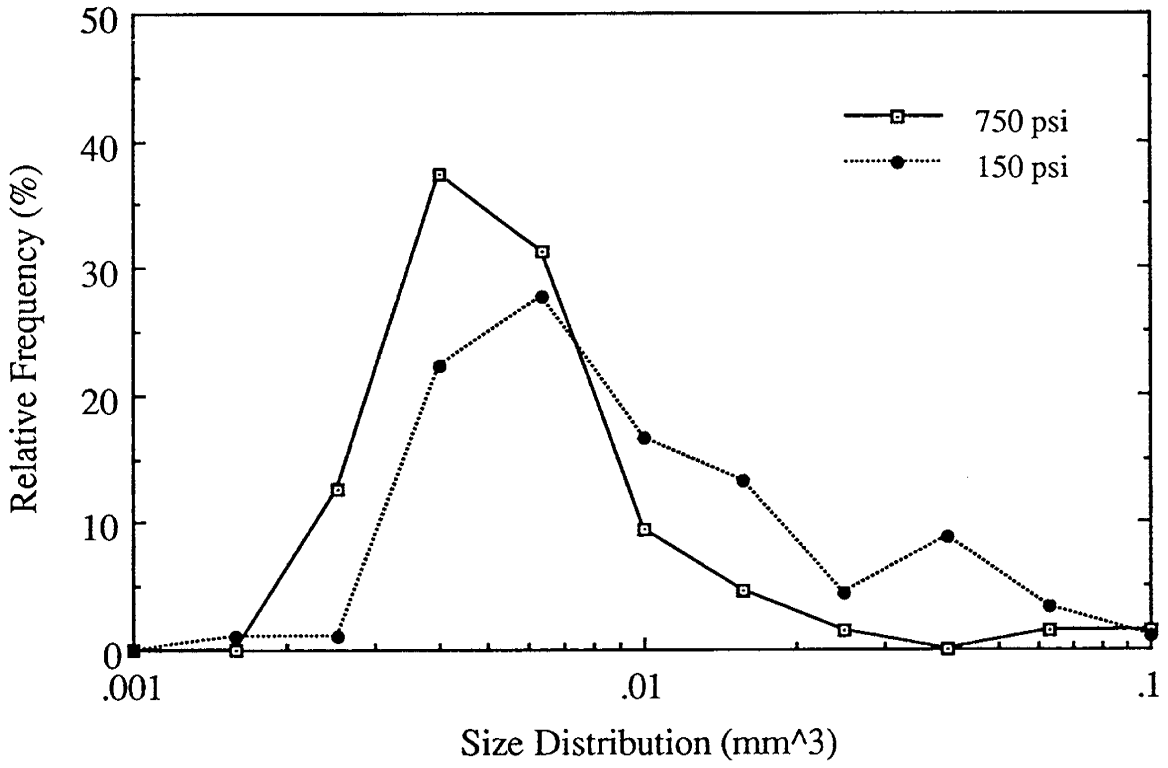

Figure 13. Bubble size distribution of foam in porous media.

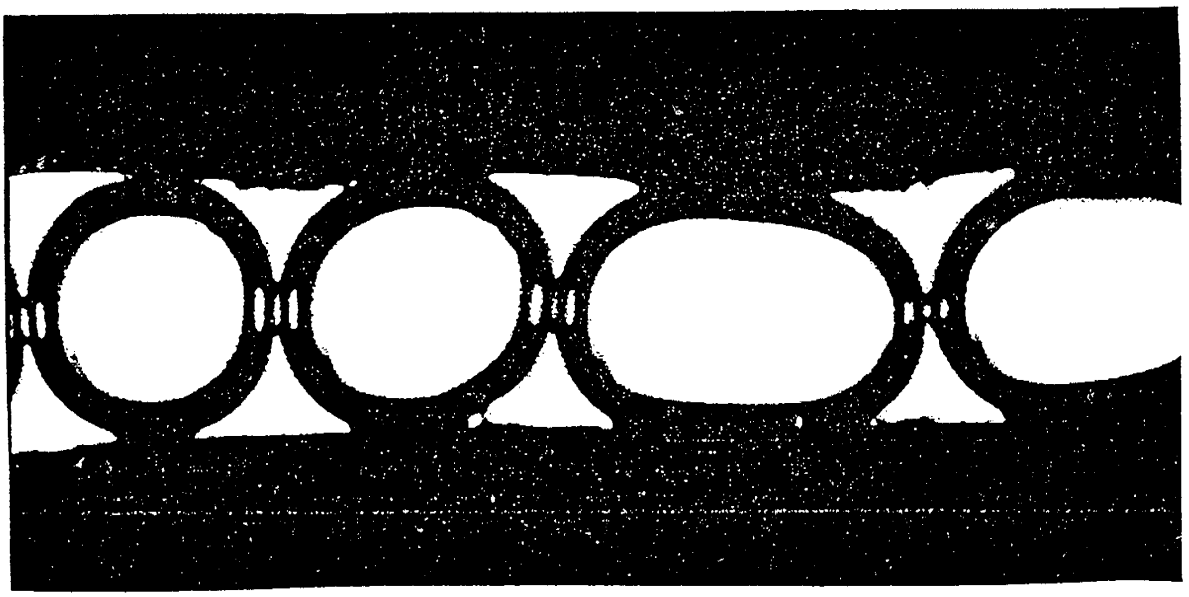

Figure 14. Bubble image in the viewing cell.

V. References and Publications

1. Craig, F. F., "The Reservoir Engineering Aspects of Waterflooding," Monograph Series, SPE, Richardson, TX, Vol. 3 (1971)
2. Anderson, W. G., "Wettability Literature Survey -- Part 2: Wettability Measurement," *JPT* (November 1986) 1246-1262
3. Brown, R. J. S. and Fatt, I., "Measurements of Fractional Wettability of Oilfield Rocks by the Nuclear Magnetic Relaxation Method," *Trans. AIME*, **207**, 262 (1956)
4. Saraf, D. N., Kumar, J., and Fatt, I., "Determination of Wettability of Porous Materials by the Nuclear Magnetic Resonance Technique," *Indian J. of Technology*, **8**, 125 (1970)
5. Williams, C. and Fung, B. M., "The Determination of Wettability by Hydrocarbons of Small Particles by Deuteron T_1 Measurements," *J. Magnetic Resonance*, **50**, 71 (1982)
6. Bangs, L. B., *Uniform Latex Particles*, Bangs Laboratories Inc., Carmel, IN (1987)
7. Morrow, N. R., H. T. Lim, and J. S. Ward, "Effect of Crude-Oil Induced Wettability Changes on Oil Recovery," *SPE Formulation Evaluation*, **1**, 89 (February 1986).
8. Hsu, W. F., Li, X., and Flumerfelt, R. W., "Wettability of Porous Media by NMR Relaxation Methods," SPE 24761, 67th Annual Technical Conference and Exhibition of SPE, October 1992, Washington, D. C.
9. Hsu, W. F., Li, X., and Flumerfelt, R. W., "Characterization of Wettability of Model Porous Media by NMR Relaxation Methods," under preparation.
10. Neumann, H. J., "Investigation on the Wettability of Formations and on Oil Migration," *Erdoel und Kohle-Erdgas-Petrochemie*, **9**(3), 171 (March 1966)
11. Poston, S. W., Perez, J. M., and Halimi, H., "Preliminary Studies: Using MRI Imaging Techniques to Study Water Imbibition Flooding," presented at the 6th Wyoming EOR Symposium, Casper, WY, May 1990
12. Murday, J. S., and Cotts, R. M., "Self-Diffusion Coefficient of Liquid Lithium," *J. Chem. Phys.*, **48**, 4938 (1968)
13. Packer, K. J., and Rees, C., "Pulsed NMR Studies of Restricted Diffusion," *J. Colloid and Interf. Sci.*, **40**, 206 (1972)
14. Li, X., Cox, J. C., and Flumerfelt, R. W., "Determination of Emulsion Size Distribution by NMR Restricted Diffusion Measurement," *AIChE J.*, **38**(10) 1671 (1992)

SUBTASK 4. MISCIBLE DISPLACEMENT STUDIES

Principal Investigator: M. P. Walsh

Department of Petroleum Engineering

I. Introduction

Approximately two-thirds of the discovered oil remains unrecoverable by conventional production practices. One means of recovering this otherwise abandoned oil is by miscible enhanced oil recovery (EOR). Miscible flooding agents (solvents) include carbon dioxide, nitrogen, enriched hydrocarbon gas, and flue gas.

Application of miscible flooding, however, is complicated by the formation of viscous fingers which complicate the process and lower volumetric sweep and oil recovery efficiency. Viscous fingering is caused by the inherently adverse mobility ratio which exists between the injected solvent and the in-place oil. Understanding the viscous fingering phenomena is key to improving the oil recovery of miscible floods. The overall objectives of Subtask 4 are to: (1) develop the CT scanner as a tool for use in dynamic flow tests and (2) study the effects of viscous fingering using the CT scanner.

Our approach to develop the CT scanner is to systematically develop all the experimental procedures necessary to use the CT scanner. This includes but is not restricted to: (1) designing a core containment device, (2) designing a flow system, (3) developing viable CT scanner operating procedures, (4) developing data transfer procedures from the CT scanner to post-processors, and (5) developing post-processing software for image reconstruction. Part of this work includes documenting encountered problems, delineating solutions, and making recommendations for future work.

Our approach to study viscous fingering is to use the CT scanning apparatus. This unique instrument allows us to non-destructively measure accurate fluid distributions as a function time and position. This in-situ data together with effluent concentration and cumulative recovery history data is much more meaningful in characterizing the displacement behavior than effluent concentration and cumulative recovery history data alone. It will be useful in the testing and validation of reservoir simulators. Validation will lead to increased confidence in applying these models as predictive tools. This type of data will also be useful in developing a unified theory for vertical sweep efficiency in miscible systems based on dimensional analysis and dimensionless groups. Dimensionless groups will be helpful to properly characterize the different attending flow regimes. The dimensionless groups will also be helpful in screening target reservoirs.

II. Theory and Development of CT Scanning

Introduction

CAT (computer assisted tomography or computerized axial tomography) also commonly known as CT (computed tomography), is a non destructive technique to obtain 2-D cross-sectional images of the interior of a 3-D object. This is a technique developed by Hounsfield,[1] whereby X-rays pass through an object and the transmitted rays strike a detector. These detected ray messages are stored as data in the CT-Scanner computer where they are simultaneously analyzed by various algorithms. With these algorithms, the computer constructs a two dimensional image or picture. The reconstructed cross-sectional image of the object is then seen on the computer monitor as shades of grey. A schematic of the entire process is shown in Figure 1. (A picture or a slice of a cross-section is called a tomograph, hence the name computed tomography).

Theory of Computed Tomography

Image Reconstruction

Image reconstruction[1,2,3] is a process by which the output signal of the X-rays, on passing through an object, can be used to mathematically construct the X-ray attenuation distribution of the cross-section of a 3-D object. Consider Figure 2a which shows an X-ray of incident intensity N_O passing through a volume element (voxel) of thickness x. If N is the intensity of the transmitted ray through the volume element, the intensity relationship generated through this volume element is linear on a logarithmic scale and is given by Bougher-Beer's law[1,4].

$$\mu=(1 / x) [\ln (N_O/N)] \tag{1}$$

where μ is called the linear attenuation coefficient.

Consider a circular object (see Figure 2b) consisting of many 2-D voxels (also called pixels), each having a different linear attenuation coefficient. Every point within a section of an object can be defined by its (x,y) coordinates in a Cartesian system. If the same beam of X-rays passes through n volume elements of equal length x, each having a different linear attenuation coefficient, then applying equation (1) to all the voxels along the beam, we have,

$$(\mu_1 + \mu_2 + ... + \mu_n) = \frac{1}{x} \ln \left(\frac{N_o}{N}\right) \tag{2}$$

where μ_i is the linear attenuation coefficient of each voxel through which the X-ray beam passes. N_O is the intensity of the beam of X-rays incident on the first voxel, and N is the intensity of the transmitted ray from the last voxel, n. When the beam of X-rays passes through different voxels at different angles, many equations similar to Eqn. (2) are generated. These linear equations created, are solved simultaneously to obtain the linear attenuation coefficient $\mu_i(x,y)$ of each volume element.

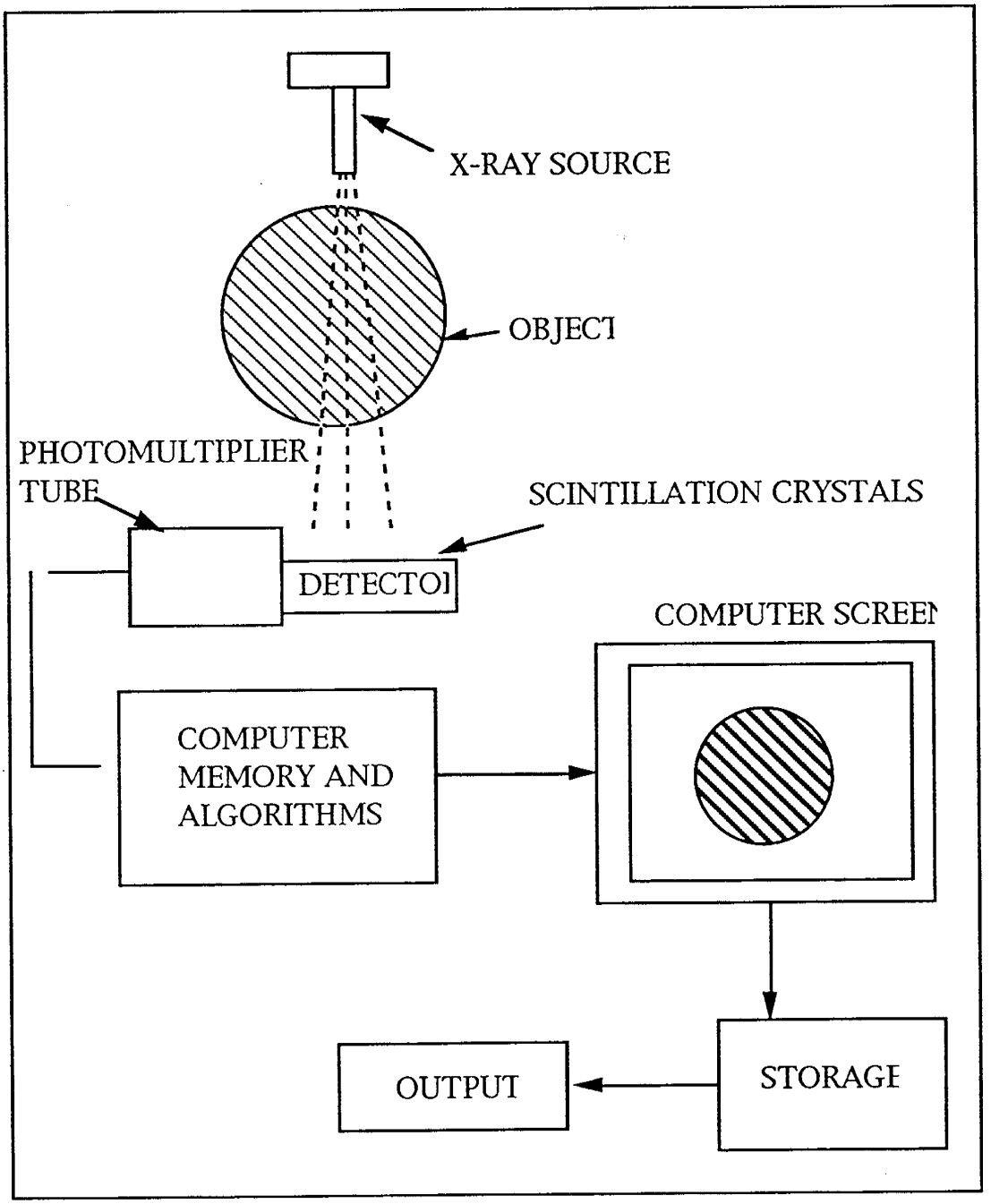

Figure 1. Block diagram of CT-Scanner setup.

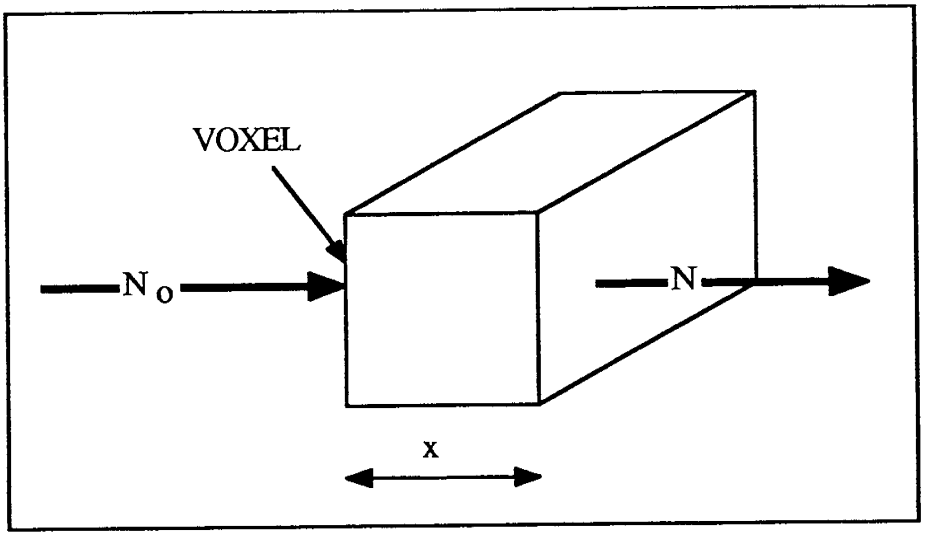

Figure 2a. X-ray passing through a voxel.

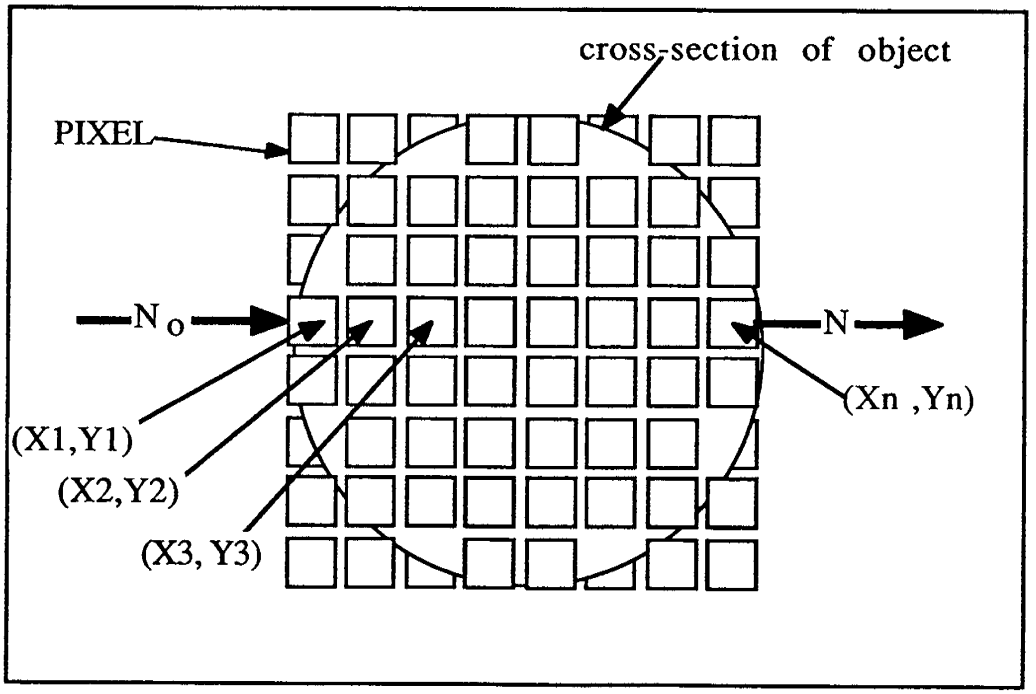

Figure 2b. Pixels in a cross-sectional object.

The left hand side of above Eqn. (2) can be replaced by the line integral of the linear attenuation coefficients. Considering the linear attenuation coefficients within the two dimensional cross section, the intensity transmitted along a particular path is given by

$$p = \ln\left(\frac{N_o}{N}\right) = \int_s^d \mu(x,y)\ dL \qquad (3)$$

where dL is the differential of path length along the ray, s is the source, d is the detector and p is called the projection value. This is the fundamental equation of computed tomography. It states that the logarithm of the ratio of the unattenuated intensity to the transmitted intensity is the line integral of the one dimensional distribution of linear attenuation coefficients. Given a sufficient number of these line integrals or projection values, the original distribution of attenuation coefficients in the object can be obtained mathematically.

Since the X-ray beam is not always monochromatic, the resulting image has artifacts (image distortion) around the periphery. These artifacts give rise to a phenomenon called beam hardening. This phenomena will be discussed later.

The **basis** of computed tomography lies in the reconstruction process. Reconstruction refers to the generation of a 2-D array of numbers for an object, given a sufficiently large set of line integrals. One of the most widely used reconstruction techniques for CT-Scanners is the Back-Projection method[2,5] or Summation method.

Other methods of reconstruction are 1) Fourier transform method 2) Integral equation method and 3) Series expansion method.

X-Ray Production[5,6]

CT-Scanners produce X-rays by allowing electrons to strike a solid target. A Coolidge tube (Figure 3) is a high vacuum tube with a filament and a target. A high potential drop is applied between the filament and the target in order to generate electrons. These electrons, which are emitted by the filament, hit a target which is a metal like copper, resulting in the production of X-rays. A large amount of heat is generated in the target during X-ray production. The target is therefore made hollow so that it can be cooled by either water or oil through a circulation process shown in Figure 3. The high potential between the target and filament is obtained by a step-up voltage transformer which operates on alternating current. Rectifiers and filters are used so as to get a steady supply of high voltage across the tube. Normally the CT-Scanner is operated at 120 kV or 140 kV.

X-ray Detection[5,7]

The X-ray beam on passing through a scanned object is absorbed/reflected and the emerging rays reach the detector (Figure 1). The detector works on the principle of photoelectric absorption. These detectors have NaI or CaF crystals which scintillate or give out photons of visible light when struck by X-rays. The amount of light emitted by the crystal is measured with a photomultiplier tube which is directly connected to a high speed computer to store this data. X-rays are emitted from a source and are received at the detector as the source travels transversely along the object and then rotates one degree at a time.

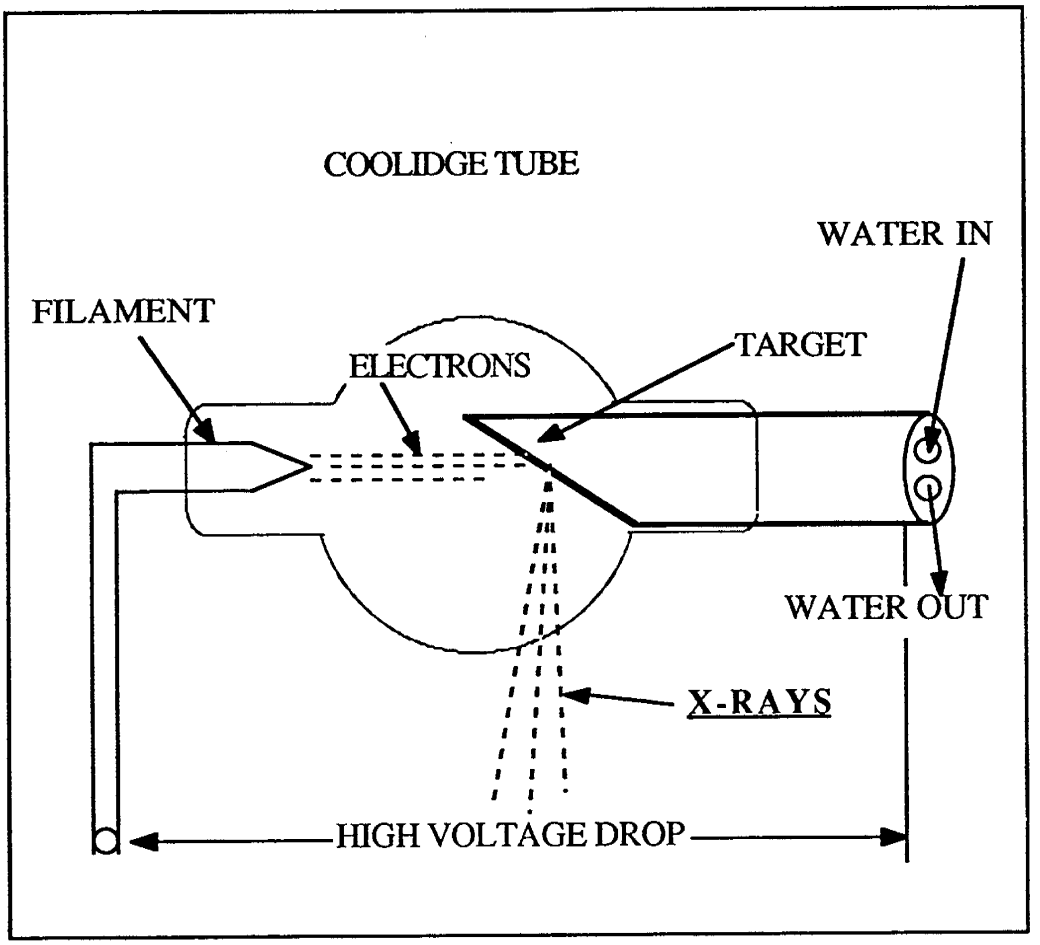

Figure 3. Production of X-rays.

Data Acquisition

The detectors acquire X-ray attenuation measurements along discrete lines through an object (Figure 4). The measurement obtained by a single detector along a line is referred to as projection data or profile data. Rotation of the source and detectors during scanning allows for acquisition of such data along many such lines at different angles. At the first step only the traversing (sideways) motion takes place. The yoke (a device on which the detectors and source are mounted) then rotates a certain angle and stops. The detector and source again traverse along the yoke. This rotate-traverse, rotate-traverse,..... motion continues until the yoke has moved 180 degrees thus obtaining projection data on all transverse movements. All this data obtained by various projection lines is stored by computer to be processed by algorithms.

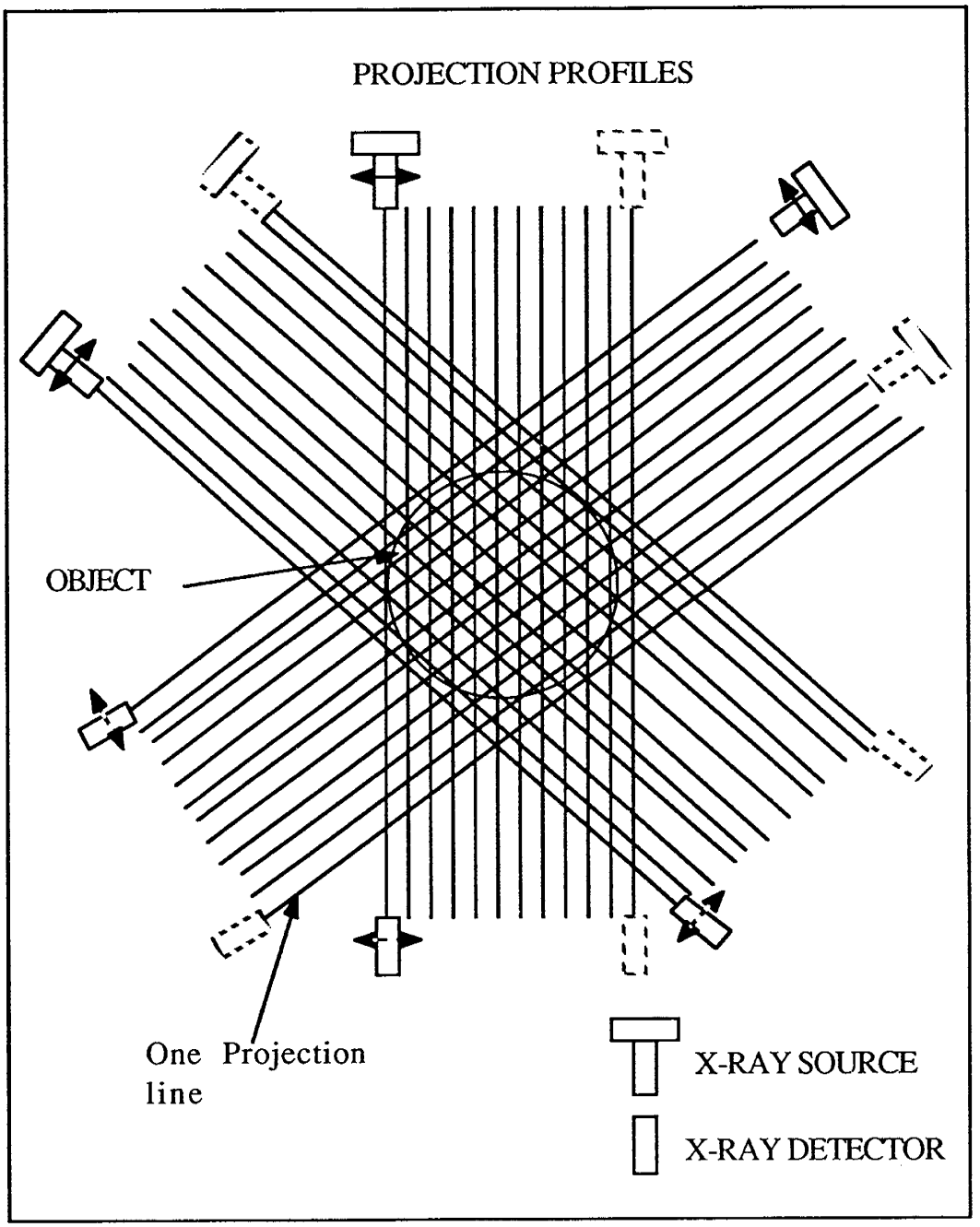

Figure 4. Profiles generated by X-rays.

Image Display[5,8]

The linear attenuation coefficients are converted into a 2-D array of integers by a computer algorithm and displayed on the computer screen as grey scale or colors. The formula used to convert the attenuation coefficients into CT numbers is given by Eqn. (4). For the sake of standardization and convenience, μ_{water} is used in the formula, which gives water a CT number of zero.

$$\text{CT number} = K(\mu - \mu_{water})/\mu_{water} \tag{4}$$

where

μ is the linear attenuation coefficient of the material
μ_{water} is the linear attenuation coefficient of water
K is a constant, usually 1000 for convenience.

Computed tomography has its own scale to distinguish between different materials. This scale is called a CT unit. Commonly used materials have a CT number shown in Figure 5. For example, water has a CT number of 0, air has a CT number of -1000, Quartz sandstone has a CT number of approximately 1700.

CT-Scanning Procedures

Beam Hardening

One of the problems encountered in CT-Scanning is beam hardening.[5,9-11] This phenomena takes place because the high energy X-rays get absorbed along the periphery of the object giving unrealistically high values of CT numbers. This effect causes a small band of high CT numbers to be seen around the outer edge of the object.

This problem is reduced in many ways. The medical industry uses foam pillows to surround the patient, thus allowing the high energy rays to be absorbed by the foam pillows and reduce this effect on the object being scanned. Other techniques to avoid this problem are by surrounding the object in water or a solution of NaI or a sheet of aluminum. Filters covering the X-ray source are also very useful.

The beam hardening correction techniques which were employed for the CT-Scanner used in this research are as follows. A copper plate about an eight inch thick is placed over the X-ray source. This tends to make the X-ray beam more monochromatic. Another correction technique called the "non linearity correction coefficients" for water is also used. Here, the CT numbers of a uniform phantom (a physical object to measure the response of a CT-Scanner) of water are taken. An in-built program called NLDGET[16] takes a specified control volume of the uniform phantom and homogenizes the entire image with the control volume.

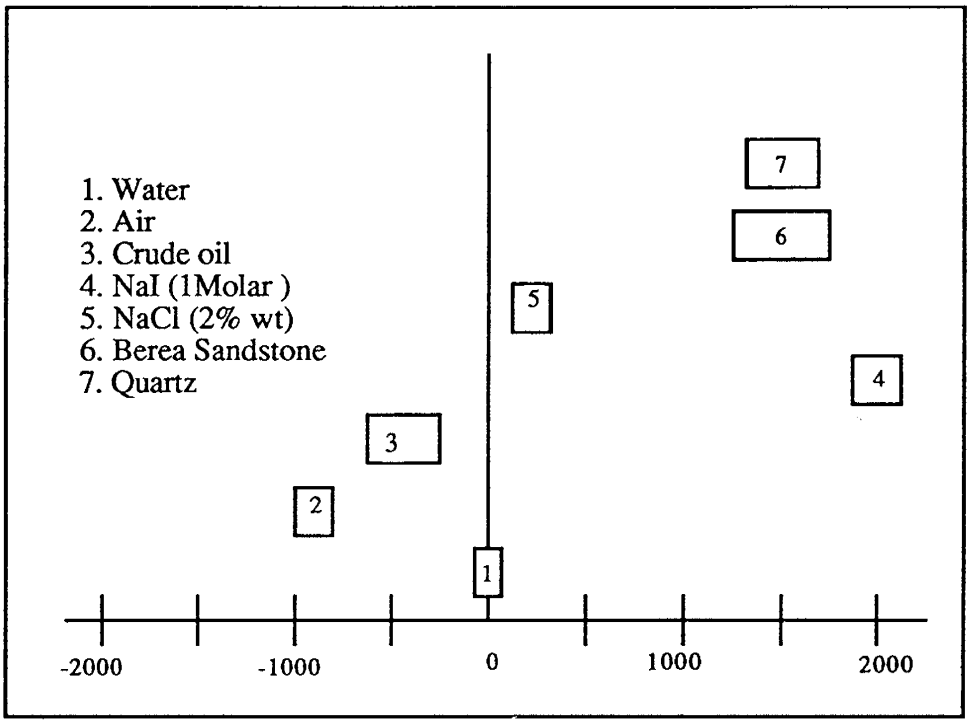

Figure 5. CT scale.

Scan Time

In order to scan the core in a dynamic displacement experiment, the process needs to be stopped. The stopping of the process gives rise to an increased amount of time for diffusion of chemical species to occur between the displaced fluid and displacing fluid. The scan time of each cross-sectional image of the CT-Scanner is about 2 minutes. Usually about 5-30 cross-sectional images (scans) at various positions along a rock sample are required. This totals to about 10 to 60 minutes of scanning time for 5-30 images. This total time could be reduced to a few seconds using more advanced CT-Scanners.

Dopant Studies

In order to differentiate between the displacing and the displaced fluid, a dopant must be added to either of the fluids to increase its CT number. The commonly used dopants are NaI and KI for water, and idododecane and bromodecane for oil. For the experiments conducted in this research, a one molar sodium iodide aqueous solution was used in the displacing fluid.

Measurement of Core Parameters

Vinegar[12-14] *et al.* developed formulas to measure porosity and fluid saturation using the CT-Scanner. Withjack[15] has shown that an optimum dopant concentration of the fluid should be used to obtain accurate values of porosity and fluid saturations. The derivation of formulas and experimental technique to measure these parameters are outlined below.

Porosity

The porosity of a rock sample is measured by scanning the porous media sample twice, once with the sample saturated with fluid-1 (usually air), and the next with the sample saturated with fluid-2 (usually water). The scanning with air is referred to as the dry scan measurement, and the scanning with water is the wet scan measurement. To obtain a formula for porosity, the following variables are defined:

$CT_{Total\text{-}1}$ = the CT number of the porous media scanned with fluid-1
$CT_{Total\text{-}2}$ = the CT number of the porous media scanned with fluid-2
$CT_{fluid\text{-}1}$ = the CT number of fluid-1
$CT_{fluid\text{-}2}$ = the CT number of fluid-2
CT_{rock} = the CT number of the dry rock
ϕ = porosity of rock

The CT number of the porous media containing fluid-1 is given by a linear combination of the CT numbers of the rock and the fluid-1, or:

$$CT_{Total\text{-}1} = \phi\, CT_{fluid\text{-}1} + CT_{rock}\,(1-\phi)$$

Similarly, the CT number of the porous media containing fluid-2 is given by:

$$CT_{Total\text{-}2} = \phi\, CT_{fluid\text{-}2} + CT_{rock}\,(1-\phi)$$

Eliminating CT rock between the top two equations and solving for ϕ, we have

$$\phi = \frac{CT_{Total\text{-}1} - CT_{Total\text{-}2}}{CT_{fluid\text{-}1} - CT_{fluid\text{-}2}} \qquad (5)$$

The experimental procedure to compute porosity is as follows: First scan the rock dry i.e. with air (fluid-1) only in the core and obtain the total CT number. Then completely saturate the core with another fluid (fluid-2) and scan the core again in exactly the same position as the previous scan to obtain a different total CT number. Now, scan the fluid-1 and fluid-2 in a vial and obtain CT number of the two fluids. Use all the above values in the Eqn. (5) to obtain porosity.

Concentration

When one miscible fluid displaces another in a porous media, it is sometimes necessary to measure the concentration of the displaced or displacing fluid as a function of position.

Vinegar[12-14] discussed a CT-Scanning technique to measure concentrations. The technique is similar to the porosity measurement technique, but here, one more fluid is introduced; the displacing fluid.

The experimental procedure to obtain concentration is as follows: First scan the rock dry, i.e. with air only in the porous media and obtain the total CT number. Then completely saturate the core with the displaced fluid (fluid-1) and scan the core again in exactly the same position as the previous scan to obtain a different total CT number. Then saturate the core with a mixture of the displacing fluid and displaced fluids (fluid-1 and fluid-2), and then scan the porous media again. Now, scan the fluid-1 and fluid-2 each in a vial and obtain the CT number of the two fluids. The variables defined below are similar to the ones defined in porosity measurement, but are denoted in a more concise form, for clarity.

I_1	=	the CT number of the dry core containing air.
I_2	=	the CT number of the core fully saturated with fluid-1
I_3	=	the CT number of the core saturated with fluid-1 & 2
S	=	the saturation of the fluid-2 or concentration of fluid-2
1-S	=	the saturation of the fluid-1 or concentration of fluid-1
μ_0	=	CT number of air
μ_1	=	CT number of the fluid-1
μ_2	=	CT number of the fluid-2

I_1 , I_2 are analogous to $CT_{Total-1}$ and $CT_{Total-2}$ in the porosity measuring method. Therefore as was done before,

$$I_1 = \phi \mu_0 + CT_{rock}(1-\phi)$$
$$I_2 = \phi \mu_1 + CT_{rock}(1-\phi)$$
$$I_3 = (1-\phi) CT_{rock} + \phi [S \mu_1 + (1-S) \mu_2]$$

Simplifying the above equations, we have

$$I_2 - I_1 = \phi [\mu_1 - \mu_0]$$
$$I_3 - I_1 = \phi [S \mu_1 + (1-S) \mu_2] + \phi \mu_0$$

Dividing the previous two equations by each other,

$$\frac{I_3 - I_1}{I_2 - I_1} = \frac{S \mu_1 - (1-S) \mu_1 + \mu_0}{\mu_1 - \mu_0}$$

Assuming μ_0 is zero we have

$$S\,\mu_1 - (1 - S)\,\mu_2 = \left(\frac{I_3 - I_1}{I_2 - I_1}\right)\mu_1$$

Solving for S, the concentration of the displacing fluid is given by

$$S = \frac{\left(\frac{I_3 - I_1}{I_2 - I_1}\right)\mu_1 - \mu_2}{\mu_1 - \mu_2} \qquad (6)$$

CT-Scanners in Petroleum Engineering Research

The petroleum industry has gained a reputation as being the largest user of the CT-Scanner outside the medical field. Since the CT-Scanner is a very useful, rapid, non-destructive technique to observe interior of objects, it has gained widespread recognition in petroleum reservoir engineering to observe fluid flow in porous media.

Slobod and Caudle[17] in 1952 were the first to use X-rays for petroleum engineering studies. They used X-rays to study areal sweepout efficiencies in secondary recovery practices. They did their experiments on a square sand pack which was half inch thick. They studied five-spot and straight line drive well spacing patterns and showed that areal sweepout efficiencies may vary by as much as 50% of the reservoir area between mobility ratios of 0.1 to 10.0.

The X-ray technique slowly developed into the CT-Scanner. It was first used by Wang[18] *et al.* at Columbia University medical school in the late 1970's and early 1980's. Their work was on two phase flow experiments in cylindrical Berea sandstone cores 5 cm in diameter and 25 cm in length. These oil and water displacement experiments were scanned at one particular cross section and at various time intervals. These scans showed the fluid distribution. They used a Delta Scan-50 CT-Scanner.

CT-Scanning technique was used by Hove[19] *et al.* for the inspection of core floods. They observed end effects in many floods and concluded that the nature of these end effects is linked to the wettability of different rocks. They showed that stabilized flow conditions are achievable in whole cores but not in cores which are butted together to form a long core. They also showed that the use of iodine containing additives enhances X-ray attenuation contrasts and allows for better visualization of the flood profiles. It was observed that inhomogeneities invariably occur in core plugs selected for floods.

Bergosh[20] *et al.* studied core analysis on naturally fractured reservoirs using CT-Scanning. They found large contrasts in porosity and permeability measurements in full diameter cores as compared to core plug samples. They recommended careful on-site retrieval of cores by field personnel trained in testing, transportation, handling and preservation of cores. This CT-Scanning has proved very useful in analyzing cores before being removed from the inner core barrel liner.

Honapour[21] *et al.* used a Picker SD 600 fourth generation CT-Scanner to study reservoir rock description. These descriptions were made on studying the densities of crystalline solids, randomly oriented crystals, and preferentially oriented mineral solids. Studies were also done on various formations and the results of porosity, permeability and pore size distribution were verified semi-quantitatively with the CT-Scanner.

Wellington and Vinegar[13], after working on this technique for nearly ten years, published their first paper in 1985 on applying CT-Scanning to reservoir engineering problems. They concluded that the CT-Scanner is an extremely useful tool to study porous fluid flow phenomena. Equations to obtain basic rock properties like porosity and saturations were presented. Displacement experiments to better understand EOR techniques were studied. They imaged core flood experiments at high temperature and pressure by using low X-ray attenuation aluminum pressure vessels. 1-Idodecane was used as a dopant for the oil phase. Their work demonstrated that surfactants in the form of foams can provide effective mobility control for tertiary CO_2 miscible displacements. These experiments were compared with the numerical simulation results run on a CRAY computer and excellent results were obtained.

A comparison of CT-Scanning and NMRI (magnetic resonance imaging) was made in 1986 by Vinegar[14] for understanding and using both techniques for reservoir engineering. He recommends that the two methods can be used simultaneously to get an understanding of fluid and rock properties.

Wellington and Vinegar[12] in their 1987 paper showed the ability of a CT-Scanner to measure compressibility and compaction to obtain a correlation with well logs and core material. Design aspects of high pressure core holders and testing of different alloys useful for CT-Scanning have been discussed.

A fourth generation General Electric CT-Scanner was used by Honarpour *et al.*[22] to do a detailed study on fractures and porosity of dolomite cores from the Upper Madison limestone group. The results were verified using other techniques like X-ray diffraction(XRD), scanning electron microscope (SEM), energy dispersive spectroscopy (EDS) and impregnated thin section analyses.

Withjack[15] showed that porosity measured by the CT-Scanner changes with a change in the voltage and also with a change in the concentration of the fluid used to saturate the core. He showed optimum values of fluids which can be used to obtain correct values for porosity.

In another paper, Withjack *et al.*[23] used CT-Scanning to characterize small-scale heterogeneities in cores and observe miscible floods in these cores. They were able to obtain a correlation between porosity and permeabilities.

Hunt *et al.*[9] characterized rocks in core analysis with a General Electric 880 CT-Scanner. Methods to reduce artifacts in CT images were shown by surrounding the sample in sand or an aqueous KI solution to decrease the beam hardening effects.

CT-Scanning was used by Chatzis[24] *et al.* to determine fluid distributions in gravity assisted inert gas injections. These studies were done on micromodels and Berea sandstone cores. They found CT to be a useful tool to determine porosity and 2-phase saturation mapping.

Kantzas,[25] at the University of Waterloo, did fundamental research in CT-Scanning. He investigated physical properties of rocks and fluids using the CT-Scanner. A software package was developed on the Sun Workstation for fast quantitative analysis of results to determine bulk density, atomic numbers, grain density, porosity and fluid saturations. He used a EMI CT5005 CT-Scanner to do his research.

CT-Scanner Specifications

To date there are five generations of CT-Scanners which have been manufactured. The CT-Scanner used for this research[16] is a second generation machine and its details are given below.

Make:	Delta-Scan 100 Series Brain Scanner
Manufacturer:	Technicar Corporation, formally Ohio Nuclear
Gantry:	Fixed position frame, Rotate-translate mechanism for X-ray tube and four BGO detectors (Dual Slice option), 30 cm patient tunnel opening, Light Localizer
Patient Table:	Manual (110) control for 25 cm vertical travel and 25 cm horizontal travel.
Control Console:	Alphanumeric keyboard, 9" B/W video monitor for both text and image display
Image Processor:	PDP-11/04 CPU, 5 Mbyte disc, 256x256 refresh type display with 64 gray levels
X-ray power supply:	120± 1kV, 25mA ± 1mA for scan operations
Data Acquisition:	X-ray source and detectors: 120kV, 25 mA maximum, Collimator, Four BGO detectors. Three scintillation detectors and one reference detector.
Motion:	512 readings-translate (2/elements), 3 degree angular increments for 62 transversals-186 data profiles per slice, 47616 data points per slice.
Data Processing System:	Back projection-Software, (approximately 15 sec required after scan completion) Convolution-Hardware, simultaneous with data acquisition.
Image display: Scan Picture:	256x256 matrix, 1.012 (± 5%) mm^2 pixel size, Resolution : 3.5 lines/cm
Image Storage:	Disk (temporary) and half inch magnetic tape.
Performance Specification:	Scan Technique Factors- Circle Diameter 25 cm (25.8 cm ± 5%), Scan time- 2 minutes ± 10% (FWQM), Slice Thickness-10 mm.

The console is also fitted with a Unidex IIIa, which is a programmable table positioner, which controls the table movement to an accuracy of about 0.0005 inches. The table has limit switches, which control initial and final position of the length of travel.

III. Experimental Procedures

Preliminary CT-Scanner Tests

CT-Scanner Warm-up Time

The purpose of this experiment was to check the warm-up time of the CT-Scanner. Eleven consecutive scans were performed on the same water phantom. Data from these images were analyzed by a computer program to give the CT number and the standard deviation.

The results obtained are shown in Table 1. The CT number is shown in column 2 and their standard deviation in column 3. Figure 6 shows a graph of image scan number versus deviation of the pixels in each scan. The graph shows slight scattering of the deviation from 0.0042 to about 0.0052. Figure 7 shows a graph of image scan number versus (CT number - average CT number). Here the average CT number is 1.006084. From the figure, as the image number increases, the abscissa variable increases. This indicated some kind of drift of data measurement in the CT-Scanner. Hence, further experimentation was done on the same water phantom.

TABLE 1

CT Image Analysis

Scan No.	CT Number	Deviation of Pixels
1	1.001030	0.004679
2	1.001743	0.004708
3	1.003576	0.004883
4	1.005022	0.004339
5	1.005833	0.005198
6	1.006404	0.004843
7	1.007592	0.004939
8	1.008488	0.004753
9	1.008832	0.004650
10	1.009173	0.004511
11	1.009233	0.005203

This time, the water phantoms were scanned repeatedly 35 times, and analyzed in a similar way as the previous experiment. The results are presented in Figures 8 and 9. Figure 8, which is similar to Figure 7, shows that the initial 11 scans had an effect similar to the one observed in the previous study. Also, as the number of scans increases, the abscissa variable reaches an approximately constant value. From this study, it was concluded that a certain amount of time was necessary for the CT-Scanner to warm up, so that the CT numbers reach a constant value for a particular object scanned.

Based on this figure and knowledge of the scan times, it is suggested that the CT-Scanner operator wait for at least an hour and a half after starting the machine to get good results for CT numbers.

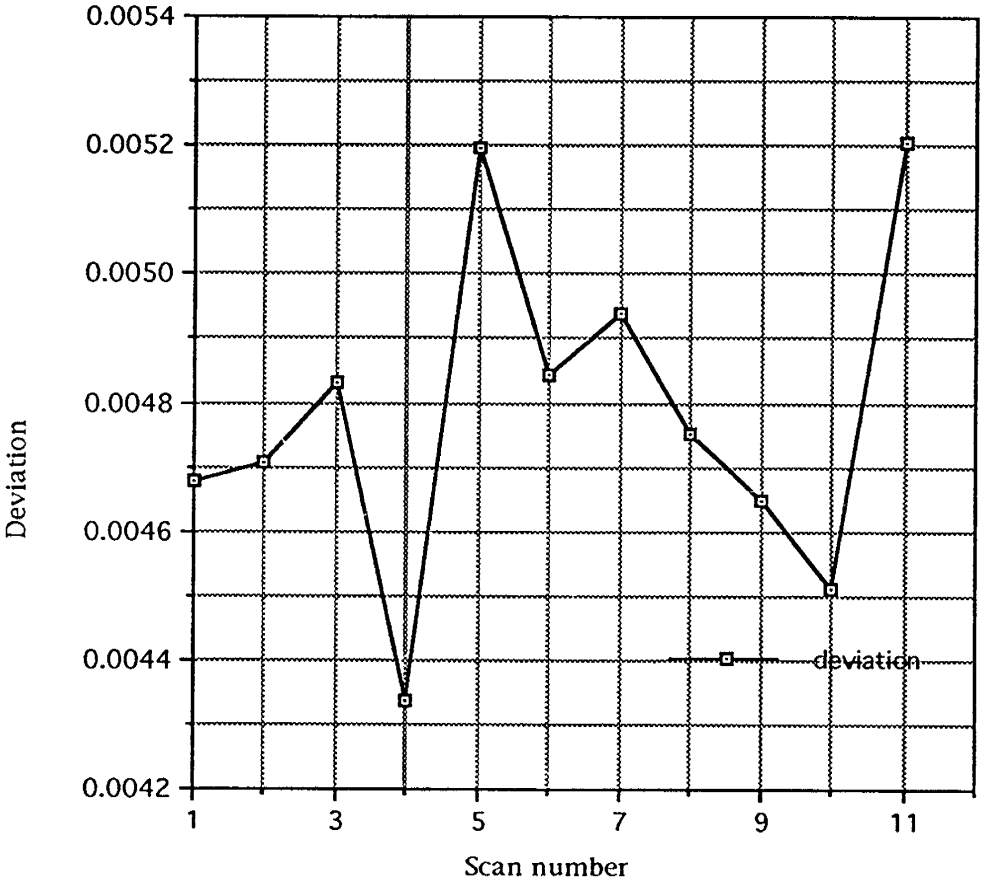

Figure 6. Scan number versus deviation.

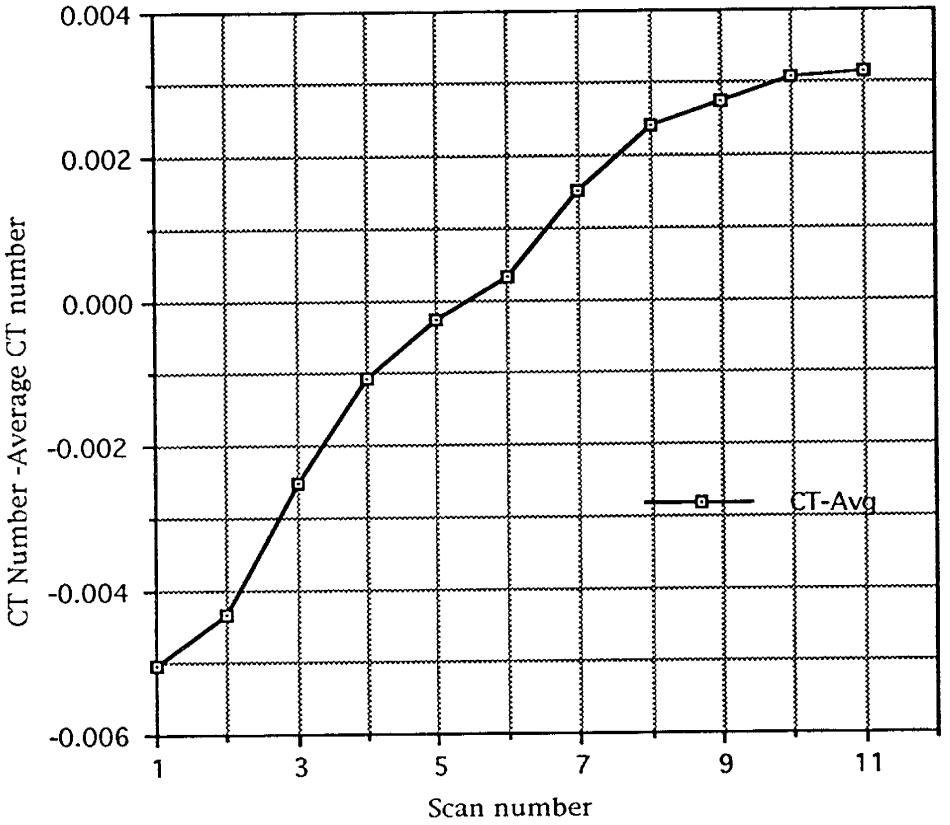

FIgure 7. Scan number versus (CT number - average CT number)

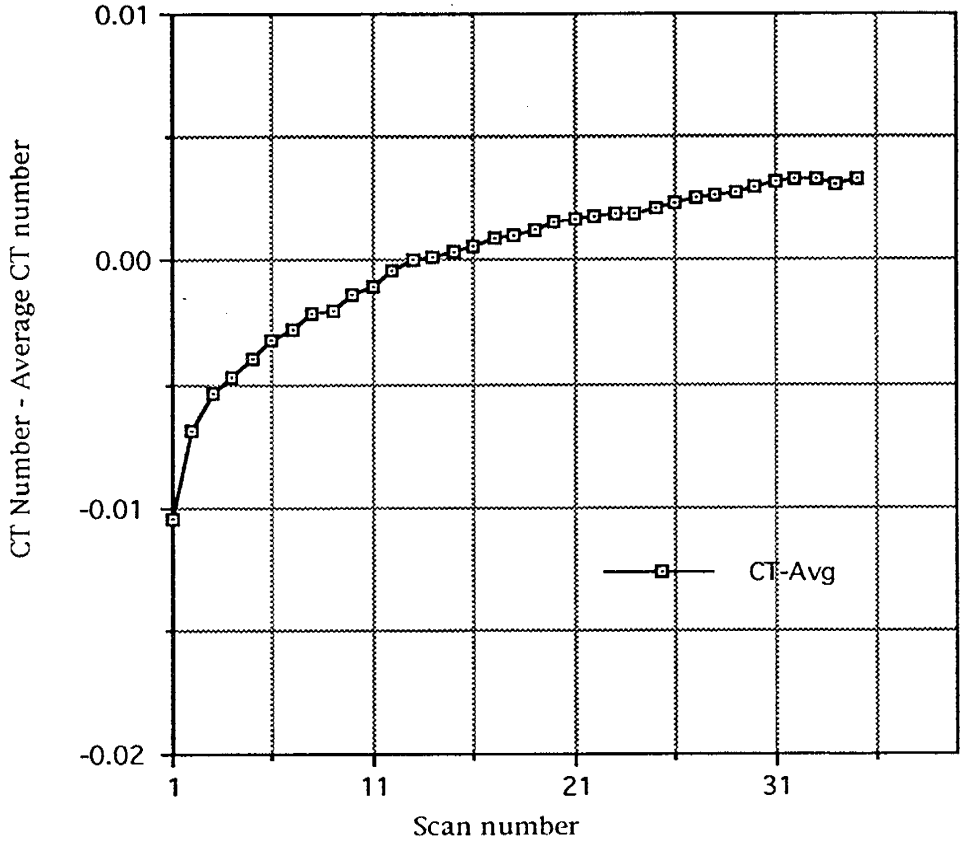

FIgure 8. Scan number versus (CT number - average CT number)

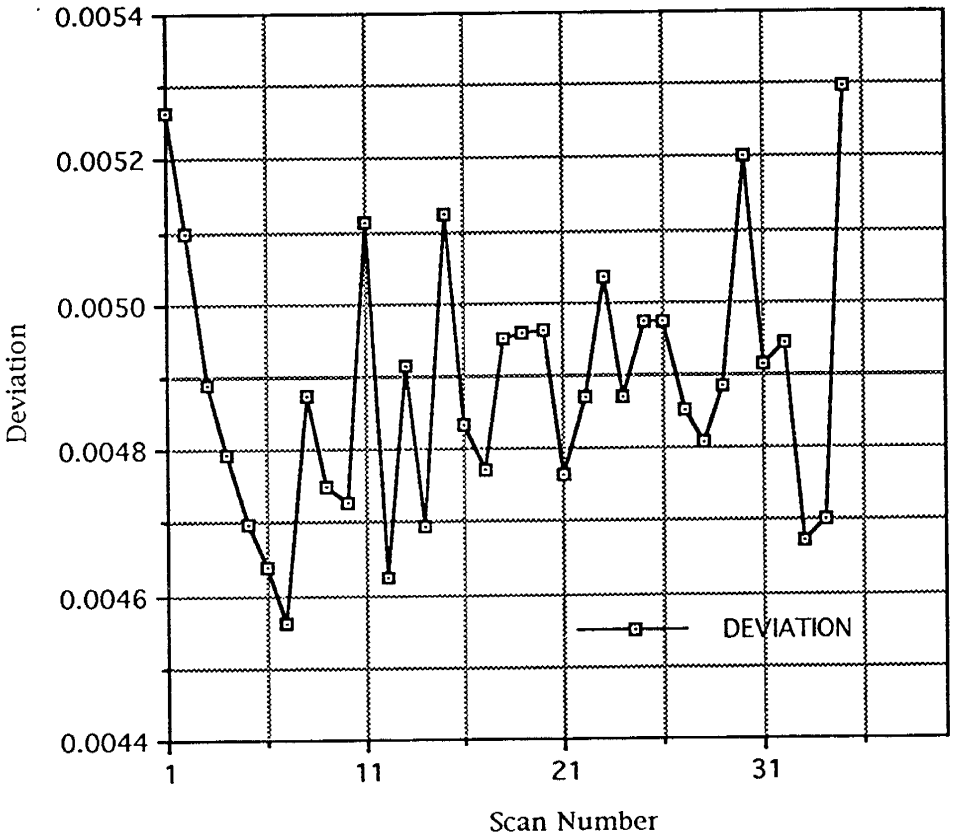

Figure 9. Scan number versus deviation.

X-ray Beam Location

An experiment was done to determine where to position an object on the CT-Scanner table with respect to the patient light. (The patient light is used to position objects in the CT-Scanner tube so that objects can be scanned properly). An aluminium rod was positioned exactly in the center of the CT-Scanner tube. The diameter of the rod was 10 mm and it was 3 feet long. The rod was filed so that the cross section end was perfectly flat and that there were no aberrations on the end of the rod. Scanning was done using a program built into the computer which automatically incremented the distance of the rod after every scan by about 0.30 mm.

The results of the experiment are shown in Figure 10. The X-axis shows the distance along the table in mm. and the Y-axis shows the CT number of the object scanned. Initially since there was no object in the image, the CT number was -1000, which is the CT number of air. The CT number gradually increased to a constant value of 2333, which is the CT number of the aluminium rod. We concluded that the object to be scanned should be kept about 5 mm away from the light source.

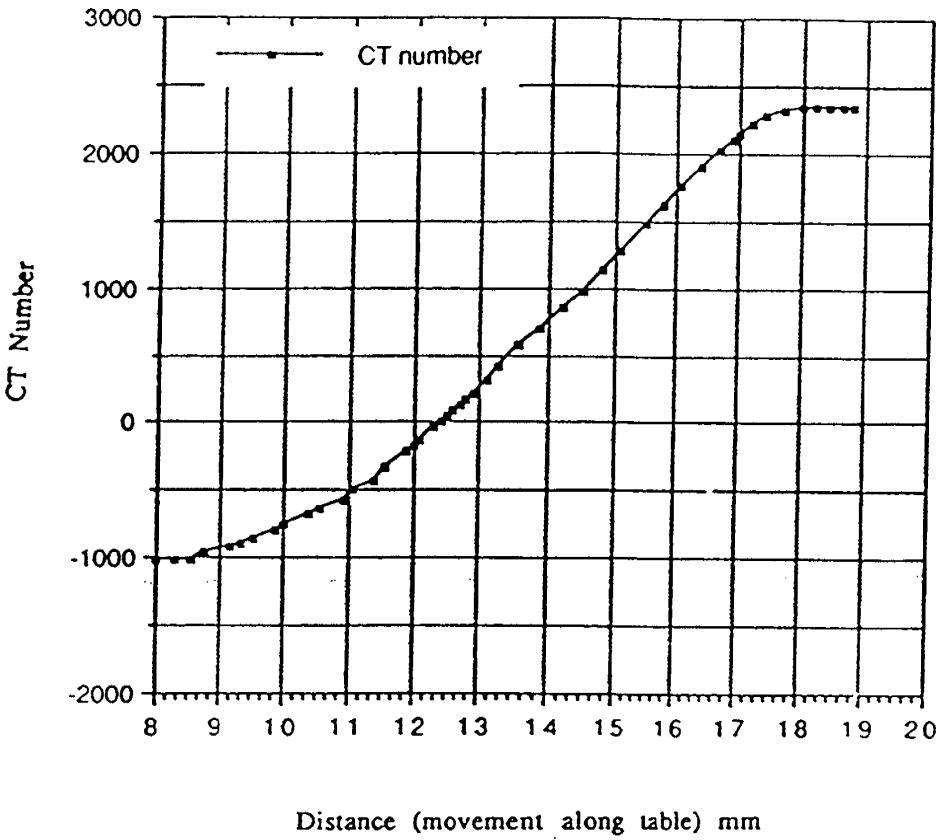

Figure 10. CT number versus distance along table.

Calibration Check for the CT-Scanner

The purpose of this experiment was to check the calibration of the CT-Scanner by verifying the CT numbers of NaI solutions. Here, two similar experiments were carried out using the same NaI solution. For the first experiment the machine was operated at 121.25-121.27 kV and at 121.26-121.35 kV for the second experiment. Both the experiments were conducted at 25 mA. Beam hardening corrections were made with quartz for the first experiment and with water for the second experiment. For the first experiment, the CT number was obtained by using 148-339 pixels, whereas for the second experiment 148 pixels were taken and was kept constant throughout the experiment. The results are shown in Figure 11.

Figure 11 shows the NaI concentration expressed in molar concentration units plotted against CT numbers. This figure is a comparison of two similar experiments, with a time difference of a day between them. The linear relationship obtained for the CT numbers with NaI concentration was compared to the CT numbers in the Withjack[15] paper and good agreement, although not exact, was found. This verified that the calibration of the machine was in agreement with the published data.

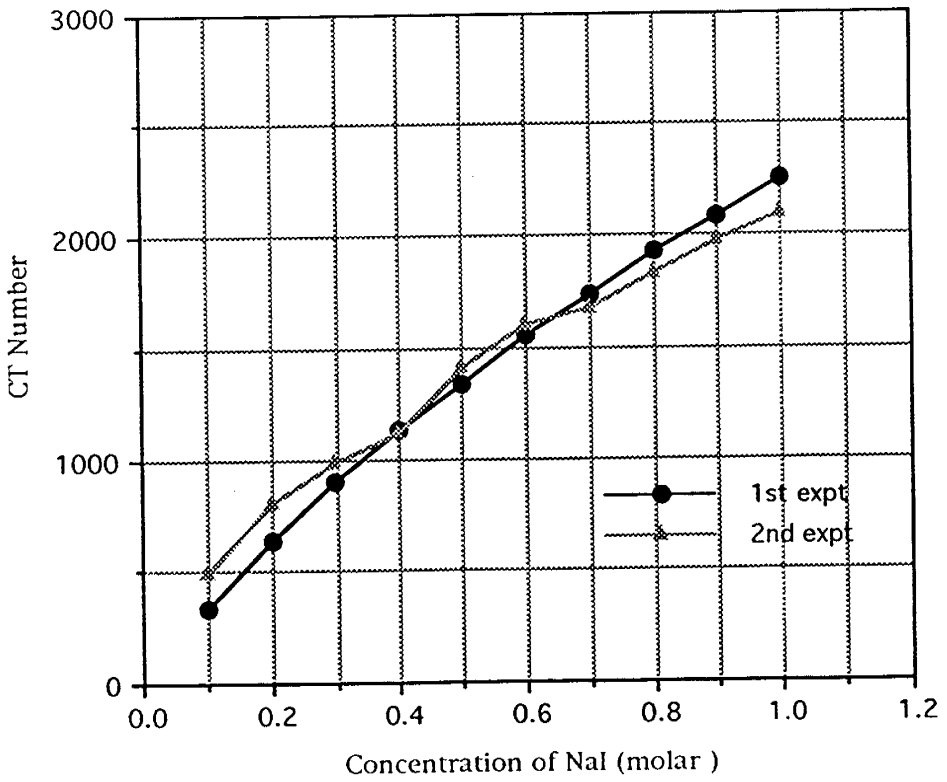

Figure 11. CT number versus concentration of NaI.

Image Analysis

The data from the CT-Scanner computer was stored on magnetic tapes and loaded onto a SPARCstation II, desktop computer work station. This computer manufactured by Sun Microsystems, Inc. is equipped with the SunOS, release 4.1.1 operating system. For analyzing the data, CATPIX ImageTool software was used.

The CATPIX ImageTool software, which was mainly used for this research, is a package developed by Shell Development Company, Bellaire Research Center, Houston. This software package is a scientific research software tool for color image processing and graphics of petrophysical and fluid flow phenomena in cores. It is now marketed by Universal Medicals, Cleveland, OHIO.

In image reconstruction, 2-D cross-sectional images (scans) taken perpendicular to the axis of the core by the CT-Scanner can be reconstructed by the CATPIX ImageTool Software package into axial vertical and horizontal reconstructions along the axis of the core. The reconstruction process is shown in Figure 12.

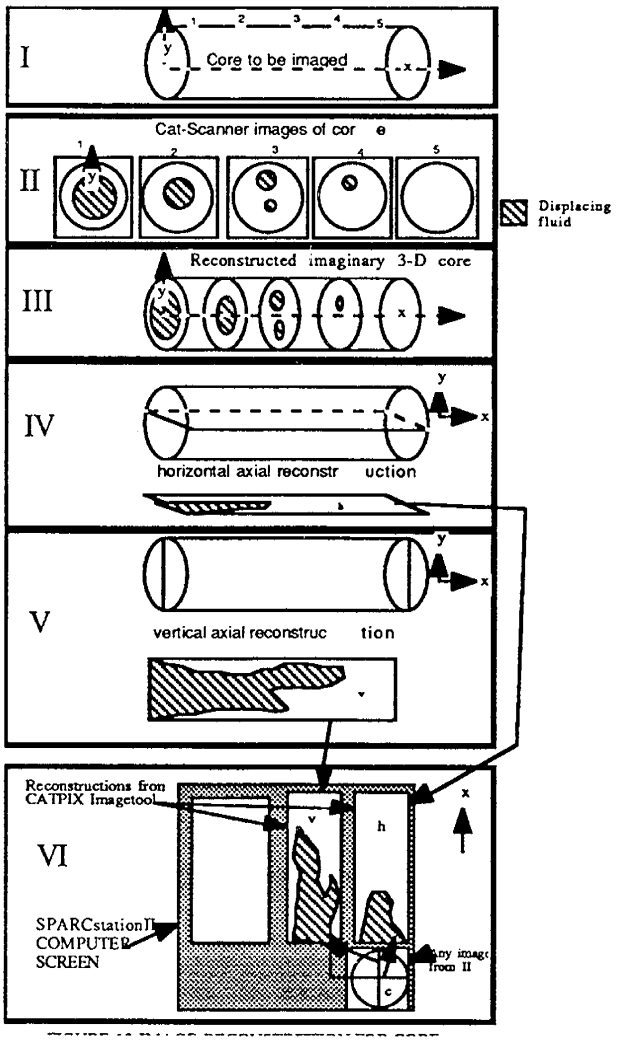

Figure 12. Image reconstruction for core.

In all the experiments, the core is placed horizontally in the CT-Scanner tube. The core has a displacing fluid injected into it, shown by hatched lines. The objective is to see the fluid displacement mechanism in the core on the computer screen.

First the core is scanned at arbitrary cross-sections, 1, 2, 3, 4 and 5, perpendicular to the core (see Figure 12- I). These five images (Figure 12-II) are stored on magnetic tape and loaded onto the SPARCstation Computer.

The computer generates an imaginary 3-D image using the five 2-D cross-sectional images from part II. Two axial reconstructions are cut along the core; one is a vertical section and the other is a horizontal section. The vertical and horizontal reconstructions can be carried out for any vertical or horizontal plane. For the sake of illustration, Figure 12 arbitrarily shows vertical and horizontal reconstructions at center locations (part IV and V).

Finally, the computer displays the reconstructions on the Sun workstation screen (shown in cross-hatched background in part VI). The three main parts on the screen are shown as v, h and c; v is the vertical reconstruction, h is the horizontal reconstruction and c is a circular cross-sectional image from part II.

A horizontal and vertical line appear on the circular image, c. These lines correspond to the exact position as to where the reconstructions are obtained along the core. This will be discussed more later.

Experimental Flow System

System Design

The schematic of the entire flow setup with the CT-Scanner is shown in Figure 13 (elevation and plan views). The porous media (core) is connected to pressure gauges and pumps as shown in Figure 13a. End caps were fitted to either end of the porous media. Each endcap had two inlets/outlets. This was done so that if any of the inlet or outlet in use during the experiment failed, the other could be used. The outlet/inlets were connected to 2 way stainless steel valves. The tubing for the entire flow system consisted of an 1/8th inch plastic tubing. A three way stainless steel Swagelok valve was connected at the outlet end of the pump. A pressure gauge was installed at the inlet end of the core and the outlet end of the core was connected to the fraction collector. The fraction collector was used in Experiments 2-4.

End Cap Design

The core was wrapped with an epoxy and fibre glass cloth. To each end were fitted specially designed end caps (See Figure 14). These end caps were made of clear plexiglass and their design is shown in Figure 14. Groves 1/8th inch wide and deep were cut concentrically as well as radially to ensure uniform distribution of the fluids on the core face. The groves were at a 20 degree angle from one another. Uniform distribution of the fluids along the core is the most important aspect in the design of the end caps. This design plays a crucial role in the fluid flow phenomenon.[26] The inlets and outlets of the endcaps had NPT taps into which male connectors were fitted. Figure 15 is the end cap design used for the Experiments 2 and 3. Here the end caps were made an inch thicker so that the wrapping could cover a greater portion of the end caps providing a firm bond between the core and the end piece.

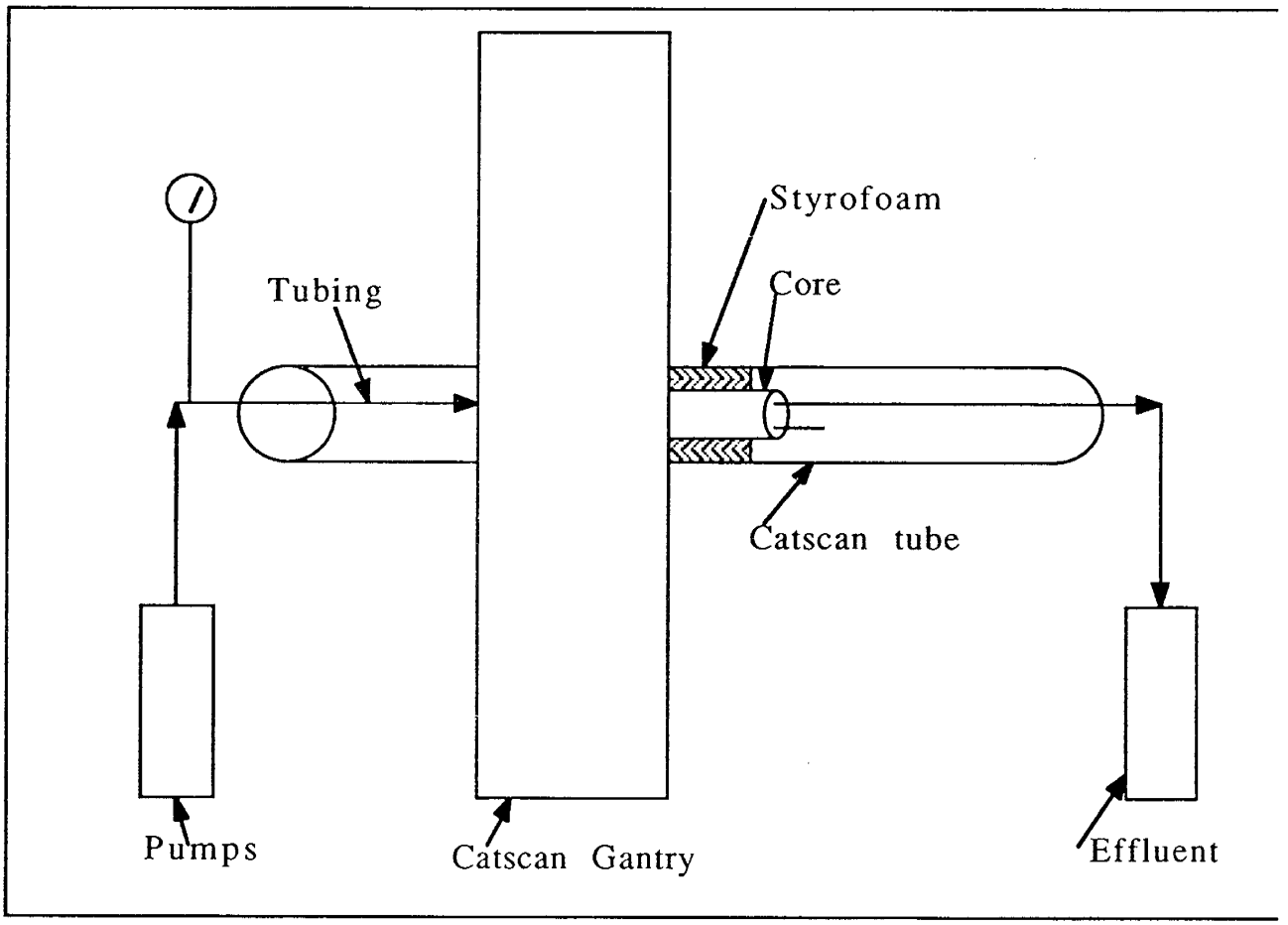

Figure 13a. Experimental setup (elevation view).

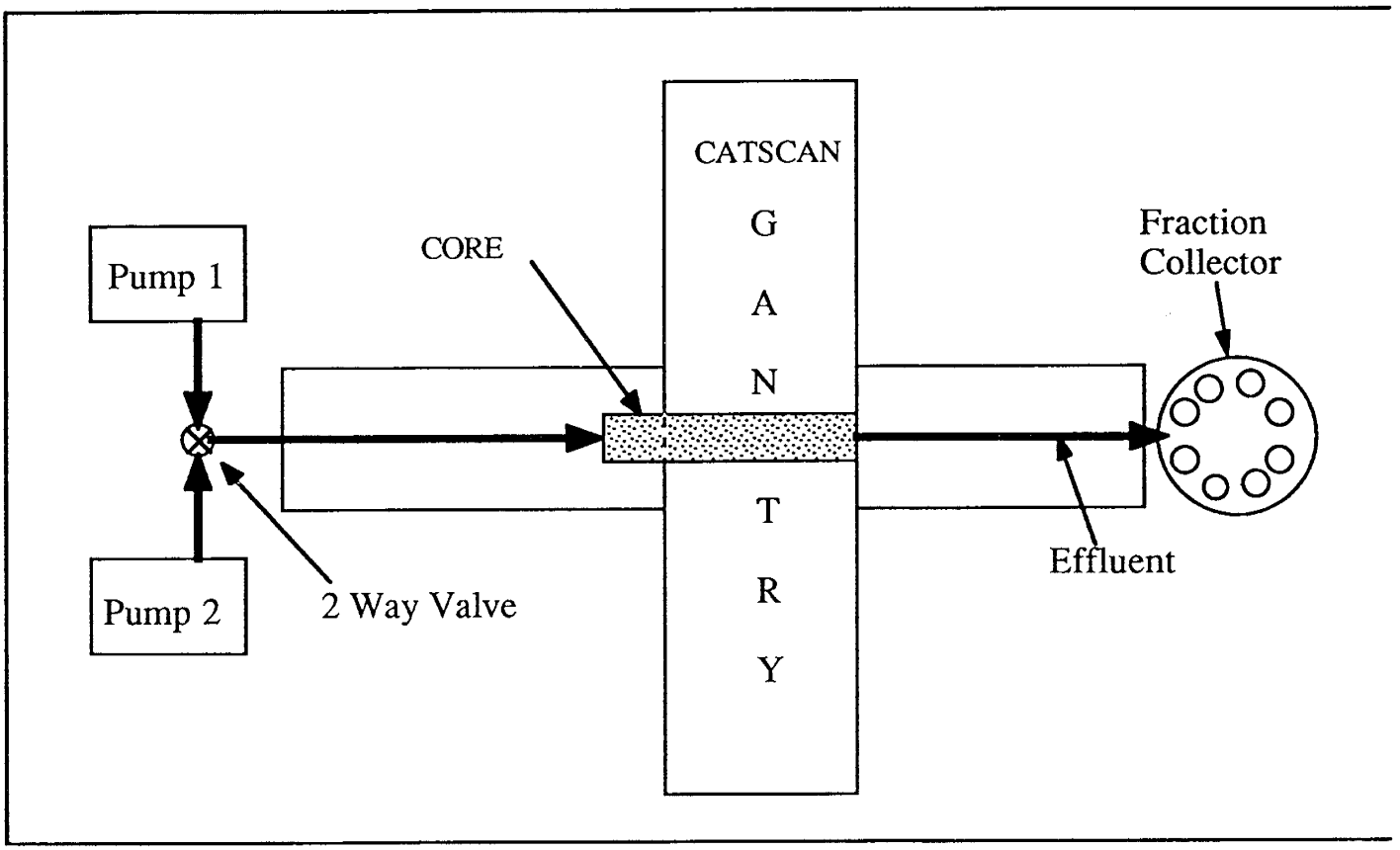

Figure 13b. Experimental setup (plane view)

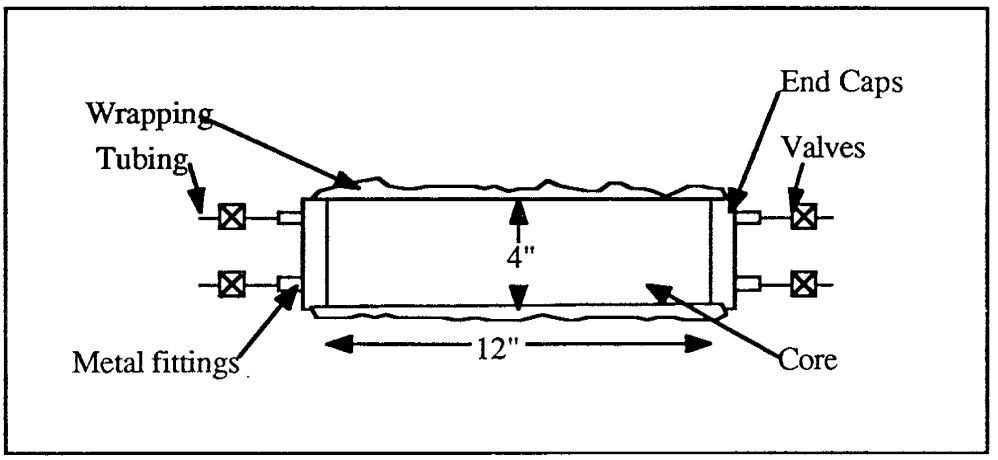

Figure 14a. Core holder design

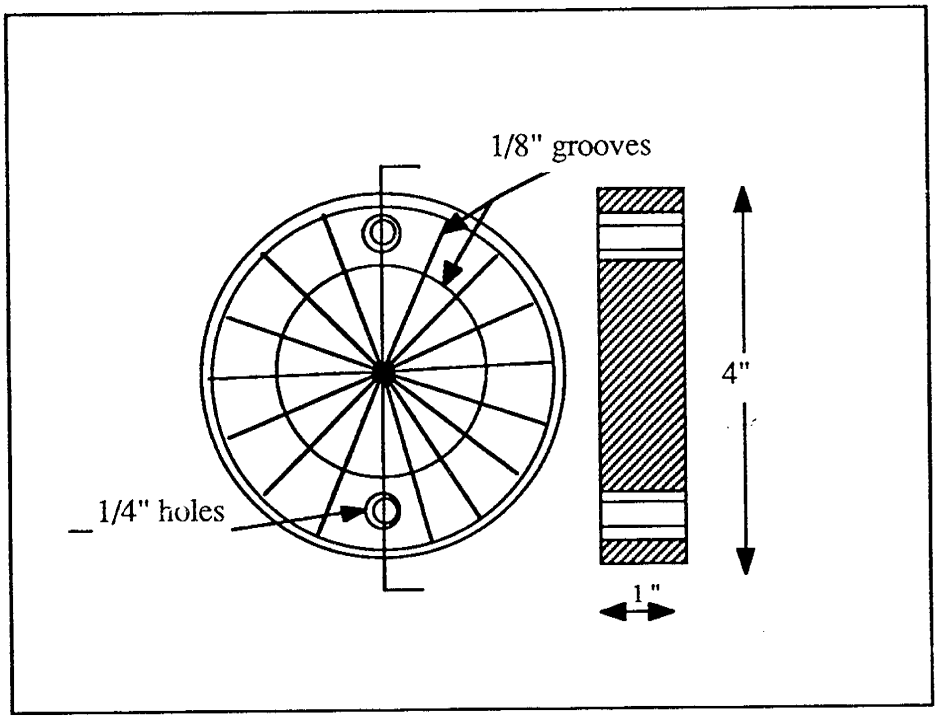

Figure 14b. End cap design (view 1)

Core Preparation

The core was epoxied to the end caps with an epoxy resin coating and fibre glass cloth. The procedure to wrap the core was as follows. First epoxy was applied in a thin film on to the core and it was allowed to dry. Cellophane tape was put over the space between the face of the core and the end cap to prevent the epoxy from seeping through the gap between the end cap and the face of the core.

The next wrapping was epoxy along with fibre glass cloth. The fibre glass cloth used for the core in Experiment 1 was cut into strips, dipped into the epoxy and wrapped around the core. The core could not be wrapped uniformly with the technique of cutting the fibre glass cloth. This was because the threads of the cut fibre glass cloth would stick out on drying. The core finally had 2 wrappings of fibre glass cloth and epoxy. It was then tested for leaks by immersing it in water and pressurizing it with air to 500 psi.

The core in Experiments 2 and 3 were epoxied with a continuous 2" roll of fibre glass cloth instead of strips. This gave a much more uniform wrapping along the core. Additionally, the second wrapping was started on the other end of the core, so that a good criss-cross wrapping could be obtained making the wrapping stronger.

Scanning Procedure

The core is fitted inside the 7" diameter CT-Scanner tube, which is specially designed for petrophysical and porous media fluid flow studies. This tube is made of plexiglass which has sections cut out, so that cores/core holders and other experimental equipment can be fixed conveniently inside the tube. The core is fitted snug inside the CT-Scanner tube by surrounding the core with Styrofoam packing material. See Figure 13a.

The core is then scanned perpendicular to the axis by moving the table (on which the CT-Scanner tube is fixed) every inch. First, a dry scan measurement is carried out. Then, the core is evacuated using a vacuum pump and then an aqueous fluid is sucked into the core. The injected volume of an aqueous fluid yields the observed pore volume. The core is then scanned again at exactly the same places where it was scanned before. This is the wet scan measurement.

The displacing fluid is then pumped into the core with a Micrometrics 760 HPLC positive displacement pump. The pumping is then stopped after a certain pore volume of fluid is injected into the core. The core is scanned at exactly the same locations on the core where the previous scanning was done. After the scanning is over, pumping is resumed and the scanning and pumping procedure repeated alternately until one to two pore volumes are pumped into the core. In all the experiments, the densities of the fluids are matched to avoid gravity segregation of the displacing fluid. Also, red food coloring was added to the displacing fluid so that the exact location of the fluid could be seen in the transparent tubing.

Reference samples of quartz and water are scanned before and after the experiment to see if there is any change in the CT numbers.

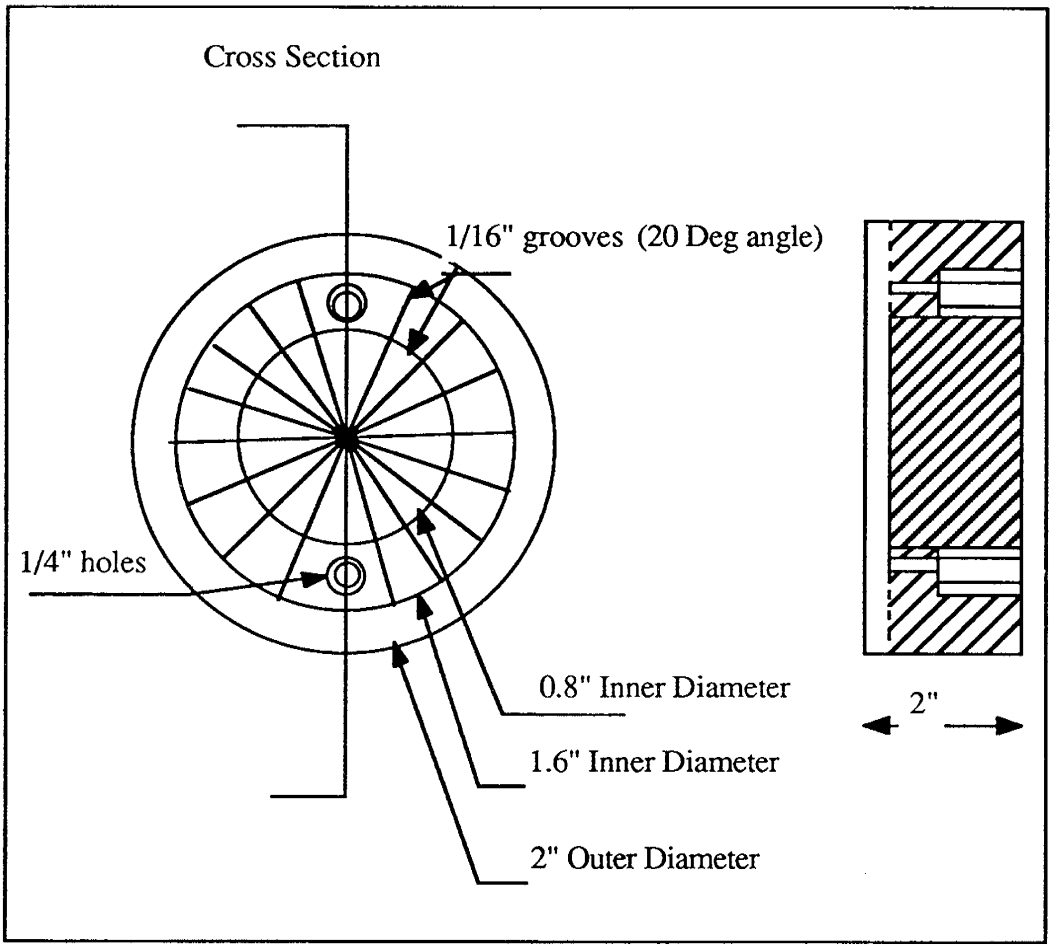

Figure 15. End cap design (view 2).

Core Cleaning Procedure

Methyl alcohol, nitrogen and air are used to clean the core. About five pore volumes of methanol are pumped at a very slow flow rate (about 1cc/min) into the core. Nitrogen is later injected into the core after the methyl alcohol flood for about 12 hours. Air is finally pumped into the core for about two days until there is no odor of methanol.

Effluent Collection

The fraction collector used in Experiments 2-4 is set at an appropriate time to collect a certain amount of the effluent repetitively. The effluent is collected in glass vials of 20 ml capacity. These vials are then scanned by the CT-Scanner to obtain the CT number of the effluent. The details of the fraction collector are given below.

Manufacturer:	Eldex Laboratories, Inc.
Electrical:	1/8 A @ 120 V, 50/60 Hz
Fuses:	1/8 A slo-blow @ 120 V
Dimensions:	(w x d x h) 10.25" x 16" x 11"
Fractions:	200 maximum.
Volume per fraction:	75 ml maximum
Operating Temperature:	4 degree C to 35 degree C.
Rack Used:	50, 20 ml scintillation vials.
Model:	UFC
Accessories:	Drop counter

IV. Experimental Results

The experimental work is effectively summarized by presenting the results of four experiments. A complete discussion of all the experiments can be found in D'Souza's thesis.[27]

Experiment 1

In the first test (Experiment 2, D'Souza thesis[27]) we displaced a 40 cp fluid with a 1 cp fluid in a four inch diameter by 1 foot long Berea sandstone core. The displaced fluid was an aqueous solution of NaCl containing glycerol. The glycerol was added to increase the fluid viscosity. The displacing fluid was an aqueous solution of NaI containing KCl. NaI acts as an X-ray absorbing agent and KCl was added to increase the displacing fluid density to equal that of the displaced fluid. Table 2 summarizes the details of the test. The mobility ratio M is the ratio of displaced and displacing fluid viscosities and in this case M=40.

The core was scanned intermittently as the displacement proceeded. The core was scanned perpendicular to the direction of bulk flow and at one inch increments, starting at a 0.5 inches inside the inlet end and ending at 0.5 inches inside the outlet end. Thus, we recorded twelve distinct images at various times. These twelve images were then reconstructed to yield the cross-sectional images parallel to the direction of flow. Figure 16 shows image reconstructions at 40% of a pore volume injected (PVI). Figure 16 is a composite of four separate figures. The Cartesian plot on the left side of Figure 16 is secondary and it shows the average CT number plotted as a function of the core length. The flow direction is from bottom to top. Since we displaced a fluid with a high CT number (2425 CT units) by a fluid with a low CT number (180 CT units), the CT plot shows a low CT number near the core entrance and a high CT number near the outlet.

TABLE 2

Details of Experiment 1

Core Details:	
Porosity:	19%
Permeability:	190 md
Rock Type:	Berea sandstone
Length:	12 inches
Diameter:	4 inches
Core geometry:	cylindrical
Fluid Details:	
Displaced Fluid:	NaCl
Concentration:	2% wt solution NaCl
Density:	1.1285
Viscosity:	1 cp
CT Number:	180
Displacing Fluid:	NaI and KCl
Concentration:	1 Molar
Density:	1.1305
Viscosity:	40 cp
CT Number:	2425 CT Units
Displacement Details:	
Scanning Interval:	12 scans every 1" spacing
Pumping Interval:	Stop every 0.1 pv.
Flow Rate:	5 cc/min
Pore Volume (Actual):	469.27 cc
Pore Volume (Observed):	440 cc
Mobility Ratio:	40
Catscan Details	
Voltage:	120.57 kV
Current:	25 mA
Water Ct Number:	-18 CT Units
Quartz CT Number:	1645 CT Units
Scan Circle:	5.08"

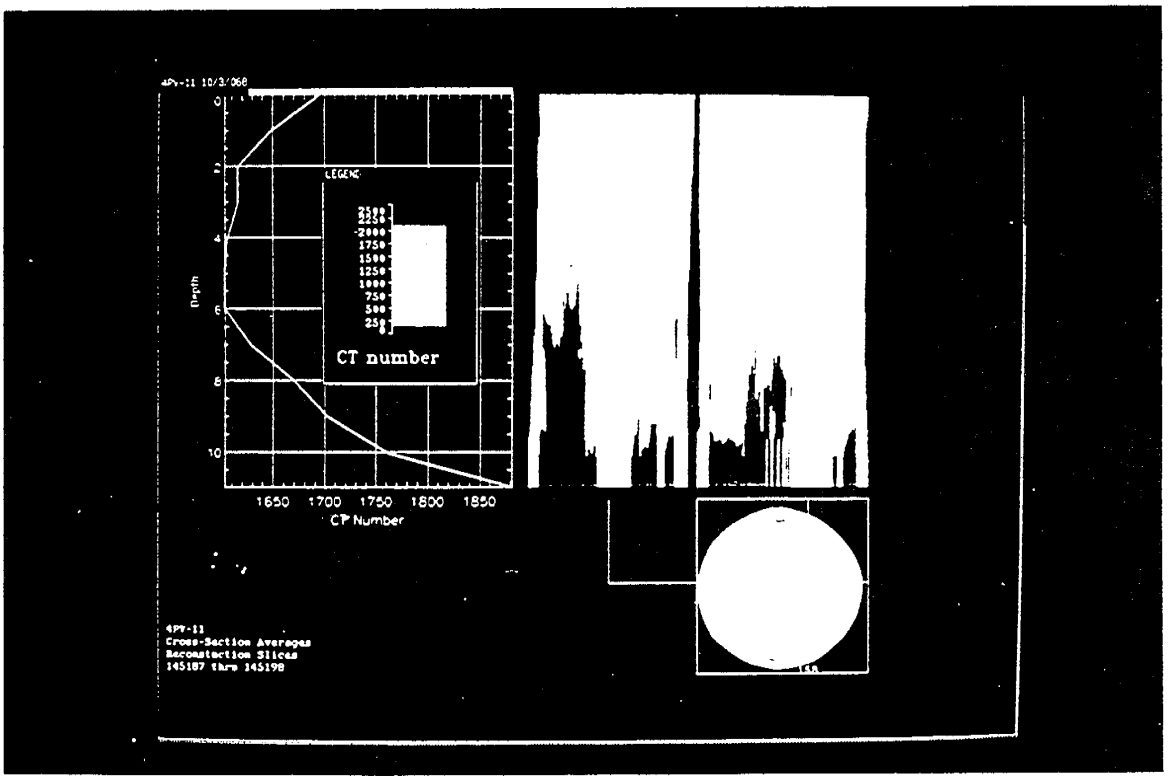

Figure 16. Image results at 40% PVI for four inch diameter by 1 foot long Berea core (M=40) (Experiment 1).

The circular image near the bottom right of Figure 16 shows the CT image of the core scanned perpendicular to flow at 0.5 inches inside the outlet end. The light color denotes the displaced fluid and the dark color denotes the displacing fluid. The actual color photograph from which this black-and-white figure was reproduced showed a gradation of colors. However, little is lost by showing only the black-and-white images. The color images are reported elsewhere.[1] As is evidenced by Figure 16, the core contains predominantly displaced fluid at 0.5 inches from the outlet of the core after 40% PVI.

The two remaining figures in Figure 16 represent image reconstructions. The image on the left side is a vertical planar image reconstruction and the image of the right side is a horizontal planar image reconstruction. The actual planar location of the vertical and horizontal reconstructions is denoted by the vertical and horizontal lines on the circular image. In this case the horizontal reconstruction is very nearly at the center of the core; the vertical reconstruction is slightly to the right side of the core. The left side of the vertical reconstruction reflects the top of the core whereas the right side reflects the bottom of the core. The left side of the horizontal reconstruction denotes the left side of the core and the right side of the reconstruction denotes the right side of the core. Both of these reconstructions show considerable viscous fingering as evidenced by the non-uniform fluid distribution. The vertical reconstruction shows a large fingering protruding along the top of the core and very little injected fluid moving along the bottom of the core. The horizontal reconstruction shows a majority of the injected fluid moving along the left side of the core.

The image processing software permits us to view any vertical or horizontal plane in the direction of flow we choose. The reconstructions in Figure 16 were arbitrarily selected and were representative of all those we examined.

Figures 17 and 18 show image reconstructions at 80% PVI. The circular image in Fig. 17 is at 2.5 inches inside the outlet end of the core. The circular image in Fig. 18 is at 3.5 inches inside the outlet end of the core. The vertical reconstructions in Figs. 17 and 18 are both very nearly along the center of the core and they show similar fluid distributions. The horizontal reconstruction in Fig. 17 is along the bottom of the core whereas the horizontal reconstruction in Fig. 18 is along the top of the core. Both show considerable fingering, with perhaps more fingering along the bottom of the core.

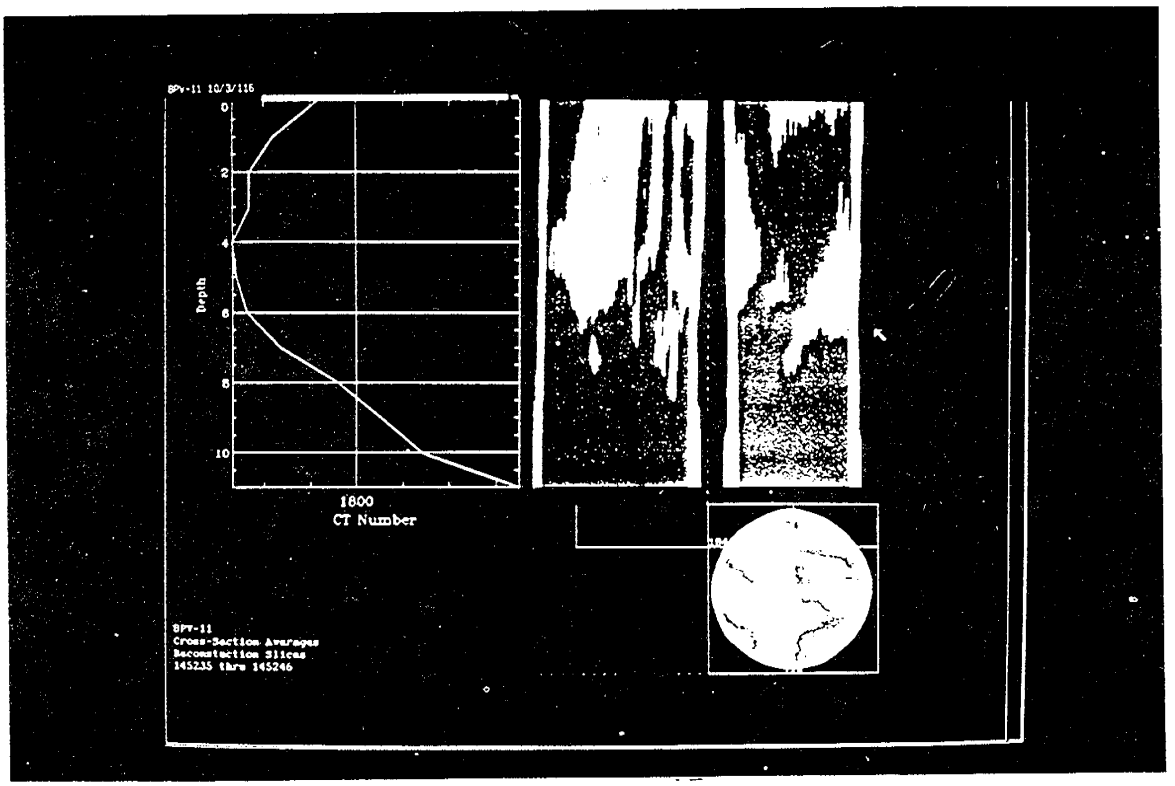

Figure 17. Image results at 80% PVI for four inch diameter by 1 foot long Berea core (M=40) (Experiment 1).

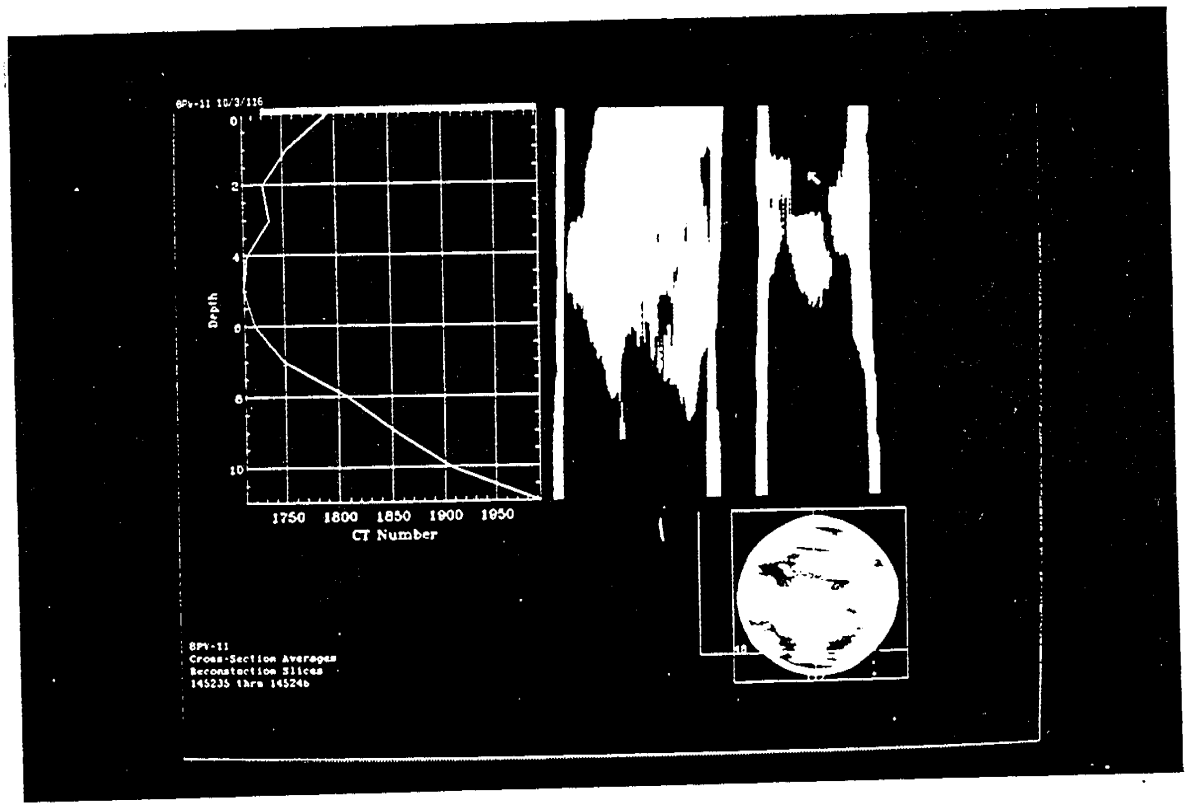

Figure 18. Image results at 80% PVI for four inch diameter by 1 foot long Berea core (M=40) (Experiment 1).

Experiment 2

In the second test (Experiment 3, D'Souza thesis[27]) we carried out a unit mobility ratio (M=1) test in a two inch diameter by 3 foot long Berea sandstone core. The details of the test are shown in Table 3. Figure 19 shows two pairs of image reconstructions at 30% PVI. The direction of flow is from top to bottom. Black represents the injected fluid and white represents the resident fluid. Each reconstruction pairs consists of a vertical reconstruction of the left and a horizontal reconstruction of the right. The left side of the vertical reconstruction denotes the bottom of the core and the right side denotes the top. Overall, these reconstructions reveal fairly uniform displacement efficiency with only minor bypassing. However, as the vertical reconstructions depict, there is a slight amount of fingering near the top and middle of the core. The circular image represents a scan at 0.5 inches inside of the inlet end and contains essentially 100% injected fluid.

TABLE 3

Details of Experiment 2

Core Details:	
Porosity:	19%
Permeability:	200 md
Rock Type:	Berea sandstone
Length:	36 inches
Diameter:	2 inches
Core geometry:	cylindrical
Fluid Details:	
Displaced Fluid:	NaCl and Glycerol
Concentration:	2% wt solution
Density:	1.1285
Viscosity:	1 cp
CT Number:	80 CT units
Displacing Fluid:	NaI
Concentration:	1 Molar
Density:	1.1305
Viscosity:	1 cp
CT Number:	2495 CT Units
Displacement Details:	
Scanning Interval:	12 scans every 1" spacing
Pumping Interval:	Stop every 0.1 pv.
Effluent Collection:	20 cc
Flow Rate:	05 cc/min
Pore Volume (Actual):	351.95 cc
Pore Volume (Observed):	340 cc
Mobility Ratio:	1
Catscan Details	
Voltage:	120.52 kV
Current:	25 mA
Water Ct Number:	-2 CT Units
Quartz CT Number:	1753 CT Units
Scan Circle:	5.08"

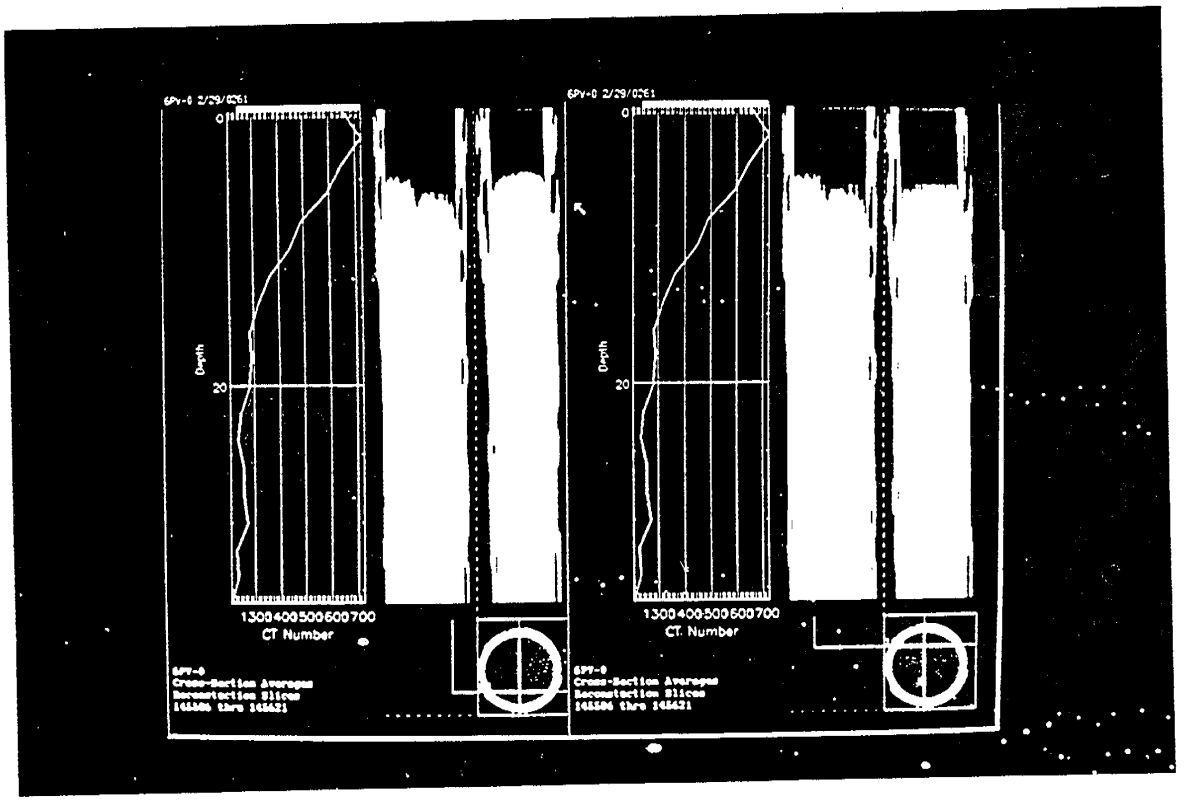

Figure 19. Image results at 30% PVI for two inch diameter by 3 foot long Berea core (M=1) (Experiment 2).

In this test we added a sample collector and measured the CT number of the eluted fluid. From this data we computed the normalized concentration history of the injected fluid. The eluted fluid concentration is normalized by its injected concentration. The CT number history for this test is shown in Fig. 20 and the corresponding normalized concentration history is shown in Fig. 21. The results in Figs. 20 and 21 were surprising in that we expected much smoother curves with a later initial breakthrough time. These results are more representative of adverse mobility ratio displacement (M>1) or a heterogeneous porous media instead of a unit mobility displacement in a presumably homogeneous system. These results suggest that we either have a heterogeneous Berea core sample or our experimental technique is in error. Or perhaps there is some gravity segregation though we have attempted to mitigate the density difference between fluids. We are presently investigating the accuracy of our experimental technique.

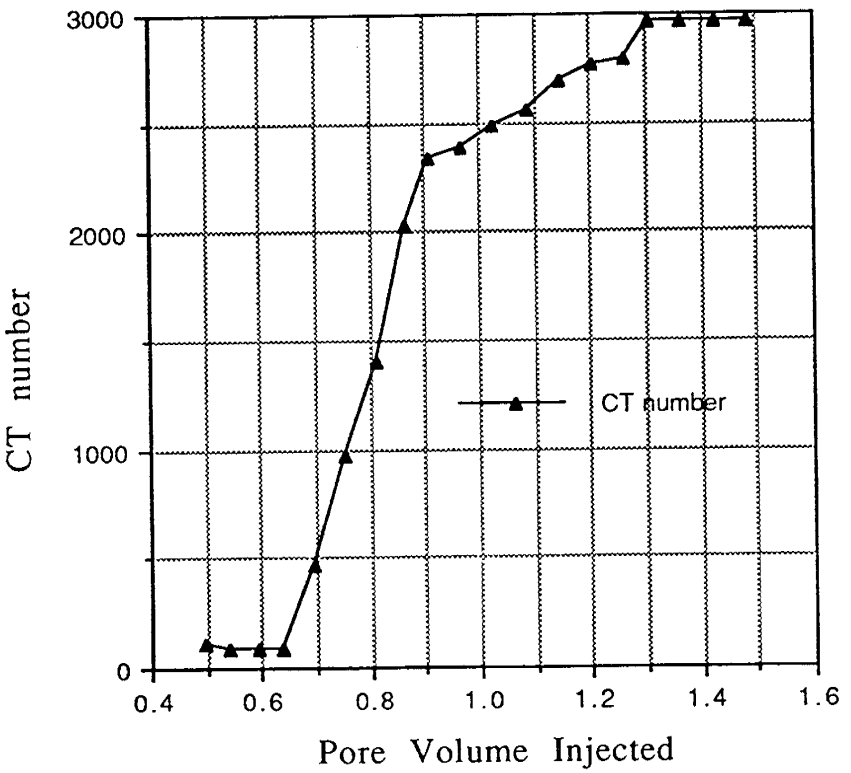

Figure 20. Effluent CT number versus PVI for Experiment 2.

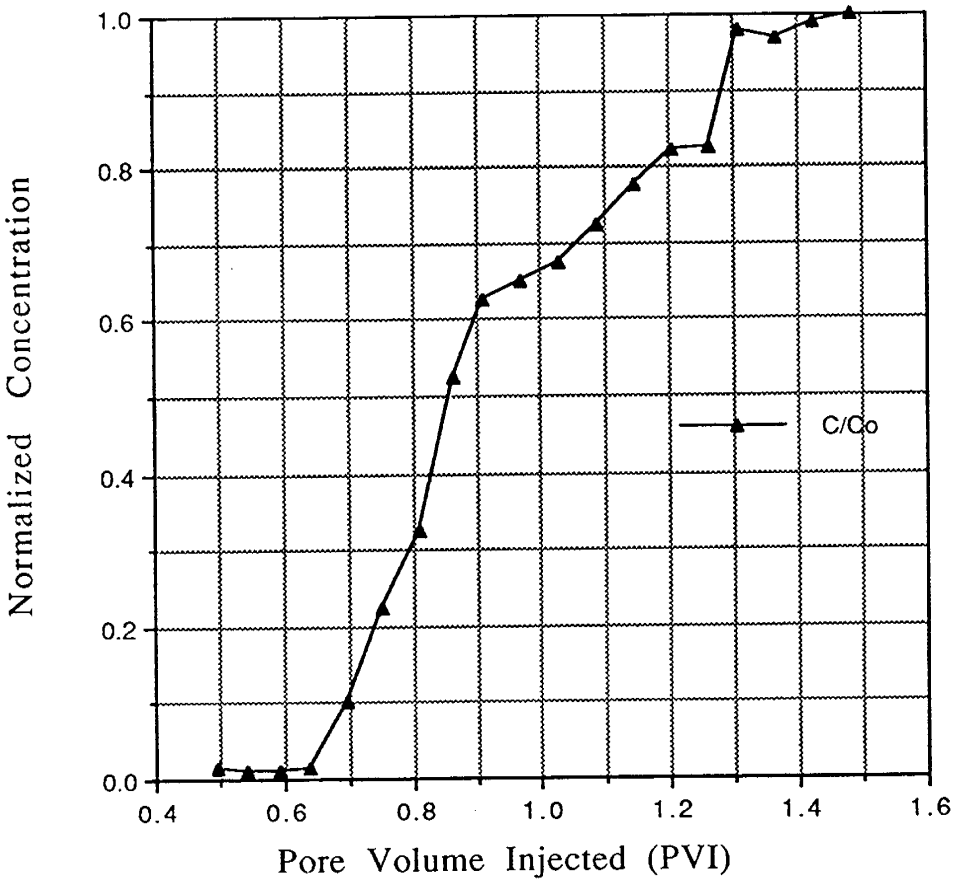

Figure 21. Effluent concentration versus PVI for Experiment 2.

Experiment 3

In the third test (Experiment 4, D'Souza thesis[27]) we carried out a unit mobility ratio (M=1) test in a two inch diameter by 1 foot long Berea sandstone core. The details of the test are shown in Table 4. Figure 22 shows two pairs of image reconstructions at 40% PVI. The direction of flow is from bottom to top. Black represents the injected fluid and white represents the resident fluid. The left side of the vertical reconstruction denotes the bottom of the core and the right side denotes the top. The horizontal reconstructions show fairly uniform displacement efficiency. The vertical reconstructions, however, show some fingering with greater advance along the top of the core than the bottom. Figs. 23 and 24 show the CT number and normalized concentration histories. As in the previous experiment, these figures were more representative of a adverse mobility ratio or gravity segregation test or a heterogeneous core. We are presently investigating and trying to confirm the cause of this result.

TABLE 4

Details of Experiment 3

Core Details:	
Porosity:	19%
Permeability:	200 md
Rock Type:	Berea sandstone
Length:	12 inches
Diameter:	2 inches
Core geometry:	cylindrical
Fluid Details:	
Displaced Fluid:	NaCl and Glycerol
Concentration:	2% wt solution
Density:	1.1505
Viscosity:	1 cp
CT Number:	120 CT units
Displacing Fluid:	NaI
Concentration:	1 Molar
Density:	1.140
Viscosity:	1 cp
CT Number:	3192 CT Units
Displacement Details:	
Scanning Interval:	12 scans @ 1" spacing
Pumping Interval:	Stop every 0.1 pv.
Effluent Collection:	5 cc
Flow Rate:	3 cc/min
Pore Volume (Actual):	117.31 cc
Pore Volume (Observed):	110 cc
Mobility Ratio:	1
Catscan Details	
Voltage:	120.5205 kV
Current:	25 mA
Water Ct Number:	-3 CT Units
Quartz CT Number:	1741 CT Units
Scan Circle:	5.08"

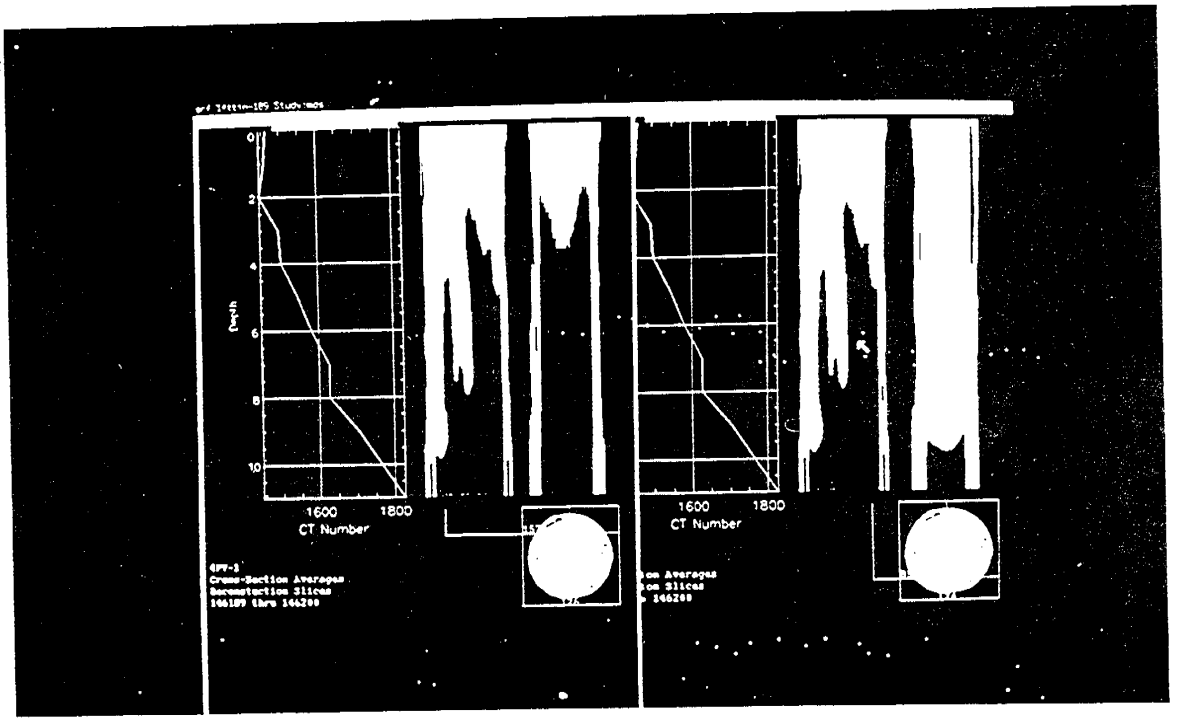

Figure 22. Image results at 40% PVI for two inch diameter by 1 foot long Berea core (M=1) (Experiment 3).

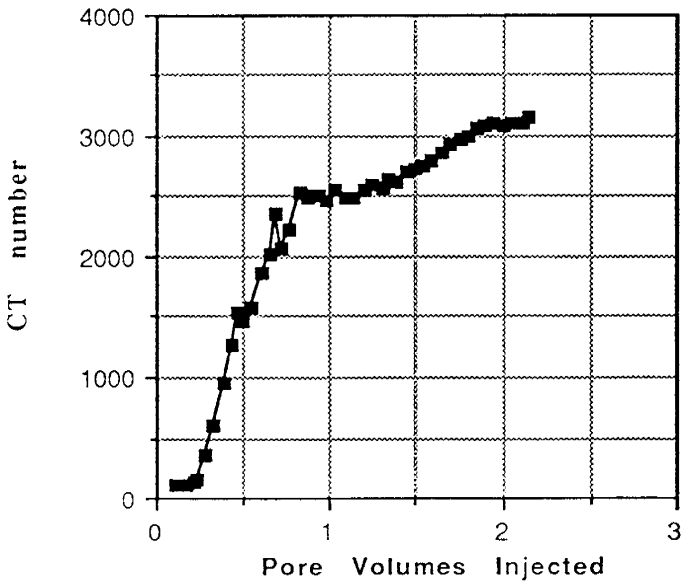

Figure 23. Effluent CT number versus PVI (Experiment 3).

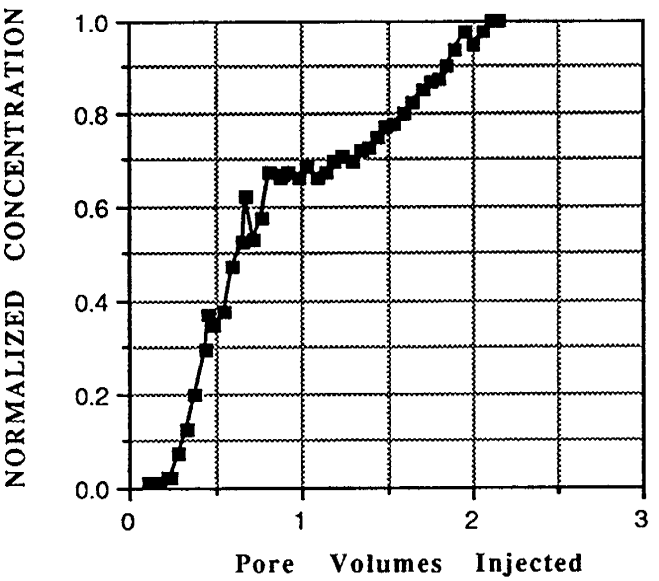

Figure 24. Effluent concentration versus PVI (Experiment 3).

Experiment 4

In the fourth and final test reported here (Experiment 5, D'Souza thesis[27]) we carried out a unit mobility ratio (M=1) test in a two inch diameter by six inch long bead pack. The details of the test are shown in Table 5. Figure 25 shows four pairs of image reconstructions at 25% PVI. The direction of flow is from bottom to top. Black represents the injected fluid and white represents the resident fluid. The left side of the vertical reconstruction denotes the bottom of the core and the right side denotes the top. The top two horizontal reconstructions show fairly uniform displacement efficiency. The top two vertical reconstructions show non-uniform fluid distribution with more fluid moving in the middle and top of the core than along the bottom of the core. The bottom two horizontal reconstructions show injected fluid only moving along the middle of the core. We are uncertain of the mechanism of the non-uniform flow but recognize it is representative of gravity segregation or fingering. Figs. 26 and 27 show the eluted CT number and normalized concentration histories. They agree with the image reconstructions and reveal less than ideal displacement efficiency.

TABLE 5

Details of Experiment 4

Core Details:	
Porosity:	26%
Permeability:	10 Darcies
Rock Type:	1mm glass beads
Core geometry:	cylindrical
Length:	12 inches
Diameter:	2 inches
Fluid Details:	
Displaced Fluid:	NaI
Concentration:	1 Molar solution
Density:	1.065 g/ml
Viscosity:	1 cp
CT Number:	2827 CT units
Displacing Fluid:	NaCl and Glycerol
Concentration:	2% wt solution
Density:	1.066
Viscosity:	1 cp
CT Number:	90 CT Units
Displacement Details:	
Scanning Interval:	6 scans @ 1" spacing
Pumping Interval:	Stop every 0.25 pv.
Effluent sample volume:	5 cc
Flow Rate:	1 cc/min
Pore Volume (Actual):	110 cc
Pore Volume (Observed):	112 cc
Mobility Ratio:	1
Catscan Details	
Voltage:	120.02 KV
Current:	25 mA
Water Ct Number:	-1 Ct Units
Quartz CT Number:	1713 CT Units
Scan Circle:	5.08"

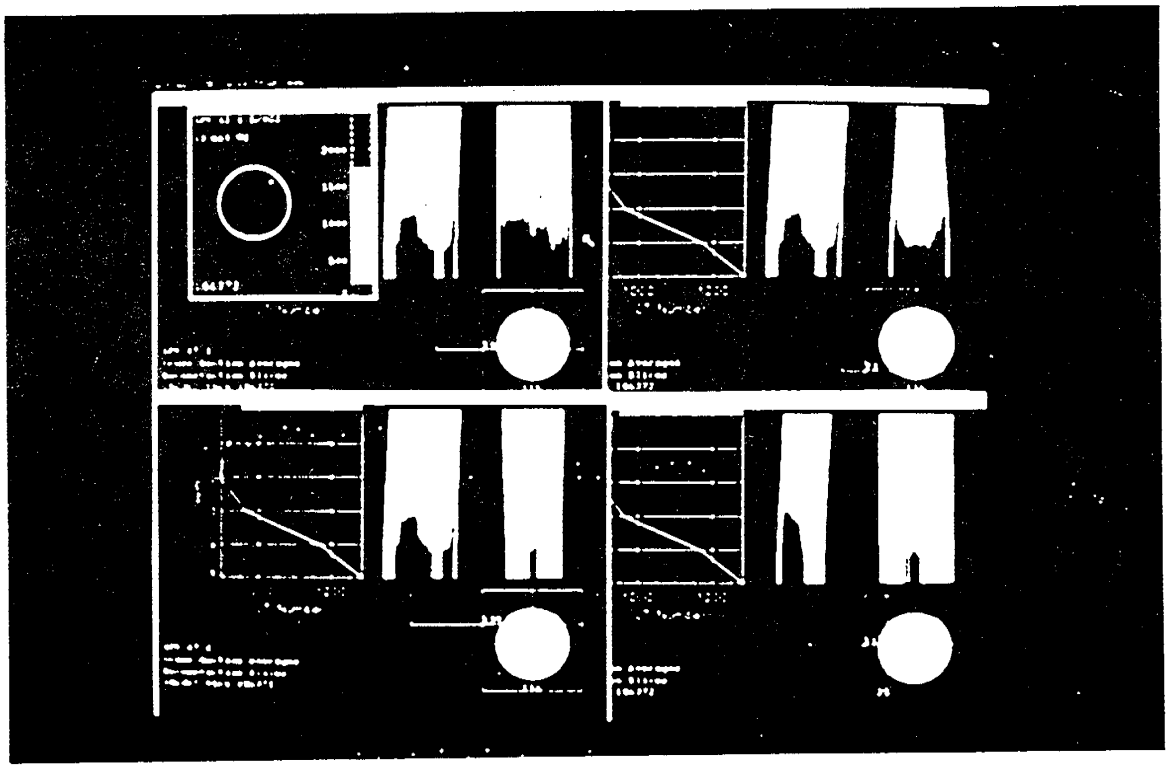

Figure 25. Image results at 25% PVI for beadpack (M=1) (Experiment 4).

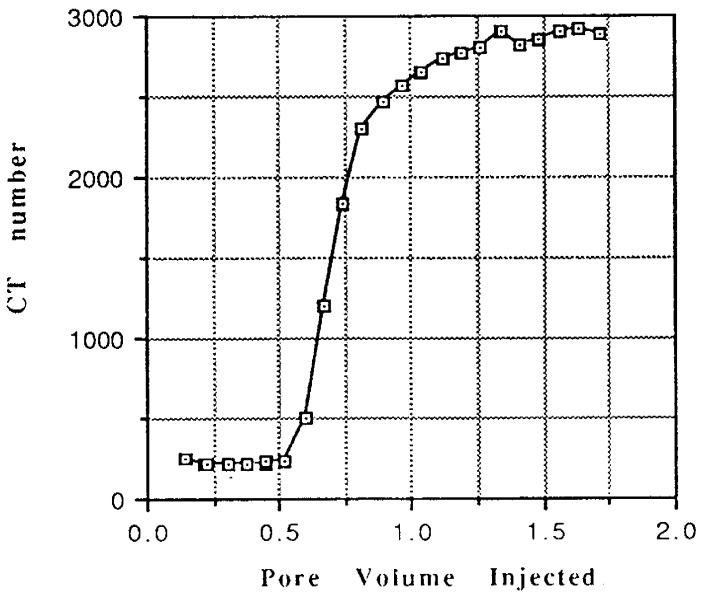

Figure 26. Effluent CT number versus PVI (Experiment 4).

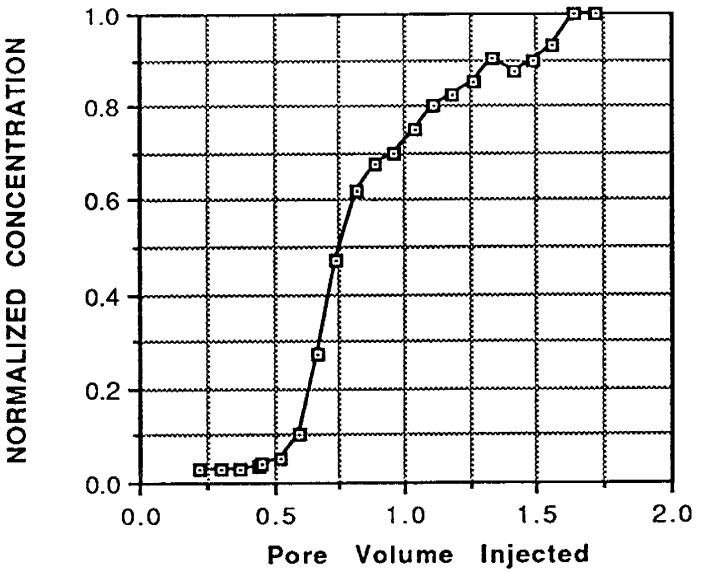

Figure 27. Effluent concentration versus PVI for Experiment 4.

V. Numerical Results

The purpose of the mathematical modeling work is to develop an effective model to simulate miscible displacement and viscous fingering. The modeling work is helpful to guide and explain the experimental work. Numerical simulation of viscous fingering using a finite-difference model is difficult in that it is computationally intensive. The extreme computational requirements stem from the need to use a very fine grid and many grid points.

Kenji Seto has carried out the mathematical modeling work and he started by using a finite-difference, miscible displacement model procured from one of Dr. Slattery's past students. Chang and Slattery[28] originally developed their computer model to simulate the miscible displacement of one fluid by another in a 3-D porous matrix. Their simulations proved successful in modeling the different physical phenomena that occur in miscible displacements. Seto started by first adapting the model for use on Texas A&M's Cray-YMP computer. Then he tested it for speed and efficiency. He found that the model exhibited poor execution times, even on a supercomputer.

Consequently Seto's initial focus was to increase execution speed and efficiency of the reservoir simulator. To determine the computationally intensive areas of the program, the simulator was analyzed by CPU accounting software resident on the Cray-YMP computer. We decided that the pressure/velocity field calculation was the most likely to benefit from a numerical method revision. The original calculation was performed using a ADI-SOR method as outlined by Peaceman and Rachford.[29] This method, being highly iterative in nature, not only gave rise to questions of its efficiency, but also accuracy.

To reconcile the accuracy question, we began by programming a "direct" solution of the pressure/velocity field. This entailed explicitly solving a large system of linear equations. The size of our problem and the limited memory capacity available on most computers prohibited the use of traditional linear equation solvers. An out-of-core linear equation solver residing in the Boeing Computer Services Library Software was employed. This software, though too slow to permit its regular use, did allow us to check the accuracy of the ADI-SOR code and the other indirect solver considered.

From our runs of the "direct solution" software, it became obvious that an iterative solver would provide the best chance of increasing the efficiency of our simulator. The Conjugate Gradient (CG) method is commonly employed to iteratively solve large linear systems. The software package, CgCodes, produced under the joint supervision of the University of Chicago at Urbana-Champaign and Los Alamos National Laboratories, was selected to perform this calculation. It has the benefit of providing very efficient routines, ease of use, and different preconditioning options. The iterative nature of the CG method makes its efficiency directly dependent upon the type of preconditioning methods used with it.

In conclusion, we have attained reasonable success with the use of diagonal scaling in conjunction with the Chebyshev adaptive polynomial preconditioning algorithm that was supplied with CgCodes. We are exploring more extensive preconditioning methods. The use of the "direct" solution software has proved invaluable by confirming the accuracy of the iterative solution and providing estimations of the error tolerances for both the ADI-SOR and CG algorithms.

Seto's work also included testing his finite-difference model and comparing results to the results of analytical solutions. His tests included the results to three specific problems: (1) the 1-D analytical solution to the convection-dispersion equation, (2) the analytical solution to the 2-D problem of a miscible fluid displacing a fluid whose viscosity is half of the displacing fluid in a two-layered system having a 3:1 permeability contrast and no crossflow, i.e., the Dykstra-Parsons Problem, and (3) the analytical solution to the 2-D problem of a miscible fluid displacing a fluid whose viscosity is half of the displacing fluid in a two-layered system having a 3:1 permeability contrast and subject to vertical equilibrium or maximum crossflow, i.e., the Hearn Problem.

The study of these problems have lead to some interesting results and some notable improvements in the the model. Prior to this study, Seto had been using a variation of the flux-corrected transport (FCT) algorithm in his model. This variation, reported by Zalesak,[30] uses the FCT method to compute the concentrations at the grid interfaces, rather than at the grid centers. To implement this scheme, the grid interface values of concentration are interpolated to produce the concentrations at the grid centers. This computational approach yielded concentration oscillations (errors) that appeared in the Dykstra-Parsons test case.

Based on a further study of this problem, it appeared that the error is caused by the interpolation formulas recommended by Zalesak. As a result, we re-derived the FCT formulas for the case of grid-centered geometry. This eliminated the need for interpolation formulas. This modification yielded a reduction in computer time requirements by an order of magnitude for the 1-D problem while yielding the equivalent error. It also yielded improvements in the accuracy of the Dykstra-Parsons problem and yielded good results for the Hearn problem.

Much of Seto's efforts have been spent adapting and upgrading his model. Due to expiration of the project and the fact that Seto did not join the project until the second year, he has not been able to apply his model to the simulation of some of our experiments. One of our recommendations for future work is to carry out numerical simulations of our experiments.

VI. Summary and Conclusions

Based on the work carried out here, we submit the following summary and conclusions:

1. The CT Scanner is indeed a useful instrument to study flow in porous media.

2. We have successfully developed effective experimental procedures to use the CT Scanner to study flow in porous media. These experimental procedures include: (1) designing a core containment device, (2) designing a flow system, (3) developing viable CT scanner operating procedures, (4) developing data transfer procedures from the CT scanner to post-processors, and (5) developing post-processing software for image reconstruction.

3. We have successfully demonstrated the utility of the CT scanner by studying stable and unstable, equal-density, miscible displacements. The unstable displacements exhibited viscous fingering, as expected. The viscous fingers are displayed as two-dimensional, cross-sectional images. The images are reconstructed using state-of-the-art image reconstruction software. Our viscous fingering results will be useful in future viscous fingering studies.

VII. Recommendations

Based on the work performed here, we submit the following recommendations:

1. Appropriate dopant concentrations must be used to obtain meaningful CT images.

2. We recommend improving the core holder design, perhaps using a special Temco Hassler sleeve made of fiberglass or aluminum.

3. We recommend using a newer generation CT scanner which has shorter scan times. The CT scan time is important because the scan time determines the time that the flow experiment must be stopped for scanning. In some cases, forty-five minute flow stoppages were required. If the flow stoppage is too long, the chemical species may migrate appreciable distances due to diffusion. Our flow tests assume migration due to diffusion during flow stoppage is negligible. In general this may not be true.

4. We recommend additional studies investigating the cause of the irregular concentration elution histories. We suspect either the method to measure the concentration was in error or excessive core heterogeneities was responsible of this irregularity; however, these speculations must be confirmed.

5. In general, we recommend additional work to develop and upgrade the CT scanner facilities for studies of flow in porous media studies. For example, we recommend adding a suitable printer to the image processing system. This study used screen photographs which exhibited poor image resolution.

6. We recommend future work to include mathematical modeling of some of our experiments.

7. We recommend future work to carry out additional displacement tests in different core lengths and diameters to formulate and verify the appropriate dimensionless groups to describe the various flow regimes (stable, moderately unstable, excessively unstable, etc.).

VIII. References

1. Hounsfield, G.N., "Computerized Transverse Axial Scanning (Tomography): Part 1. Description of System," *British Journal of Radiology*, **46**, 1016-1022 (Dec. 1976).
2. Gordon, R., Herman, G.T., and Johnson, S.A., "Imaging Reconstruction from Projections," *American Science* , 56-68 (Oct. 1975)
3. Brooks, R.A., and DiChiro, G., "Theory of Reconstruction in Computed Tomography," *Radiology* ,**117**, 561-572 (Dec. 1975).
4. McCullough, E.C., and Payne, J.T., "X-ray Transmission Computed Tomography," *Medical Physics*, 4(2), 85-98 (Mar./Apr. 1977).
5. Morgan, C.L., *Basic Principles of Computed Tomography*, University Park Press, Baltimore (1983).
6. McCullough, E.C., "Photon Attenuation in Computed Tomography," *Medical Physics*, 2(6), 307-320 (1975).
7. Brooks, R.A., and DiChiro, G., "Split-Detector Computed Tomography: A Preliminary Report," *Radiology* ,**126**, 255-257 (Jan. 1978).
8. McCullough, E.C., Baker, H.L., Houser, O.W., and Reese, D.F., "An Evaluation of the Quantitative and Radiation Features of a Scanning X-Ray Transverse Axial Tomograph: The EMI Scanner," *Radiology*, **111**, 709-715 (June, 1974).
9. Hunt, P.K., Engler, P.and Bajsarowicz, C., "Computed Tomography as a Core Analysis Tool: Applications and Artifact Reduction Techniques," SPE paper 16952, presented at the 1987 SPE Annual Technical Conference and Exhibition, Dallas, TX, September 27-30 (1987).
10. Gado, M. and Phelps, M., "The Peripheral Zone of Increased Density in Cranial Computed Tomography," *Radiology* **117**, 71-74 (Oct. 1975).
11. McCollough, E.C., Payne, J.T., Baker, H.L., Hattery, R.R., Sheedy, P.F., Stephens, D.H., and Dedgauus, E., "Performance Evaluation and Quality Assurance of Computed Tomography Scanners, with Illustrations from the EMI. ACTA and Delta Scanners," *Radiology* **120**, 173-188 (July 1976).
12. Wellington, S.L., and Vinegar, H.J., "X-ray Computerized Tomography," *J. Pet. Tech.*, 885-898 (August 1987).
13. Wellington, S.L., and Vinegar, H.J., "CT studies of Surfactant Induced CO_2 Mobility Control," paper SPE 14393 presented 1985 SPE Annual Technical Conference and Exhibition, Las Vegas, Nevada, September 23-25 (1985).
14. Vinegar, H.J., "X-ray CT and NMR Imaging of Rocks, "*J. Pet. Tech.*, 257-259 (March 1986).

15. Withjack, E.M., "Computed Tomography for Rock Property Determination and Fluid Flow Visualization," paper SPE 16951 presented at the 1987 SPE Annual Technical Conference and Exhibition, Dallas, Texas, September 27-30 (1987).
16. *Operator's Manual, Delta Scan 100 Series Brain Scanner*, Manual Number 961036: Technicare Corporation, Deltascan Division, Ohio (February 1980).
17. Slobod, R.L., and Caudle, B.H., "X-ray Shadowgraph Studies of Areal Sweepout Efficiencies," *Trans., AIME* , **195**, 265-70 (1952) .
18. Wang, S.Y., Ayral, S., and Gryte, C.C., "Computer Assisted Tomography for the Observation of Oil Displacement in Porous Media," *Soc. Pet. Eng. J.* , 53-55 (Feb. 1984).
19. Hove, A.O., Ringer, J.K., and Read, P.A., "Visualization of Laboratory Corefloods With the Aid of Computerized Tomography of X-rays," *SPEFE* , 148-154 (May 1987).
20. Bergosh, J.L., Marks, T.R., and Mitkus, A.F., "New Core Analysis Techniques for Naturally Fractured Reservoirs," paper SPE 13653 presented at the 1985 SPE Regional Meeting, Bakersfield, California, March 27-29 (1985).
21. Honarpour, M.M., Cromwell, V., Hatton, D., and Stachwell, R., "Reservoir Rock Descriptions Using Computed Tomography (CT)," paper SPE 14272 presented at the 1985 SPE Annual Technical Conference and Exhibition, Las Vegas, Nevada, September 22-25 (1985).
22. Honarpour, M.M., McGee, K.R., Crocker, M.E. Maerefat, N.L., and Sharma, B., "Detailed Core Description of a Dolomite Sample From the Upper Madison Limestone Group," paper SPE 15174 presented at the 1986 SPE Rocky Mountain Regional Meeting, Billings, Montana, May 19-21.
23. Withjack, E.M., Graham, S.K., and Yang, C.T., "CT Determination of Heterogeneities and Miscible Displacement Characteristics," *SPEFE* , 447-452 (Dec. 1991).
24. Chatzis, I., Kantzas A., and Dullien, F.A.L., "On the Investigation of Gravity-Assisted Inert Gas Injection Using Micromodels, Long Berea Sandstone Cores, and Computer-Assisted Tomography," paper SPE 18284 presented at the 1988 SPE Annual Technical Conference and Exhibition, Houston, Texas, October 2-5.
25. Kantzas, A., "Investigation of Physical Properties of Porous Rocks and Fluid Flow Phenomenon in Porous Media Using Computer Assisted Tomography," *In-Situ*, **14**(1), 77-132 (1990)
26. Mohanty, K., Personal Communications, October 1992.
27. D'Souza, M. A., "Examination of Viscous Fingering Using the CAT-Scanner", M.S. Thesis, Department of Petroleum Engineering, Texas A&M University, College Station, TX (1992).
28. Chang, S.H. and Slattery, J.C., "Nonlinear Stability Analysis of Miscible Displacements," *Transport in Porous Media*, **5**, 49 (1990).
29. Peaceman, D.W. and Rachford, H.H., "Numerical Calculation of Multidimensional Miscible Displacements," *Soc. Pet. Eng. J.*, **2**, 327 (1962).
30. Zalesak, S.T., "Advances in Computer Methods for Partial Differential Equations - V," R. Vichnevetsky and R.S. Stepleman, editors, IMACS Rutgers University (1984).

☆U.S. GOVERNMENT PRINTING OFFICE: 1994 - 560-030/00008